Title
Probing Atomic-Scale Properties of Organic and Organometallic Molecules by Scanning Tunneling Spectroscopy

Author
Yamachika, Ryan

Publication Date
2009

Peer reviewed|Thesis/dissertation

Probing Atomic-Scale Properties of Organic and Organometallic Molecules by Scanning Tunneling Spectroscopy

by

Ryan Tsuyoshi Yamachika

A dissertation submitted in partial satisfaction of the

requirements for the degree of

Doctor of Philosophy

in

Physics

in the

Graduate Division

of the

University of California, Berkeley

Committee in charge:

Professor Michael F. Crommie, Chair
Professor Steven G. Louie
Professor Jeffrey R. Long

Fall 2009

Probing Atomic-Scale Properties of Organic and Organometallic Molecules by Scanning Tunneling Spectroscopy

by

Ryan Tsuyoshi Yamachika

Abstract

Probing Atomic-Scale Properties of Organic and Organometallic Molecules by Scanning Tunneling Spectroscopy

by

Ryan Tsuyoshi Yamachika

Doctor of Philosophy in Physics

University of California, Berkeley

Professor Michael F. Crommie, Chair

The study of molecular physics has become increasingly important from both a scientific and technological viewpoint. The physical behavior of materials at nanometer length scales holds many surprises and the potential technological applications of molecular science are vast. This dissertation focuses on the fundamental physics of molecules adsorbed to metallic and semiconducting surfaces.

Using a scanning tunneling microscope, four different molecular systems, C_{60}, Gd@C_{82}, tetramantane, and tetracyanoethylene (TCNE), were studied. The main effects investigated were (1) how can the properties of these molecules be atomically controlled, (2) how do metal surfaces affect molecular properties, (3) how do electron-electron and electron-vibration coupling influence molecular behavior, and (4) how do spins behave in molecule-scale structures. For C_{60} we demonstrate a fine control of molecular properties such as energy levels, electron-electron interactions, and electron-vibration interactions via potassium doping. We also find that metal surfaces strongly influence the electronic screening and ordering of adsorbed molecules. In Gd@C_{82} and tetramantane molecules, the spatial distribution of the electron-vibration coupling is found to be very inhomogeneous at sub-nanometer ($< 10^{-9}$ m) length scales. In titanocene, we find that Au(111) induces molecular dissociation, with titanocene fragments displaying a spin-induced Kondo effect. The final molecule, TCNE, displays variable surface coupling and also enables tunable magnetic exchange coupling between covalently bonded spin centers in $V_x(TCNE)_y$ complexes.

Contents

List of Figures

List of Abbreviations

DFT	Density Functional Theory
dI/dV	Differential Conductance
DOS	Electronic Density of States
e_c	Absolute value of the Electron Charge
E_F	Fermi energy
FT	Fourier Transform
FE	Field Emission
FWHM	Full Width at Half Maximum
HOMO	Highest Occupied Molecular Orbital
IETS	Inelastic Tunneling Spectroscopy
JT	Jahn-Teller
LDOS	Local Density of States
LT	Low Temperature (around 77 K or lower)
LUMO	Lowest Unoccupied Molecular Orbital
ML	Monolayer
NDR	Negative Differential Resistance
NRG	Numerical Renormalization Group
rms	Root Mean Square
RT	Room Temperature
STM	Scanning Tunneling Microscopy *or* Scanning Tunneling Microscope
STS	Scanning Tunneling Spectroscopy
UHV	Ultra High Vacuum

Acknowledgments

There are many people to thank for their support throughout the time that the work for this dissertation was done. The people you work with will influence success as much as the research does, so I have been fortunate to work with many people that are both helpful and enjoyable to work with. The first is Professor Mike Crommie. He allowed me to work in his group and let me work with a flexible schedule. He wants his students to succeed and will do what he can to help them.

There are many people to thank that I directly worked with. I learned from them, but they are also great to work with and made lab work more enjoyable. I learned most of the experimental details of STM from Mike Grobis, who also introduced me to much of the theory. In addition, there were many people directly involved with doing the experiments, analyzing data, fixing the STM, and writing the papers with me: postdocs Kastumi Nagaoka, Andre Wachowiak, Yayu Wang, Daniel Wegner, Chenggang Tao, grad students Xinghua Lu, Xiaowei Zhang, and undergrads Steve Sharma, Melissa Panlasigui, and Yasaman Bahri.

There are also others in the group to thank who I sometimes work with or discuss stuff with: postdocs Armen Kirakosian, Luis Berbil-Bautista, Yossi Yayon, Yuanbo Zhang, Sarah Burke, grad students Jongweon Cho, Matthew Comstock, Niv Levy, Victor Brar, Yen-chia Chen, Kacey Meaker, Ivan Pechenezhskiy, Maria Longobardi, Lorenzo Maserati undergrads Nate Jenkins, Annie Endozo, Travis Zach, Lorenzo Flores and Yuri Zuev. They are again great to work with and make the work more enjoyable.

There are also many theory collaborators who provided computational and theoretical assistance. They helped model the experimental data and explain the theory. For DFT related theory, Professor Steven Louie and his group members Khoonghong Khoo, Jeff Neaton, Jay Sau, and Manos Kioupakis have provided much assistance. Mark Pederson has helped us with magnetism related DFT. For strong correlations theory, Professor Joel Moore and his group member Noah Bray-Ali, as well as Professor Dung-Hai Lee have helped us understand the Kondo effect, as well as other many-body effects in our data.

There are also many collaborators who synthesized the molecules that we studied. Without their high quality samples, many of our experiments would not be possible. Professor Jeffrey Long and group members Lianne Beltran, Bart Bartlett, and Jeff Rheinhardt synthesized the magnetic molecules that we studied. H. Kato and H. Shinohara made very pure $Gd@C_{82}$ which we were not able to obtain elsewhere. Jeremy Dahl donated the diamondoids which we studied.

There are also other people in the department who provided help. Anne Takizawa and Donna Sakima are staff members who ensure that all the paperwork and bureaucratic details are completed, and nicely remind you when they are not. Two members of Zettl's group, Masa Ishigami and Shaul Aloni, provided both much technical assistance when we were studying carbon nanotubes and also useful discussions about CNT and STM.

Finally, my family and relatives have supported me throughout this time, especially my immediate family Roddy, Paula, Roddy Jr., and Pam.

Part I

Introduction

1

Why Study Single Molecules?

In technology as well as in physics, we strive to push the limits of what is possible. One particular limit is size. Semiconductor devices are getting smaller on a yearly basis, and are nearing nanometer length scales (10^{-9} m). Physicists are also trying to delve deeper into what happens at these tiny length scales, a regime where counter-intuitive quantum effects dominate. Since this size regime is the length scale of single molecules, the study and understanding of what happens to single molecules in a condensed matter environment is becoming increasingly important for both science and technology. For this reason, the study of single molecules at surfaces will be the main topic of this dissertation.

This chapter is devoted to introducing single molecule behavior from both the technological, as well as the physics viewpoints. Since new technology is based on new underlying physics, an overview of single molecule devices will be described first, followed by a summary of some underlying molecular physics. The chapter will close with an overview of this thesis.

1.1 Molecular Devices

One of the often cited laws in electronics is Moore's law [148], published in 1965 by Gordon Moore (who went to UC Berkeley as an undergrad). His law states that the number of components on an integrated circuit will double every two years, implying that the size of the components will shrink to improve performance. Moore's law has held up well in the last thirty years and will eventually lead us to nanometer sized circuit components.

At nanometer length scales, however, electrical devices are governed by quantum mechanical effects, such as electron tunneling, and will not behave as more familiar present-day devices [155]. Current semiconductor technology will likely reach its speed and power efficiency limits before this size scale is reached. To advance beyond this will require new technology, which in turn will require a new understanding of fundamental scientific issues.

Nanoscience is an emerging field of science that is concerned with these issues. This is the science of materials structured at the nanometer scale. Nanoscience has the potential

to transform our current technology since it points the way toward creating devices based on the properties of nanometer-sized molecular structures instead of bulk semiconductors. Many nanometer-size devices have already been realized [9], such as the C_{60} molecular transistor [158], the nanotube radio [97], logic gates via molecular motion [78], and rotational actuators [49]. In addition, molecule-based spintronics raises new possibilities for electronic and magnetic devices [19, 90]. The promise and potential of such devices helps motivate the research presented in this dissertation.

1.2 Molecular Physics Overview

At nanometer sizes, many bulk properties are transformed. This forces us to rethink the underlying physics of devices in the single molecule regime. The physics of such devices are affected drastically by properties such as molecule-molecule interactions, molecule-electrode interactions, and electron-electron interactions.

Molecule-molecule interactions, for example, are typically much weaker than atom-atom interactions in a bulk semiconductor device. Atoms in a molecule tend to arrange in a way that saturates dangling bonds, causing molecules to interact weakly with other molecules. This is unlike semiconductors which are comprised of atoms that interact strongly with each other due to dangling bonds. For example, in bulk C_{60}, the C_{60}-C_{60} binding energy is $\sim 0.1\,\text{eV}$, about 10 times smaller than typical atomic binding energies [62]. The weak interactions between molecules causes clusters or multilayers of molecules to have properties similar to single molecule properties. This is unlike bulk semiconductors whose band properties deviate substantially from atomic properties due to strong atom-atom interactions.

In molecular devices, the molecules contact other substances, such as electrodes, and the molecule-electrode interaction can differ from bulk semiconductor-electrode interactions. Since molecules have discrete energy levels, these discrete states will interact with the continuum of states of electrodes, an effect which does not occur in semiconductor devices which contain no discrete states. Understanding molecule-electrode interactions requires new theories incorporating ideas such as the Fano-Anderson model (§4.4.1), and new experiments.

Electron-electron interactions in single molecules can also behave quite differently from what is seen in solids. Electron-electron interactions (§3.4.2) are neglected in many solids due to electronic screening (§9.2), but typically cannot be neglected in single-molecule-based systems. Electron-electron interactions, for example, can lead to metal-insulator transitions (§4.3, chapter 9), an effect not normally seen in semiconductor devices.

One of the most important classes of molecules for different applications are carbon-based molecules, since this class of molecules is easily fabricated, has a wide range of useful properties, and is potentially biologically compatible. This class of molecules will be the focus of this dissertation. The next sections of this chapter provide a brief overview of the physics of carbon-based molecules that is relevant for molecular nanostructures embedded in a condensed matter environment. We will focus on three types of molecules: sp^2 bonded fullerenes, sp^3 bonded diamondoids, and molecules having a magnetic component.

1.2.1 Fullerenes and Diamondoids: Overview

The most useful molecules are those with many experimentally controllable interactions. Fullerenes fit this prerequisite nicely since many of their interactions, such as electron-electron interactions, are tunable via exohedral potassium (K) doping. This is why many of the studies in this dissertation involve the fullerene C_{60}.

A ball and stick model of C_{60} and a rough sketch of its energy levels are given in figure 1.1. When we dope C_{60} with K, the K atom donates one of its electrons to C_{60}. This electron

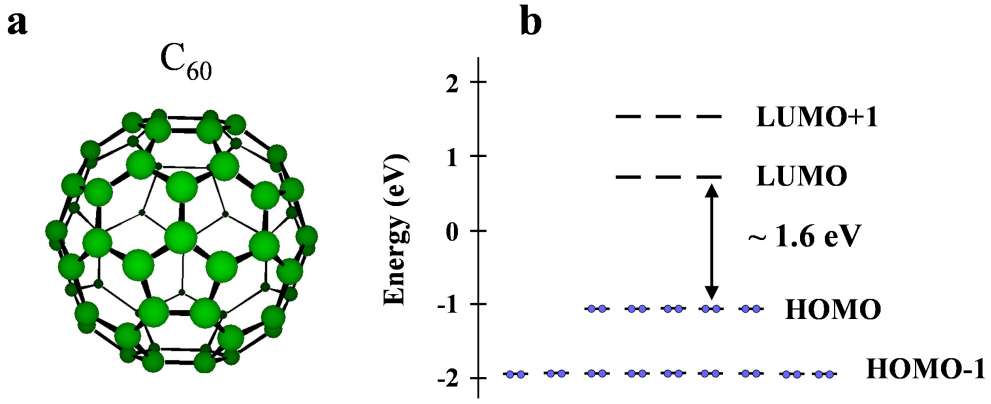

Figure 1.1: (a) Ball and stick model of C_{60}. (b) Energy levels of C_{60} from [60].

then occupies one of the C_{60} LUMO states. This process of electron donation has a number of consequences: it changes the energy of the molecular states relative to the chemical potential (chapter 6), it changes the electron-electron interactions (chapter 9), and it can modify the molecular electron-vibration interaction in the form of changes to the Jahn-Teller effect (chapter 7).

The relative magnitudes of the various interactions in C_{60} are unusual in that electron-vibration interactions, inter-molecular hybridization [207, 62], and electron-electron interactions [3, 139] are all at the same energy scale (~ 0.5–$3\,\mathrm{eV}$). These interactions compete with each other to determine the properties of the system, and since they are all similar in magnitude, small changes in any of these parameters can make one interaction win out over another. This competition between interactions causes fullerene systems to display a wide variety of behavior when the strengths of the interactions are modified via alkali metal doping, such as metal-to-insulator transitions (chapters 7, 9), superconductivity and magnetism in bulk compounds [75, 1], and novel electronic and orientational phases in thin films (chapter 8, [189, 86, 207, 22, 156]).

The unusual combination of competing interactions in C_{60} can lead to electronic properties very analogous to those seen in high-T_C superconductors. High-T_C superconductors, for example, are hole-doped Mott insulators where the mechanism of superconductivity is still controversial. Since hole-doping K_xC_{60} can be performed by removing one K per C_{60}, hole-doping the Mott insulator K_4C_{60} (ref. [55]) gives a superconductor (K_3C_{60}), analogous

to what is seen for high-T_C materials. The qualitative phase diagrams in figure 1.2 of both high-T_C superconductors and C_{60} are strikingly similar. Since the physics behind high-T_C

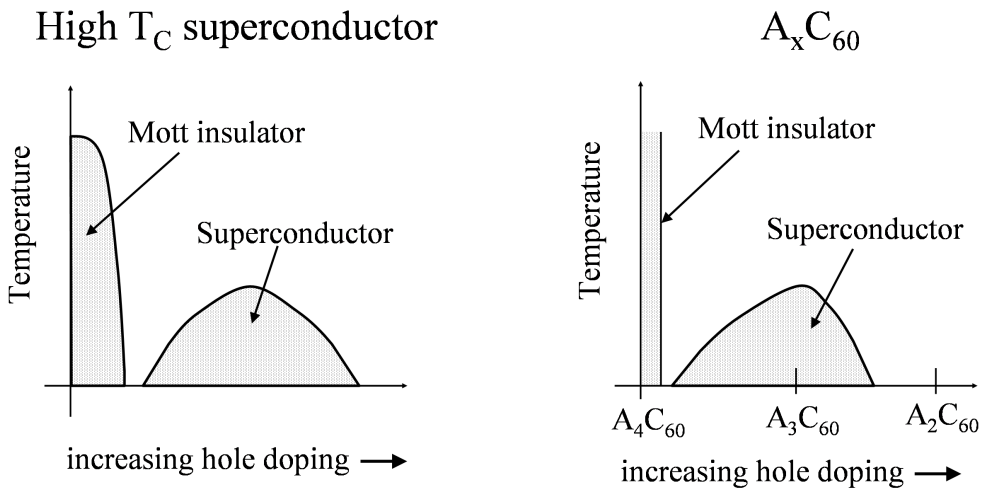

Figure 1.2: Phase diagrams of a high-T_C superconductor and A_xC_{60}, where A = alkali metal, from [209].

superconductors is unusual, the similarity between high-T_C superconductors and fullerenes helps to demonstrate the unusual physics that can happen in fullerene-based molecular materials.

In addition to modifying the properties of fullerenes by exohedral K doping, they can also be modified by endohedral doping. Gd@C_{82} (where a single Gd atom is inserted into a C_{82} cage) is an example of this. The structure of Gd@C_{82} and a sketch of its electronic energy levels, derived from [52, 128, 106], are given in figure 1.3. There is a 3 electron charge

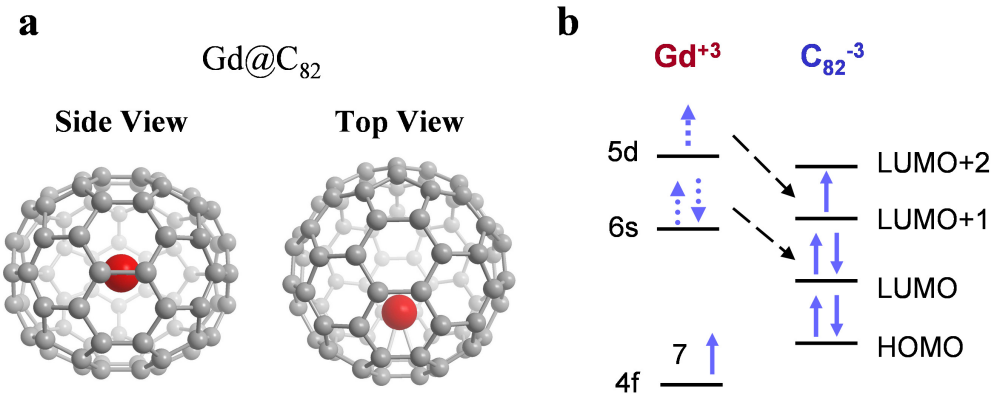

Figure 1.3: (a) Ball and stick model of Gd@C_{82}. (b) Electronic energy levels of Gd and C_{82} in a Gd@C_{82} fullerene.

transfer from Gd to C_{82} which can give rise to magnetism.

While fullerenes are sp^2 bonded carbon molecules, carbon can also form sp^3 bonds, the best known example being diamond. Molecules derived from sp^3 bonded carbon, with dangling bonds terminated with hydrogen, are known as diamondoids. They represent another class of carbon molecules with potential interesting field emission [208], thermal, and mechanical properties [137, 172].

1.2.2 Magnetic molecules: Overview

The growing field of molecule-based magnetism involves understanding magnetism at molecular sizes. Here it is important to understand the influence of substrates on the properties of magnetic molecules since molecular charge, spin, and magnetic anisotropy can change as molecules come into contact with a surface [179, 14]. To study these effects, two magnetic molecules, titanocene chloride dimers and tetracyanoethylene (TCNE), were studied in this dissertation.

The titanocene chloride dimer, $[Cp_2TiCl]_2$ with $Cp = C_5H_5$, is known in chemistry for its utility as an inexpensive reducing agent in organic synthesis [170, 54, 12, 6], but it also has magnetic properties [101]. The magnetic properties originate from the anti-ferromagnetic coupling between the spins of the two titanium atoms and make the molecule an interesting choice for studying molecular magnetism.

Tetracyanoethylene (TCNE) is a strong π-electron acceptor with a large electron affinity [33] that easily forms charge-transfer complexes where it pulls electrons from neighboring metal atoms or molecules [50, 140]. For complexes of the form $M(TCNE)_x$, where M is a paramagnetic transition-metal ion, molecule-based ferromagnetism is present in these complexes and the Curie temperatures can be high [136, 212, 146, 93]. Bulk $V(TCNE)_x$ ($x \sim 2$), for example, has a Curie temperature $T_C \sim 400\,\mathrm{K}$ (references [136, 167, 185, 113]). However, the origin of the ferromagnetism is not well understood, making TCNE an interesting candidate to explore molecule-based magnetism.

1.3 Dissertation Overview

This dissertation will focus on the fundamental physics of molecular nanostructures in contact with a surface. Some of the outstanding questions that will be addressed are

1. How can we modify and control the properties of adsorbed molecules at the atomic scale?

2. How do different substrates, such as metal electrodes, affect the properties of a molecule?

3. How do electron-electron, electron-vibration, and molecule-molecule interactions influence the properties of single molecules in a condensed matter environment?

Some of the main conclusions of this work are that the electronic properties of molecules can be precisely modified and controlled at the atomic scale, a metallic surface can substantially

change the energies and ordering of molecules, electron-electron and electron-vibration interactions can induce metal to insulator transitions, and electron-vibration interactions are inhomogeneous at molecular length scales.

To perform the studies described here, it is critical to utilize a local probe with sub-nanometer resolution. This is why a scanning tunneling microscope (STM) is used in all the experiments in this dissertation. The unique combination of high spatial resolution ($\lesssim 1\,\text{Å}$) and the ability to modify and manipulate molecules makes the STM ideal for studying the properties of molecular nanostructures at surfaces.

This dissertation contains three main parts. The first part is an introduction to the theory and experimental techniques necessary to understand the work performed here. This is comprised of four chapters. The first (chapter 2) gives a simplified view of the theory of tunneling. The second (chapter 3) presents a more general description with corrections to many commonly made approximations. The third (chapter 4) describes much of the background physics of nanostructures used in the dissertation. The fourth (chapter 5) describes the instrumental details of the scanning tunneling microscope and related equipment used for all the experiments.

The second part of the dissertation describes specific experimental studies performed on three carbon-based molecules: C_{60}, Gd@C_{82}, and diamondoids. The main results for C_{60} are that metal surfaces substantially affect the electron-electron interactions in C_{60}, and that the properties of single C_{60} molecules and C_{60} films can be controlled via atomic doping with K atoms. These properties include molecular energy levels, electron-phonon interactions, electron-electron interactions, and local ordering. For the second molecule, Gd@C_{82}, we are able to spatially map out the strength of the electron-vibration interaction, and show that it is spatially very inhomogeneous. In the last molecule, diamondoid tetramantane, we see a very inhomogeneous electron-vibration interaction, but we also see very localized HOMO orbital behavior and a large ($> 5\,\text{eV}$) quasiparticle HOMO-LUMO gap, unlike C_{60} and Gd@C_{82}.

The third part of this dissertation describes our studies of titanocene and TCNE molecules on surfaces. Titanocene is seen to display fragmentation on Au(111). The fragments form well-ordered phases where one type of fragment has a magnetic moment. The other magnetic molecule, TCNE, exhibits variable substrate interaction with different metal surfaces. On Ag(001), the TCNE-substrate interaction leads to strong charge transfer and the molecules on this surface can be combined with vanadium via molecular manipulation with the STM tip to form $V_x(TCNE)_y$ structures. Depending on the particular structure of the $V_x(TCNE)_y$ complex and its orientation relative to the Ag(001) substrate, the strength of the TCNE-mediated spin coupling between V atoms can be adjusted.

2

Scanning Tunneling Microscopy Principles

This chapter will introduce a standard theory to describe scanning tunneling microscopy. This theory will be used often in the dissertation to explain intuitively and quantitatively what an STM measures. However, there are important corrections to the standard theory that should be known, and these corrections will be discussed in the following chapter.

In scanning tunneling microscopy (STM), a sharp metal tip is placed very close ($\sim 6\,\text{Å}$) to a conducting sample that we wish to study (figure 2.2). Although the tip and sample are not touching, when a voltage is applied to the tip relative to the sample, the electrons from the tip may still move into the sample by a quantum mechanical process called tunneling. Qualitatively, the probability for an electron to travel across the vacuum between tip and sample depends exponentially on the tip-sample distance, which is what gives the STM its high spatial resolution. Quantitatively, the formal mathematical theory of electron tunneling in STM was given first by Bardeen [11] and then by Tersoff and Hamann in [186]. A slightly different and more detailed derivation will be given in this section. The main results will be the general equation for the tunneling current (2.2) and the simplified form for differential conductance (2.5).

2.1 Tunneling

2.1.1 General expression for tunneling

To formally describe electron tunneling in STM, we would like to apply Fermi's Golden Rule to calculate the transition rate for electrons to move from the tip to the sample. This rate of transition multiplied by the electron charge is the tunneling current measured in STM experiments. Fermi's Golden Rule states that if ψ_i and ψ_f are eigenstates of a Hamiltonian H, then the transition rate W from state ψ_i to ψ_f due to the presence of a perturbing Hamiltonian H' is

$$W_{i\to f} = \frac{2\pi}{\hbar}\left|\langle\psi_f|H'|\psi_i\rangle\right|^2\rho_f(E_i) \tag{2.1}$$

where $\rho_f(E_i)$ is the density of states at the energy of the initial state ψ_i (page 332 in [174]). The only problem to applying Fermi's Golden Rule to tunneling is that the initial state $|\psi_i\rangle$ and final state $|\psi_f\rangle$ should be eigenstates of a single system, but for tunneling we like to separate the initial state (a tip state) from the final state (a sample state) and treat the initial and final states as existing on two different systems. Despite this problem, in the case of tunneling we may still justify the use of Fermi's Golden rule. This will be discussed in §2.2 and in this section we will assume that Fermi's Golden Rule can be applied.

Starting with Fermi's Golden Rule, to describe electron tunneling in STM we will need to make 5 additional assumptions. These additions will assume that the initial state is in the STM tip and the final state is in the sample, as follows:

1. The tip states may form a continuum. In this case, we must multiply (2.1) by the number of tip electrons that participate in tunneling $\rho_t(E_t)\,dE_t$. The transition rate $dW_{t\to s}$ of electrons from tip to sample due to states within an energy range dE_t around energy E_t is
$$dW_{t\to s} = \frac{2\pi}{\hbar}\big|\langle\psi_s|H'|\psi_t\rangle\big|^2\rho_s(E_t)\rho_t(E_t)\,dE_t$$
where ψ_s and ψ_t represent the sample and tip wavefunctions respectively, while ρ_s and ρ_t represent the sample and tip density of states, respectively.

2. An electron transition from a state ψ_t to ψ_s can only take place if ψ_t is occupied by an electron and ψ_s is unoccupied. Since the electron occupancy is given by the Fermi-Dirac distribution $f(E) = [\exp(\frac{E-\mu}{kT}) + 1]^{-1}$, we must multiply ρ_t by the probability $f(E)$ that the states are occupied and multiply ρ_s by the probability $1 - f(E)$ that the states are unoccupied
$$dW_{t\to s} = \frac{2\pi}{\hbar}\big|\langle\psi_s|H'|\psi_t\rangle\big|^2\rho_s(E_t)\big(1 - f(E_t)\big)\rho_t(E_t)f(E_t)\,dE_t$$

3. When we apply a voltage difference V_t to the STM tip relative to the sample, we assume we simply shift the density of states of the tip by $-e_cV_t$, where e_c is the absolute value of the electron charge. The Fermi-Dirac distribution also shifts since the voltage changes the chemical potential by $-e_cV_t$. The shifted Fermi-Dirac distribution can be written as $f(E + e_cV_t) = [\exp(\frac{E+e_cV_t-\mu}{kT}) + 1]^{-1}$ where μ is the chemical potential with no applied voltage. The transition rate is now
$$dW_{t\to s} = \frac{2\pi}{\hbar}\big|\langle\psi_s|H'|\psi_t\rangle\big|^2\rho_s(E_t)\big(1 - f(E_t)\big)\rho_t(E_t + e_cV_t)f(E_t + e_cV_t)\,dE_t\,.$$

4. If the wavefunctions $\psi_{s,1}$, $\psi_{s,2}$, …, $\psi_{s,N(E_t)}$ on the sample give rise to $N(E_t)$ distinct matrix elements at energy E_t, we must sum over the $N(E_t)$ contributions from each

different matrix element [174]

$$dW_{t\to s} = \frac{2\pi}{\hbar}\sum_{n}^{N(E_t)} \left|\langle\psi_{s,n}|H'|\psi_t\rangle\right|^2 \rho_{s,n}(E_t)\big(1-f(E_t)\big)\rho_t(E_t+e_cV_t)f(E_t+e_cV_t)\,dE_t$$

where $\rho_{s,n}$ now represents the number of states per energy on the sample with matrix element $\langle\psi_{s,n}|H'|\psi_t\rangle$.

5. We must take into account transitions from the sample states back to the tip states at energy E_t

$$dW_{s\to t} = \frac{2\pi}{\hbar}\sum_{n}^{N(E_t)} \left|\langle\psi_t|H'|\psi_{s,n}\rangle\right|^2 \rho_{s,n}(E_t)f(E_t)\rho_t(E_t+e_cV_t)\big(1-f(E_t+e_cV_t)\big)\,dE_t\,.$$

We will subtract this off of $dW_{t\to s}$ next.

Using the previous assumptions, the total electron transition rate between sample and tip is then

$$\begin{aligned} W &= \int (dW_{s\to t} - dW_{t\to s}) \\ &= \frac{2\pi}{\hbar}\int_{-\infty}^{\infty}\sum_{n}^{N(E_t)} \left|\langle\psi_{s,n}|H'|\psi_t\rangle\right|^2 \rho_{s,n}(E_t)\rho_t(E_t+e_cV_t)\big[f(E_t)-f(E_t+e_cV_t)\big]\,dE_t \end{aligned}$$

and the total tunneling current at voltage V_t is

$$\begin{aligned} I(V_t) &= -e_cW \\ &= \frac{2\pi e_c}{\hbar}\int_{-\infty}^{\infty}\sum_{n}^{N(E_t)} \left|\langle\psi_{s,n}|H'|\psi_t\rangle\right|^2 \rho_{s,n}(E_t)\rho_t(E_t+e_cV_t)\big[f(E_t+e_cV_t)-f(E_t)\big]\,dE_t \end{aligned}$$

(we have defined positive current to mean electrons tunnel from tip to sample). Normally in STM, we express everything in terms of the *sample bias* which is the voltage of the sample relative to the tip $V_{\text{sample}} = -V_t$. This is the convention even when we apply the voltage to the tip. In terms of the sample bias $V_{\text{sample}} = V$,

$$I(V) = \frac{2\pi e_c}{\hbar}\int_{-\infty}^{\infty}\sum_{n}^{N(E_t)} \left|\langle\psi_{s,n}|H'|\psi_t\rangle\right|^2 \rho_{s,n}(E_t)\rho_t(E_t-e_cV)\big[f(E_t-e_cV)-f(E_t)\big]\,dE_t\,. \quad (2.2)$$

This is a general first order expression for the tunneling current for non-interacting electrons.

2.1.2 Simplified expression for tunneling

In order to simplify (2.2), a few standard approximations are used, as follows:

1. We assume in STM that the tip DOS is a constant, ρ_T.

2. We approximate the matrix elements using Bardeen's matrix element expression (§2.2). Tersoff and Hamann [186] have calculated the Bardeen matrix element assuming that the wave functions at the end of the tip are s-waves centered at position $\vec{r}_0$. The matrix element has the form $A(\phi, R)\psi_{s,n}(\vec{r}_0)$ where ϕ is the work function, assumed to be the same for both tip and sample, R is the radius of the potential at the end of the tip, and A is a function which depends on both ϕ and R. Using these approximations, the tunneling current at tip position $\vec{r}_0$ and sample voltage V is

$$I(\vec{r}_0, V) = \frac{2\pi e_c}{\hbar}\rho_T A^2(\phi, R) \int_{-\infty}^{\infty} \sum_n^{N(E_t)} \left|\psi_{s,n}(\vec{r}_0)\right|^2 \rho_{s,n}(E_t)\big[f(E_t - e_cV) - f(E_t)\big]\, dE_t$$

   Usually, the differential conductance, dI/dV, at tip position $\vec{r}_0$ and sample voltage V is a more useful quantity:

$$\frac{dI}{dV}(\vec{r}_0, V) = \frac{2\pi e_c}{\hbar}\rho_T A^2(\phi, R) \int_{-\infty}^{\infty} \sum_n^{N(E_t)} \left|\psi_{s,n}(\vec{r}_0)\right|^2 \rho_{s,n}(E_t)\frac{\partial f(E_t - e_cV)}{\partial V}\, dE_t\,. \quad (2.3)$$

3. Since most data is taken at low temperatures, $\partial f(E_t - e_cV)/\partial V \approx e_c\delta(E_{\rm F} + e_cV)$, and dI/dV takes a simpler form

$$\frac{dI}{dV}(\vec{r}, V) = \frac{2\pi e_c^2}{\hbar}\rho_T A^2(\phi, R) \sum_n^{N(E_{\rm F}+e_cV)} \left|\psi_{s,n}(\vec{r})\right|^2 \rho_{s,n}(E_{\rm F} + e_cV) \quad (2.4)$$

Equation 2.4 describes what an STM measures. It is slightly different from what is normally written, e.g. in [186]. To see the usual form, we think of the sample density of states ρ_s as being the sum over many delta functions, very closely spaced energetically: $\rho_s(E) = \sum_k \delta(E - E_k)$. Since, in general, every wavefunction $\psi_{s,n}$ of the sample has a different matrix element, and since $\rho_{s,n}$ is defined as the density of states with matrix element $\langle\psi_{s,n}|H'|\psi_t\rangle$, then $\rho_{s,n}$ is just the density of states of the wavefunction $\psi_{s,n}$; i.e., $\rho_{s,n}(E) = \delta(E - E_n)$. The expression for dI/dV then simplifies to

$$\frac{dI}{dV}(\vec{r}, V) \propto \sum_n^{N(E_{\rm F}+e_cV)} \left|\psi_{s,n}(\vec{r})\right|^2 \delta\big((E_{\rm F} + e_cV) - E_n\big) = \mathrm{LDOS}(\vec{r}, E_{\rm F} + e_cV) \quad (2.5)$$

where LDOS stands for local density of states (defined by (4.1)) of the sample. This is the familiar expression for dI/dV and is the fundamental equation that describes what an STM

measures. All of the various STM measurement techniques described below will use the result (2.5).

2.2 Tunneling matrix elements

Sometimes Fermi's Golden Rule is used to calculate electron tunneling rates, but this is not necessarily justified, as pointed out in [186]: Fermi's Golden Rule describes transitions between eigenstates of one system and not transitions between an eigenstate of one system (the tip) and an eigenstate of another system (the sample). However, Fermi's Golden Rule can be extended so that it is applicable to tunneling. This section will discuss the extended version of Fermi's Golden Rule and how this extended rule can be applied to tunneling. Then the tunneling matrix element in Fermi's Golden Rule will be rewritten in the more symmetric form known as the Bardeen matrix element.

2.2.1 Extended Fermi's Golden Rule

Fermi's Golden Rule is usually stated as the following: for a system with Hamiltonian H_0 and eigenstates $H_0|\psi_n\rangle = E_n|\psi_n\rangle$, if a constant perturbation with Hamiltonian H' is applied to the system, then after a long enough time, (2.1) may be applied to calculate the first order transition rate between two eigenstates of the unperturbed system. From this statement, we see that Fermi's Golden Rule describes transitions between eigenstates $|\psi_n\rangle$ of H_0 and not transitions between an eigenstate $|\psi_n\rangle$ and an arbitrary state $|\alpha\rangle$. While this restriction that we only consider transitions between eigenstates of H_0 is sufficient to prove Fermi's Golden Rule, we will see that it is not a necessary condition.

This is a statement of an extended version of Fermi's Golden Rule. Suppose $|\psi_n\rangle$ are eigenstates with energies E_n of the time-independent Hamiltonian H_0 and

$$H_P(t) = \begin{cases} 0, & \text{for } t < 0 \\ H', & \text{for } t \geq 0 \end{cases}$$

is a perturbing Hamiltonian as a function of time t. H' is a constant and the total Hamiltonian for the system is $H = H_0 + H_P$. If the time-independent normalized state $|\alpha\rangle$ satisfies the following conditions

$$(H_0 + H')|\alpha\rangle = E_\alpha|\alpha\rangle \tag{2.6}$$

$$\text{and} \quad \langle\alpha|\psi_n\rangle = 0 \text{ for all } n. \tag{2.7}$$

Then, in the limit $t \to \infty$, the transition rate from $|\psi_I\rangle$ to $|\alpha\rangle$ is

$$W_{I\to\alpha} = \frac{2\pi}{\hbar}\left|\langle\alpha|H'|\psi_I\rangle\right|^2 \rho_f(E_I)\,. \tag{2.8}$$

where ρ_f is the density of final states. This result means Fermi's Golden Rule can be used to calculate the transition rate between $|\psi_I\rangle$ and $|\alpha\rangle$ as long as $|\alpha\rangle$ satisfies (2.6) and (2.7).

To prove this result, we first assume that the system is in the state $|\Psi(t)\rangle = e^{-iE_I t/\hbar}|\psi_I\rangle$ for $t < 0$, which is an eigenstate of the total Hamiltonian $H = H_0 + H_P = H_0$ for $t < 0$. Then for $t \geq 0$, the perturbing Hamiltonian causes $|\Psi(t)\rangle$ to not be an eigenstate of the total Hamiltonian $H = H_0 + H'$ anymore. In general, $|\Psi(t)\rangle$ for $t \geq 0$ will be in a superposition of eigenstates

$$|\Psi(t)\rangle = a(t)e^{-iE_\alpha t/\hbar}|\alpha\rangle + \sum_n c_n(t)e^{-iE_n t/\hbar}|\psi_n\rangle \, .$$

Note that $|a(t)|^2$ represents the probability of being in state $|\alpha\rangle$ after time t. If we plug $|\Psi(t)\rangle$ into the time dependent Schrödinger equation

$$(H_0 + H')|\Psi(t)\rangle = i\hbar\frac{\partial}{\partial t}|\Psi(t)\rangle$$

we can simplify the result using (2.6) and $H_0|\psi_n\rangle = E_n|\psi_n\rangle$. After this simplification, we can multiply the resulting equation on the left by $\langle\alpha|$ and simplify the result using $\langle\alpha|\alpha\rangle = 1$ and (2.7) to get

$$\frac{d}{dt}a(t) = -\frac{i}{\hbar}\sum_n c_n(t)e^{i(E_\alpha - E_n)t/\hbar}\langle\alpha|H'|n\rangle$$

This expression may be solved by successive approximation. For example, we take the right hand side of the equation as the zeroth order approximation (to zeroth order, $|\Psi(t)\rangle$ is in state I, so $c_n(t) = \delta_{n,I}$), then the resultant equation

$$\frac{d}{dt}a(t) = -\frac{i}{\hbar}e^{i(E_\alpha - E_I)t/\hbar}\langle\alpha|H'|I\rangle$$

determines the first order approximation to $a(t)$. If we now look at the derivation of Fermi's Golden Rule in §5.6 in [174], we see that this result is exactly equation 5.6.17, and hence, the rest of the steps leading to (2.8) will be exactly the same as those in §5.6 in [174].

2.2.2 Extended Golden Rule in tunneling

To justify using Fermi's Golden Rule to describe electrons tunneling from an STM tip to a sample, one must then argue why the sample eigenstates $|\psi_{s,n}\rangle$ satisfy conditions (2.6) and (2.7). This is where the approximations of Bardeen come in. These are the approximations:

1. Assume that the potential for the sample is localized to the sample and potential for the tip is localized to the tip. This is a reasonable approximation for tunneling.

2. Assume that all tip wavefunctions are localized to the tip and all sample wavefunctions are localized to the sample. This should be a reasonable approximation for the bound states.

3. Assume that the tip and sample are sufficiently far apart so that there is little overlap between tip and sample wavefunctions, and tip and sample are sufficiently far apart so that the tip potential is zero in the region of space occupied by the sample and sample potential zero in the region of space occupied by the tip.

A sketch of the potentials and wavefunctions under these approximations is given in figure 2.1.

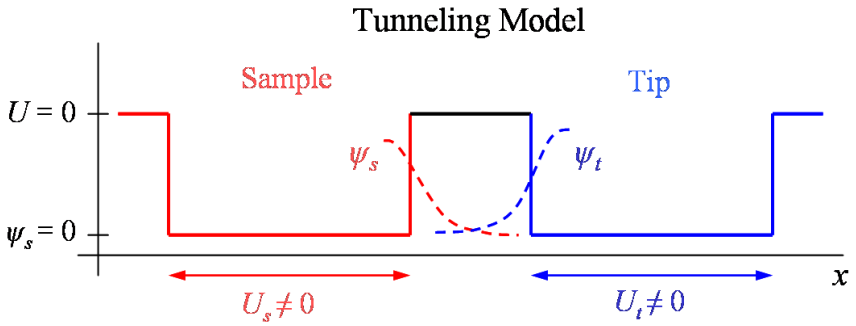

Figure 2.1: Approximate potentials (solid lines) and wavefunctions (dashed lines) for the STM tip and sample in Bardeen's approximation. Only certain regions have non-zero potential and non-zero wavefunctions.

We will now use these assumptions to show (2.6) and (2.7). Suppose

$$H_s = \frac{\vec{p}^2}{2m} + U_s\,, \quad H_t = \frac{\vec{p}^2}{2m} + U_t\,, \quad \text{with} \quad \vec{p} = \frac{\hbar}{i}\nabla \tag{2.9}$$

are the Hamiltonians for the sample and tip, respectively. The sample eigenstates are $\psi_{s,n}$ while the tip eigenstates are $\psi_{t,n}$. We then consider the sample potential U_s as a perturbation to the tip, so $H_0 = H_t$ and $H' = U_s$. We want to show that $\psi_{s,n}$ satisfies (2.6) and (2.7).

We first show (2.6). We want to show $\psi_{s,n}$ satisfies $(H_0 + H')\psi_{s,n} = E_{s,n}\psi_{s,n}$. Since $H_0 + H' = p^2/2m + U_t + U_s$,

$$(H_0 + H')\psi_{s,n} = (H_s + U_t)\psi_{s,n} = E_{s,n}\psi_{s,n} + U_t\psi_{s,n}\,.$$

To satisfy (2.6), we must show $U_t\psi_{s,n} = 0$. By assumption 1, the potential U_t is localized to the tip while assumption 2 states $\psi_{s,n}$ is localized to the sample; more precisely, by assumption 3, U_t is zero in the sample while $\psi_{s,n}$ is zero in the tip. Hence, U_t is zero whenever $\psi_{s,n}$ is non-zero and U_t is non-zero whenever $\psi_{s,n}$ is zero. The product $U_t\psi_{s,n}$ must then be zero everywhere. We may also see that the product $U_t\psi_{s,n}$ is zero from figure 2.1. Therefore, $(H_0 + H')\psi_{s,n} = E_{s,n}\psi_{s,n}$ and (2.6) is satisfied.

Next, show (2.7). By assumption 3, the sample and tip wavefunctions have little overlap, so that $\langle\psi_{s,n}|\psi_{t,n}\rangle \approx 0$. So (2.7) is satisfied approximately. This can also be seen in figure 2.1. We have now shown that all conditions to apply Fermi's Golden rule have been satisfied,

which means we may apply (2.1) to electrons tunneling between tip and sample; i.e.,

$$W_{t\to s} = \frac{2\pi}{\hbar}\left|\langle\psi_{s,n}|H'|\psi_{t,m}\rangle\right|^2 \rho_s(E_t)\,,$$

where $\rho_s(E_t)$ is the sample DOS at the energy E_t of the state $|\psi_{t,m}\rangle$.

2.2.3 Bardeen's matrix elements

From the derivation above, we see that the perturbing Hamiltonian is just the potential energy of the sample $H' = U_s$. In this case, one can simply write the matrix elements in Fermi's Golden Rule as

$$M_{nm} \equiv \langle\psi_{s,n}|H'|\psi_{t,m}\rangle = \langle\psi_{s,n}|U_s|\psi_{t,m}\rangle = \int_V \psi^*_{s,n}(\vec{r})U_s\psi_{t,m}(\vec{r})\,d\vec{r}$$

where the integral is taken over the volume V where $U_s \neq 0$. In principle, this is all that must be calculated to find the transition probabilities. However, by doing a few mathematical manipulations, the matrix element can be written in a more symmetric form completely in terms of the tip and sample wavefunctions.

One first rewrites $\psi^*_{s,n}U_s$ in the integral in terms of derivatives of $\psi^*_{s,n}$ by using $H_s\psi^*_{s,n} = E_{s,n}\psi^*_{s,n}$ (equation 2.9). One then has an integral with $E_{s,n}\psi_{t,m}$ in it. One may rewrite this term as $E_{t,m}\psi_{t,m}$ since energy is conserved, so $E_{s,n} = E_{t,m}$, and one may then substitute for $E_{t,m}\psi_{t,m}$ using $H_t\psi_{t,m} = E_{t,m}\psi_{t,m}$ (equation 2.9). Writing H_t explicitly in terms of derivatives then allows us to use the derivative identity $\nabla\cdot(f\vec{A}) = f\nabla\cdot\vec{A} + \nabla f\cdot\vec{A}$ to rewrite the matrix element as

$$M_{nm} = \frac{\hbar^2}{2m}\int_V \nabla\cdot(\psi_{t,m}\nabla\psi^*_{s,n} - \psi^*_{s,n}\nabla\psi_{t,m})\,d\vec{r} + \int_V \psi^*_{s,n}U_t\psi_{t,m}\,d\vec{r}\,.$$

The second integral is zero since we integrate over the volume where $U_s \neq 0$ and $U_t = 0$ in that region (figure 2.1). Applying the divergence theorem to the remaining integral gives the *Bardeen matrix element*

$$M_{nm} = \frac{\hbar^2}{2m}\int_A (\psi_{t,m}\nabla\psi^*_{s,n} - \psi^*_{s,n}\nabla\psi_{t,m})\cdot d\vec{A}$$

where the integral is taken over any surface that separates tip from sample. More details about the Bardeen matrix elements can be found in §2.2 of [29], while corrections to the matrix elements can be found in chapter 3 of [29].

2.3 STM Topography

We first define the plane of the sample's surface to be the xy-plane and the direction perpendicular to the surface as the z direction (figure 2.2). In STM topography, we apply a constant voltage to the tip or sample (figure 2.2 shows it applied to the tip, which is equivalent to applying $V = -V_{\text{tip}}$ to the sample) and move the tip in the xy-plane with a feedback mechanism that controls the movement of the tip in the z direction so that the tunneling current $I(V)$ is kept constant (figure 2.2). The plot of the change in the z position of the

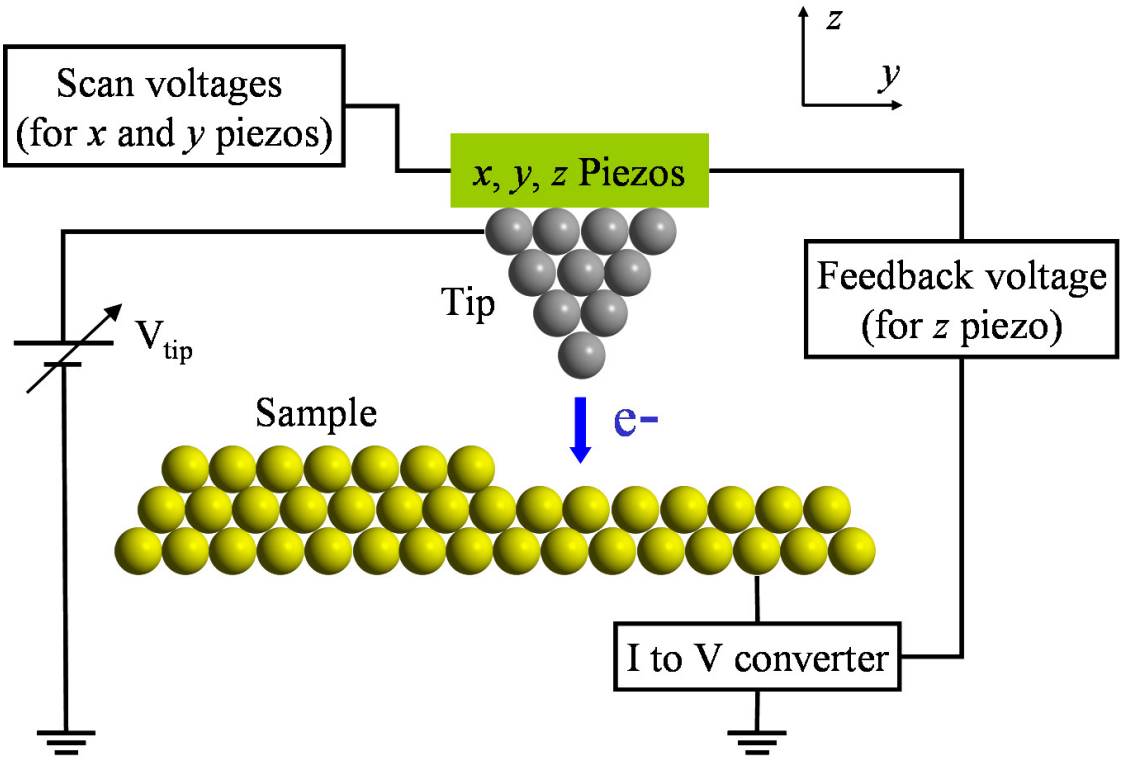

Figure 2.2: Diagram showing the basic setup of an STM. A constant voltage V_{tip} is applied to the tip while voltages are applied to piezos to move the tip in the x and y directions. The tunneling current is measured by a current to voltage converter connected to the sample and the tunneling current (after conversion to a voltage) enters feedback electronics which applies a voltage to the z piezo to move the tip in the z direction so that the tunneling current is kept constant.

tip as a function of x and y is a constant-current topograph. Since the current is given by

$$I(\vec{r}, V) = \int_0^V \frac{dI}{dV}(\vec{r}, V)\, dV \propto \int_0^V \text{LDOS}(\vec{r}, E_{\text{F}} + e_c V)\, dV$$

the feedback adjusts the tip height to keep the integral of the LDOS from 0 to V constant. What we then plot in a topograph is a surface where the integral of the LDOS is constant. If the voltage is sufficiently small, then $I(\vec{r}, V_0) = \int_0^{V_0} dI/dV\, dV \sim dI(\vec{r}, V_0)/dV \propto \text{LDOS}(\vec{r}, E_\text{F} + e_c V_0)$, so that the topograph shows a surface of constant LDOS near the Fermi energy. Since $\text{LDOS}(\vec{r}, E_\text{F} + e_c V) \sim \sum |\psi(\vec{r})|^2$ what a low bias topograph shows is a surface where the sum of the squares of the wavefunctions near E_F is constant; i.e., it shows the spatial distribution of the orbitals near E_F.

2.4 Elastic Spectroscopy

In dI/dV spectroscopy (also simply called spectroscopy), we keep the tip at a fixed position $\vec{r}_0$ and measure dI/dV as we change the voltage. We normally do not numerically differentiate $I(V)$; instead, we use a lock-in amplifier to measure dI/dV (appendix A). Since $dI(\vec{r}_0)/dV \propto \text{LDOS}(\vec{r}_0, E_\text{F} + e_c V)$, what we then measure is the sample's LDOS at position $\vec{r}_0$ as a function of energy. Since $\text{DOS}(E) = \sum_n \delta(E - E_n)$, we may think of $\text{LDOS}(\vec{r}, E_0) = \sum_m |\psi(\vec{r})|^2 \delta(E - E_0)$ roughly as the density of states at energy E_0 multiplied by the square of all wavefunctions with energy E_0 at position $\vec{r}$.

Since the dI/dV measures LDOS which is not the same as the DOS, to get a better measure of the density of states of the sample, we may average dI/dV spectroscopy curves taken at various positions over the sample. This gives a better measure of the DOS because the integral of $\text{LDOS}(\vec{r}, E)$ over all space is $\text{DOS}(E)$ (§4.1); hence, by averaging spectroscopy curves over different points in space, we are effectively integrating LDOS over space, and the more positions in space we average over, the closer the average becomes to the integral, and the closer the average dI/dV is to the DOS.

2.5 dI/dV maps

A dI/dV map is taken by keeping the tip voltage constant and scanning the surface in the x and y directions while keeping the feedback on (so that I is constant). We then measure dI/dV during this process and plot it as a function of (x, y). The resulting plot is called a dI/dV map.

Since $dI(\vec{r}, V_0)/dV \propto \text{LDOS}(\vec{r}, E_\text{F} + e_c V_0) \sim \sum \left|\psi(\vec{r})\right|^2$ where we sum over all orbitals with energy $e_c V_0$, when we take a dI/dV map, we map out the values of the sum of the squares of the orbitals at energy $e_c V_0$ at the position $\vec{r}$. The position $\vec{r}$ is determined by the current I since, as we scan, the feedback moves the tip to keep the current constant. This means that a dI/dV map measures $\sum \left|\psi(\vec{r})\right|^2$ along a surface where I is constant. This is not the same as mapping out an orbital since an orbital is usually drawn as an isosurface, a surface where $\sum \left|\psi(\vec{r})\right|^2 = C$ for some constant C. This distinction is important when comparing data to calculations [129].

2.6 Inelastic Spectroscopy

We normally assume that when electrons tunnel into a molecule, the electrons then hop off the molecule onto the surface without losing energy. This is called *elastic tunneling*. However, it is also possible for the electrons to lose energy in the molecule via some other mechanism. Such a process is called *inelastic tunneling*. For example, the electron could excite a molecular vibration. This would cause the electron to lose energy $\hbar\omega$ where ω is the frequency of the vibrational mode. Since the electron must have energy $E \geq \hbar\omega$ to excite the vibration, we will see a sudden onset of current due to inelastic tunneling when $|E| \geq \hbar\omega$. Normally, the additional inelastic current increases the total current, resulting in a sudden rise in dI/dV at the energies $E = \pm\hbar\omega$.

The change in the dI/dV signal due to the excitation of a vibration can be quantitatively calculated as [58]

$$\Delta \left.\frac{dI}{dV}\right|_{e_cV=\hbar\omega} \sim \left|\langle\psi_{E_\mathrm{F}}|V_{\text{el-ph}}|\psi_{E_\mathrm{F}+\hbar\omega}\rangle\right|^2$$

which can be written as

$$\Delta \left.\frac{dI}{dV}\right|_{e_cV=\hbar\omega} \sim \left|\sum_i \frac{dE_{\psi_{E_\mathrm{F}}}}{dQ_i}\frac{1}{\sqrt{\omega}}\right|^2 \tag{2.10}$$

where Q_i represents the displacement of the i^{th} atom in the direction of the molecular vibration and the sum is taken over all atoms in the molecule.

When the atoms vibrate, the molecular energies will change slightly since the position of the atoms are changing. Equation (2.10) tells us that the more the energy of the molecular states near E_F change due to the vibration mode, the larger d^2I/dV^2 is. It also tells us that larger frequency phonons have smaller d^2I/dV^2.

2.7 d^2I/dV^2 maps

For a d^2I/dV^2 map, we keep V constant and keep the feedback on so that I is also constant. We then scan the surface in the x and y directions and measure d^2I/dV^2 as a function of (x, y). A plot of d^2I/dV^2 as a function of (x, y) is called a d^2I/dV^2 map. Normally we choose V so that e_cV is the energy where strong inelastic tunneling occurs. In this case, a d^2I/dV^2 map plots the strength of the inelastic signal as a function of position.

For the case of a molecular vibrational mode, the dI/dV signal will again change suddenly at $V = \pm\hbar\omega/e_c$ due to the vibrational mode. The spatial dependence of the change in dI/dV at this voltage is [58]

$$\Delta \left.\frac{dI}{dV}\right|_{e_cV=\hbar\omega}(\vec{r}) = \left|\sum_i \left\langle \frac{d\psi_{E_\mathrm{F}}}{dQ_i}\middle|\vec{r}\right\rangle \frac{1}{\sqrt{\omega}}\right|^2 , \tag{2.11}$$

where Q_i has the same meaning as in (2.10).

When the atoms in the molecule oscillate due to a vibrational mode, the wavefunctions will change slightly since the positions of the atoms are changing. Equation (2.11) means that the position with the largest d^2I/dV^2 signal is the position where the molecular wavefunctions near E_{F} change the most due to the vibration.

3

Corrections to the STM Theory

The theory presented in chapter 2 is the basic theory of the scanning tunneling microscope, and has been successfully used to explain qualitatively and quantitatively the STM data of many samples, such as metal surfaces. Although it may be sufficient from a theoretical viewpoint, for experiments the basic theory has approximations that do not always exist in the real world. As a result, there are corrections to the theory that are important for anyone interpreting STM data to know. This chapter will describe corrections to the basic STM theory that are important to correctly interpret the experimental data presented in this dissertation. The following is a list of corrections; each will be explained in more detail in the next sections:

1. The basic theory assumes $T = 0\,\mathrm{K}$ which is not true in experiments. The effect of non-zero temperatures will be to broaden features in spectroscopy.

2. The tunneling matrix elements were derived assuming spherically symmetric wavefunctions on the tip, which is not always true. Atomic resolution cannot be explained with spherically symmetric tip wavefunctions.

3. The tunneling matrix elements are not constant, which was assumed earlier. They are a function of the voltage applied to the tip. This causes a non-constant tip DOS (usually the tip DOS is assumed constant) to become noticeable at negative sample biases. It also leads to negative differential resistance, which is most prominent when the sample has localized states, such as a molecule on an insulating surface.

4. Whenever electrons tunnel from tip to sample or sample to tip, we are either adding an electron or removing an electron from a sample which contains many electrons. This means that we need to take into account many-body effects, such as electron-electron interactions, which were not taken into account in chapter 2. In a metal, the electron-electron interactions are usually screened, so we do not have to consider them. This is not the case in a single molecule.

3.1 Thermal broadening

3.1.1 Elastic tunneling

Instead of $T = 0\,\mathrm{K}$ assumed before, consider elastic tunneling when $T \neq 0\,\mathrm{K}$. From (2.3), if the tunneling matrix elements are constant, we see that the sample DOS is convoluted with the derivative of the Fermi-Dirac distribution:

$$\frac{dI}{dV} \propto \int \rho_s(E) B_{T1}(E - e_c V)\, dE \equiv \rho_s * B_{T1} \quad \text{with} \quad B_{T1} = -\frac{df(E)}{dE}\,.$$

Since $-f'(E) = -df/dE$ is a peak with a maximum value of $1/4k_BT$ at $E = \mu$ and a FWHM given by $2k_BT\ln(3+2\sqrt{2}) \approx 3.5k_BT$, the effect of non-zero temperatures is to convolute the DOS with this peak. Effectively, this means that peaks in the STM-measured DOS will be broader than peaks in the true DOS by about $3.5k_BT$, an effect called *thermal broadening*.

It is sometimes possible to remove the effect of this broadening to recover ρ_s. Since dI/dV is a convolution between ρ_s and $-f'(E)$, we may deconvolute dI/dV from $-f'(E)$ using the convolution theorem to get back ρ_s. Let $\mathrm{FT}[g(E)](y) \equiv \mathrm{FT}[g(E)]$ denote the Fourier transform as a function of y of the function $g(E)$. Then $\mathrm{FT}[dI/dV] \propto \mathrm{FT}[\rho_s * -f'] = \mathrm{FT}[\rho_s]\,\mathrm{FT}[-f']$. Since we know the temperature and $\mu = 0$, we may then calculate $\mathrm{FT}[-f']$ and divide this part out, yielding

$$\rho_s \propto \mathrm{FT}^{-1}\left[\frac{\mathrm{FT}[dI/dV]}{\mathrm{FT}[-f']}\right]\,,$$

where FT^{-1} represents the inverse Fourier transform. However, numerically this procedure does not always work since $\mathrm{FT}[-f'](y)$ is almost 0 for large values of y. We are then dividing by a function which is almost 0 and the result tends towards ∞. Ideally, the numerator $\mathrm{FT}[dI/dV]$ would also go to 0 whenever $\mathrm{FT}[-f']$ does, but this is not the case due to noise or other experimental errors.

However, if one knows that ρ_s should be the function $h(E)$, one may get around this problem. In this case, what is normally done is to convolute $h(E)$ with $-f'$, then fit this curve to dI/dV; i.e., we fit $h * -f'$ to dI/dV. The best fit then yields parameters which tell us the function $h(E) = \rho_s$.

3.1.2 Inelastic tunneling

For inelastic tunneling, the thermal broadening of d^2I/dV^2 is a little different [109]. In this case, the measured second derivative

by the convolution

$$\left[\frac{d^2I(V)}{dV^2}\right]_{\text{measured}} = \int_{-\infty}^{\infty}\left[\frac{d^2I(V-E)}{dV^2}\right]_{\text{true}} B_{T2}(E)\,dE = \left[\frac{d^2I}{dV^2}\right]_{\text{true}} * B_{T2}$$
$$\text{where } B_{T2}(E) = \frac{1}{k_BT}e^x\frac{(x-2)e^x+x+2}{(e^x-1)^3} \quad \text{with} \quad x = \frac{E}{k_BT}$$

Since we have a convolution between two functions, in principle one may use the same methods for elastic tunneling to remove the effect of thermal broadening.

3.2 Non-spherical tip states and atomic resolution

In general, the wavefunction of the atoms at the end of the STM tip is what should matter the most. Usually W or PtIr tips are used in STM and these are transition metals with d orbitals. These d orbitals are more localized than the valence s orbitals, so as long as the tip-sample distance is large enough ($\gtrsim 4$ Å, which is true for almost all experiments in this dissertation), the spherically symmetric tip wavefunctions assumed in chapter 2 is a good approximation.

However, spherically symmetric tip states may not be true for transition metal tips when the tip-sample separation is ~ 4 Å, as tunneling into the d orbital may be important in this regime. Furthermore, theory predicts that one cannot get atomic resolution in STM images from spherically symmetric tip states (§1.3, 6.3, chapter 7 in [29]). This is consistent with the experimental observation that atomic resolution is easiest to achieve when molecules with non-spherically symmetric states, such as CO, are on the tip.

To address this issue, the effect of other orbitals have been included (chapter 3 in [29]) to improve on the spherical-tip approximation, as well as tip-sample interactions (chapter 7 in [29]). These corrections give a better approximation to the tunneling matrix elements, especially at close (~ 4 Å) tip-sample separations. Atomic resolution, as well as other effects, such as the inversion of topography images (bumps appear as dips and dips appear as bumps) can be explained by including non-spherically symmetric tip states and tip-sample interactions.

3.3 Tunneling matrix elements

3.3.1 Negative differential resistance

The tunneling matrix elements can also be affected by the voltage that is applied to the STM tip. A simple one dimensional model based on the WKB approximation can be used to estimate the magnitude of this effect [59]. Qualitatively, as we increase the STM sample voltage, the effective tunneling barrier that the electrons see increases; hence, it is possible to see the tunneling current decrease when the STM sample voltage is increasing. For

voltages where $I(V)$ decreases as V increases, $dI/dV < 0$, so the differential conductance is negative. A negative dI/dV is known as negative differential resistance (NDR) [59] (or negative differential conductance). The lower panel in figure 3.2 shows a simulated dI/dV spectrum with NDR around $V \sim 1.5\,\mathrm{V}$ and $V \sim 3.1\,\mathrm{V}$. The details of the simulation are discussed next.

3.3.2 Enhancement of tip states at negative bias

Figure 3.1 shows an energy diagram for tunneling when the sample bias V is negative and positive. From figure 3.1a, we see that the electrons on the tip with lower energy will see a larger tunneling barrier, and hence, will have a smaller probability of tunneling (the length of the blue arrows in the diagram represents the relative probability of tunneling). So at positive sample bias, the tunneling current (and also dI/dV) will be dominated by tunneling into the empty states of the sample with energy $E_\mathrm{F}+e_cV$. Similarly, in figure 3.1b, at negative sample bias, the tunneling current (and dI/dV) will be dominated by DOS of the tip at energy $E_\mathrm{F} + e_cV$. Therefore, if the DOS of the tip is not constant, it will have a large impact on the dI/dV at negative sample bias.

This qualitative result can be quantified for a one dimensional system. Starting from equation (2.2), we use the Tersoff-Hamann approximation to Bardeen's matrix elements (§2.1.2), so that

$$\left|\langle\psi_{s,n}|H'|\psi_t\rangle\right|^2 \propto \left|\psi_{s,n}(\vec{r}_0)\right|^2 .$$

We then use the WKB approximation to calculate $\left|\psi_{s,n}\right|^2$ in the vacuum region, assuming the energy barrier is a trapezoid (as in figure 3.1)

$$\left|\psi_{s,n}\right|^2 \approx \exp\left(-2\kappa \int_0^L \sqrt{\phi - E + e_cVx/L}\,dx\right)$$

where $\kappa = \sqrt{2m_e/\hbar^2}$, ϕ is the work function, and L is the length of the vacuum region. In this approximation, the tunneling matrix elements depend only on the energy, hence, they may be taken out of the sum in (2.2). Everything else except for $\rho_{s,n}$ may be taken out of the sum as well, so the summation can be performed using $\sum_n \rho_{s,n} = \rho_s$. We further take $T = 0\,\mathrm{K}$ so that the Fermi functions become step functions. The tunneling current becomes (with $E_\mathrm{F} = 0$)

$$I(V) \sim \int_0^{e_cV} \exp\left(-2\kappa \int_0^L \sqrt{\phi - E + e_cVx/L}\,dx\right) \rho_s(E)\rho_t(E - e_cV)\,dE\,. \tag{3.1}$$

After plugging in the reasonable values $\phi = 5\,\mathrm{eV}$ and $L = 5\,\text{Å}$, dI/dV may be calculated numerically from this expression for a given ρ_s and ρ_t.

Figure 3.2 shows the results of a numerical simulation using (3.1). The top panel shows the DOS for the tip and sample that was used to calculate the dI/dV curve shown in the bottom panel. There are a few important features to note in the simulated dI/dV.

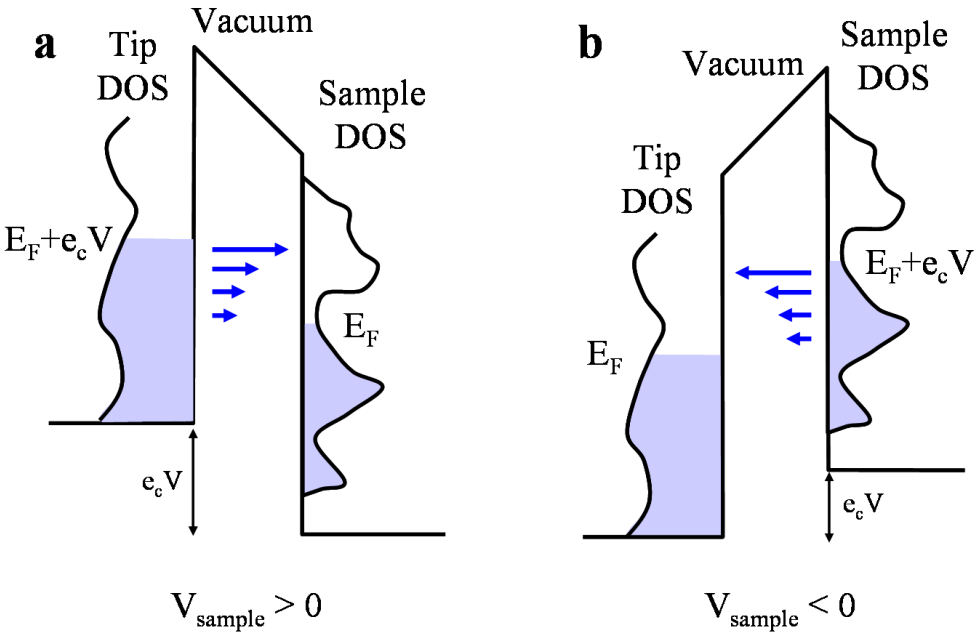

Figure 3.1: Enhancement of tip DOS at negative sample bias. The blue shaded areas under the tip and sample DOS curves represent states which are occupied by electrons. (a) Tunneling at positive sample bias is dominated by tunneling into empty sample states. (b) Tunneling at negative sample bias is dominated by tunneling into empty tip states. The length of the blue arrows represent the relative size of the tunneling probability. Electrons with higher energy have a higher probability of tunneling (since they see a smaller tunneling barrier) and contribute the most to the tunneling current.

1. The dI/dV curve has NDR around $V = 1.5\,\mathrm{V}$ and $V = 3.1\,\mathrm{V}$.

2. Although the sample DOS has peaks with the sample amplitude, the corresponding peaks in dI/dV are not the same amplitude. The peak amplitudes at positive sample bias are larger than those at negative sample bias.

3. The tip DOS is not constant, and this affects the dI/dV curve the most at negative sample biases, which was explained qualitatively earlier.

3.4 Many-body corrections

When an electron tunnels from the STM tip into the sample, it can interact with other particles in the sample, for example, phonons, plasmons, or other electrons. These extra interactions which arise from the added electron will modify the DOS of the sample, so the STM actually measures this modified DOS, and not the DOS $\rho_s(E)$ in §2, which does not include many-body interactions. So, to describe what STM measures, we need to describe

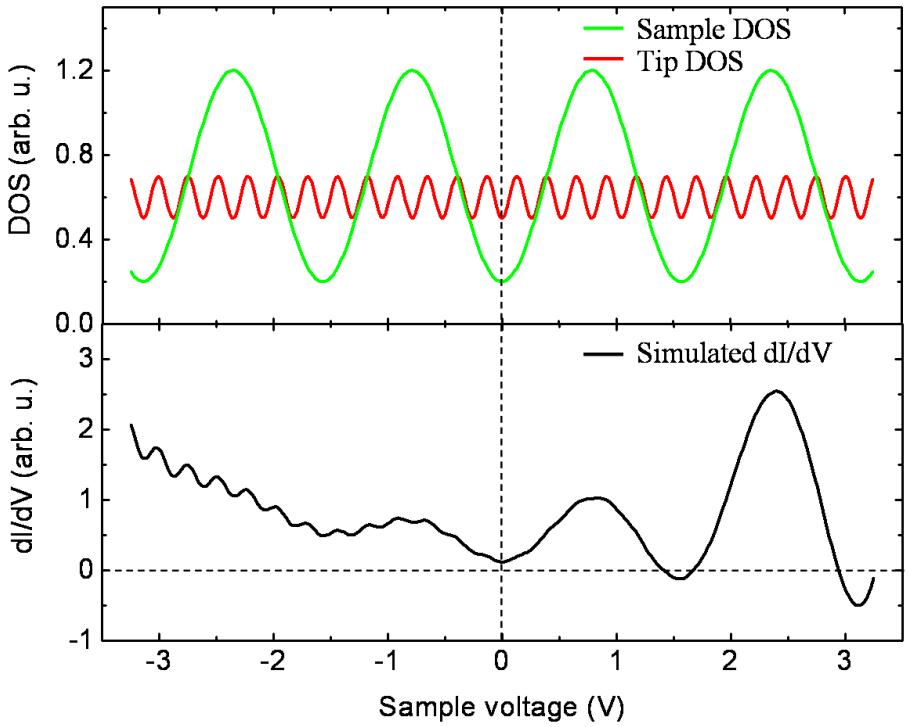

Figure 3.2: The lower panel shows the simulated dI/dV spectrum obtained by using the tip and sample DOS shown in the upper panel. Although the sample DOS has periodic peaks of the same amplitude, the amplitude of the corresponding peaks in the simulated dI/dV changes drastically. Also, the tip DOS has a substantial impact on the simulated dI/dV when $V < 0$. NDR occurs when the sample bias is around $V \sim 1.5\,\mathrm{V}$ and $V \sim 3.1\,\mathrm{V}$

how these many-body interactions affect the DOS. In general, to take into account many body interactions, we may replace the tip and sample DOS in chapter 2 with tip and sample spectral functions [5]. This is not always so simple since the spectral functions (§4.1.2) for the tip and sample are not always known. Luckily, there still are simple models to help describe many-body effects in terms of quasiparticles, and these will be discussed next.

3.4.1 Quasiparticles

It is usually difficult to consider how interactions with other particles affects the electron DOS; it is easier to calculate the DOS for a system of non-interacting particles. So, normally the combined system of electron added by STM + other particles the electron interacts with is treated as a single particle called a *quasiparticle*, and if these electron quasiparticles are defined cleverly, they can be treated as a non-interacting (or at least weakly interacting) system of particles. When the quasiparticles are weakly interacting instead of non-interacting,

we can apply perturbation theory to correct for the weak interactions. Since the quasiparticles already include many-body interactions, their energy levels are the energy levels of the electron including many-body interactions. Thus, to describe STM measurements, we need to find the quasiparticle density of states. This is normally a difficult theoretical problem which require techniques such as Green's functions (§4.1.2), but sometimes simple models can be used, such as the one that will be given in §3.4.2.

A common example of a quasiparticle in condensed matter physics is the particle which consists of an electron + the lattice the electron is in. The interactions between the electron and lattice are complicated, but this complex system can be treated as a new particle with charge $-e_c$ and mass m^*, the effective mass of the electron. These quasiparticles are then treated as almost non-interacting particles, and most electronic properties of the system are calculated in terms of these non-interacting quasiparticles.

3.4.2 Electron-electron interactions

The main many-body effect to consider for the experiments presented in this dissertation is the electron-electron interaction. This effect is significant in molecules such as C_{60} [130]. This section will describe how to define the effect of electron-electron interactions in single molecules as quasiparticles and what the density of quasiparticle states is. We will find that the quasiparticle DOS, which is the STM measured DOS, will have an energetic separation between HOMO and LUMO which is larger than the HOMO-LUMO energetic separation in the non-interacting electron DOS. This will be the main difference between the quasiparticle DOS and the non-interacting electron DOS.

Quasiparticle HOMO-LUMO gap

Suppose that a molecule contains N electrons. The i^{th} electron on the molecule will repel the j^{th} electron; call the electrostatic energy of these two electrons $U_{ij} \geq 0$. We define average electron-electron repulsion energy, called the *charging energy* or *on-site Coulomb interaction*, as $U = \frac{1}{P}\sum_{i>j} U_{ij}$, where $P = 1+2+\cdots+N-1 = N(N-1)/2$ is the number of distinct electron-electron pairs. Let ϵ_i represent the energy levels of the molecule without electron-electron interactions, then the total electronic energy of the molecule including electron-electron interactions is

$$E_N = \frac{N(N-1)}{2}U + \sum_{i=1}^{N} \epsilon_i \,. \tag{3.2}$$

In STM, electrons are either tunneling from the tip to the molecule or from molecule to tip. First consider an electron tunneling from the tip to an unoccupied state of the molecule, the LUMO+n (the $(n+1)^{\text{th}}$ lowest unoccupied orbital). The LUMO+n is now occupied by

an electron, so the total electronic energy of molecule is

$$E_{N+1}^{\mathrm{LUMO}+n} = \frac{(N+1)N}{2}U + \sum_{i=1}^{N}\epsilon_i + \epsilon_{N+n+1} = E_N + NU + \epsilon_{\mathrm{LUMO}+n}\,.$$

where $\epsilon_{N+n+1} = \epsilon_{\mathrm{LUMO}+n}$. We assumed that both ϵ_i and U do not change much from the addition of one electron.

We now define the electron quasiparticle as the added electron plus all other electrons it interacts with. The energy of this quasiparticle will be the energy of the added electron which includes the electron-electron interactions, and will be the energy we actually measure in STM. We now need to define the quasiparticle's energy. To understand how to define it, consider first a simpler system. For any system of non-interacting electrons, if we calculate the total electronic energy of the system after adding an electron and subtract this from the neutral system's ground state energy, we get the energy of the state the electron was added to. Using this as a guide, we define the energy of the quasiparticle's LUMO+n as

$$EQP_{\mathrm{LUMO}+n} = E_{N+1}^{\mathrm{LUMO}+n} - E_N = NU + \epsilon_{\mathrm{LUMO}+n}\,.$$

This expression makes sense since when we add an electron to the molecule, the other N electrons already on the molecule will repel it. The repulsion from each electron on the molecule adds an energy U. Hence, the actual energy that we measure for the LUMO+n, the energy of the quasiparticle's LUMO+n, is increased from $\epsilon_{\mathrm{LUMO}+n}$ by NU.

Now consider the case when an electron tunnels from an occupied molecular state, the HOMO$-m$ (the $(m+1)^{\mathrm{th}}$ highest molecular orbital), to the tip. The HOMO$-m$ now has an electron missing, so the total electronic energy of the molecule is

$$E_{N-1}^{\mathrm{HOMO}-m} = \frac{(N-1)(N-2)}{2}U + \sum_{i=1}^{N}\epsilon_i - \epsilon_{N-m} = E_N - (N-1)U - \epsilon_{\mathrm{HOMO}-m}$$

with $\epsilon_{\mathrm{HOMO}-m} = \epsilon_{N-m}$. Again, if we consider any system of non-interacting electrons, the energy of the HOMO$-m$ is the energy of the neutral system minus the energy of the system after an electron has been removed from the HOMO$-m$. So we will define the energy of the quasiparticle's HOMO$-m$ as

$$EQP_{\mathrm{HOMO}-m} = E_N - E_{N-1}^{\mathrm{HOMO}-m} = (N-1)U + \epsilon_{\mathrm{HOMO}-m}\,.$$

Again, this makes sense since the electron in the HOMO$-m$ is repelled by $N-1$ other electrons, each increasing $\epsilon_{\mathrm{HOMO}-m}$ by U.

The difference in energy between the quasiparticle's LUMO and HOMO (called the quasiparticle HOMO-LUMO gap) is then

$$EQP_{\mathrm{gap}} = EQP_{\mathrm{LUMO}} - EQP_{\mathrm{HOMO}} = \epsilon_{\mathrm{LUMO}} - \epsilon_{\mathrm{HOMO}} + U\,. \tag{3.3}$$

We see that the effect of the electron-electron interactions is to increase the energy separation between HOMO and LUMO by the charging energy U [130].

If we now calculate the difference in energy between any two unoccupied states, we get

$$EQP_{\mathrm{LUMO}+i} - EQP_{\mathrm{LUMO}+j} = \epsilon_{\mathrm{LUMO}+i} - \epsilon_{\mathrm{LUMO}+j} \,.$$

So the energetic separation between unoccupied states is the same whether we include electron-electron interactions or not. Similarly, the energetic separation between any two occupied states is independent of whether we include electron-electron interactions or not. So the main effect of electron-electron interactions using this simple model is to increase the non-interacting electron's HOMO-LUMO gap by U. This quasiparticle HOMO-LUMO gap is what we then expect to measure in STM experiments.

Experimentally determining the quasiparticle gap

It is possible to experimentally extract the value of EQP_{gap} using two commonly measured experimental quantities, the ionization energy and electron affinity. The ionization energy is the minimum energy necessary to remove an electron from the neutral molecule; i.e., it is the difference in energy between the molecule with one electron removed from the HOMO and the neutral molecule with N electrons

$$IE = E_{N-1}^{\mathrm{HOMO}} - E_N = -EQP_{\mathrm{HOMO}} \,.$$

We have defined the potential energy of the electron removed from the HOMO to be zero when the electron is infinitely far away from the molecule.

The electron affinity is the ionization energy of a singly negatively charged molecule. A singly negatively charged molecule has an extra electron in the LUMO, so the minimum energy necessary to remove an electron from the negatively charge molecule is the energy necessary to remove the electron from the LUMO. This is the difference in energy between the molecule with N electrons and the molecule with an extra electron in the LUMO

$$EA = E_N - E_{N+1}^{\mathrm{LUMO}} = -EQP_{\mathrm{LUMO}} \,.$$

The quasiparticle HOMO-LUMO gap can then be written as

$$EQP_{\mathrm{gap}} = IE - EA \,. \tag{3.4}$$

So the ionization energy and electron affinity gives us an idea of how large we can expect the STM measured gap EQP_{gap} to be. The only problem with using (3.4) is that IE and EA are normally measured for molecules in gas phase while in STM, we normally have molecules on a conducting surface. On a conducting surface, U is smaller since electrons on a molecule form image charges in the metal, and these positive image charges tend to attract the electrons on the molecule together [151]. This tends to cancel the electron-electron repulsion, effectively reducing U.

4

Theoretical Background for Molecular Nanostructures

The purpose of this chapter is to both introduce the necessary theory to understand this dissertation and to introduce important theoretical concepts and notation frequently encountered in publications in this field.

4.1 LDOS, PDOS, and DOS

One of the important quantities to understand in STM is the local density of states (LDOS) since the STM directly measures it (chapter 2). However, different people will define the LDOS in different ways, so a particular definition of LDOS in one publication may not be exactly what an STM measures (e.g., the definition in §18.33 in [138]). This may be especially confusing to those who are new to this field. To remove any potential confusion, in this dissertation, the LDOS will be defined below so that it is always what the STM measures. Another quantity called the projected density of states (PDOS) will be defined, and all other definitions of LDOS seen in publications can be stated in terms of a PDOS. The exact definitions of LDOS and PDOS, as well as how they are related to each other, will be given in this section.

Furthermore, many theoretical results in many-body physics are stated in terms of Green's and spectral functions, and to compare these theoretical results to STM data, one must understand how they are related to the LDOS and PDOS. For this reason, Green's and spectral functions will be introduced, and it will be shown how they are related to the LDOS and PDOS.

4.1.1 Definitions

The LDOS of a system with Hamiltonian H and eigenstates $\psi_n(\vec{r})$ at position $\vec{r}$ and energy E is defined as

$$\mathrm{LDOS}(\vec{r}, E) \equiv \sum_n \left|\psi_n(\vec{r})\right|^2 \delta(E - E_n) \tag{4.1}$$

where the sum is taken over all eigenstates (although only the terms with $E_n = E$ actually contribute to the sum). The LDOS of a system at energy E and position $\vec{r}$ can be thought of as the value of the sum of the squares of all the system's wavefunctions with energy E at position $\vec{r}$.

The LDOS is related to the DOS, which can be seen if we integrate the LDOS over all space

$$\begin{aligned}\int_{\text{all space}} \text{LDOS}(\vec{r}, E)\, dV &= \sum_n \int_{\text{all space}} \left|\psi_n(\vec{r})\right|^2 \delta(E - E_n)\, dV \\ &= \sum_n \delta(E - E_n) \\ &\equiv \text{DOS}(E)\,.\end{aligned}$$

So the LDOS integrated over all space is just the DOS for that system.

The PDOS is closely related to the LDOS. The PDOS for a system with eigenstates $|n\rangle$ projected onto the state $|\Phi\rangle$ at energy E is defined as

$$\text{PDOS}\big(|\Phi\rangle, E\big) \equiv \sum_n \left|\langle\Phi|n\rangle\right|^2 \delta(E - E_n)$$

The PDOS of a system at energy E projected onto state $|\Phi\rangle$ represents roughly the amount of the system's wavefunctions at energy E contained in the state $|\Phi\rangle$. We can also think of a PDOS at energy E roughly as $\text{LDOS}(\vec{r}, E)$ integrated over the region of space taken up by the wavefunction $\Phi(\vec{r}) = \langle\vec{r}|\Phi\rangle$, but this is only a rough way of thinking of the PDOS, and is not always true.

To see how the PDOS and LDOS are related, let $|\vec{r}\rangle$ denote an eigenstate of the position operator, then

$$\begin{aligned}\text{PDOS}\big(|\vec{r}\rangle, E\big) &= \sum_n \left|\langle\vec{r}|n\rangle\right|^2 \delta(E - E_n) \\ &= \sum_n \left|\psi_n(\vec{r})\right|^2 \delta(E - E_n) \\ &= \text{LDOS}(\vec{r}, E)\end{aligned}$$

where $\psi_n(\vec{r}) = \langle\vec{r}|n\rangle$ is the position space representation of the wavefunction. So we see that the LDOS is just a special case of the PDOS.

4.1.2 Green's and spectral functions

The Green's function and spectral functions will be introduced briefly in this section, and in the next section, it will be shown how they are related to the LDOS and PDOS.

One of the systematic and powerful ways of solving many-body problems is to use Green's

functions. Once we know the Green's function for a system, we can calculate various properties of that system, such as the DOS. The problem of calculating various properties of a system can then be boiled down to one problem: find the Green's function for that system.

The Green's function may be obtained from the Green's operator. In general, the Green's operator for a linear differential operator $\hat{D}(t)$, which contains derivatives with respect to the variable t, is the operator $\hat{G}(t)$ which satisfies

$$\hat{D}(t)\hat{G}(t) = \delta(t) \, .$$

Since the Schrödinger equation $\hat{H}|\psi\rangle = i\hbar\frac{\partial}{\partial t}|\psi\rangle$ can be rewritten as

$$\hat{D}_S(t)|\psi\rangle = 0 \quad \text{with} \quad \hat{D}_S(t) = i\hbar\frac{\partial}{\partial t} - \hat{H} \, ,$$

$\hat{D}_S(t)$ is an important differential operator for quantum mechanics and condensed matter physics. The Green's operator in condensed matter physics is then defined as the Green's operator for the linear differential operator $\hat{D}_S(t)$; this means that $\hat{G}(t)$ satisfies

$$\hat{D}_S(t)\hat{G}(t) = \left(i\hbar\frac{\partial}{\partial t} - \hat{H}\right)\hat{G}(t) = \delta(t) \, . \tag{4.2}$$

At this point, the usage of $\hat{D}_S$ to construct the Green's operator seems somewhat arbitrary. We may have used other differential operators to define the Green's operator, such as the kinetic energy operator, but in the next section, we will see that using $\hat{D}_S$ to define the Green's operator will allow us to calculate many quantities from it.

We may now explicitly construct $\hat{G}(t)$ for a time independent Hamiltonian. Since the time evolution operator $\hat{U}(t) = e^{-i\hat{H}t/\hbar}$ satisfies $\hat{D}_S(t)\hat{U}(t) = 0$ (equation 2.1.25 in [174]), $\hat{U}(t)$ almost satisfies (4.2); it only does not satisfy the equation when $t = 0$. To satisfy (4.2) at $t = 0$, note that the derivative of a step function $\theta(t)$ (defined below) is $\delta(t)$, so we may construct the Green's operator from $\theta(t)$ and $\hat{U}(t)$. If we let $\hat{G}(t) = \frac{1}{i\hbar}\theta(t)\hat{U}(t)$, then a quick calculation shows $\hat{D}_S(t)\hat{G}(t) = \hat{U}(t)\delta(t) = \hat{U}(0)\delta(t) = \delta(t)$, so that $\hat{G}(t)$ satisfies (4.2). Finally, the Green's operator for a time independent Hamiltonian $\hat{H}$ is (§7.11 in [174])

$$\hat{G}(t) = \frac{1}{i\hbar}\theta(t)e^{-i\hat{H}t/\hbar} \quad \text{with} \quad \theta(t) = \begin{cases} 1 & \text{for } x > 1 \\ 0 & \text{for } x \leq 0 \, . \end{cases}$$

$\hat{G}(t)$ defined in this way is called a *retarded Green's operator*. We see that the Green's operator for a system is essentially the time evolution operator for that system.

The Green's operator contains all the information about how a system evolves over time. However, we normally want information related to the energy of the system. To extract information about the energy of a system from the Green's operator, it is more convenient to convert $\hat{G}(t)$ to an operator that depends on energy. As a function of energy,

the Green's operator is defined as the Fourier transform of $\hat{G}(t)$:

$$\hat{G}(E) = \int_{-\infty}^{\infty} e^{i(E+i\alpha)t/\hbar}\hat{G}(t)\,dt = \frac{1}{i\hbar}\int_{0}^{\infty} e^{i(E+i\alpha-\hat{H})t/\hbar}\,dt = \frac{1}{E+i\alpha-\hat{H}}\,.$$

The small imaginary part $i\alpha$ was added to the exponential in the integral in order for the integral to converge. In the end, we will take $\alpha \to 0$.

Often, we must deal with many-body systems. For these systems, it is convenient to express the many-body Hamiltonian $\hat{H}$ as

$$\hat{H} = \hat{H}_{SP} + \hat{\Sigma}$$

where $\hat{H}_{SP}$ is a single particle Hamiltonian and Σ takes into account the interactions of a single particle with all the other particles in the system. The term Σ is usually complex and is called the *self-energy* since it takes into account the contributions to the total energy of a system due to one part of a system interacting with another part of the same system. With this notation, the Green's operator becomes

$$\hat{G}(E) = \frac{1}{E+i\alpha-\hat{H}_{SP}-\hat{\Sigma}}\,.$$

The Green's function can finally be defined as the function which is the expectation of the operator $\hat{G}(E)$ in the state $|n\rangle$

$$G(n,E) = \langle n|\hat{G}(E)|n\rangle\,.$$

This is the form of the Green's function that is often used, such as in [133]. However, sometimes the Green's operator $\hat{G}(t)$ is called the Green's function, even though it is an operator. This convention appears in [138].

It will be convenient later to represent the Green's operator in another form. If the states $|n\rangle$ with energy E_n denote the eigenvalues of the total (many-body) Hamiltonian $\hat{H}$, then $\hat{G}(E)$ can be expressed using the identity operator $\hat{I} = \sum_n |n\rangle\langle n|$ as

$$\hat{G}(E) = \hat{G}(E)\hat{I} = \sum_n \frac{|n\rangle\langle n|}{E+i\alpha-E_n}\,. \tag{4.3}$$

Another important operator which appears frequently in theoretical calculations is the electron spectral operator $\hat{A}(E)$. This operator is proportional to the imaginary part of $\hat{G}(E)$ (§3.3 in [133])

$$\hat{A}(E) = -2\,\mathrm{Im}\big\{\hat{G}(E)\big\}\,. \tag{4.4}$$

The spectral function is then the imaginary part of the Green's function.

From the spectral operator or function, many measurable properties of a system can be calculated. For example, two important quantities for STM, the local density of states

(LDOS) and projected density of states (PDOS), can be obtained from the spectral operator.

4.1.3 LDOS and PDOS in terms of spectral functions

In this section, we will show how two important quantities, the LDOS and PDOS can be derived from the Green's and spectral operators and functions. We first write the LDOS in terms of the spectral operator. Using (4.3) and (4.4), the spectral operator can be written as

$$\hat{A}(E) = 2\sum_n \frac{\alpha}{(E-E_n)^2+\alpha^2}|n\rangle\langle n|$$

Since the coefficient of $|n\rangle\langle n|$ in the sum is just a Lorentzian, as $\alpha \to 0$, the Lorentzian tends to $\pi\delta(E-E_n)$. If we now calculate $\langle\vec{r}|\lim_{\alpha\to 0}\hat{A}(E)|\vec{r}\rangle$ we get

$$\begin{aligned}\big\langle\vec{r}\big|\lim_{\alpha\to 0}\hat{A}(E)\big|\vec{r}\big\rangle &= 2\sum_n \langle\vec{r}|n\rangle\langle n|\vec{r}\rangle\pi\delta(E-E_n)\\ &= 2\pi\sum_n \big|\psi_n(\vec{r})\big|^2\delta(E-E_n)\\ &= 2\pi\,\mathrm{LDOS}(\vec{r},E)\end{aligned}$$

where $\psi_n(\vec{r}) = \langle\vec{r}|n\rangle$ denotes the representation of state $|n\rangle$ in position space. This implies

$$\mathrm{LDOS}(\vec{r},E) = \frac{1}{2\pi}\big\langle\vec{r}\big|\lim_{\alpha\to 0}\hat{A}(E)\big|\vec{r}\big\rangle$$

Section 2.1 shows that the STM measures the LDOS of a system, hence the STM essentially measures the spectral function in position space.

The PDOS is obtained from the spectral function in a similar way to the LDOS; the difference is that we use an arbitrary state $|\Phi\rangle$ instead of the position eigenstate $|\vec{r}\rangle$. Following a derivation similar to the derivation for LDOS, the PDOS can be written as

$$\mathrm{PDOS}\big(|\Phi\rangle,E\big) \equiv \sum_n \big|\langle\Phi|n\rangle\big|^2\delta(E-E_n) = \frac{1}{2\pi}\big\langle\Phi\big|\lim_{\alpha\to 0}\hat{A}(E)\big|\Phi\big\rangle$$

Hence, as $\alpha \to 0$, the PDOS is proportional to the spectral function $A(\Phi,E) = \langle\Phi|\hat{A}(E)|\Phi\rangle$.

4.2 Tight Binding

Since the wavefunctions in a solid arise from hybridization between atomic orbitals, one would think that there is a way of deriving, or at least approximating, the wavefunctions of a solid in terms of localized atomic orbitals. We would especially expect this when the atomic orbitals on neighboring atoms do not overlap much, resulting in little hybridization between atomic orbitals. In this regime, the wavefunctions for the solid should be similar

to the atomic wavefunctions, and we may be able to write the solids' wavefunctions simply as linear combinations of atomic wavefunctions. This leads to the main idea behind what is called *tight binding*: little overlap between neighboring atoms' wavefunctions in a solid leads to wavefunctions for the solid which can be expressed as linear combinations of the atomic orbitals. This section will describe how this idea can be put into a more precise mathematical form. The presentation here will be different from the presentation of tight binding given in §8.4 in [138] and chapter 10 in [7], but the concepts will be the same.

To develop tight binding, start with a solid with N atoms located at positions $\vec{R}_n$. Then we may write the Hamiltonian for a single electron in this system as

$$\hat{H} = \frac{p^2}{2m} + \sum_{i=1}^{N} U(\vec{r} - \vec{R}_i)$$

where $U(\vec{r}) = -Ze^2/r$ is the coulomb potential for an atom with nuclear charge Z. Now suppose each atom in the solid has one atomic state $|i\rangle$ which satisfies $\left(\frac{p^2}{2m} + U(\vec{r} - R_i)\right)|i\rangle = E_0|i\rangle$. Then assume that the set of all atomic orbitals $\{|i\rangle\}$ forms an orthonormal basis for the wavefunctions of the solid. This is not necessarily true, but is a reasonable approximation if the atomic orbitals of neighboring atoms do not overlap much, in which case we would expect weak interaction between the neighboring atoms, and the wavefunctions for the solid should be similar to the atomic wavefunctions. With this assumption, we can calculate the matrix elements of the Hamiltonian using the $\{|i\rangle\}$ basis

$$\begin{aligned} H_{ij} &= \left\langle i \middle| \frac{p^2}{2m} + U(\vec{r} - \vec{R}_j) \middle| j \right\rangle + \langle i | \sum_{n \neq j} U(\vec{r} - \vec{R}_n) | j \rangle \\ &= E_0 \langle i | j \rangle + \langle i | \sum_{n \neq j} U(\vec{r} - \vec{R}_n) | j \rangle \\ &= E_0 \delta_{ij} + \langle i | \sum_{n \neq j} U(\vec{r} - \vec{R}_n) | j \rangle \end{aligned}$$

where δ_{ij} is the Kronecker delta. The matrix H can be written simply as

$$H = E_0 I + t \quad \text{with} \quad t_{ij} = \langle i | \Delta U | j \rangle, \quad \Delta U = \sum_{n \neq j} U(\vec{r} - \vec{R}_n) \tag{4.5}$$

where I is the identity matrix. This is the tight binding Hamiltonian. From this matrix expression for H, we may then calculate the eigenvalues and eigenvectors for the Hamiltonian. Since the first term $E_0 I$ is a diagonal matrix, the eigenvalues E_n of H can be written as

$$E_n = E_0 + E_n^t \tag{4.6}$$

where E_n^t is the n^{th} eigenvalue of t. Hence, the eigenvalues of H can be found from the eigenvalues of the matrix t, and we may think of the eigenvalues of t as being corrections

to the atomic energy E_0 due to the presence of all the atoms. The matrix element t_{ij} when $i \neq j$ is also called the *hopping integral* while the matrix element t_{ii} is called the *on-site energy*. The reason for this terminology will be more apparent when the Hamiltonian is written in second quantized notation. The way one calculates the value of t_{ij} will be given in §4.2.4.

If pairs of atomic eigenstates $|i\rangle$ and $|j\rangle$ contain significant overlap (i.e., $\langle i|j\rangle \neq 0$), then the set of eigenstates $\{|i\rangle\}$ is not truly orthogonal. Although we assumed an orthogonal basis when deriving tight binding, this does not matter to first order, as discussed in appendix B of [71].

4.2.1 Tight binding of H_2

Although most textbooks apply tight binding to a periodic lattice, it may also be applied to any system, even single molecules. As an example, consider the hydrogen molecule H_2. We will take the $1s$ orbitals as the basis. If we assume that the hopping matrix element between the $1s$ orbitals on different atoms is $t_{12} = t_{21} = t_s$ while the on-site energy is $t_{11} = t_{22} = \epsilon$, then the Hamiltonian matrix is

$$H = \begin{pmatrix} E_{1s} & 0 \\ 0 & E_{1s} \end{pmatrix} + \begin{pmatrix} \epsilon & t_s \\ t_s & \epsilon \end{pmatrix} = \begin{pmatrix} E_{1s} + \epsilon & t_s \\ t_s & E_{1s} + \epsilon \end{pmatrix} \tag{4.7}$$

which has eigenvalues

$$E = E_{1s} + \epsilon \pm t_s \tag{4.8}$$

with eigenvectors

$$\frac{1}{\sqrt{2}}\big(|s,1\rangle \pm |s,2\rangle\big)$$

where $|s,1\rangle$ represents the $1s$ orbital on H atom 1 and $|s,2\rangle$ is the $1s$ orbital on H atom 2. We see that the energy levels of H_2 are offset from the energy of the $1s$ orbitals by the amounts $\epsilon \pm t_s$. Since t_s is normally negative, tight binding predicts that the ground state wavefunction of H_2 is the bonding orbital $(|s,1\rangle + |s,2\rangle)/\sqrt{2}$ with energy $E_0 = E_{1s} + \epsilon + t$ while the anti-bonding orbital $(|s,1\rangle - |s,2\rangle)/\sqrt{2}$ is higher than the energy of the bonding orbital by $2t_s$; hence we see in this case that the hopping integral is also a measure of the energetic splitting between orbitals.

4.2.2 Tight binding in second quantization

Any function or operator V which acts on single particles can be represented in second quantized notation (§2.1 in [184] has a thorough introduction to second quantization) as

$$V = \sum_{i,j} \Big(|i\rangle\langle i|\Big) V \Big(|j\rangle\langle j|\Big) = \sum_{i,j} \langle i|V|j\rangle \Big(|i\rangle\langle j|\Big) = \sum_{i,j} \langle i|V|j\rangle c_i^\dagger c_j$$

where the operators $c_i^\dagger$ and c_j create an electron in state $|i\rangle$ and destroy an electron in state $|j\rangle$ and the sum is taken over all possible values of i and j. Applying this to (4.5) gives the tight binding Hamiltonian in second quantized notation

$$\hat{H} = E_0 \sum_{i,\sigma} c_{i,\sigma}^\dagger c_{i,\sigma} + \sum_{i,j,\sigma} t_{ij} c_{i\sigma}^\dagger c_{j\sigma} \tag{4.9}$$

where $c_{i\sigma}^\dagger$ and $c_{i\sigma}$ create and destroy an electron with spin σ on atom i and t_{ij} is again the hopping integral. From this expression, we see that the Hamiltonian represents destroying an electron on atom i and then creating one on atom j with energy t_{ij}. Hence, the hopping integral can be thought of as the energy gain when electrons are allowed to hop from one atom to another in the solid. Delocalization of particles tends to reduce the kinetic energy of the particles, so when electrons hop between different atoms, the electrons become more delocalized, and that reduces the energy of the electrons. In addition, the potential energy of the electron is lowered by the attractive Coulomb potential of all the atoms in the solid. So combined, the kinetic and potential energies of the electron are lower in a solid than in an isolated atom.

There are various other approximations that can be made to the tight binding Hamiltonian (4.9). The differing approximations lead to the different forms of the tight binding Hamiltonian seen in the literature. A short list will given below of the various assumptions made to (4.9) that appear in the literature, as well as the resulting Hamiltonians.

1. The first term is usually ignored since it only shifts all energies by a constant E_0, and we normally do not care about uniform shifts to the energies. The Hamiltonian is then

$$\hat{H} = \sum_{i,j,\sigma} t_{ij} c_{i\sigma}^\dagger c_{j\sigma} \, . \tag{4.10}$$

2. In addition to the previous assumption, the on-site energies, t_{ii}, are often the same value for all i; i.e., $t_{ii} = t_0$. To see why this may be true, consider a lattice with one atom per unit cell. From the definition of t_{ij} in (4.5), we can interpret t_{ii} as the shift in energy from first order perturbation theory of the atomic orbital energy on the i^{th} atom due to the potential of all other atoms. However, due to translational symmetry, it cannot matter which atom we consider; the potential that atom 1 feels due to all other atoms is the same as the potential that atom 10 feels due to all other atoms. This means all matrix elements t_{ii} are the same. When all diagonal elements of t are the same, all eigenvalues E_n^t of t can be written as $E_n^t = t_0 + E_n^0$, where E_n^0 are the eigenvalues of t with $t_{ii} = 0$. Hence, we may take $t_{ii} = t_0 = 0$ since any non-zero t_0 only shifts all eigenvalues by the constant t_0, and we usually do not care about constant shifts to the eigenvalues. The Hamiltonian in this case is

$$\hat{H} = \sum_{i \neq j,\sigma} t_{ij} c_{i\sigma}^\dagger c_{j\sigma} \, . \tag{4.11}$$

3. In addition to the previous assumptions, since hopping of an electron between atoms that are a few lattice constants apart is unlikely, we normally restrict the sum to only include hopping between nearest neighbors. The resulting Hamiltonian is

$$\hat{H} = \sum_{(i,j),\sigma} t_{ij} c^\dagger_{i\sigma} c_{j\sigma} \,, \tag{4.12}$$

   where the notation (i, j) means that atoms i and j are nearest neighbors.

4. In general, $t_{ij} = t^*_{ji}$. However, the matrix elements t_{ij} are sometimes real, hence $t_{ij} = t_{ji}$. Assuming t_{ij} is real and assuming all the previous assumptions, the Hamiltonian becomes

$$\hat{H} = \sum_{(i,j),\sigma} t_{ij} [c^\dagger_{i\sigma} c_{j\sigma} + c^\dagger_{j\sigma} c_{i\sigma}] \,, \tag{4.13}$$

   however the sum is taken over distinct nearest neighbors pairs; i.e., if i and j are nearest neighbors, then (i, j) appears in the sum, but not (j, i). The notation (i, j) in this case is the same as the notation in (4.12), but the meanings are different. The two meanings are used interchangeably in the literature, so one must infer the meaning from the Hamiltonian.

5. Usually $t_{ij} < 0$, so the Hamiltonian (4.13) is sometimes written

$$\hat{H} = \sum_{(i,j),\sigma} -t_{ij} [c^\dagger_{i\sigma} c_{j\sigma} + c^\dagger_{j\sigma} c_{i\sigma}] \,, \tag{4.14}$$

   where t_{ij} in this equation is defined as the negative of t_{ij} in the definition (4.5).

The various forms of the Hamiltonian (4.9), (4.10), (4.11), (4.12), (4.13) and (4.14) can be seen in the literature.

4.2.3 Tight binding and perturbation theory

In tight binding, we start with a large number of degenerate atomic orbitals and construct the t matrix using the degenerate atomic states, then calculate the eigenvalues of t to get the corrections to the atomic energies, as mentioned earlier (equation (4.6)). This reminds one of degenerate perturbation theory [57], where one has degenerate states and calculates the matrix elements of a perturbation using the degenerate states, then finds the eigenvalues of the resulting perturbation matrix, which gives the first order correction to the energies. In the case of tight binding, the perturbation for the j^{th} atom would be the potential $U_j = \sum_{n \neq j} U(\vec{r} - \vec{R}_n)$ from (4.5). However, this perturbation changes for each atom, so it is not clear how to write the Hamiltonian in the form $H = H_0 + H'$ where H' is a single perturbation to the solvable Hamiltonian H_0.

Since there is still a strong similarity between tight binding and degenerate perturbation theory, there may be some underlying reason for the similarity. The origin of the similarity

can be seen from the Hamiltonian in second quantized notation, equation (4.9). If we write the tight binding Hamiltonian as

$$H = H_0 + H'$$
$$H_0 = E_0 \sum_{i,\sigma} c^\dagger_{i\sigma} c_{i\sigma}$$
$$H' = \sum_{i,j,\sigma} t_{ij} c^\dagger_{i\sigma} c_{j\sigma}$$

then, for a single electron in the system described by this Hamiltonian, we can calculate exactly the solutions of H_0 (they are just the degenerate atomic states $|i\rangle$) and treat H' as a perturbation. From degenerate perturbation theory, we first calculate the matrix elements of H' using the degenerate states $|i\rangle$; they are just t_{ij}. Then we calculate the eigenvalues of the matrix t to get the first order energy corrections to the atomic energies E_0. This shows that we may think of tight binding as the first order correction to the atomic energies to get the energies of a solid.

The relationship between tight binding and perturbation theory will be useful since we may then use perturbation theory to calculate higher order corrections to the energy. For example, for the case of non-degenerate orbitals, the second order correction to the atomic energies are

$$\Delta E_2 = \sum_{i \neq j} \frac{|t_{ij}|^2}{E_j - E_i} \,. \tag{4.15}$$

In this case, when hopping is between orbitals of differing energies, the hopping is called *virtual hopping*.

4.2.4 Calculating the hopping integral

In the previous examples and equations, everything is written in terms of the hopping integral t_{ij} and there is no explicit calculation of this matrix element. This is because in tight binding, one does not calculate t_{ij} from first principles; i.e., one does not calculate $\langle i| \sum_{n \neq j} U(\vec{r} - \vec{R}_n)|j\rangle$ from the atomic potential $U(\vec{r})$. Instead, to calculate t, one normally compares the tight binding expressions to experiment or another theoretical calculation and chooses a value for t so that the tight binding results agree numerically with these other methods.

For example, one can experimentally measure the difference in energy E_Δ between the H_2 bonding and anti-bonding orbitals. Since, according to tight binding (4.8), this energy difference must be $2t_s$, we can calculate that $t_s = E_\Delta/2$. Another common method for calculating t is to calculate a band structure using DFT (§4.5), and calculate the band structure for the same system using tight binding, then choose t so that the two band structures are numerically similar.

This procedure for finding t may seem unusual, since we need to know the energies of a

system from another calculation method or from experiment to calculate t, but if we already have the energies for a system, then why do we need tight binding to calculate those same energies? The reason is, once we have calculated t for one system, we may then use this value for other systems. For example, once we know t for graphite, we may use the same value for carbon nanotubes or C_{60}.

4.2.5 Basis functions

In tight binding, we normally assume that the matrix elements t_{ij} are non-zero only for nearest neighbors (e.g., in equation (4.12)). This assumption will be true as long as the basis functions we use to calculate t_{ij} are localized at atomic sites, so they do not necessarily have to be atomic orbitals. In the situation where the localized basis functions are taken as atomic orbitals, tight binding is also called linear combination of atomic orbitals (LCAO). Another possible localized basis is the set of Wannier functions since Wannier functions are often (but not always) localized at the atomic sites and form an orthonormal basis (§8.4 in [138]).

4.3 Mott-Hubbard insulators

The tight binding model is a simple model which can work well in many situations. However, for certain substances such as MnO, tight binding would predict it to be a conductor when it is in fact an insulator. Tight binding completely fails to predict the electronic properties for this material. When a substance which should be a conductor according to single particle theories, such as tight binding, is actually an insulator, it is called a *Mott insulator*. One theory behind why this occurs is due to Hubbard and such insulators are sometimes also called *Mott-Hubbard insulators*. Hubbard took the simple tight binding Hamiltonian (equation (4.14)) and added a term which takes into account electron-electron repulsion (§26.6 in [138]).

$$\hat{H} = \sum_{(i,j),\sigma} -t_{ij}[c^\dagger_{i\sigma}c_{j\sigma} + c^\dagger_{j\sigma}c_{i\sigma}] + U\sum_j c^\dagger_{j\uparrow}c_{j\uparrow}c^\dagger_{j\downarrow}c_{j\downarrow}\ .$$

This Hamiltonian is called the *Hubbard Hamiltonian*. The term $c^\dagger_{j\uparrow}c_{j\uparrow}c^\dagger_{j\downarrow}c_{j\downarrow}$ is non-zero only when state j has two electrons on it, one with spin $\uparrow$ and one with spin $\downarrow$. So the second term in the Hamiltonian adds an additional energy U whenever an orbital has two electrons on it. The energy U represents the electrostatic repulsion energy between two electrons in the same state, and is sometimes called the *Hubbard U* (Hubbard argued that the repulsion energy between an electron in one state and an electron in another state is ~ 10 times smaller, so did not include this effect in the Hamiltonian).

The addition of the Coulomb repulsion term to the tight binding Hamiltonian makes the Hubbard Hamiltonian much harder to solve. However, one can still get a qualitative idea of its behavior. For example, take the case where each atomic orbital contains one electron (so that it is half filled) (figure 4.1). When an electron from one orbital hops to a neighboring

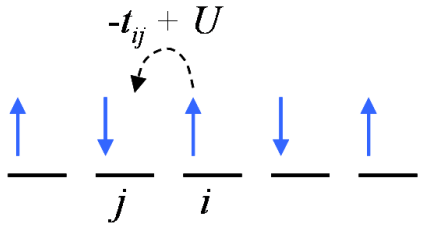

Figure 4.1: In the Hubbard model, when an electron hops from one atom to another, it reduces its energy by the amount t_{ij}, but increases in energy by U due to the Coulomb repulsion between electrons

orbital, the tight binding term in the Hubbard Hamiltonian predicts that the energy of the electron will change by $-t_{ij}$. However, since the neighboring orbital already has an electron, the Coulomb repulsion between the electrons increases the energy of the hopping electron by U. Hence, qualitatively, we see that if $-t_{ij} + U < 0$, it is energetically favorable for electrons to move from one atom to another, and we have a conductor, but if $-t_{ij} + U > 0$, it is energetically unfavorable for electrons to hop between atoms, and the electrons remain immobile at their atomic sites, leading to an insulator.

Normally, the hopping matrix element t_{ij} is related to the bandwidth $W \approx t_{ij}$ (figure 4.2). Therefore, when

$$\frac{U}{W} \approx 1$$

we get a metal to insulator transition. When $U/W > 1$ we have an insulator while for $U/W < 1$ we have a conductor. Figure 4.2 shows a qualitative sketch of the DOS for a system when $U/W < 1$ and $U/W > 1$. For $U/W > 1$, we see two peaks; the lower energy peak is called the *lower Hubbard band* while the higher energy peak is called the *upper Hubbard band*. The Fermi energy lies between these peaks and $\mathrm{DOS}(E_\mathrm{F}) = 0$, meaning we have an insulator. For $U/W < 1$, the lower and upper Hubbard bands overlap, resulting in a non-zero DOS at E_F, implying the system is a conductor. In the limit $U = 0$, the lower and upper Hubbard bands become a single peak; this is the limit where the electrons are non-interacting. Hence, we see that the effect of electron-electron repulsion energy U is to take single peaks in the non-interacting electron DOS and split them into two peaks.

There has been much theoretical work on Hubbard Hamiltonian, but not many exactly solvable cases. A general review is given in [8]. An exact solution exists in one dimension [124]. Unfortunately, the intuitive model given above does not seem to apply in this case since $U = 0$ gives a conductor while $U > 0$ gives an insulator. Other approximate solutions also exist which predict a metal to insulator transition for $U/W \approx 1.15$ (§13.2 in [48]) or $U/W \approx 1.5$ [98] for half filled bands.

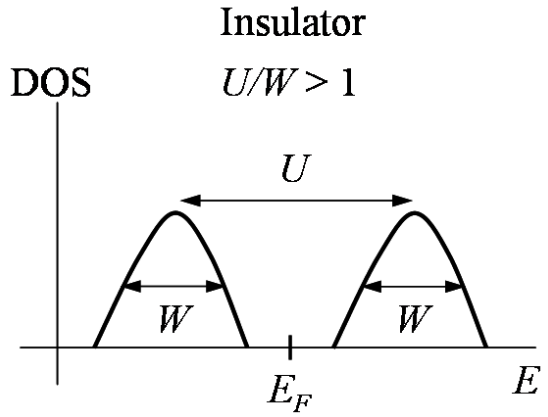

(a) The lower and upper Hubbard bands are completely separated, resulting in an insulator

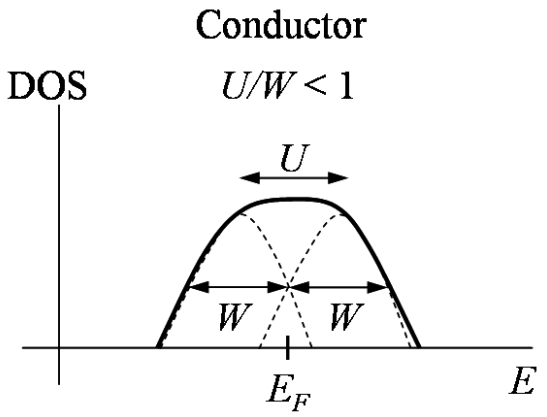

(b) The lower and upper Hubbard bands (dotted curves) overlap, so the total DOS (solid curve) has states at E_{F}, resulting in a conductor

Figure 4.2: Variations in the DOS of a system due to the Hubbard U.

4.4 Adsorbates on Surfaces

We would often like to study the intrinsic properties of molecules or atoms, but to study them by STM, we must first place them on a conducting surface. So to understand the intrinsic properties of the molecules we wish to study, we must first understand how the conducting surface modifies the electronic and magnetic properties of that molecule. This section will present simple theories behind electronic and magnetic interactions between molecules and surfaces. These theories are not exact solutions to the problem of molecule-substrate interactions, so experiments are still needed to better understand molecule-substrate interactions.

4.4.1 The Fano-Anderson model

When a molecule with discrete energy levels is placed on a surface with a continuous set of energy levels, the molecular orbitals can hybridize with the surface orbitals to produce new states. Theories treating the interaction between discrete states and continuum states as a perturbation exist [53], and may be intuitively easier to grasp, but exact solutions which neglect electron-electron interactions also exist. These exact solutions were derived by Fano [47] and Anderson [2]. Their discrete state-continuum state interaction model will be called the Fano-Anderson model here and will be discussed next.

A complete derivation of the result can be found in chapter 6 of [166] (by taking $U = 0$ in the Hamiltonian) and derivations can also be found in chapter 4 of [133] and in [152]. A statement of the results will be presented here.

When an atom or molecule with a localized state $|\phi\rangle$ with energy E_ϕ is placed in contact

with a bulk metal, then the electronic states of the metal can interact with and hybridize with the localized state to produce new states. If $a^\dagger$ and a are the creation and destruction operators for an electron on the initially localized state $|\phi\rangle$ while $c_{\vec{k}}^\dagger$ and $c_{\vec{k}}$ are the creation and destruction operators for a bulk metal electron with wavevector $\vec{k}$ and energy $E_{\vec{k}}$, then the Hamiltonian (§4.2 in [133]) for this system neglecting electron-electron interactions is

$$\hat{H} = E_\phi a^\dagger a + \sum_{\vec{k}} \left[E_{\vec{k}} c_{\vec{k}}^\dagger c_{\vec{k}} + V_{\vec{k}} c_{\vec{k}}^\dagger a + V_{\vec{k}}^* a^\dagger c_{\vec{k}} \right] . \tag{4.16}$$

The first term describes the energy of an electron on the localized state while the second term describes the energy of the bulk metal electrons. The third and fourth terms describe the energy gain $V_{\vec{k}}$ when an electron hops from the metal to the localized state or vice versa.

If the states $|n\rangle$ with energy E_n represent the solutions to this Hamiltonian, then the expectation value of the Green's operator (§4.1.2) for this system in the localized state $|\phi\rangle$ can be calculated:

$$\langle \phi | \lim_{\alpha \to 0} \hat{G}(E) | \phi \rangle = \lim_{\alpha \to 0} \sum_n \frac{\left| \langle \phi | n \rangle \right|^2}{E + i\alpha - E_n} = \frac{1}{E - E_\phi - \Sigma_{\text{ret}}(E)}$$

where $\Sigma_{\text{ret}}(E) = \Delta(E) + i\Gamma(E)$ is called the retarded self-energy with

$$\Gamma(E) = \text{Im}\{\Sigma_{\text{ret}}(E)\} = \pi \sum_{\vec{k}} \left| V_{\vec{k}} \right|^2 \delta(E - E_{\vec{k}})$$

and $\Delta(E)$ is just the Hilbert transform (which is the same as the Kramers-Kronig transform) of $\Gamma(E)$

$$\Delta(E) = \text{Re}\{\Sigma_{\text{ret}}(E)\} = \frac{1}{\pi} P \int \frac{\Gamma(E')}{E - E'} \, dE'$$

where P denotes the Cauchy principal value of the integral. This Green's function leads to the result

$$\text{PDOS}(|\phi\rangle, E) = \frac{1}{\pi} \frac{\Gamma(E)}{\left[E - E_\phi - \Delta(E) \right]^2 + \Gamma(E)^2} . \tag{4.17}$$

4.4.2 Electronic properties of adsorbates

To understand what the Fano-Anderson model implies for the electronic properties of adsorbates on surfaces, take an example. Assume that $\Gamma(E)$ is roughly independent of energy, then $\Delta(E) \approx 0$, and (4.17) represents a Lorentzian centered at energy $E_\phi + \Delta(E) \approx E_\phi$ with width (FWHM) $2\Gamma(E)$. This means that when a localized state $|\phi\rangle$ hybridizes with states from a continuum, the new system they form contains hybridized states which resemble $|\phi\rangle$ within an energy range of $2\Gamma(E)$ around the localized state energy E_ϕ. Outside of this energy range, the states of the new system are essentially the same as the continuum

states before addition of the localized state. Hence, the hybridization happens in an energy window of $2\Gamma(E)$ around E_ϕ.

A more mathematical way to interpret the PDOS in (4.17) comes from Fano [47]. The states $|\Psi_E\rangle$ for the system consisting of the localized state hybridized with continuum can be written as a linear combination of the localized state $|\phi\rangle$ plus the metal states $|\psi_E\rangle$

$$|\Psi_E\rangle = \lambda_E|\phi\rangle + \int b_{E,E'}|\psi_{E'}\rangle\, dE' \,.$$

Then Fano showed that

$$\big|\lambda_E\big|^2 = \mathrm{PDOS}\big(|\phi\rangle, E\big) = \frac{1}{\pi}\frac{\Gamma(E)}{\big[E - E_\phi - \Delta(E)\big]^2 + \Gamma(E)^2} \,.$$

Since λ_E tells us the amount of the localized state $|\phi\rangle$ in the total wavefunction $|\Psi_E\rangle$ for the entire system, we see that the amount of the original wavefunction $|\phi\rangle$ contained in the total wavefunction $|\Psi_E\rangle$ is maximum at an energy $\Delta(E)$ above the original energy E_ϕ of the localized state and the amount of $|\phi\rangle$ in $|\Psi_E\rangle$ decreases quickly away from this maximum. The average lifetime of an electron in the state $|\phi\rangle$ is $\hbar\Gamma(E)/2\pi$ from [47].

Although (4.17) is an exact solution to the Hamiltonian, there is still an unknown parameter $V_{\vec{k}}$, which is an energy that measures how strongly the localized state interacts with the continuum. If $|V_{\vec{k}}|$ is small compared to typical binding energies in a solid ($\sim 3\,\mathrm{eV}$), then the interaction between localized state and continuum is weak and the adsorbate is said to be *physisorbed*. There are no significant changes to the localized state in this regime, and the adsorbate may be bonded to the surface only by weak Van der Waals forces. However, if $|V_{\vec{k}}|$ is comparable to typical binding energies in a solid, then the interaction between localized state and the continuum is large and the adsorbate is said to be *chemisorbed*. In this regime, there may be significant changes to the localized state.

The Fano resonance

Fano also described the probability for an electron to be excited from an initial state $|i\rangle$ to either the hybridized impurity state $\big|\Psi\big\rangle$ or the unhybridized continuum state $|\psi\rangle$. If the operator which describes transitions between states is T, then the ratio $f(E)$ of these transition probabilities is

$$f(E) = \frac{\big|\langle\Psi|T|i\rangle\big|^2}{\big|\langle\psi|T|i\rangle\big|^2} = \frac{(\epsilon+q)^2}{\epsilon^2+1} \quad \text{with} \quad \epsilon = \frac{E - E_\phi - \Delta(E)}{\Gamma(E)/2}$$

and q is related to the relative strengths of transitions from $|i\rangle$ to $|\psi\rangle$ and from $|i\rangle$ to a modified localized state (different from the hybridized localized state) described in [47]. The line shape described by $f(E)$ is called a *Fano line shape* or *Fano resonance*. The expression for the Fano resonance can be generalized using self-energies to obtain other expressions of

the Fano resonance [131].

4.4.3 Magnetic properties of adsorbates

Magnetic adsorbates can interact with surfaces in various ways, such as the RKKY interaction. Spin sensitive local probes, such as spin polarized STM, have the ability to obtain local magnetic and spin properties of a system. However, even without a spin sensitive probe, one may still access certain spin properties of a system.

One way to detect spin indirectly would be through inelastic excitation of one spin state to another [83]. When the tunneling electrons' energy exceeds the spin excitation energy, then one may induce spin transitions.

Another way of detecting spins is through an effect known as the *Kondo effect*. When a magnetic impurity such as a molecule or atom is placed in contact with a bulk metal, the resistance of the sample begins to increase as the temperature is lowered below a certain temperature, which is the opposite of what is normally expected (it usually decreases or remains constant). In this situation, what is happening is that the spin of the impurity interacts with the spins of the conduction electrons at low temperatures, forming a many-body impurity-conduction electron ground state. This interaction between impurity spin and conduction spins is known as the *Kondo effect*.

This effect can be described mathematically. Let $a_\sigma^\dagger$ and a_σ be the creation and destruction operators for an electron on the localized state with spin σ and $c_{\vec{k}\sigma}^\dagger$ and $c_{\vec{k}\sigma}$ be the creation and destruction operators for an electron with wavevector $\vec{k}$ and spin σ in the continuum, then the Hamiltonian which describes the Kondo effect, called the Kondo Hamiltonian, is given by (§7.1 in [166])

$$\hat{H}_K = \sum_{\vec{k},\sigma} E_{\vec{k}} c_{\vec{k},\sigma}^\dagger c_{\vec{k},\sigma} - \sum_{\vec{k},\vec{k'}} \frac{J_{\vec{k}\vec{k'}}}{\hbar^2} \begin{pmatrix} c_{\vec{k'}\uparrow}^\dagger & c_{\vec{k'}\downarrow}^\dagger \end{pmatrix} \vec{S} \begin{pmatrix} c_{\vec{k}\uparrow} \\ c_{\vec{k'}\downarrow} \end{pmatrix} \cdot \begin{pmatrix} a_\uparrow^\dagger & a_\downarrow^\dagger \end{pmatrix} \vec{S} \begin{pmatrix} a_\uparrow \\ a_\downarrow \end{pmatrix}$$

where $\vec{S} = \hbar\vec{\sigma}/2$ and the components of $\vec{\sigma}$ are the Pauli matrices

$$\sigma_x = \begin{pmatrix} 0 & 1 \\ 1 & 0 \end{pmatrix}, \quad \sigma_y = \begin{pmatrix} 0 & -i \\ i & 0 \end{pmatrix}, \quad \sigma_z = \begin{pmatrix} 1 & 0 \\ 0 & -1 \end{pmatrix}$$

The Kondo Hamiltonian can be derived from the more fundamental Fano-Anderson model [2], but we need to add an extra term to the Hamiltonian (4.16) to describe the electron-electron interactions and will explicitly include spin in the Hamiltonian (§6.2 in [133], §26.5 in [138]). The more general Fano-Anderson Hamiltonian (normally called the Anderson Hamiltonian) is

$$\hat{H} = E_\phi[a_\uparrow^\dagger a_\uparrow + a_\downarrow^\dagger a_\downarrow] + U a_\uparrow^\dagger a_\uparrow a_\downarrow^\dagger a_\downarrow + \sum_{\vec{k}\sigma} \left[E_{\vec{k}} c_{\vec{k}\sigma}^\dagger c_{\vec{k}\sigma} + V_{\vec{k}} c_{\vec{k}\sigma}^\dagger a_\sigma + V_{\vec{k}}^* a_\sigma^\dagger c_{\vec{k}\sigma} \right].$$

This Hamiltonian can be transformed into the Kondo Hamiltonian using a similarity transformation. Since similarity transformations do not change the eigenvalues of a Hamiltonian, this type of transformation is allowable. By using a similarity transformation called the Schrieffer-Wolff transformation (chapter 11 in [184], chapter 7 in [166]), the Hamiltonian above can be converted to a Hamiltonian

$$\hat{H}' = \hat{H}_K + \hat{H}_{\text{other}}$$

where $\hat{H}_K$ is the Kondo Hamiltonian and $\hat{H}_{\text{other}}$ represents terms which do not involve single occupancy of the impurity orbital. In the Kondo effect, we assume that we have magnetic impurities, so that the impurity must have a singly occupied state, hence, $\hat{H}_{\text{other}}$ is not relevant to describe the Kondo effect. So to second order in $V_{\vec{k}}$, the Anderson Hamiltonian leads to the Kondo Hamiltonian with a spin interaction energy given by

$$J_{\vec{k}\vec{k}'} = V_{\vec{k}'}V_{\vec{k}}\left[\frac{1}{E_{\vec{k}'} - (E_\phi + U)} + \frac{1}{E_{\vec{k}} - (E_\phi + U)} - \frac{1}{E_{\vec{k}} - E_\phi} - \frac{1}{E_{\vec{k}'} - E_\phi}\right]$$

The relationship between the Kondo and Anderson Hamiltonians allows us to view the Kondo effect in terms of virtual hopping of electrons on and off the impurity (chapter 7 in [166]), where the electrons hopping from the continuum have opposite spin to the spin of the impurity. Because of this anti-alignment of continuum and impurity spins, we can then think of the continuum electrons as forming a singlet state with electron on the impurity state.

The Kondo many-body singlet state can be characterized by a quantity known as the Kondo temperature T_K

$$T_K = \frac{1}{k_B} D \sqrt{\frac{U\Gamma}{|E_\phi||E_\phi + U|}} \exp\Big(-\pi \frac{|E_\phi||E_\phi + U|}{2U\Gamma}\Big) .$$

where $\Gamma = \pi|V|^2\rho(E_{\text{F}})$ is the width of the hybridized localized state $|\phi\rangle$ and D is the bandwidth of the conduction band. The energy $k_B T_K$ represents roughly the binding energy of the Kondo singlet state, and hence, we will only see the Kondo singlet state below a temperature T_K.

To understand the effect of the Kondo resonance on the electronic properties of the system, the PDOS of the localized impurity for $T < T_K$ can be calculated using Fermi liquid theory [150]

$$\text{PDOS}(|\phi\rangle, E) \approx \frac{1}{\pi}\frac{1}{\Gamma + \gamma(E,T)}$$
$$\text{with} \quad \gamma(E,T) = \frac{\Gamma}{2}\left(\frac{E}{k_B T_K}\right)^2 + \pi^2 \frac{\Gamma}{2}\left(\frac{T}{T_K}\right)^2$$

where $\Gamma \sim 100\,\text{meV}$ is the energy for electrons to hop on or off the localized state $|\phi\rangle$. This

PDOS is a Lorentzian with a FWHM of $2\sqrt{(\pi k_B T)^2 + 2(k_B T_K)^2}$ centered at $E = 0 = E_F$. This Lorentzian is known as the Kondo resonance. For low temperatures ($T \ll T_K$), the FWHM is $\sim 2.8 k_B T_K$.

Often in STM, the Kondo resonance does not appear as a peak, but as various different line shapes. This can be explained by electrons tunneling into two different possible states, the hybridized magnetic impurity states, or the unhybridized conduction electron states. This ability to tunnel into two different states gives rise to a Fano resonance instead of a Lorentzian (§4.4.2). Near E_F and for $T < T_K$, the tunneling differential conductance can be written in terms of the Fano line shape as [131]

$$\frac{dI(V)}{dV} \propto \frac{(q+\epsilon)^2}{1+\epsilon^2} \quad \text{with} \quad \epsilon = \frac{e_c V - E_0}{k_B T_K}$$

where E_0 is a parameter measuring the offset of the Fano resonance from E_F and q represents the relative strengths of tunneling into the modified localized state and the unhybridized continuum states (§4.4.2). The STM dI/dV spectroscopy curves for the Kondo resonance are usually fit to the Fano line shape with E_0, q, and T_K taken as fit parameters. Fitting spectroscopy data to the Fano line shape is normally how one obtains the Kondo temperature T_K from STM data.

4.5 Density Functional Theory

It is usually difficult to include many-body interactions in a computation, since the computational time grows quickly with the number of electrons. For example, for N_e electrons and N_B basis functions, we need to consider $N_B!/N_e!(N_B - N_e)!$ Fock states; so when we construct the Hamiltonian matrix from these states, it will be a square matrix with $N_B!/N_e!(N_B - N_e)!$ rows (§5.1 in [184]). With only 10 electrons and 50 basis functions the Hamiltonian matrix has $\approx 10^{10}$ rows, while with 100 electrons and 200 basis functions, the Hamiltonian matrix has $\approx 9 \times 10^{58}$ rows. These are large matrices to diagonalize. To do any calculation with a large number of electrons, for example $N_e \geq 100$, we need a better method than diagonalizing a Hamiltonian.

One of the important breakthroughs came in the 1960's and 1970's. Hohenberg and Kohn proved an important theorem, that one only needs to calculate the ground state electron number density $n(\vec{r})$ to get the ground state properties of a system (§5.1 in [184], §9.3 in [138]). One does not need to calculate the wavefunction of every electron, just a single function, the electron number density. This result dramatically reduces the amount of computations necessary to calculate the ground state properties of a system.

From Hohenberg and Kohn's theorem, it can be derived that there is a universal functional $F[n]$ such that when a potential energy $U[n]$ for a particular system is added to it, the function n which minimizes $F[n] + U[n]$ is the ground state electron number density of the system (§9.3 in [138]). This theory which relates ground state properties of a system to minimization of functionals of electron densities is known as *density functional theory*. It

has been extremely successful at predicting the properties of systems where other methods such as Hatree-Fock fail and earned Kohn the Nobel prize in chemistry in 1998.

4.5.1 The Kohn-Sham equations

The functional $F[n]+U[n]$ that we need to minimize is in general unknown, but can still be written in a more explicit form. Since it is easier to solve for the wavefunctions for a system of non-interacting particles, expressing $F[n] + U[n]$ as a non-interacting particle equation can make it easier to solve. This is done by first assuming the total number density $n(\vec{r})$ can be written as the sum of N wavefunctions $n(\vec{r}) = \sum_{j=1}^{N} |\psi_j(\vec{r})|^2$, but these wavefunctions are not necessarily the electron wavefunctions. Kohn and Sham then derived that the functions ψ_j which minimizes $F[n] + U[n]$ must satisfy the Kohn-Sham equations

$$H_{KS}[n]\psi_j(\vec{r}) = E_j\psi_j(\vec{r}) \tag{4.18}$$

$$\text{with} \quad H_{KS}[n] = -\frac{\hbar^2}{2m}\nabla^2 + V_{\text{eff}}[n] \tag{4.19}$$

$$\text{and} \quad V_{\text{eff}}[n] = \left[U(\vec{r}) + \int \frac{e^2 n(\vec{r}')}{|\vec{r} - \vec{r}'|}\, d\vec{r}' + \frac{\partial E_{xc}[n]}{\partial n}\right]. \tag{4.20}$$

This is effectively like the Schrödinger equation for a single particle in the potential V_{eff} and the solutions ψ_j of the Kohn-Sham equations would allow us to calculate an exact many-body ground state number density for the system. However, there are two important differences between the Kohn-Sham equations and the Schrödinger equation. First, V_{eff} depends on n, and n depends on ψ_j, hence, we cannot find V_{eff} unless we already know the solutions to the Kohn-Sham equations. Second, everything unknown about F has now been pushed into the functional E_{xc}, called the *exchange-correlation functional*. The exact form of this functional is unknown and is normally approximated. One approximate functional commonly used in calculations is $E_{xc} = -(\frac{3}{\pi}n(\vec{r}))^{1/3}$ which is just the energy of a free electron gas with density $n(\vec{r})$, however, in a free electron gas, the number density is a constant whereas in general it is a function of position. Hence, this approximate functional assumes that locally, the electrons behave like a free electron gas and the approximation is called the local density approximation (LDA). Since a free electron gas does not include interactions between electrons, a DFT calculation using LDA also does not correctly include all electron-electron interactions.

4.5.2 DFT calculations

A DFT calculation is usually based on the Kohn-Sham equations (4.18). One first needs an initial guess for n so that one knows $H_{KS}[n]$. One also needs a complete basis set of functions $\{|i\rangle\}$. Then the following steps are iterated.

1. The matrix elements $\langle i|H_{KS}[n]|j\rangle$ are calculated to find $H_{KS}[n]$ in a matrix form.

2. Once one constructs the matrix representation for $H_{KS}[n]$, then one can calculate its eigenvalues, which are energies ϵ_j, and eigenvectors ϕ_j.

3. Once one has the functions ϕ_j, then $n'(\vec{r}) = \sum_j |\phi_j|^2$ can be recalculated and a new Hamiltonian $H_{KS}[n']$ can be constructed.

4. The first step is now repeated with $H_{KS}[n']$.

Hopefully, at some point, n does not change with any more iterations, at which point we have found the solution to (4.18). This iteration procedure is called a self-consistent field (SCF) iteration.

The next parts below will describe the details of the various components of a DFT calculation.

Basis functions and E_{xc}

The main parameters that limit the accuracy of DFT calculations in theory are the basis functions used to calculate the matrix elements of $H_{KS}[n]$ and the exchange-correlation functional E_{xc}. The basis functions limit the accuracy of the calculation since a complete basis has an infinite number of functions, so a finite set of functions must be used in any calculation. This finite set of functions is normally called the *basis* in DFT calculations.

Most DFT codes allow you to choose different sets of functions for a basis. A single function in the basis which is localized on an atom is commonly called ζ (zeta), so sets of basis functions are often defined in terms of ζ. For example, if one has a system with N atoms and uses a set of basis functions where one basis function is localized on each atom (N basis functions total), this set of basis functions would be referred to as a single-ζ or single-zeta (SZ) basis. If one uses instead a set of functions with two functions localized on each atom ($2N$ basis functions total), this would be referred to as a double-ζ or double-zeta (DZ) basis. Basis functions localized to atoms tend to be like atomic wavefunctions, so they may be similar to atomic s or p orbitals. For example, a DZ basis may consist of two functions per atom, one like a $1s$ orbital, and the other like a $2s$ orbital. If we take this DZ basis and add yet another function for every atom to this basis, a p like orbital, this would be referred to as including polarization, and the resultant basis would be called double-ζ + polarization (DZP). In general, adding polarization means one adds another atomic-like wavefunction per atom to a set of basis functions, but the additional functions have higher angular momentum then the functions already in the basis. For example if a basis consists of one p orbital per atom, including polarization would mean adding one d orbital per atom.

The set of basis functions will influence the numerical solutions to the Kohn-Sham equations. For example, when using the SIESTA code to do a DFT calculation on a system with N atoms, SIESTA uses basis functions which are localized to the positions of the atoms; i.e., the basis functions are zero beyond a certain distance away from the atoms. In general, this basis can work well [66]. However, since the basis functions are localized, SIESTA cannot reproduce delocalized wavefunctions well.

One way of getting around artifacts due to the localized basis in SIESTA is to use another program, such as VASP, which uses a plane wave basis. This basis will give more accurate results for delocalized wavefunctions, but usually takes much longer to run a calculation. Another way to get around a localized basis is to add *ghost atoms*. Ghost atoms are atoms with negative atomic numbers, and SIESTA assumes such atoms have no charge, mass, or electrons, so adding such atoms to a system does not change it. However, SIESTA still takes these non-existent atoms into account when constructing the basis, so the code includes atomic-wavefunction-like functions localized at the positions of ghost atoms in the basis. This effectively increases the number basis functions as well as the spatial extent of the set of basis functions.

The exchange-correlation functional E_{xc} also limits the accuracy of DFT calculations since its exact form is not known and one must always approximate it. In addition to LDA, there are other approximate functionals for E_{xc} such as GGA and BLYP (chapter 5 in [184]). These functionals try to build on LDA by adding corrections to it, but are not necessarily more accurate than LDA.

Pseudopotentials

We are normally interested in the electronic properties of systems near the Fermi energy. Since these properties arise mainly from the valence orbitals and electrons of atoms, it is not necessary to take into account the atoms' core electrons in the calculation. Removing the core electrons will reduce unnecessary calculations by a considerable amount. Removing the core electrons is done by using a *pseudopotential*. A pseudopotential is a potential that, when used as the potential energy in Schrödinger's equation, would produces eigenstates of the Schrödinger equation that mimic the valence wavefunctions of atoms correctly, but not the core electron wavefunctions. They have been shown to reproduce many important features of solids correctly [210].

Relaxation

Normally, the coordinates of the atoms in a system are not known exactly. Since DFT can find the energy of a system as a function of the coordinates of the atoms, by finding the positions of the atoms which minimizes the total energy of the system, we will find the equilibrium position of the atoms. The process of finding the position of the atoms to minimize the energy of the system is called *relaxation*. This process uses a numerical method such as steepest descent or conjugate gradient [24] to iteratively move the atomic positions from an initial starting point to find the positions of the atoms which minimize the total energy. Since most numerical methods will only find a relative minimum in energy close to the initial energy (except for Monte Carlo methods [121]), many DFT calculations will also only find relative minima in energy, and not the absolute lowest energy configuration. However, finding a relative minimum in energy instead of the absolute minimum is a problem of the numerical technique used, not a problem of DFT.

Many-body corrections

The Kohn-Sham equation (4.18) with LDA does not correctly take into account many-body effects such as electron-electron interactions. These may be taken into account using methods such as LDA+U [176], or the GW approximation [76]. In the LDA+U method presented in [176], the effect of the electron-electron interaction in a molecule can be taken into account by finding the on-site Coulomb repulsion U (§3.4.2). Once we find U, we know the correction to the HOMO-LUMO gap (equation 3.3). In general, the Coulomb repulsion energy U depends on which orbital we add an electron to. If we add an electron to the LUMO+n, the Coulomb repulsion $U_{\text{LUMO}+n}$ to add an electron to this state may be calculated by simply adding an electron to the LUMO+n and recalculating the LUMO+n energy using DFT with LDA for E_{xc}. The difference between the LUMO+n energy with one electron in it and the LUMO+n energy with no electrons in it gives $U_{\text{LUMO}+n}/2$. Similarly, one may calculate the U for the HOMO$-n$ with the same procedure, except we remove an electron from the state instead of adding it. The quasiparticle HOMO-LUMO gap (§3.4.2) is larger than the non-interacting HOMO-LUMO gap by $U_{\text{HOMO}}/2 + U_{\text{LUMO}}/2$. This method is quite simple and can be done on a laptop in under an hour, even for molecules of 60 atoms.

However, if a molecule is near a metallic surface, then the image charge from the surface can effectively reduce U. Effects from image charges are not correctly taken into account when LDA is used in a DFT calculation since image charges are a result of electron-electron interactions (an electron near a metal repels the nearby electrons in the metal, creating a net positive image charge). Luckily, simple image charge models based on classical electrostatics can take this into account [176, 151].

A more systematic approach to calculating many-body energy corrections is a first order approximation called the GW approximation. In the name GW, G stands for the Green's function for the system while W is the screened Coulomb potential. One may take, for example, $W = V_{\text{ext}}/\epsilon$, where V_{ext} is the externally applied potential and ϵ is the Lindhard dielectric function (equations (5.15) and (5.16) in [213]). The first order correction to the self-energy is found from the product of G and W. In the GW approximation method, one first finds the number density n from the Kohn-Sham equations with LDA. Then the screened Coulomb potential W can be found from n, and G can be written in terms of W and G (so G is expressed in terms of itself). To solve for G when it is defined in terms of itself, it can be numerically calculated self-consistently, and once we know G, we can find the electronic properties of the system (§4.1.2). However, this method is computationally intensive and is usually done on a computing cluster, unlike LDA+U, which can be done on a laptop.

5 Instrumentation

5.1 Scanning Tunneling Microscope

The STM used for all the experiments is a home-built ultra-high vacuum (UHV) STM. The base pressure is $\sim 1 \times 10^{-10}$ torr and base temperature ~ 7 K. The original STM design and construction was carried out by M. F. Crommie, W. Chen, and V. Madhavan. The details of the STM used in the experiments have been presented in the theses of Wei Chen [31], Vidya Madhavan [132], and Tiberiu Jamneala [95], and Michael Grobis [60]. Only an overview of the system will be presented here. Modifications of the STM which are not included in the previous theses will be given in §5.1.7. Details of how to build specific parts of the STM will be given in appendix C.

An overview of the cryogenic UHV STM is shown in figure 5.1. The various parts of the system can be broken down into the following categories:

1. UHV chambers
2. cryogenic system
3. vibrational isolation
4. STM scanner
5. electronics and software

A brief description will be given below for each category.

5.1.1 STM chambers

The chamber and pumping system allow for base chamber pressures at or below 1×10^{-10} torr. The STM chambers are made from 304 stainless steel to allow for baking above 100°C during initial pump down and for low outgassing once at UHV. A combination of a

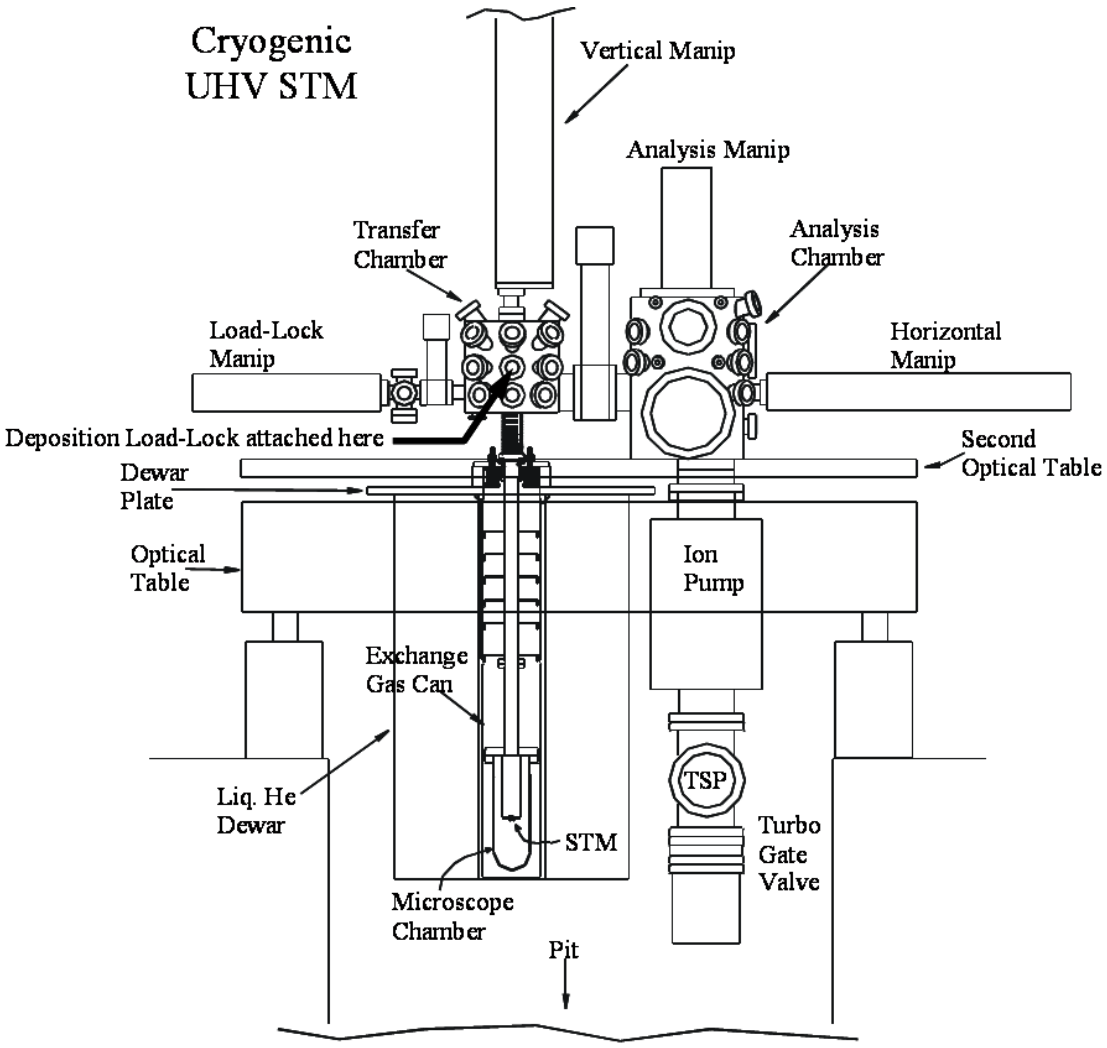

Figure 5.1: STM UHV chambers

500 l/s turbo pump and a diaphragm backed turbo pumping station is used to bring the system from ambient conditions to high vacuum. The turbo pumping system also pumps the system during bake-out, which lasts 3–5 days. During normal operation, the chambers are pumped by two ion pumps (a 75 l/s pump in the transfer chamber and a 500 l/s pump in the analysis chamber) and occasional running of the titanium sublimation pumps (TSPs).

5.1.2 Cryogenics

The microscope chamber sits inside an 80 liter liquid He dewar. The hold time for this dewar is 12 days. A He exchange gas can separates the chamber from direct contact with the liquid He. The He exchange gas is important for three reasons: (1) minimize vibrations from He boil off, (2) avoid the Paschen effect; i.e., avoid pressure ranges (~ 100 mTorr)

where high voltage arcing (corona discharge) can occur, and (3) control desired operating temperature. A series of radiation shields in the exchange gas can are employed to minimize the thermal radiation from the transfer chamber, which is at room temperature, from getting to the microscope chamber. All the wires in the exchange gas can that run from room temperature down to the microscope chamber are stainless steel coaxial cables (Cooner wire part #AS632-1SSF) to reduce heat loss since stainless steel has low thermal conductivity (which means it has high electrical resistance). This cryogenic setup allows operation at a base temperature of 7 K when the exchange gas pressure is ~ 5 mTorr of He gas.

5.1.3 Vibration Isolation

Extensive care is taken to minimize vibrational coupling to the STM. The UHV chambers are mounted on a dual stage optical table with vibrational isolation legs between each stage. The microscope chamber is suspended by two bellows which allow for acoustic mismatch between the transfer chamber and microscope chamber. The whole UHV system is enclosed in a sound proof room to minimize acoustic disturbances. Under normal conditions, ambient vibrational disturbances do not limit the noise. Though typically 3 mÅ rms of "vibrational" noise can be seen on the tip, this noise is thought to be electronic in origin. Even with this noise, high quality images can be readily achieved with 0.5 pA stabilization currents. Images have also been obtained with lower currents, however, the Ithaco 1211 preamp is only calibrated to an accuracy of 1 pA, so while stabilization currents as low as 5 fA have been used, the accuracy of such a current cannot be guaranteed.

5.1.4 STM scanner

The main part of the STM where most experimental data is taken is the STM scan stage (located in the microscope chamber), which is shown in figure 5.2. The STM scanner, called the bug, consists of a series of carefully machined macor pieces (body and support), piezoelectric (piezos) ceramics (coarse and fine motion), and a shielded metallic tip (shield cannot be seen in the figure). Fine (50 μm) gold wires bring electrical contact to the various STM components. The STM bug rests on a piece called the walker plate. This plate consists of a thin glass plate (75 μm thick) below which reside a series of metallic electrodes, below which lies another glass plate (not shown in figure 5.2). Details on the construction of the walker plate is given in appendix C. The electrodes are used for (1) clamping the bug electrostatically to the glass plate and (2) coarse motion of the bug along the glass plate. The STM tip is made from either W or PtIr(80:20) wire (10 mil thick). Since a sharp tip apex is desired, it is common practice to chemically etch the tips (§5.2.1).

5.1.5 STM electronics and software

The essential STM functionality is controlled by a combination of home built electronics boxes (Z-Box, XY-Box, FE Box, Walker Box, Ground breaking box), commercial elec-

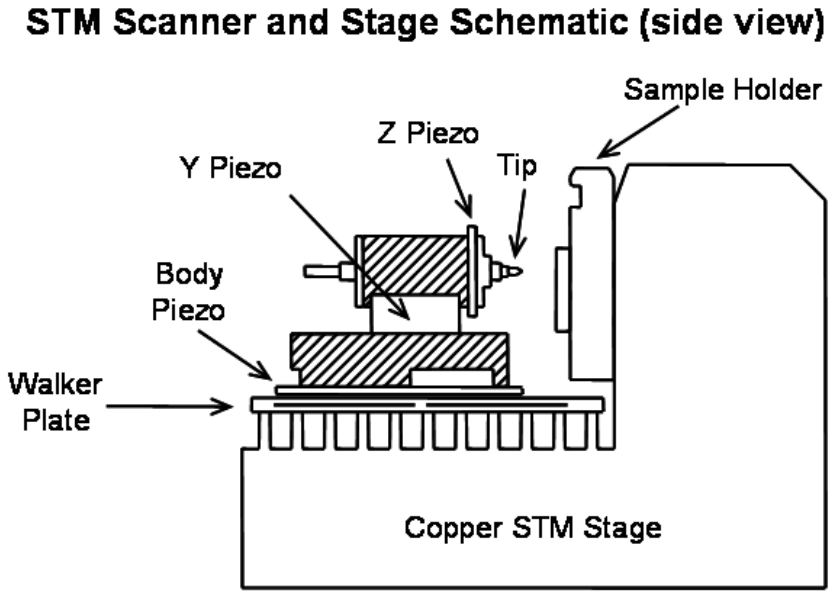

Figure 5.2: STM stage and scanner. The X piezo lies directly behind the Y piezo in this view and cannot be seen in the diagram. The sample receiver (the part that holds the sample holder) is not shown in the diagram.

tronics (Ithaco 1211, Electronic Development Corporation 522, Data Precision 8200), and computer DAQ boards (GPIB, NI PCI-6052E, NI PCI-MIO16XE) all controlled by a central computer. In addition to the essential electronics, there is additional commercial electronics to do spectroscopy (HP 33120A function generator, Princeton Applied Research 5210 lock-in amplifier), an STM temperature controller (LakeShore 340), and a home built audio box to aid with atomic/molecular manipulation (built by the UC Berkeley Physics Electronics Shop, Job # 98-05).

The Z Box, XY Box, FE Box, and Walker Box were designed by Bill Earle at Boston University and were built there. There are manuals for all these boxes. To help test if these boxes are operating properly, there are, in addition, two electronics boxes that were built at UC Berkeley. The first is a digital control word generator (figure 5.3) that can be used to control the home built boxes in place of a computer (built by the UC Berkeley physics electronics shop, job # 99-30). This box is useful for testing and repairing the home built electronics (especially if the physics electronics shop does the repairing) since one would need a computer with the STM software installed to control these boxes otherwise. The new Z-Box (used from 2009 on) has its own digital signal generator (figure 5.3). The second electronics box is an exponentiating box; it takes an input voltage and the output voltage is the exponential of the input: $V_{\text{out}} \sim e^{V_{\text{in}}}$. This box is used to check if the Z-Box feedback is working properly since it simulates the exponential dependence of the tunneling current on the -Z output voltage.

There are a few notes about the commercial electronics. The Data Precision 8200

STM digital word generator

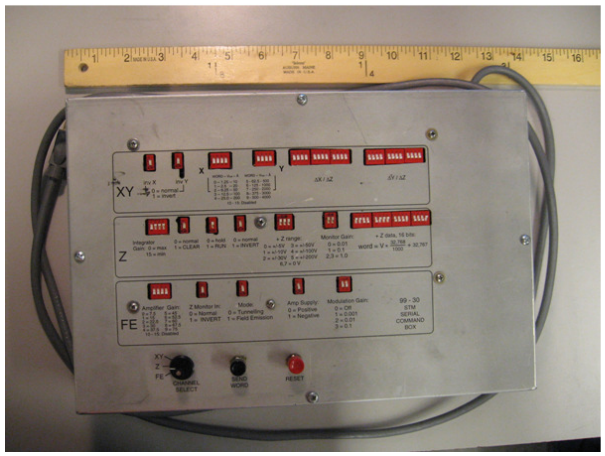

New Z-Box digital word generator

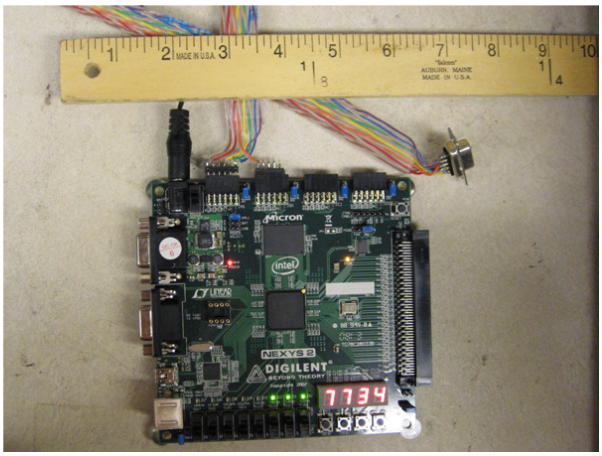

Figure 5.3: Electronics to generate the digital control words for the various STM home-built electronics. The ruler in the pictures is in inches.

voltage calibrators that are used for the -X and -Y voltages are no longer made. Only used/refurbished units can be bought. A spare one was purchased from REPCAL Test equipment (www.repcaltestequip.com). However, the standard Data Precision 8200 has a resistor that may burn out. This resistor is number R51 and is located near the rear panel, next to the J301 output. It is normally a $68\,\mathrm{k}\Omega \pm 5\%$, $\frac{1}{4}\,\mathrm{W}$ carbon resistor and should be replaced with a $68\,\mathrm{k}\Omega \pm 5\%$, $1\,\mathrm{W}$ carbon resistor. The spare Data Precision 8200 from REPCAL has the standard R51 resistor which should be replaced before using it.

The second note about the commercial electronics is that the Ithaco 1211 input voltage should not be larger than $15\,\mathrm{V}$. A resistor can be placed directly onto the input to prevent high voltages on the tip in FE mode from destroying the Ithaco 1211. After correspondence with Ithaco about our setup in 2009, they recommended using a low noise $47\,\mathrm{k}\Omega$, $1\,\mathrm{W}$ resistor such as Vishay Dale part # RN70E4702FB14 inside of a pomona aluminum box, pomona part # 2391 (some of these specifications and part numbers are in the Ithaco manual, but are listed incorrectly).

All of the electronics for the STM is controlled by home-written software. The original version of the software was written in LabView, but since around 2002, newer versions have been written in C++. Nate Jenkins wrote most of this software with help from Mike Grobis. Yuri Zuev, Xiaowei Zhang, and I have corrected bugs and added new features to the software.

5.1.6 Coarse movement and approach

Coarse movement

Coarse motion is achieved by a sequence voltages applied to the body piezo and walker plate electrodes. For example to move forward, one first clamps the rear of the body piezo by applying high voltages to the two back electrodes. One then expands the body piezo (which then expands forward since its back is clamped) by removing any high voltage across of the piezo's electrodes. Then one clamps the front of the body piezo by applying high voltages to the front two electrodes and releases the rear of the body piezo by removing the high voltages from the real electrodes. Next, one contracts the body piezo by applying a high voltage across of its electrodes. This entire sequence is called one step. Typical step sizes at $T = 7\,\mathrm{K}$ vary between $0.1\,\mu\mathrm{m}$ when the walking is not too good, to $1\,\mu\mathrm{m}$ when the walking is good. Moving by a sequence of these steps is called walking. To move the STM bug to a desired location one then takes as many steps as necessary in the correct direction.

The coarse motion does not always work ideally. A number of different things can aid the coarse motion. The stage can be tilted forward to help move the STM forward. The step size also depends on where the STM bug is on the walker plate, so if the STM does not walk backwards, for example, then moving left first and walking backwards next may help it move backwards. If the STM gets stuck somewhere, then tapping on the sample tilt feedthrough can help move the STM to a new area, and the walking may be better in that area. It is also believed that the glass plates on the walker plate can charge up, effectively creating a voltage between the glass plate and body piezo, making it harder for the STM to move. Warming up the STM for a few hours at least to $\sim 40\,\mathrm{K}$ while the walker plate electrodes are grounded seems to help remove the charge. Higher temperatures help more; e.g., warming up the STM to room temperature seems to remove more charge. After cooling the STM back down to $\sim 7\,\mathrm{K}$, the walking is usually good again.

Field emission approach

The coarse movement step size ($\sim 0.1\,\mu\mathrm{m}$ to $1\,\mu\mathrm{m}$) is typically larger than the range of the Z-piezo ($\lesssim 0.1\,\mu\mathrm{m}$). This means that we can easily crash into the surface with one coarse step forward if we do not know how close the STM is to the surface. To get a rough idea of how close the STM tip is to a surface, we may apply a high voltage to the tip to get a small current (a process called field emission), where the magnitudes of the current and voltage gives us an idea of how far away the tip is from the surface. Typically, when $V_{\mathrm{tip}} \sim -450\,\mathrm{V}$ and $I \sim 1\,\mathrm{nA}$, then the tip is $\sim 80\,\mu\mathrm{m}$ from the surface. Field emission (FE) can be used to help approach a surface. To use FE to approach a surface, one moves the STM tip towards a sample with the coarse approach while applying a high voltage to the tip and the feedback electronics in the Z-Box changes the voltage on the tip to keep the field emission current ($\sim 1\,\mathrm{nA}$) constant. By monitoring the voltage applied to the tip, we have an idea of how close the tip is to the sample. Typically, the initial voltage applied to the tip is the maximum voltage $\sim -450\,\mathrm{V}$ when the tip is far (a few mm) from the surface and $I = 0\,\mathrm{nA}$

in this case. When the tip is $\sim 80\,\mu$m from the surface, $V_{\text{tip}} \sim -450\,$V and $I \sim 1\,$nA. When the tip voltage is around $-30\,$V and $I = 1\,$nA, the tip is a few hundred Ångstroms from the sample, and one may use the z-piezo to move the tip towards the surface from that point on.

Capacitance approach

Approaching a sample using field emission can destroy a sample due to the large voltages and electric fields required. This is why another method of approaching the surface was necessary. Since the tip and sample form a capacitor, by measuring the tip-sample capacitance, we get an idea of how close the tip is to the surface. The tip-sample capacitance is measured by applying an ac voltage (1 V, 1 kHz) to the tip and measuring the induced current in the sample through the Ithaco 1211 current to voltage converter. Output of the Ithaco 1211 then goes to a lock-in, whose output is proportional to the tip-sample capacitance. When the tip is several Ångstroms away from the sample, the typical R output of the lock-in (§A.1.2) will be 70–80 mV when the Ithaco 1211 has a 10^{-10} A/V gain and 1 ms time constant.

5.1.7 Modifications

This section will describe some of the important changes to the STM as of December 2009 which are not in previous theses.

- Braces to level and guide the position of the optical floating tables when they are not floated have been installed. The optical tables must be positioned correctly when unfloated so that samples can be transferred in and out of the STM stage without dropping them (which has happened in the past).
- There are small changes to the STM scanner; these will be discussed in detail in appendix C.
- Starting in 2002, a newer version of the STM software, written in C++ instead of LabView, has been used.
- We either ground or filter all lines that go into the exchange gas can with in-line RF filters by Mini-circuits (part # BLP-1.9+).
- The Data Precision 8200 voltage supply used for the -X and -Y electrodes on the X and Y piezos have a resistor that has been replaced, as described in the previous section.
- There is a new home-built electronics box that is not essential, but is useful. This box was built by Annie Endozo and allows us to measure the capacitance between the body piezo and the walker plate electrodes (figure 5.2) using a computer instead of by hand. This box allows us to quickly figure out the general position of the STM by

measuring the capacitance between the body piezo bottom electrode and each of the four electrodes on the walker plate.

- There is a second new home-built electronics box built by Yuri Zuev that prevents the STM tip from crashing into the surface when the software crashes or when the computer is restarted. This box is again not essential, but is useful. When a switch on this box is turned on, this box keeps the body piezo and walker plate voltages turned on, even if the computer is restarted (restarting the computer would normally cause these voltages to turn off, making the tip crash).

- In the FE Box, the power supply that generates the high voltage for the tip in FE mode burned out and was replaced with a 500 V power supply, so the maximum voltage that can be applied to the tip in FE mode is now around 500 V instead of around 900 V.

- A new Z-box has been used starting in January 2009. This Z-box was designed by Bill Earle and built at Boston University, like the old Z-box. There are many internal changes in the new Z-box, but there are only a few changes relevant for the user.

  1. The voltages on all outputs are set to 0 V when the new 2009 Z-box is first turned on. The old pre-2009 Z-box would apply +200 V to −Z and −70 V to +Z when it was turned on, which may cause the Z-piezo to depolarize when the Z-box turns back on after a power outage.
  2. The range of the −Z output can be controlled on the new 2009 Z-box. The range can be set to ±400 V, ±200 V, ±100 V, or ±50 V. The old pre-2009 Z-box only had one −Z range, ±200 V. Note that the maximum voltage range on the old pre-2009 Z-box (400 V) is smaller than the maximum voltage range on the new 2009 Z-box (800 V). This means that the Z-piezo can expand twice as much with the new Z-box as on the old one, allowing us to scan taller objects. However, the larger voltage range on the new Z-box may also mean more noise and less resolution, which is why smaller voltage ranges are also available.
  3. The +Z voltage range is smaller on the new Z-box. It is around −70 V to around +475 V instead of −70 V to +900 V on the old Z-box.
  4. The Z-monitor gains are different on the new Z-box. They are 0.025, 0.05, 0.2, 1, instead of 0.05, 0.2, 1, 10, on the old Z-box. Since we need to read the Z-monitor into the computer and the computer card can only read voltages in the range ±10 V, this change was made so that the new −Z voltages ranges can be scaled down to the ±10 V range.

  We chose not to get proportional gain on the new Z-box since it would have added an unknown amount of time and expense to the development of the new Z-box.

  The new Z-Box also has its own digital control word generator (figure 5.3) so that it may be controlled without a computer, which is useful when the electronics shop needs to repair the new Z-Box.

5.2 Tip Preparation

The STM tips used in the experiments were prepared outside of vacuum before inserting them into the STM tip holder. The STM has no tip exchange mechanism; i.e., there is no way of replacing the tip without venting the chamber. Since regaining UHV after venting the chamber takes around 1 week, it would be very time consuming to replace the tip. So once a tip is placed in the STM tip holder and the chambers are under UHV, any additional tip preparation should be done in vacuum.

The STM tips used in the experiments were either W or PtIr. The W tips were 10 mil W wire where one end was cut at an angle to create a pointed end. The PtIr tips were 10 mil wire which were chemically etched to create a sharp, pointed end.

5.2.1 PtIr Tip etching

There are general methods to chemically etch a PtIr tip so that it has a sharp apex [173]. The PtIr tips used in our experiments were etched using a procedure from Katsumi Nagaoka. There seems to be a better tip etching method given in [144] used by J. A. Stroscio with a larger yield of sharper and smoother tips; Victor Brar knows the details of this method.

The PtIr tip used for all the experiments in this dissertation was etched in February 2003. The same tip was used for all the experiments. It was made using Katsumi Nagaoka's method, which will be described below.

PtIr wire (80% Pt, 20% Ir, 10 mil diameter) was purchased from Goodfellow. A Ni wire with one end wound into a loop is placed in a 10 mL beaker and the PtIr wire, held by tweezers, is placed through the Ni wire loop (figure 5.4). A hose clamp may be used to hold the Ni wire in place. A 4 : 1 mixture of $NaNO_3$: NaCl by weight is placed in the beaker, enough to cover the Ni wire loop. A hot plate (Thermolyne Cimarec 1 in this case) is needed to heat the $NaNO_3$: NaCl mixture until is melts ($\sim 300°C$). A glass funnel is placed over the entire setup to trap hot air or else the temperature will not be high enough to melt the $NaNO_3$: NaCl mixture.

After the $NaNO_3$: NaCl mixture melts, apply a DC voltage $\sim +2$ V to $+3$ V to the PtIr wire relative to the Ni wire. This will cause the $NaNO_3$: NaCl to chemically eat away at the PtIr around the area where the Ni wire loop is. After it looks like the $NaNO_3$: NaCl has eaten through the entire wire near the Ni wire loop, remove the PtIr wire and rinse it with distilled water. Sometimes the melted $NaNO_3$: NaCl becomes hard to see through as the PtIr is being etched, so it may be hard to see when the PtIr wire has been eaten up by the $NaNO_3$: NaCl. In this case, one may have to periodically pull the wire out to see if it has been completely etched. The tip etching process takes a few minutes.

Sometimes, a small area near the tip apex have black residue on it due to the tip etching procedure. This residue does not seem to be removed with HF. However, the tip may be periodically rinsed in distilled water during the tip etching process to help prevent this black residue from building up near the tip apex.

After the tips have been etched, they were further cleaned by annealing them in vacuum.

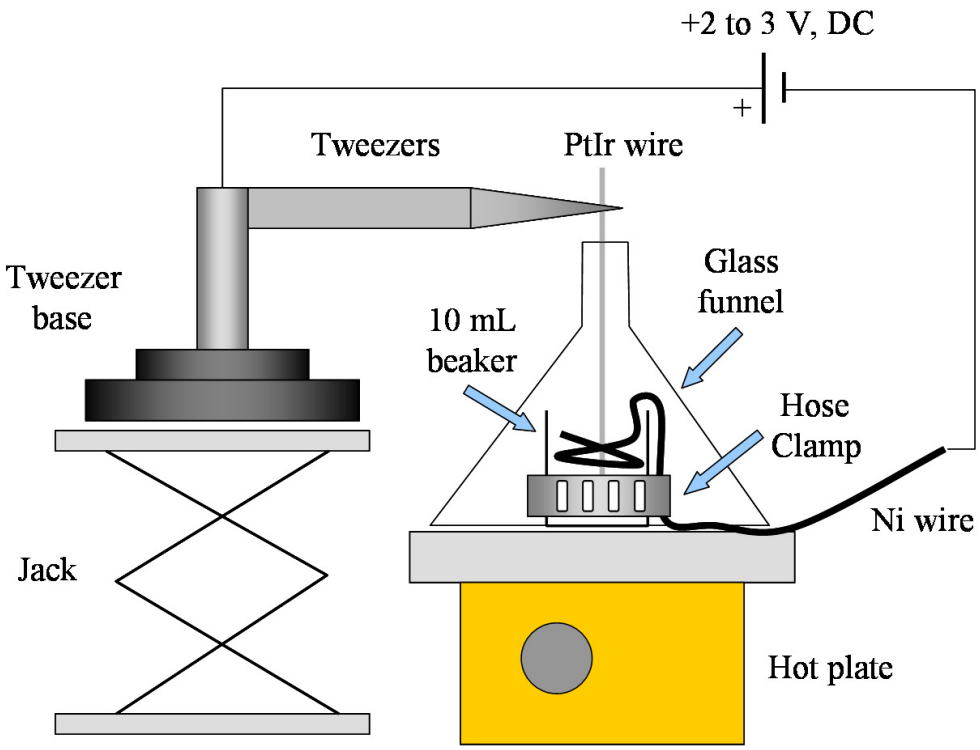

Figure 5.4: PtIr tip etching setup

However, annealing may also make the tip apex blunt, so this process need not be done for tips etched in the future. The etched tips were annealed by spot welding the non-etched end of the PtIr wire to a 12 mil W wire, then running ~ 5.5 A through the W wire in high vacuum ($\sim 1 \times 10^{-7}$ Torr) for around 10 hours. The PtIr wire may also be annealed before the tip etching procedure (in addition to annealing it after), but this was not done on every tip, and may not help much since the tips were annealed after etching anyway.

5.2.2 Tip preparation in vacuum

There are two general ways of modifying the tip in vacuum. The first involves field emission (FE): A high voltage and high current is applied to the tip when it is far from the surface; this is called field emitting the tip. This procedure is normally used when large changes to the tip are desired; for example, after exposing the tip to air, FE should be used to clean the tip. This procedure is done by going into FE mode and setting the set current to $\sim 10\,\mu$A, then moving the tip with the coarse approach until the voltage on the tip is around -400 V.

The second way of modifying the tip is by moving it into a metal substrate, then pulling it out again, a process called tip poking. If the tip is very unstable, or if the tip apex is very jagged instead of a smoothly tapering to a point, then poking using higher voltages ($\sim \pm 10$ V) and high currents (~ 50 nA) can help to stabilize the tip and make it less jagged,

but it may also destroy a large area (50 nm × 50 nm) of the sample.

If larger tip changes are desired, then changing the current to voltage converter gain is important when poking to get higher currents through the tip. If one leaves the gain at 10^{-9} A/V when poking the tip for example, then the current to voltage converter limits the maximum current through the tip to ~ 10 nA, and one cannot achieve the larger currents necessary for large tip modifications.

In general, moving the tip in and out of the surface with a slower speed is less damaging to the tip; i.e., it causes less tip changes and may give sharper tips.

Molecules tend to stick better at step edges, so if a molecule is stuck on the tip, then moving the tip close to a step edge can get the molecule off.

5.3 Surface Preparation

Preparing clean and flat surfaces of substrates is critical for studying the intrinsic properties of molecules since impurities on the substrates may affect the properties of the molecules adsorbed on them. For this reason, substrates are cleaned and kept in ultra high vacuum (UHV); the base pressure of the chambers is typically $\sim 2 \times 10^{-10}$ Torr.

5.3.1 Sputtering and annealing

Cleaning the single crystal noble metal substrates (Ag, Au, Cu) used for all the experiments follows standard procedures [149] which consists of Ar sputtering and annealing. Argon sputtering is when the substrate surface is bombarded with Ar^+ ions with a kinetic energy between 0.5 keV and 2 keV. The sputtering knocks off impurities from the surface. The sputtering is followed by annealing the substrate, which is heating the substrate to desorb impurities from the surface and smoothens out the surface. Annealing is done by *e*-beam heating, where we bombard the substrate with high energy (~ 1 keV) electrons, which then lose their energy in the substrate in the form of heat. The methods used for *e*-beam heating are similar to the methods used for *e*-beam evaporation (§5.4.2).

5.3.2 Hydrogen artifacts and removal

After the sample is moved to the STM stage at 7 K, it can remain clean for around four to five weeks. After that amount of time, the sample has accumulated significant amounts of hydrogen, although it cannot be seen directly; there are no noticeable protrusions or depressions on the surface in the STM images due to hydrogen. The evidence for hydrogen accumulation comes from other sources:

1. The tunneling current becomes more noisy and images become more streaky.

2. Spectroscopy done in a -100 mV to 100 mV range can give curves that resemble that of a superconductor [65].

3. Spectroscopy within ±100 mV will depend strongly on tip lateral position and tip height from the sample.

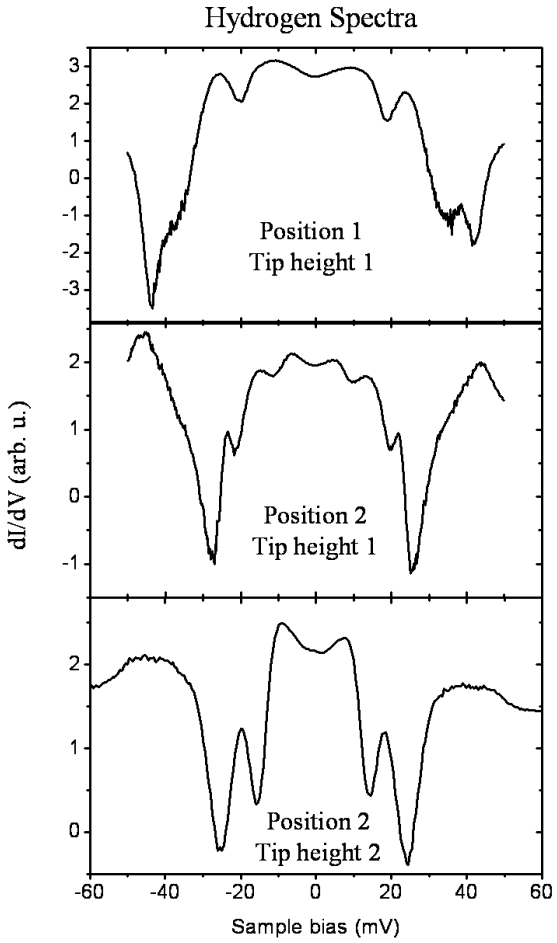

Figure 5.5: After the STM was not warmed up to ∼ 40 K for four weeks, the following spectra were acquired. All spectra were taken with the same STM tip. Top panel: Spectroscopy taken at one lateral position on the sample (over the center of a TCNE molecule) using initial settings $V = 50$ mV, $I = 0.5$ nA, 0.5 mV rms ac modulation. Middle panel: Spectroscopy taken with the same settings as the top panel, but at a different lateral position on the sample (over the center of a nearby $V(TCNE)_2$ complex). Bottom panel: Spectroscopy taken at the same lateral position on the sample as the middle panel (center of the same $V(TCNE)_2$ complex), but with initial settings $V = 100$ mV, $I = 0.5$ nA, 1 mV (rms) ac modulation.

Figure 5.5 shows the different types of spectra in a ±60 mV range on a sample that can result after the sample has been in the STM stage for four weeks. These spectra are due to accumulated hydrogen in the system [65], and are not due to the intrinsic properties of the

sample. The graphs also demonstrate how sensitive the spectra are to tip lateral position and tip height. The spectra in the top and middle panels were taken using the same stabilization parameters (so the tip height above the sample is roughly the same), but the top spectrum was taken over the center of a TCNE molecule while the middle taken over the center of a $V(TCNE)_2$. The middle and bottom graphs were taken at the same lateral position on the surface (over the center of the same $V(TCNE)_2$), but the stabilization parameters were different, making the tip further away from the sample for the bottom graph.

To remove hydrogen from the system, standard tip preparation procedures in vacuum (§5.2.2) do not work (at least, not for long); the STM must be warmed up to remove hydrogen, usually to $\sim 40\,\mathrm{K}$ for a few hours. However, since warming up the microscope chamber also desorbs adsorbed gas from the chamber walls, the desorbed gas contaminates the sample, and the sample should be cleaned again.

Before the publication of [65], spectra such as those in figure 5.5 were known to be due to artifacts, but the origin of the artifacts were unknown. Since such artifacts due to hydrogen are sensitive to tip position and difficult to remove by tip preparation in vacuum, a tip which displayed such artifacts was called a "tip from hell."

5.4 Deposition Techniques

In our experiments, we need to deposit molecules or atoms onto a surface such that they are separated from each other. This is usually accomplished by sublimating a macroscopic quantity of the molecule or atom so that it forms a gas. When a substrate such as a Ag(001) crystal is placed in this gas, individual molecules or atoms will hit and stick to the substrate's surface. By controlling the pressure of the gas, we can control the number of molecules or atoms which hit the surface, and with a low enough pressure, we can get isolated molecules or atoms on a surface. However, molecules and atoms are often mobile on a surface at room temperature, so to keep them isolated, we need to cool the sample.

A device which allows us to sublimate molecules or atoms and control their sublimation pressure is called an *evaporator*. There are four types of evaporators used for our experiments.

5.4.1 Knudsen cell evaporator

All of the molecules studied except TCNE will sublimate in ultra high vacuum at temperatures above room temperature. This allows us to put the molecules in a quartz tube and heat the tube by running current through a W wire to sublimate the molecules (figure 5.6). This type of evaporator is called a *Knudsen cell evaporator*. The sublimated molecules then hit the sample surface.

The temperature that we heat the quartz determines the pressure of molecules and is used to control the amount of molecules deposited onto the surface. The temperature is measured using a thermocouple.

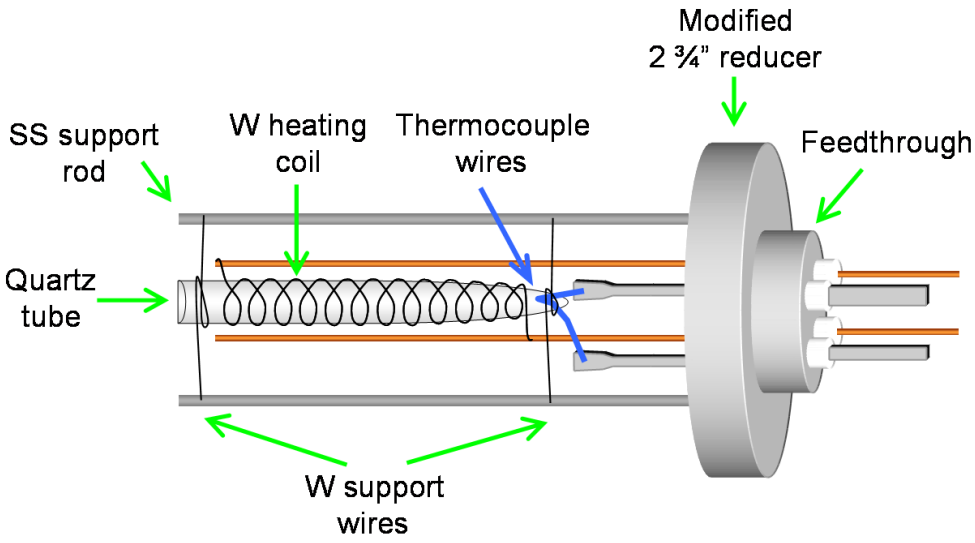

Figure 5.6: Knudsen cell evaporator

5.4.2 Electron beam evaporator

For depositing metals, which usually have much higher evaporation temperatures than molecules (higher than the melting point of the quartz crucible in the Knudsen cell), a Knudsen cell cannot be used. A different type of evaporator, called an *electron beam evaporator* (*e*-beam evaporator), is required. For this evaporator, a high voltage (2 kV) is applied to the metal which we want to deposit and a filament is placed near the high voltage metal (figure 5.7a). The feedthrough is usually a TSP feedthrough. The filament is either thoriated W wire, which begins to glow when $\sim$2 A is passed through it, or a Granville-Phillips ion gauge filament, which requires $\sim$5 A to glow. The metal is either directly attached to a Mo rod by wrapping W wire around it and the Mo rod (figure 5.7a), or one end of a wire (W, Mo, or Ta) is wrapped around and spot welded to the metal while the other end of the wire is wrapped around and spot welded to the Mo rod (figure 5.7b). The second method (figure 5.7b) of attaching the metal to the Mo rod has the advantage that there is less heat loss to the Mo rod since there is no direct contact between the hot metal and the Mo rod, which means we require less current through the filament to heat the metal and the Mo rod will outgas less. However, this method has the disadvantage that when the metal and wire get hot, they can bend and touch the shield, causing a short.

When the filament is heated by passing a current through it, thermally emitted electrons are accelerated to the metal because of the high voltage applied to it, and when the electrons hit the metal with high energy, they release their energy in the form of heat, rapidly heating the metal. By controlling the current that flows from the filament to the metal through vacuum (called the emission current) we can control the temperature of the metal. A shield is also normally placed around the metal and filament for two reasons *1*) It prevents metal from being evaporated in all directions, which prevents the metal from contaminating other

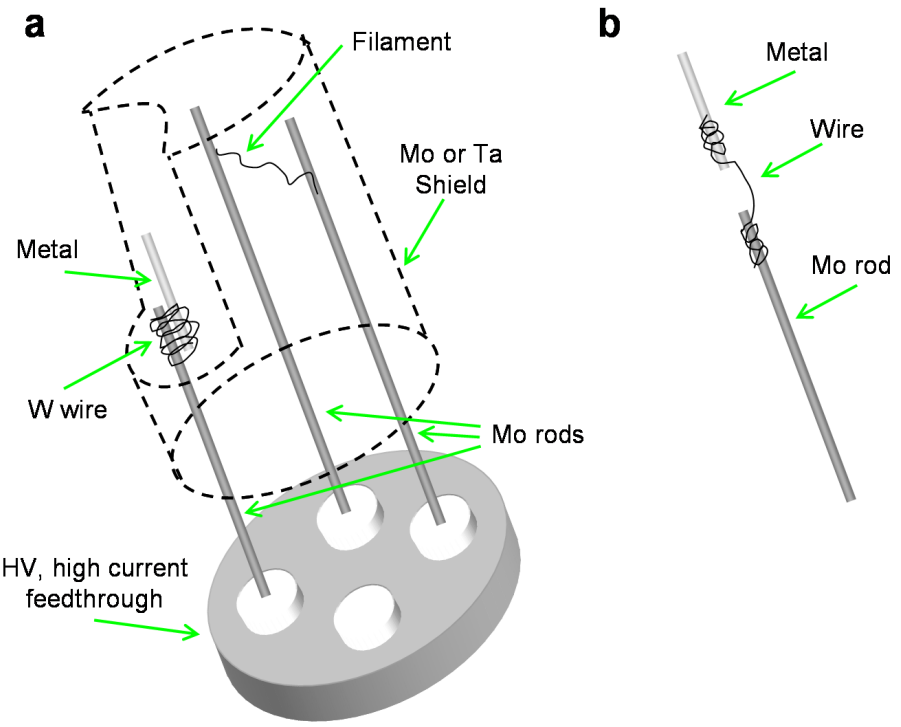

Figure 5.7: *e*-beam evaporator setup. (a) Complete schematic of an *e*-beam evaporator with the metal directly attached to the Mo rod and the shield is drawn transparent. (b) A second way of attaching the metal to the Mo rod by using a W, Mo, or Ta wire.

evaporators or covering viewports with metal. *2*) It also changes the local electric field around the metal that we evaporate. Since we apply a high voltage to this metal, the evaporated metal atoms are charged and the electric fields can alter the direction the metal atoms are flying. The shield can significantly alter the number of atoms that fly towards the sample.

5.4.3 K getter evaporator

The deposition of K atoms is more difficult due to the high reactivity of K when exposed to moisture in the air. For the deposition of K atoms, K getters were purchased from SAES getters in Milan, Italy. To use these getters, a current of ~ 5 to 8 A were passed through the getter, which causes K atoms to be released.

5.4.4 Leak valve evaporator

Since TCNE sublimates at room temperature in UHV, a different method was used to deposit this molecule. The molecules were placed as a solid in a small glass belljar which was attached to a UHV leak valve (figure 5.8). The belljar was first pumped to rough

vacuum (~ 10 mTorr) and then filled with 1 atm of Ar gas. Since TCNE is toxic, when we pump on it, we must make sure that the exhaust of the pump goes into the fume hood. This process of pumping and flushing with Ar was repeated at least ten times. Then finally the belljar is pumped to rough vacuum and the pump/flush valve is closed. The TCNE at room temperature and in rough vacuum will sublimate, forming a gas of TCNE in the belljar and leak valve. Opening the leak valve then allows this gas to hit the sample.

Since the TCNE gas can diffuse everywhere in the chamber, we must turn off ion gauges, ion pumps, or anything else which has hot filaments or high energy electrons since these may break the molecules. Any broken molecules may end up on the sample surface, contaminating the surface.

With leak valve evaporators, we want the distance between the leak valve and the sample to be small (a few inches) so that most of the molecules which come out of the leak valve will hit the sample surface. If the distance between leak valve and sample is large, many molecules which come out of the leak valve will not hit the surface, so we will need a higher pressure of TCNE gas in the chamber to get the same amount of molecules on the surface. A higher pressure of TCNE in the chamber means more TCNE will contaminate the chamber and the base pressure in the chamber will be worse. For this reason, because of the geometry of our chamber, the setup used to deposit TCNE onto a sample at room temperature is different from the setup used to deposit TCNE onto a sample at low temperature, which will be explained below.

RT leak valve evaporator

To deposit TCNE onto a sample at room temperature, we must first turn off ion gauges and ion pumps in the load lock so that they do not break the molecules. Then we can simple move the sample into the sample-transfer load lock (figure 5.1). When the leak valve is opened, the TCNE gas then hits the sample. The distance between leak valve and sample is ~ 3 in with this setup.

LT leak valve evaporator

To deposit TCNE molecules onto a sample that has been cooled below room temperature, we cannot use the sample-transfer load lock since we cannot cool the sample in that load lock. The sample can only be cooled in the transfer chamber (figure 5.1), and the distance between the sample and the leak valve on the main chamber would be relatively large (around 12 inches). So to reduce the distance between the evaporator and sample, we attached a long threaded tube to a modified double-sided blank flange which was attached to the leak valve (figure 5.9). This modified double-sided blank flange (with knife edges on both sides) has a hole drilled completely through it and one side of the hole has 1/8" NPT threads so that we may screw a the threaded tube of pipe onto the end of it. The tube was made out of stainless steel 304. This assembly was then attached to a linear motion feedthrough which was attached to the deposition load lock (figure 5.1) on the main chamber. When the tube

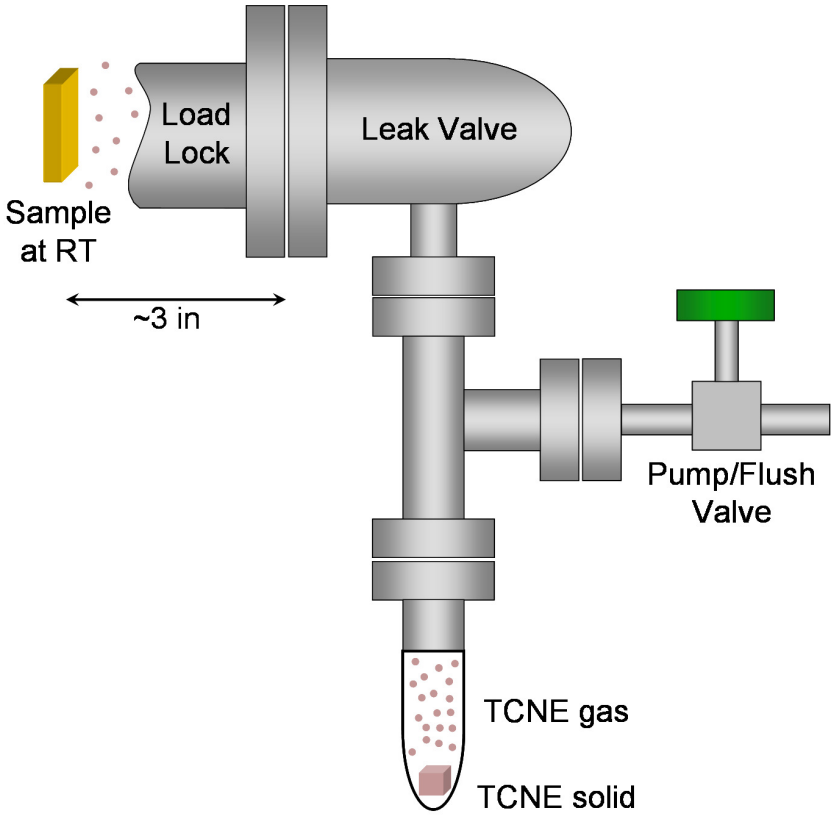

Figure 5.8: Leak valve evaporator setup for depositing TCNE onto a sample at room temperature

is completely moved toward the sample, the distance between the end of the tube and the sample is ~ 5 in.

To deposit TCNE using this evaporator,

1. the sample is first moved into the STM at 7 K.
2. The load lock is normally baked with the gate valve closed until the base pressure after the load lock has cooled to room temperature is $\sim 1 \times 10^{-8}$ torr.
3. After the sample is cooled for a few hours, it is picked up using the vertical manipulator (figure 5.1) and moved it into the main chamber.
4. The load lock gate valve is opened and the tube is moved toward the cold sample using the linear motion feedthrough.
5. The leak valve is opened to deposit the molecules onto the surface.

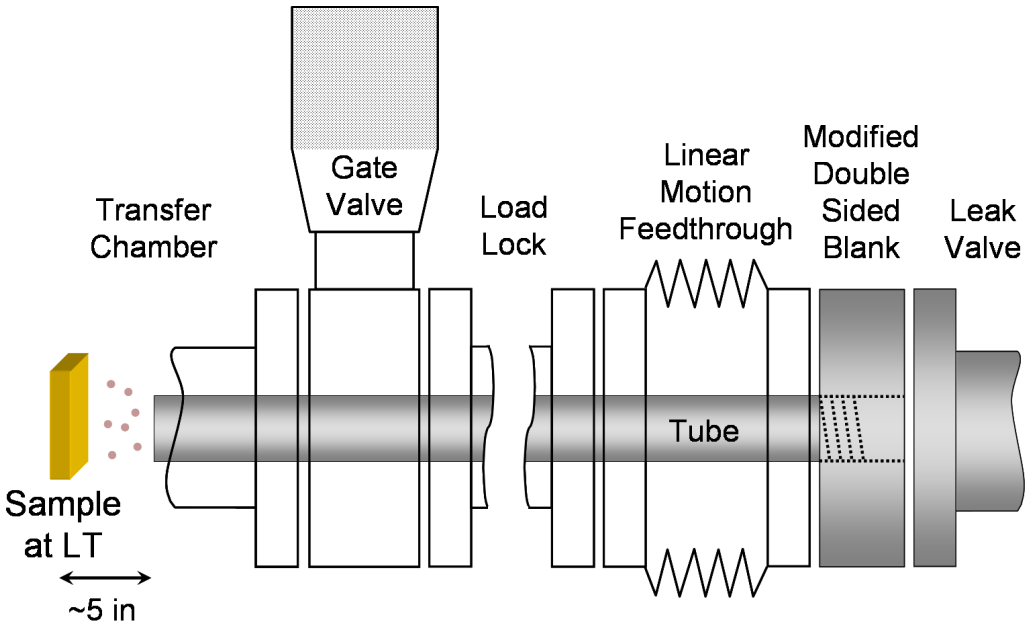

Figure 5.9: Leak valve evaporator for depositing TCNE onto a sample held at low temperature ($\sim 80\,\mathrm{K}$). The schematic shows the evaporator when the tube has been moved toward the sample using the linear motion feedthrough. When the tube is moved sufficiently far away from the sample, the end of the tube is in the load lock, so we may close the gate valve.

Part II

Fullerenes and Diamondoids

6

Controllably Doping a Single C_{60} Molecule

A central technique for controlling the functionality of bulk semiconductor devices is the ability to tune the electronic properties of semiconductors via charge doping atoms [183]. Now that semiconductor devices are shrinking down to nanometer length scales, questions arise as to whether charge doping will have the same effect at these small length scales. Progress has been made using new compounds [73] and electronic gating [158], but directly attaching single dopant atoms to individual molecules has not been accomplished yet. This chapter will present our progress towards accomplishing this goal by controllably doping single C_{60} molecules through the attachment and/or removal of single potassium (K) atoms. This study will address one of the central questions in this dissertation: how to modify and control the properties of single molecules at the atomic scale. Although C_{60} has been doped with K in the past [201, 45, 189, 207, 26], the experiments were not done on single C_{60} molecules, only molecules in bulk or monolayers.

To modify the properties of a single C_{60} molecule (i.e., an isolated adsorbed molecule at a surface), we need to be able to control the molecule over nanometer length scales. Since the development of the STM, such minute adjustments to structure are possible. The STM has the impressive ability to manipulate and move nanometer-size structures, giving one the capability to alter the characteristics of single molecules such as C_{60}.

Sliding individual C_{60} molecules over K atoms with the STM causes the K atoms to attach to the C_{60} molecule, which dopes the molecules with electrons donated from the K atoms. This process causes the C_{60} molecular energy levels to rigidly shift in energy, as well as to split degeneracies and induce a Kondo effect.

This chapter will discuss using the STM as both an experimental tool to construct individual K_xC_{60} complexes, as well as a measurement tool to analyze the electronic properties of the created complexes. It is based on our published paper, ref. [205].

The experiments were performed with our home-built LT UHV STM ($T = 7\,\mathrm{K}$) with a PtIr tip and a Ag(001) substrate. The Ag(001) single crystal was cleaned by sputtering and annealing (§5.3), cooled to $\sim 80\,\mathrm{K}$, then C_{60} molecules were deposited onto the substrate from a Knudsen cell evaporator (§5.4.1). The C_{60}/Ag(001) sample was then cooled to

$T = 7\,\mathrm{K}$ before deposition of K atoms from a K getter (§5.4.3).

6.1 Doping C_{60} by STM manipulation

By using the molecular manipulation capabilities of the STM [42, 100], we can construct K_xC_{60} individual complexes [205]. Initially, we had tried to move the K atoms on Ag(001), but were unable to. So we moved the C_{60} molecules towards the K atoms. We then found that the K atoms will attach themselves to the C_{60} molecule. This allows us to create K_xC_{60} by simply moving the C_{60} to x K atoms, one at a time. Figure 6.1a shows this process. K_6C_{60} can easily be made using this method. More than six K atoms are difficult to attach since the K_6C_{60} complexes seem to repel K away. However, stoichiometries as high as K_7C_{60} have also been made with this method.

The topograph of a K_xC_{60} complex, in general, changes very little. Figure 6.1b shows the average of many radial cross-sections taken on a K_6C_{60} complex and a C_{60} molecule. The K_6C_{60} complex is shorter than C_{60} by 2%, but is wider by 21% at a height of 0.25 Å.

To study the electronic structure of K_xC_{60}, dI/dV spectroscopy was performed (§2.4). Figure 6.1c shows the typical spectrum for K_xC_{60} for $0 \leq x \leq 7$. Each curve is the average of spectroscopy performed on many different molecules at various points over the same molecule. These curves demonstrate a few trends when C_{60} is doped with K atoms. (1) The LUMO+1 resonance (around 1.7 V in C_{60}) and LUMO resonances (around 0.5 and 0.05 V in C_{60}, [129]) shift closer to E_F with increased K doping. (2) The LUMO resonance shape changes substantially as the K doping increases. (3) The width of one LUMO resonance narrows substantially with K doping. These changes were only observed when the K atoms were close enough to the C_{60} molecule so that they were not resolvable from the C_{60} molecule.

To see the effect of K doping on the spatial distribution of C_{60} molecular orbitals, dI/dV maps were done (figure 6.2). dI/dV maps of the LUMO+1 orbital on K_6C_{60} and C_{60} (figures 6.2b and c) both reveal bright rings (figure 6.2a), which are known to appear near the C_{60} pentagons [129]. dI/dV maps on K_6C_{60} reveal three distinct states at around -0.4 V, -0.1 V, and 0.03 V. The state at 0.03 V on K_6C_{60} looks similar to the state on C_{60} at 0.5 V (figure 6.2g). These dI/dV maps (figures 6.2f and g) both have a bright triangular center surrounded by bright spots. These dI/dV maps show that, although K doping shifts the energy of the states, it does not significantly alter the spatial distribution of C_{60}'s molecular orbitals. Differences in the dI/dV maps are likely due to different configurations of the atoms at the end of the STM tip.

The doping process can also be reversed. Figure 6.3a shows the process where a K_4C_{60} is moved over an impurity to form K_3C_{60}. The impurity is likely oxygen or carbon monoxide. These impurities also form stable complexes with K, and when the K_4C_{60} is moved over them, a single K atom sticks to them, creating K_3C_{60}. Spectroscopy (figure 6.3b) shows that a single K atom was removed. This process has been used to reverse the doping levels on K_xC_{60} for $x = 1$ to 4.

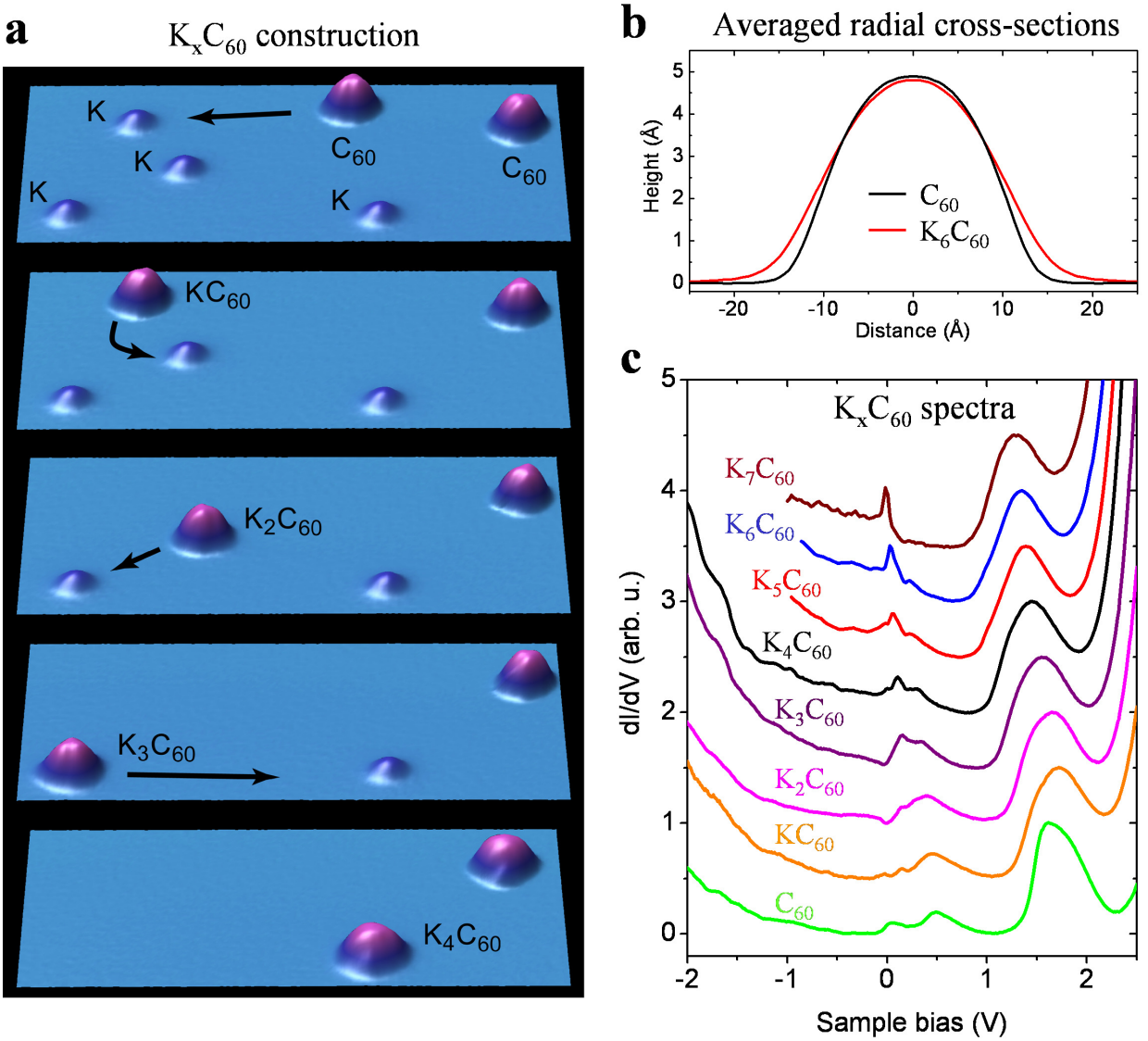

Figure 6.1: (a) STM constant current topographs ($V = 2\,\mathrm{V}$, $I = 500\,\mathrm{fA}$, $227\,\text{Å} \times 115\,\text{Å}$) showing the construction of K_4C_{60} by STM manipulation. The arrows show the direction the molecule was moved using the STM tip. (b) Averaged radial cross-sections taken over K_6C_{60} and C_{60}. (c) dI/dV spectra taken on K_xC_{60}, $x = 0$ to 7. Each spectrum is averaged over many K_xC_{60} complexes (except K_7C_{60}) and is normalized so the LUMO+1 has the same height.

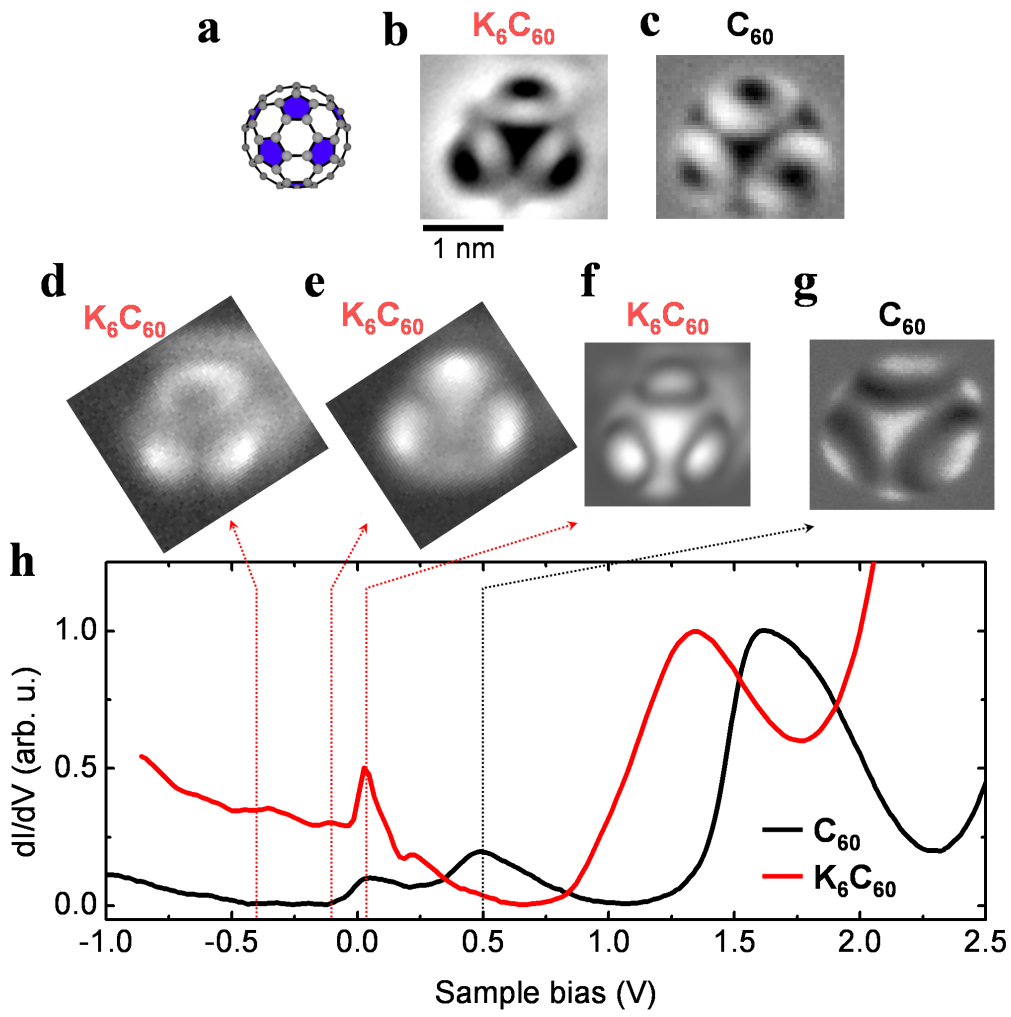

Figure 6.2: dI/dV maps taken on C_{60} and K_6C_{60} showing the spatial distribution of their molecular orbitals. (a) Structural model showing the orientation of the C_{60} molecule in the dI/dV maps. The pentagons are highlighted in blue. dI/dV maps taken at the LUMO+1 energy of (b) K_6C_{60} at 1.35 V, (c) C_{60} at 1.55 V. dI/dV maps taken near E_F on K_6C_{60} at (d) $V = -0.4$ V, (e) -0.1 V, (f) 0.03 V, and a dI/dV map on C_{60} at (g) 0.5 V. (h) dI/dV spectra on K_6C_{60} and C_{60}.

6.2 Modeling K_xC_{60}

6.2.1 Charge Transfer

We can estimate the amount of charge transferred from K atoms to the C_{60} molecule using a simple method which relates charge transfer to changes in the energetic position of the

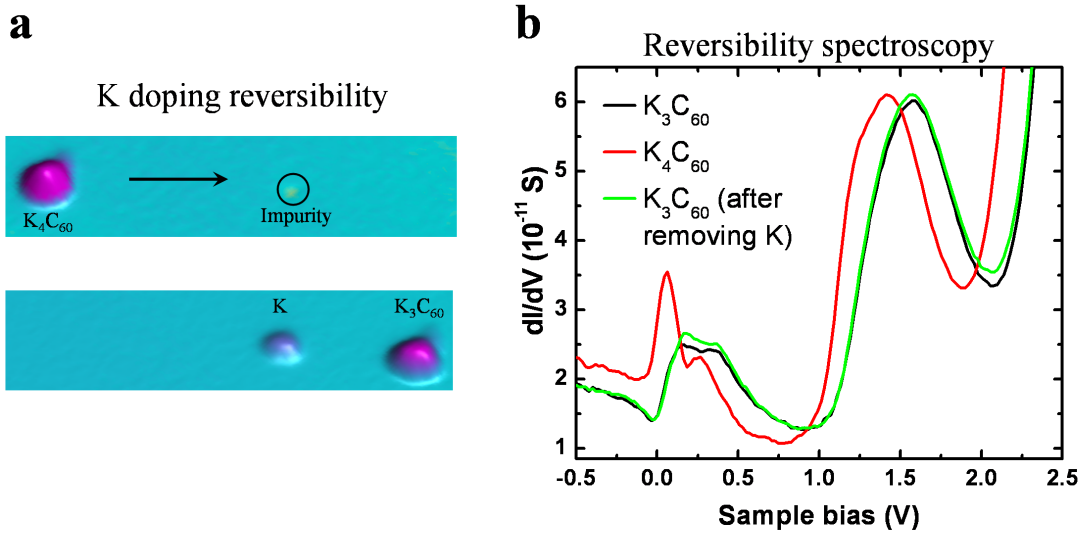

Figure 6.3: Reversing the doping process. (a) Topographs ($V = 2\,\mathrm{V}$, $I = 0.5\,\mathrm{pA}$, $285\,\text{Å} \times 75\,\text{Å}$) showing K_4C_{60} being converted to K_3C_{60} by moving it over an impurity. (b) Spectroscopy on K_3C_{60} before converting it to K_4C_{60} (black curve), after conversion to K_4C_{60} (red curve), and after reversing it back to K_3C_{60} (dotted green curve).

molecular resonances. This model is similar to the one presented in photoemission experiments [85]. This model assumes that the DOS does not change with electron addition, only the occupancy of the states change [26]. Changes to the molecular DOS with K doping limit the accuracy of this model. Since the LUMO can accommodate 6 electrons (including spin degeneracy), if the LUMO is completely filled, it must be completely below E_F, while if the LUMO is completely empty, it must be completely above E_F. Therefore, if the LUMO starts out as completely empty and we add 6 electrons to it, E_F must increase by roughly the width of the LUMO, which is 0.8 eV from the spectroscopy data. Since E_F always corresponds to $V = 0$ in dI/dV spectroscopy, we should see the LUMO resonance (and all other resonances) shift down by $\sim 0.8\,\mathrm{V}$ in the data when the LUMO is completely filled. To calculate the charge transfer using this simple model, we then need to calculate the shift in the C_{60} resonances with the addition of K atoms.

We use Gaussian fits of the K_xC_{60} LUMO+1 resonances (figure 6.4) to track the shifts of the molecular resonances since the LUMO+1 does not change its shape with K addition, making it simpler to fit. A linear background was subtracted from the data before fitting the resonance. An example of the fit quality is shown in figure 6.4a, which is a fit of the C_{60} LUMO+1. Fits for K_xC_{60}, $x = 1$ to 4 were of comparable quality. When the center of each Gaussian is plotted as a function of number of K atoms added to C_{60} (figure 6.4), we see that the centers of the Gaussians shift at a rate of $85\,\mathrm{mV} \pm 15\,\mathrm{mV}$ per added K atom. This means that only $85\,\mathrm{mV}/800\,\mathrm{mV} = 11\%$ of the LUMO is getting filled with the addition of

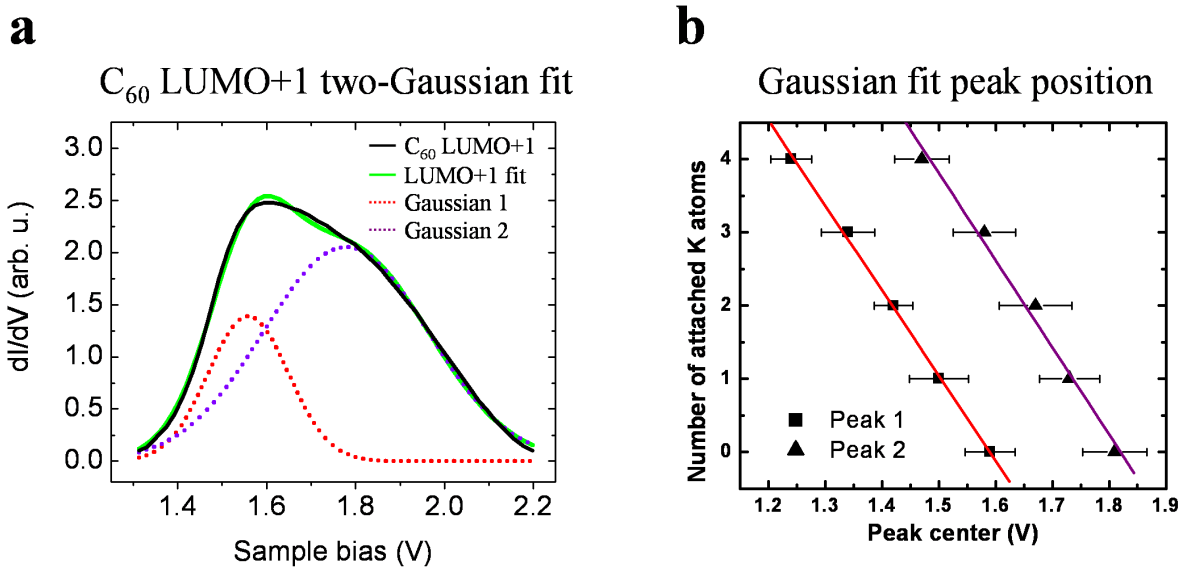

Figure 6.4: Two-Gaussian fits to the LUMO+1 of K_xC_{60}. (a) Experimental C_{60} LUMO+1 resonance (black curve) after a linear background was subtracted. The best fit to the LUMO+1 is the green curve and the two Gaussians that make up the best fit are the red and purple dotted curves. (b) Voltages of the center of the two Gaussians in the best fit plotted as a function of K doping level.

each K atom. This corresponds to a charge transfer of around 11% of 6 electrons, which is $\sim$0.6 electrons per K atom. This is less than what is seen in K doped bulk [201, 45] C_{60} and monolayer C_{60} [189, 207, 26] samples, where K donates an entire electron to C_{60}. This difference is likely because of differences in the local environment of each K atom: each K atom is surrounded by C_{60} molecules in bulk and monolayer samples, but they are not in single K_xC_{60}.

However, this simple charge transfer model does not explain the change in the line shapes of the LUMO resonance under K doping and does not taken into account the effect of the K atoms. To get a more quantitative idea of the electronic properties of K_xC_{60}, a combination of DFT and NRG was used.

6.2.2 DFT and NRG

We use density functional theory (DFT) calculations to explain the effect of adding K atoms to a C_{60} molecule on a Ag(001) surface. However, although DFT reproduces the shift of electronic states and the observed LUMO degeneracy breaking well, it does not explain the experimental appearance of the sharp resonance pinned at the Fermi energy for K_xC_{60}, $x > 4$. To investigate this anomalous peak further, numerical renormalization group (NRG) calculations were performed and show that one of the three split C_{60} LUMO states interacts

with the surface in a way to produce a narrow resonance (the Kondo resonance, §4.4.3) near E_F.

The results of the DFT calculations are shown below. All calculations were performed by Jeff Neaton, who was working in Steven Louie's group at that time, using SIESTA (§4.5, [180]) with norm-conserving pseudopotentials [190] and a double-ζ basis set [175] (s and d orbitals for Ag, and s and p orbitals for C). The supercell contained a K_xC_{60} molecule ($x = 0$, 3, or 6), on 200 Ag atoms in 4 atomic layers. The C_{60} molecule is initially positioned with a hexagon facing the surface, as experimentally observed, and the atomic positions of all atoms, except the bottom two Ag layers, are relaxed until the force on each atom is less than 0.025 eV/Å. The calculation was repeated for a C_{60} molecule positioned at different adsorption sites, and in the calculated lowest-energy configuration, the molecule sits 1.85 Å above a Ag(001) hollow site. The relaxed structures for K_3C_{60} and K_6C_{60} are plotted in figure 6.5d. The K atoms in K_3C_{60} form an equilateral triangle in a plane $\sim$3 Å above the Ag(001) plane and lie near the centers of the C_{60} hexagons. The K atoms in K_6C_{60} are also nearly coplanar, but $\sim$0.1 Å higher off Ag(001) than in K_3C_{60} and prefer to be next to the centers of the C_{60} hexagons.

To compare the DFT results with the averaged experimental dI/dV spectra, the PDOS was calculated for the atoms on the upper hemisphere of the C_{60} molecule (away from the substrate). These results are presented in figure 6.5b for K_xC_{60}, $x = 0$, 3, 6 adsorbed on Ag(001). (Similar results were obtained by integrating the LDOS onto the tails of wavefunctions in a hemispherical spatial region 2 Å above the C_{60} molecule.) For all three dopant levels, our calculations reveal broad LUMO-like molecular resonances near E_F, and a single, broadened LUMO+1 resonances centered $\sim$1.2 eV higher in energy, in agreement with experiment and previous studies [129]. As the number of surrounding K atoms increases, the LUMO resonances drift toward lower energies relative to E_F, indicating a systematic charge transfer to the molecule with increasing K. The LUMO+1 resonance also shifts toward the Fermi level with increasing potassium concentration, in excellent agreement with the experimental trend (figure 6.5a). The DFT energy of the LUMO+1 resonance relative to the Fermi level is underestimated by about 0.5 eV compared with experiment because of the usual errors associated with unoccupied states in DFT. Quasiparticle self-energy corrections (§3.4.2) should better align these energies with experiment [87, 151, 176], but are beyond the scope of this work.

With no K atoms attached to C_{60}, our calculations (figure 6.5b) reveal two resonances just above E_F, one slightly weaker centered at $\sim$0.13 eV and another slightly stronger at $\sim$0.38 eV, in remarkable agreement with the experimental spectrum.

To better understand the origin of the calculated splitting, the C_{60} molecule is lifted off the substrate by 1.5 Å (without subsequent relaxation). The recalculated PDOS is shown in figure 6.5c, and the width of the molecular resonances and their splitting can be seen to decrease with increasing molecule-substrate separation. The four-fold symmetric hollow adsorption site breaks the t_{1u} symmetry of the LUMO, which, in the gas-phase, has three-fold orbital degeneracy. Thus, the hollow site symmetry results in three singly-degenerate levels, two of which remain relatively close together. As the molecule is moved away from the

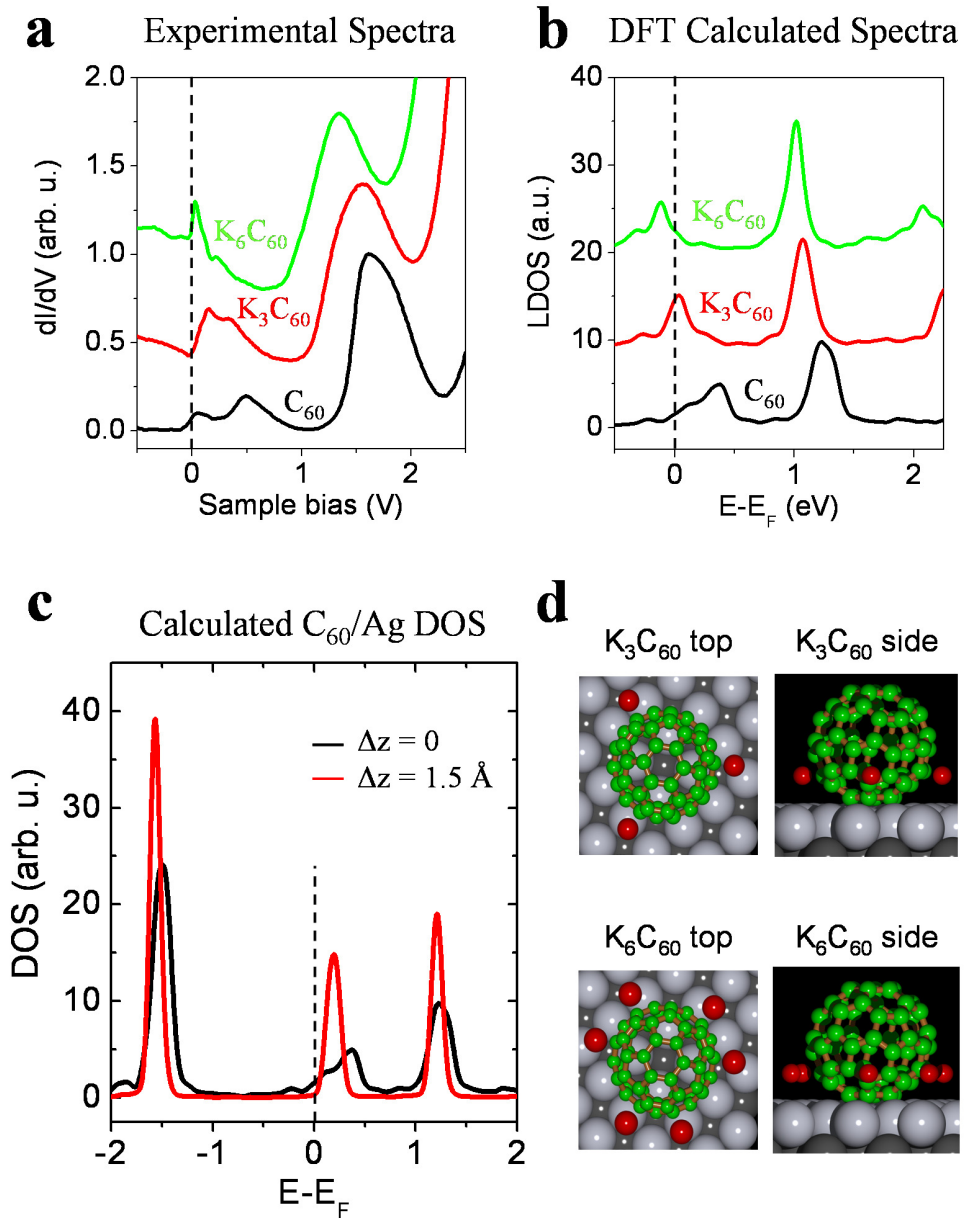

Figure 6.5: DFT on K_xC_{60} on Ag(001). (a) Experimental dI/dV spectra shown earlier. (b) DFT calculated PDOS for K_xC_{60}, $x = 0$, 3, 6. (c) PDOS for C_{60} on Ag(001) for two different heights above the Ag(001) plane. Δz represents the increase in C_{60}-Ag distance from the relaxed C_{60}-Ag distance. (d) DFT relaxed structures for K_3C_{60} and K_6C_{60}.

surface, the electronic coupling between the LUMO and the substrate diminishes, resulting in a reduction of the magnitude of the splitting of the LUMO manifold.

Although the agreement between experiment and the DFT calculations is excellent for C_{60} on Ag(001), the narrow peak appearing near E_F for K_xC_{60}, $x \geq 4$, is absent from the DFT calculated PDOS. Due to the unusually narrow widths of the experimental peaks for K_xC_{60}, $x \geq 4$, which is not expected for molecules on surfaces, and the lack of any narrow peaks in the DFT calculations, we conclude that the narrow resonance near E_F must be due to a correlated electronic excitation that is not captured by DFT. The fractional charge state of K_xC_{60} for $x \geq 4$ calculated by DFT suggests that there is a partially filled orbital which can lead to a Kondo effect: this is a strong correlation phenomenon which produces narrow features near E_F that DFT would not be expected to reproduce.

To explore further the possibility of a Kondo resonance for $x \geq 4$, Noah Bray-Ali in Joel Moore's group performed numerical renormalization group (NRG) calculations [81] using a model Hamiltonian that best fits the information provided by experiment and our DFT calculations. Our main assumption is that there is only one C_{60} resonance moving through E_F for K_xC_{60}, $x \geq 4$. Because the substrate removes the three-fold LUMO degeneracy, this approximation is acceptable. This is different from previous theories [39] which assume degenerate LUMO states. The resulting single-orbital Anderson model contains three parameters: the bare resonance energy E_d, the non-interacting (bare) level width ($\Delta = 135\,\text{meV}$ for all curves in the top panel in figure 6.6), and the intra-orbital interaction energy ($U = 405\,\text{meV}$ for all curves in the top panel of figure 6.6).

The results of these calculations are shown in figure 6.6. The only adjustable parameter is E_d, which is taken to move linearly with doping from $81.5\,\text{meV}$ ($x = 4$) to $-121.5\,\text{meV}$ ($x = 7$). For these parameters, the number of electrons in the impurity orbital is intermediate between zero and one; this range of parameters is referred to as the "mixed-valence" regime of the Anderson model. Although the widths of the NRG spectral functions are slightly wider than the observed widths, the energetic positions of the resonances agree with experiment. Strong correlations slow down the motion of the center of the observed resonance with doping as it nears the Fermi level from above and cause the resonance to narrow. The narrowing of the density of states peak in the mixed-valence regime was previously obtained using the NRG technique [81, 34]. A slightly improved fit to the data can be obtained by increasing the number of fit parameters, but an adequate model of the evolution of the center orbital with increasing K doping as a mixed-valence Kondo effect requires only a linearly decreasing bare orbital energy, with all other parameters kept constant.

6.3 K_xC_{60} Heterostructures

Once a K_xC_{60} complex is created, it can be manipulated by STM towards a K_yC_{60} complex. These two complexes stick together forming a heterostructure. One important way these structures deviate from the behavior of isolated K_xC_{60} complexes is in the amount of charge transfer between K and C_{60}. K seems to donate more charge to C_{60} in these heterostructures

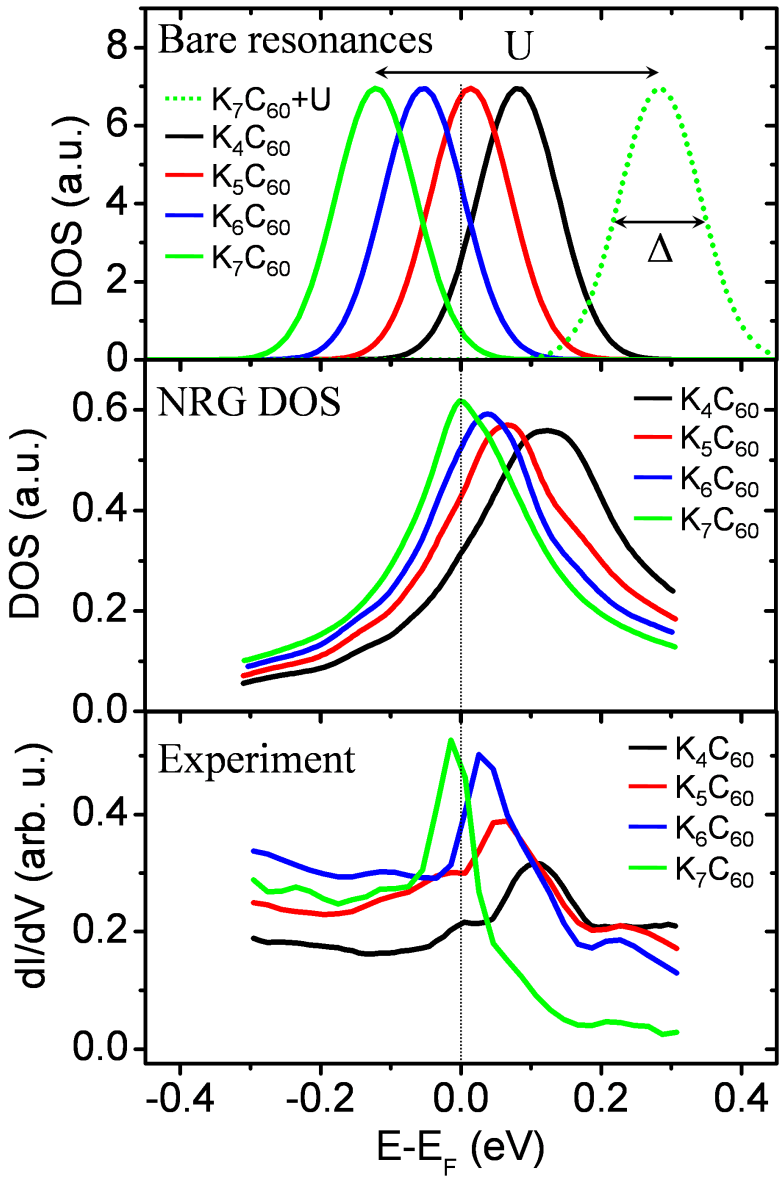

Figure 6.6: Top panel: the bare resonances used for the NRG calculations. Middle panel: NRG calculated PDOS. Lower panel: dI/dV spectra from experiment

than in isolated K_xC_{60} complexes.

Figure 6.7a shows the topograph of a K_6C_{60}/C_{60} heterostructure. The K_6C_{60} and C_{60} molecules are hard to distinguish in the topography. They are easier to distinguish in the dI/dV map of the same heterostructure in figure 6.7b, where the K_6C_{60} appears brighter than the C_{60}.

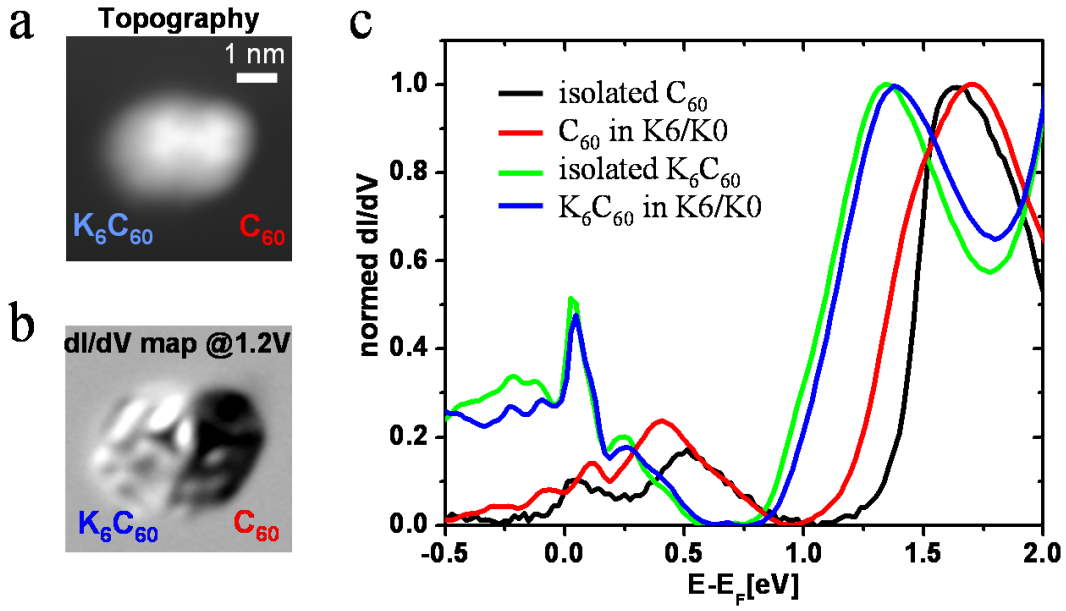

Figure 6.7: A K_6C_{60}/C_{60} heterostructure. (a) Topograph of the heterostructure. (b) dI/dV map of the same heterostructure taken at 1.2 V. (c) Spectroscopy of the K_6C_{60} and C_{60} in the heterostructure compared to the spectroscopy of isolated K_6C_{60} and C_{60} complexes. K6/K0 in the caption refers to K_6C_{60}/C_{60}.

dI/dV spectroscopy on the K_6C_{60}/C_{60} heterostructure (figure 6.7c) reveals that the spectrum of a K_6C_{60} complex in the K_6C_{60}/C_{60} heterostructure (blue curve) looks almost identical to an isolated K_6C_{60} spectrum (green curve), while the spectrum for a C_{60} molecule in K_6C_{60}/C_{60} looks substantially different from the spectrum of an isolated C_{60} (black curve).

Since changes in the spectroscopy are related to charge transfer, the spectroscopy results suggest that attaching C_{60} to K_6C_{60} does not significantly alter the charge state of K_6C_{60} but it does change the charge state of the isolated C_{60} appreciably. The amount of charge transfer can be estimated from the position of the LUMO+1, as in §6.2.1. Since the energetic position of the left LUMO+1 shoulder for C_{60} in K_6C_{60}/C_{60} is around 0.1 V lower than the energetic position of the left LUMO+1 shoulder in isolated C_{60}, the C_{60} in K_6C_{60}/C_{60} has gained an additional charge of around 0.6 electrons after it is attached to K_6C_{60}. Hence, the total electron charge on the heterostructure is larger than the charge on each molecule when separated.

This effect may be due to the influence of the local environment of K on the K-C_{60} charge transfer. In K doped bulk C_{60} [201, 45] and monolayer C_{60} [189, 207, 26] samples, K donates an entire electron to C_{60}. Hence, if K is surrounded by numerous C_{60} molecules, as it is in bulk and monolayer samples, then the charge transfer is different than the 0.6 electron charge transfer from K to C_{60} in isolated K_xC_{60} complexes, where the K atoms

are surrounded by only one C_{60}. By adding a C_{60} molecule to K_6C_{60}, the K atoms in the K_6C_{60}/C_{60} complex are now surrounded by more C_{60} molecules, causing the charge transfer from K to C_{60} in K_6C_{60}/C_{60} to become more like the bulk and monolayer charge transfer values. Since the bulk and monolayer charge transfers are higher than the isolated K_xC_{60} charge transfers, the charge transfer from K to C_{60} in K_6C_{60}/C_{60} is also higher. The exact mechanisms behind the additional charge transfer will require further study.

6.4 Conclusions

Using the STM, single C_{60} molecules have been reversibly doped with individual K atoms on Ag(001). Experimental dI/dV spectra show that the main effect of this doping process is to rigidly shift C_{60} molecular states with doping. In addition, other more subtle features also appear in the experimental spectra, such as splittings, dips, and peaks near E_F. DFT calculations reproduce most of the essential features of the spectroscopy, except for the sharp peak near E_F in K_xC_{60} for $4 \leq x \leq 7$. This peak can be accounted for with NRG calculations, which show it arises from a mixed-valence Kondo effect.

It is still not clear why the narrow resonance at E_F is only seen in K_xC_{60} when $x \geq 4$. One reason for the lack of a Kondo peak for $x < 4$ is that the Kondo temperature might be too low to see a Kondo effect: instead a Coulomb-blockade dip appears at the Fermi level at temperatures above the Kondo temperature. Alternately, the Fano-like dips that appear for K_xC_{60}, $x < 4$, suggest that there might also be a Kondo effect at lower dopings, but instead of a sharp resonance, we observe a Fano line shape caused by tunneling through multiple channels. The underlying physics behind the lower doped C_{60}'s is not completely understood and requires further study.

7

K_xC_{60} Metal-to-Insulator Transitions

The interplay between molecular electronic and atomic structure is particularly important in fullerenes, because of the unusual combination of large electron-vibration interaction and large electron-electron interactions with small electronic bandwidths, causing all interactions to be of comparable energies [207, 62]. Since the conductive characteristics of a system are heavily influenced by the relative magnitude of these properties, small changes in these properties due to changes in interactions such as intermolecular hybridization, electron-electron interactions, and structural distortions can tip these systems from one side of the metal-insulator divide to the other. Metal-to-insulator transitions have been studied extensively in C_{60}^- based systems [105, 41, 89, 21], but the role played by the structural distortions is still under debate [21, 160, 46, 32, 69, 25, 38, 104].

The STM gives one the unique ability to simultaneously investigate local structural distortions and electronic properties of a system, allowing one to analyze the effect of structural distortions on electronic properties, thus allowing one to determine the role these distortions play in C_{60} metal-to-insulator transitions. This ability stems from the capability of STM to measure the DOS, giving us electronic information, as well as from the capability of STM to directly image electronic wavefunctions at various energies, giving us structural distortion information, since the spatial distribution of wavefunctions are directly related to structural distortions.

Our STM imaging of the wavefunctions of individual K_xC_{60} complexes in a K_xC_{60} monolayer (ML) on Au(111) gives strong evidence that a specific type of structural distortion caused by the Jahn-Teller (JT) effect exists in this system and that this distortion plays a crucial role in driving the K_xC_{60} ML from a metal for $x = 3$ to an insulator at $x = 4$.

Since the JT effect is related to electron-vibration interactions, this chapter will address one of the central questions in this dissertation: how do electron-vibration interactions in single molecules affect their isolated and aggregate properties. It will discuss how the electron-vibration induced structural JT distortions in K_xC_{60} monolayers on Au(111) result in a metal-to-insulator transition in this system. This chapter is based mainly on a paper we published in ref. [191].

7.1 The Jahn-Teller Effect

Symmetries are inevitably linked to degeneracies by Noether's theorem. Structural symmetries are closely linked to electronic degeneracies with high structural symmetry leading to large degeneracies in the electronic energy levels. Breaking the structural symmetry can result in breaking the electronic degeneracy. For a molecule with degenerate orbitals, only some of which are occupied by electrons, structural distortion of the molecule can lower the energy of occupied electronic levels while raising the energy of empty ones, reducing the molecular total electronic energy (figure 7.1). Hence, under the right circumstances, it

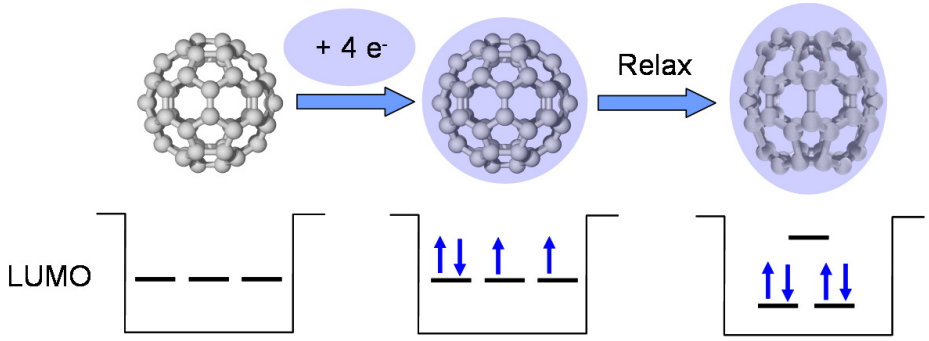

Figure 7.1: The JT distortion occurs when a system has degenerate orbitals, but only some of the degenerate orbitals are occupied by electrons. This partial occupancy of degenerate orbitals is usually achieved by adding or removing charge from a system; in this case K atoms can donate electrons to C_{60}, negatively charging it. The structure of the system then distorts and breaks the electronic degeneracies, lowering the electronic energy.

will be energetically favorable to break structural symmetries. Structural symmetry breaking resulting in the lowering of electronic energy via degeneracy breaking is known as the *Jahn-Teller effect* [92].

Jahn and Teller derived the conditions under which the JT effect occurs in the 1937 [92]. For molecules that are not linear, a structural distortion will cause degeneracy breaking in any set of degenerate states whose degeneracy is not due to Kramer's degeneracy. (Kramer's degeneracy occurs when the Hamiltonian H for a system commutes with the time reversal operator Θ and the system has a half-odd integer spin. In this situation, any eigenstate $|\psi\rangle$ of H is degenerate with $\Theta|\psi\rangle$). However, the magnitude of the energetic splitting between the JT split states depends on the strength of the electron-vibration interaction, and may be too small to observe in some molecules.

7.2 JT effect in K_xC_{60} monolayers

The high symmetry (icosahedral) of C_{60} leads to large degeneracies, and this combined with its strong electron-vibration interactions makes C_{60} a good candidate to observe the

JT effect. Although the energetic splitting of degenerate C_{60} orbitals has been seen in previous experiments, the JT split wavefunctions have not been imaged before, and it is this additional information which links the electronic and structural properties.

The electronic wavefunctions at one particular energy in a JT distorted molecule are directly impacted by the symmetry of the JT distortion since the JT splitting of degenerate states leads to very different occupied and empty wavefunctions compared with undistorted molecules. By comparing STM images of the molecular wavefunctions above and below E_F, we can determine the presence or absence of a JT splitting, and furthermore, with the aid of theoretical analyses, can determine the structure which lead to the wavefunctions.

STM images above and below E_F reveal that K_4C_{60} has a JT distortion while dI/dV spectroscopy shows it is an insulator. This provides evidence that the lack of DOS near E_F in K_4C_{60}, and hence its insulating behavior, is related to the JT splitting of the C_{60} orbitals, since the JT splitting tends to reduce the energy of occupied states while increasing the energy of unoccupied states, creating a lack of states in the DOS near E_F. STM images on K_3C_{60}, on the other hand, reveal the lack of a JT distortion while dI/dV spectroscopy on K_3C_{60} reveals it is metallic. This combination of results on both K_4C_{60} and K_3C_{60} strongly suggests that the transition from metal to insulator in K_xC_{60} monolayers when x changes from 3 to 4 is related to the Jahn-Teller effect.

The JT effect only happens when not all orbitals in a degenerate set of orbitals are filled, which is not the case in pure C_{60}. To obtain the situation which makes the JT effect possible, we added charge to the molecule. To accomplish this experimentally, we add K atoms to C_{60}. Since each K atom donates approximately one electron to the physisorbed C_{60} molecules, the charge state of C_{60} molecules in the K_xC_{60} ML was controlled by controlling the local K concentration [207, 189, 26].

All experiments were performed using a home-built UHV STM at $T = 7\,\mathrm{K}$ with a PtIr tip. The Au(111) surface was cleaned by sputtering and annealing (§5.3). C_{60} was then deposited at coverages between 80% ML and 90% ML onto the clean Au(111) substrate cooled to 80 K. C_{60} coverages were determined from STM images. K was deposited progressively from a calibrated K getter (§5.4.3) onto the C_{60}/Au(111) sample, followed each time by an anneal at $490 \pm 10\,\mathrm{K}$ for 15 min. K evaporators were calibrated by deposition of K onto a clean Ag(100) substrate cooled to 80 K and counting single K atoms in topographic STM images acquired at 7 K. dI/dV spectra acquired using standard lock-in techniques (§2.4).

Low-temperature STM studies were performed on K_xC_{60} monolayers on Au(111) for $0 \leq x \leq 5$. At lower K concentrations $0 \leq x \leq 3$, the energetic position of the C_{60} states rigidly shift to lower energies as the K concentration increases (figure 7.2). However, this trend stops at $x = 4$ where the STM spectrum evolves from a metal at $x = 3$ to one that is characteristic of an insulator at $x = 4$. This electronic transition is accompanied by a dramatic orientational rearrangement of the C_{60} molecules. This data strongly suggests that something special happens between $x = 3$ and 4.

We will now focus on K_xC_{60} for $x = 3$ and 4. When the average x in K_xC_{60} falls between 3 and 4, the system is an inhomogeneous mixture of two stoichiometries. The local phase separation can be seen in figure 7.3. K_3C_{60} exhibits a triangular lattice backbone with a

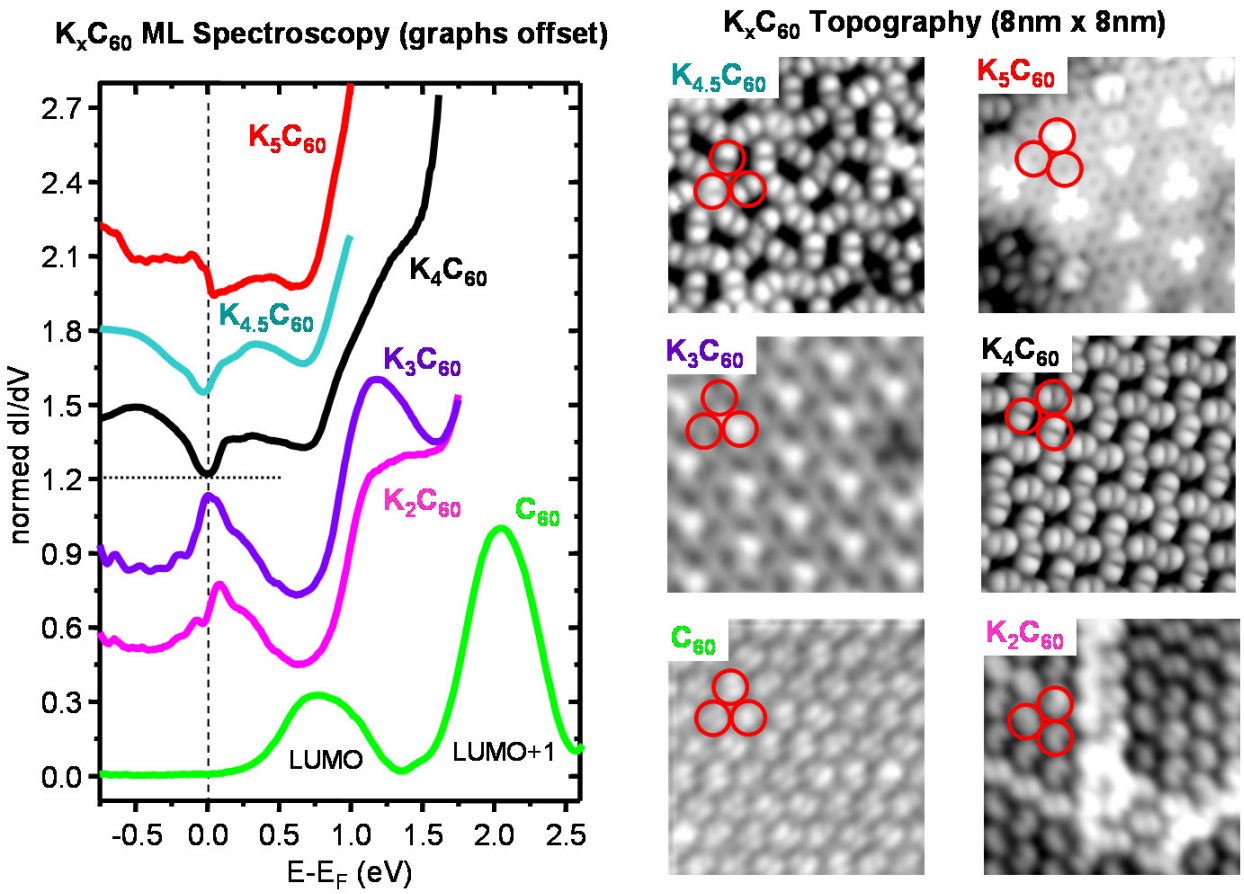

Figure 7.2: Topography and dI/dV spectroscopy on K_xC_{60} monolayers on Au(111). The LUMO and LUMO+1 resonances for C_{60} shift to lower energies in K_2C_{60} and K_3C_{60}. However, $x \geq 4$, this trend stops. Individual C_{60} molecules are circled in red in the topographic images.

"bright molecule" supermodulation (figure 7.4B), which may be a K-induced ordering. The exact form of the supermodulation varies across the K_3C_{60} surface and exhibits pronounced disorder in some regions, whereas it disappears altogether in others. However, metallic dI/dV spectra (figure 7.3) are observed regardless of the details of the supermodulation. The K_xC_{60} ML undergoes a dramatic restructuring from $x = 3$ to 4 that transforms the underlying triangular supermodulation into a nearly rectangular structure with four molecules per unit cell (figure 7.5A). This structure is free of supermodulation and contains much larger ordered areas than the K_3C_{60} structures. The dI/dV spectrum for K_4C_{60} exhibits an energy gap of 200 ± 20 mV that is roughly symmetrical about E_F (figure 7.3).

The difference in electronic wavefunctions between the $x = 3$ and $x = 4$ phases can be seen by comparing STM images of the filled and empty states straddling E_F (figures 7.4 and 7.5). Constant current topographic images at $V = -200$ mV (filled states) and $V = +200$ mV (empty states) for the same patch of K_3C_{60} surface (figure 7.4A and B) show

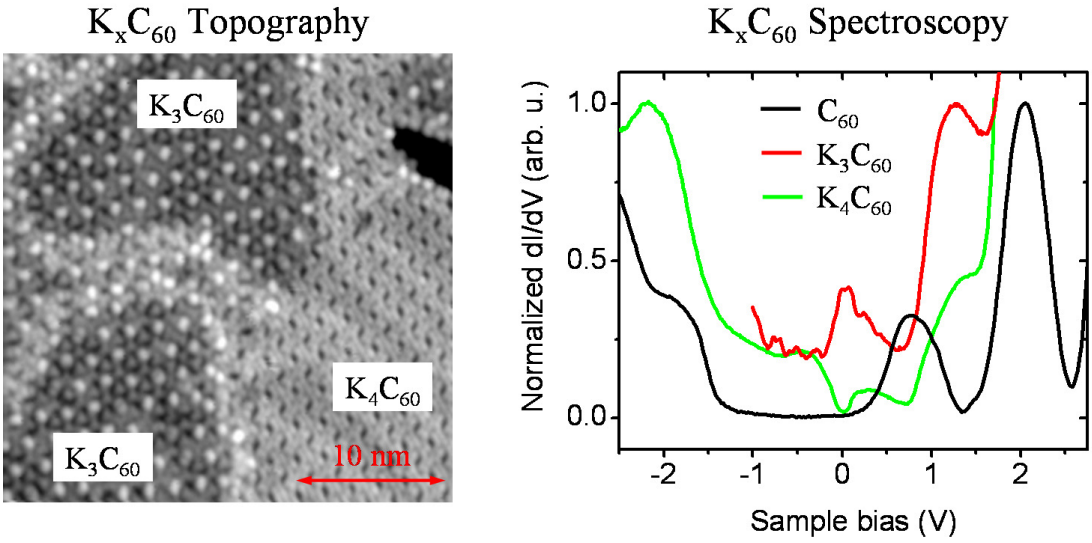

Figure 7.3: Phase separation in K_xC_{60} for $3 \leq x \leq 4$. The topograph ($V = 0.5\,\mathrm{V}$, $I = 10\,\mathrm{pA}$) shows the two coexisting phases K_3C_{60} and K_4C_{60}. The spatially averaged dI/dV spectrum taken on only K_3C_{60} shows metallic behavior, while the spatially averaged dI/dV spectrum for K_4C_{60} shows an energy gap at E_F. A bare C_{60} spectrum is shown for comparison. All spectra were normalized so that the highest peak has a maximum value of 1.

little change upon bias reversal. A collection of dI/dV spectra measured at different points within a $4\,\text{Å} \times 4\,\text{Å}$ region of the K_3C_{60} ML (figure 7.4C) shows some variability, but all of the spectra reveal a similar peak near E_F ($V = 0$), indicative of a metal.

However, empty and filled state images of K_4C_{60} shows a striking difference (measured at $V = -200\,\mathrm{mV}$ and $V = +200\,\mathrm{mV}$, respectively). Filled-state images (figure 7.5A) show that each C_{60} molecule is bisected by a single nodal line (i.e., a dark stripe), while empty-state images (figure 7.5B), display an additional nodal line on each molecule that is rotated by 90° with respect to the node seen in the filled-state image. This prominent difference in topography for filled and empty states does not exist in K_3C_{60}. dI/dV spectroscopy on the K_4C_{60} phase (figure 7.5C) shows that instead of a peak at E_F, a 200 mV energy gap exists, indicating that K_4C_{60} is an insulator.

The dramatic difference in the filled- and empty-state topography of figure 7.5 can be attributed to a JT distortion. When four K atoms are added to C_{60}, the molecule receives four extra electrons, and a C_{60} molecule is expected to undergo a JT distortion whereby the three degenerate LUMO states split (figure 7.1) into a group of twofold orbitally degenerate levels at lower energy and one orbital at higher energy [27, 112, 134]. The four extra electrons reside in the two lower energy levels, making the distortion energetically favorable.

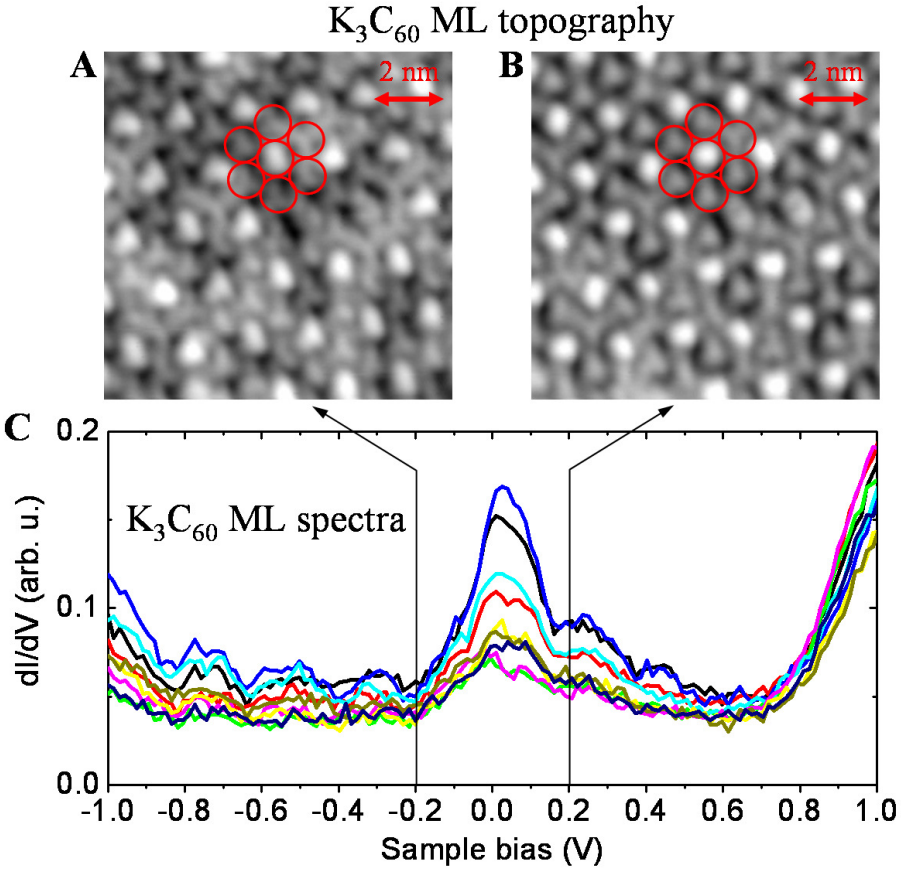

Figure 7.4: K_3C_{60} ML on Au(111). (A) Constant current STM topograph of K_3C_{60} on Au(111) at $V = -0.2\,\mathrm{V}$, $I = 20\,\mathrm{pA}$, showing occupied electronic states near E_F. (B) Topograph of the same region at $V = +0.2\,\mathrm{V}$, $I = 20\,\mathrm{pA}$, showing empty electronic states near E_F. Single molecules are circled in red. (C) dI/dV spectroscopy on K_3C_{60} taken on a 3×3 grid of equally spaced points with a $2\,\text{Å}$ spacing between points.

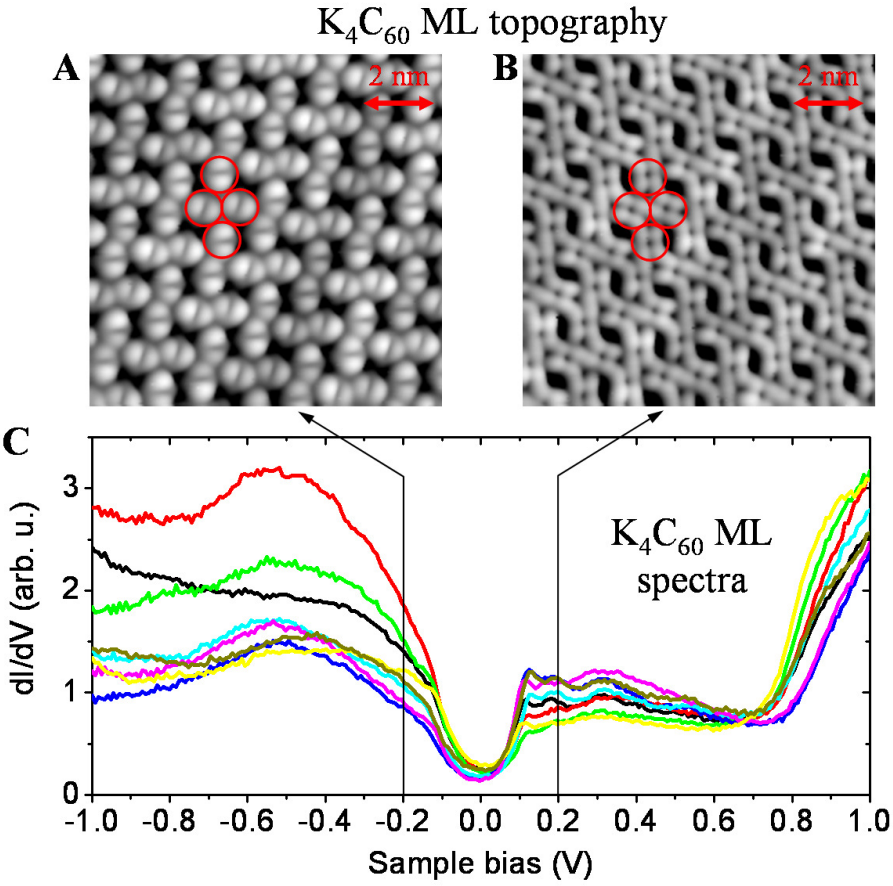

Figure 7.5: K_4C_{60} ML on Au(111). (A) Constant current STM topograph of K_4C_{60} on Au(111) at $V = -0.2\,\mathrm{V}$, $I = 10\,\mathrm{pA}$, showing occupied electronic states near E_F. The topography does not change over the bias range $-0.10\,\mathrm{V}$ to $-0.7\,\mathrm{V}$. (B) Topograph of the same region at $V = +0.2\,\mathrm{V}$, $I = 10\,\mathrm{pA}$, showing empty electronic states near E_F. Single C_{60} molecules are circled in red. The topography does not change over the bias range $+0.10\,\mathrm{V}$ to $+0.6\,\mathrm{V}$. (C) dI/dV spectroscopy on K_4C_{60} taken at various points.

7.3 DFT calculations on K_4C_{60}

The effect of a small molecular distortion can be thought of as adding a perturbing Hamiltonian H' to an undistorted molecule's Hamiltonian, and by degenerate perturbation theory, H' will split degenerate states, like the C_{60} LUMO, in a way that diagonalizes H'. Different distortions will yield different perturbations H', which then lead to different splittings. This implies an intimate relation between the electronic orbitals and the specific type of distortion induced by the JT effect. To determine that relation, we compared our STM topographic images with calculated molecular LDOS by using the density functional theory (DFT) code SIESTA with *ab initio* pseudopotentials, a local orbital basis, and the local density approximation for the exchange-correlation functional. The calculations were performed by Khoonghong Khoo in Steven Louie's group. Different locally stable distorted structures for isolated C_{60}^{4-} were found by total energy minimization. Their electronic LDOS's were then compared to our STM topography and the distorted structure which best reproduced the experimental images was selected. Figure 7.6 shows two views of the best-fit structure, which has D_{2h} symmetry, where the atomic displacements have been exaggerated by a factor of 30. Apart from using an improved basis set [102], a finer real space grid (0.1 Å mesh), and excluding the surface, details of the calculation method are similar to those in [130].

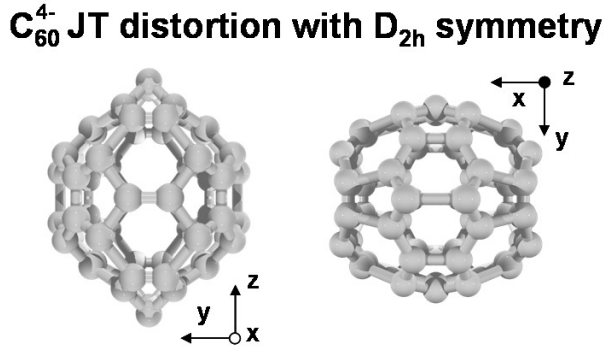

Figure 7.6: Two views of the JT distorted C_{60}^{4-} structure whose LDOS best reproduces experimental images. This structure has D_{2h} symmetry. The Au(111) surface would lie in the xy-plane if one compares this to experiment. The distortion has been exaggerated by a factor of 30 to make it visible.

To calculate the various stable structures, the molecule was given a small initial distortion having either D_{2h}, D_{3d}, or D_{5d} symmetry, and then allowed to relax to minimize the energy. These distortions were chosen by symmetry considerations [27, 112, 134]. The resulting displacements can be expressed in terms of phonon modes within the H_g and A_g even symmetry classes. The lowest energy deformation having D_{2h}, D_{3d}, or D_{5d} symmetry each show an essentially identical total energy reduction from the undistorted structure of 0.3 eV per molecule. In all three cases, the molecular JT distortion splits the 3-fold degenerate LUMO by 0.11 eV into doubly degenerate occupied levels and a single unoccupied level. However, only the D_{2h} distortion results in electronic wave functions that match the STM

images above and below E_F; see figure 7.7 for the calculated wavefunctions with D_{3d} and D_{5d} symmetry. Therefore, we believe that the D_{2h} distortion is stabilized in the K_4C_{60} ML on Au(111), possibly due to the K-C_{60} interaction or Au-C_{60} interaction, which were not included in the calculation. The calculated D_{2h} distortion of the C_{60} cage (figure 7.6) creates

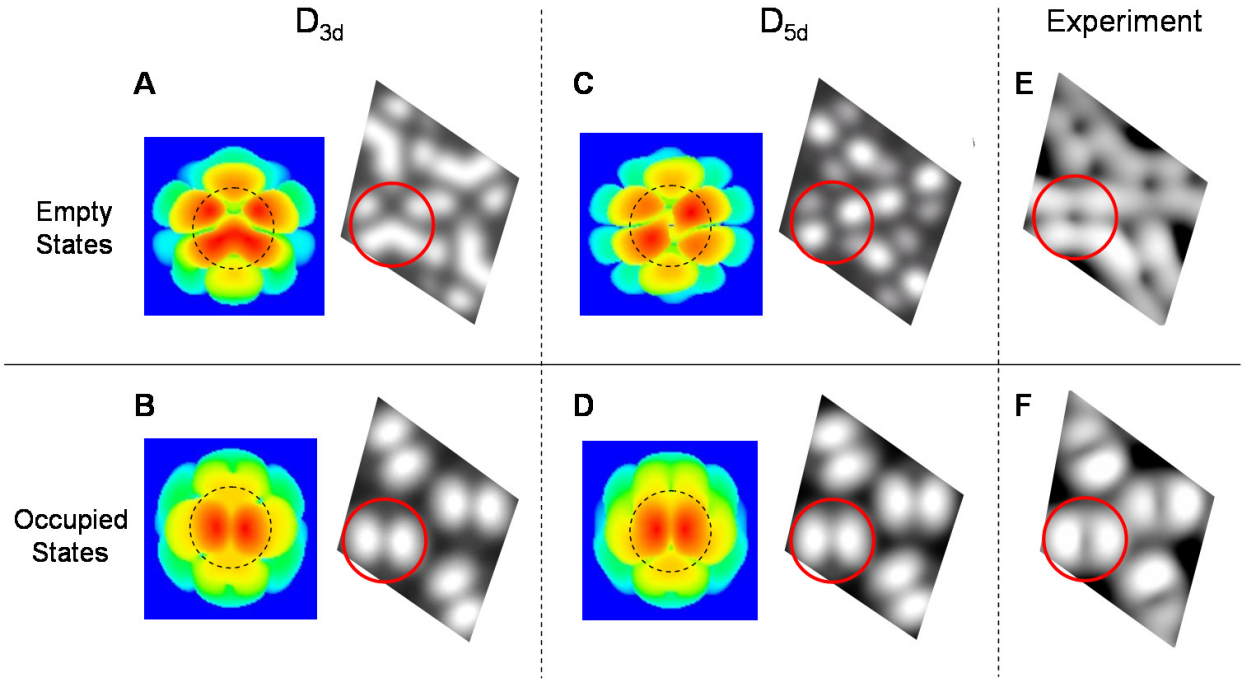

Figure 7.7: DFT calculated C_{60}^{4-} JT distortions having D_{3d} or D_{5d} symmetry. The red circles mark the position of a single C_{60} molecule. (A) Theoretical 2-D projection of a D_{3d} distorted C_{60}^{4-} molecule isosurface and simulated unit cell showing empty state wavefunctions. (B) HOMO wavefunctions for the D_{3d} JT split levels. Isosurfaces are about 3 Å outward from carbon centers. All single molecule projected isosurfaces have an orientation such that a horizontal 6-6 bond would be in the center of the structural model. Regions within black dashed circles are preferentially imaged in monolayer topographs due to finite tip size. (C) and (D): same as (A) and (B), but for a D_{5d} distorted C_{60}^{4-}. (E) Experimental STM topography for the K_4C_{60} ML unit cell empty states and (F) filled states.

an oblate spheroid, with the short axis along the y direction of the figure. Most of the bond distortion occurs in the equatorial xz plane.

The isosurfaces of the LDOS (plot of the set $\{\vec{r}\colon \sum_n \left|\Psi_n(\vec{r})\right|^2 = C\}$, where $\vec{r}$ is the position vector, $\Psi_n(\vec{r})$ is an eigenstate, n ranges over degenerate eigenstates at a particular energy, and C is a real constant) of the energy-split states for the D_{2h} distorted C_{60}^{4-} can be seen in figure 7.8A and B, for the unique orientation that fits our experimental data (here the Au surface lies in the xy plane of the figure).

The most pronounced feature in the calculated C_{60}^{4-} HOMO wavefunctions (figure 7.8B)

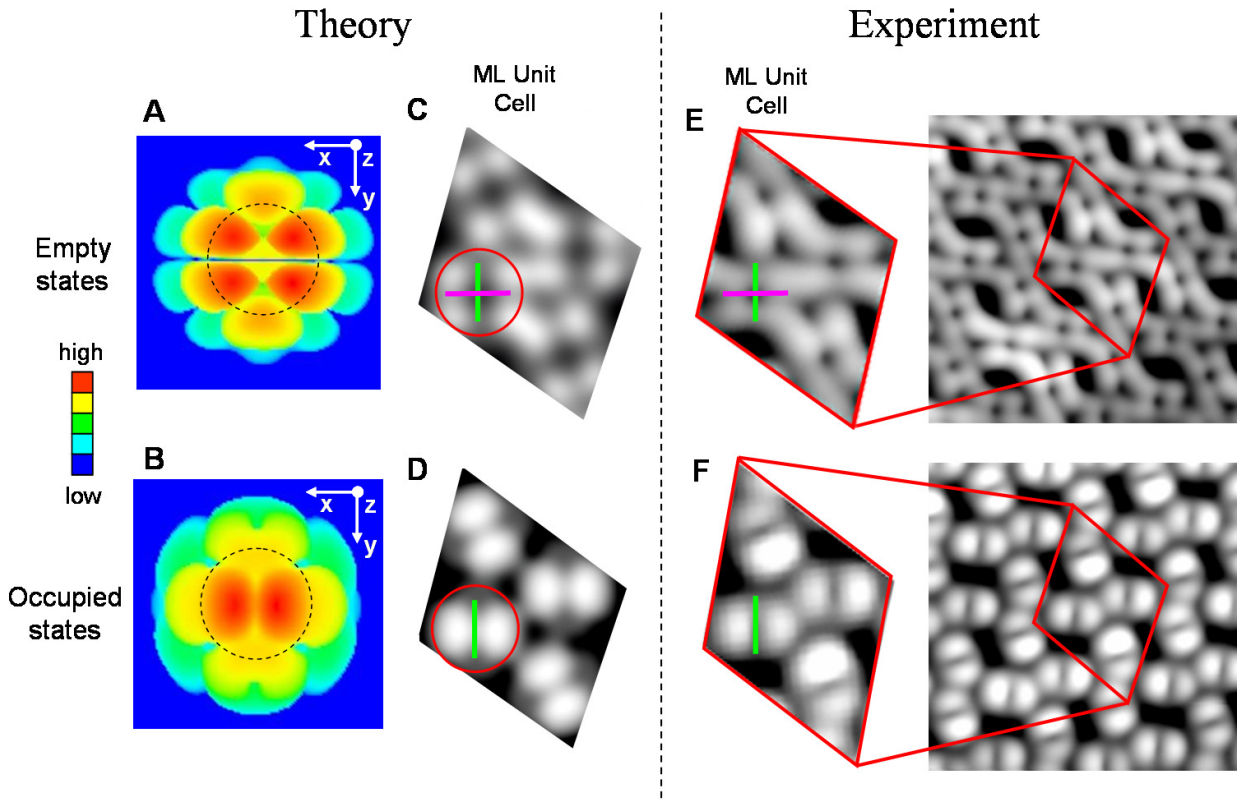

Figure 7.8: Comparison between the DFT calculated D_{2h} JT distorted C_{60}^{4-} and experiment. The Au(111) surface lies parallel to the xy plane of the figure. (A) Two-dimensional projection of the C_{60}^{4-} isosurface showing the wavefunction for the highest filled-state and (B) wavefunctions for the lowest empty states at ~ 3 Å outward from carbon centers. Regions within the dashed circles are preferentially imaged by STM in ML topographs because of finite tip size. The regions within the dashed circles are repeated and arranged in (C) and (D) to simulate the experimental unit cell. Nodal lines are marked in purple and green and single molecules are circled in red. (E) and (F) are experimental K_4C_{60} unit cells for comparison.

is a strong linear depression that bisects the highest region (red regions) into two areas. The highest regions of the LUMO wavefunction (figure 7.8A) are similar to the highest regions of the occupied wavefunctions, except for the addition of a pronounced linear depression that lies at an angle of 90° from the linear depression seen in the occupied wavefunctions. This new node lies exactly in the xz equatorial plane, where the greatest JT-induced changes in bond length occur, thus marking the spatial location of the JT distortion in the molecular wavefunction. By taking the regions enclosed by dashed circles in figures 7.8A and B, and repeating and arranging them, simulated ML topographs (figure 7.8C and D) have been constructed, and are in good agreement with experimentally observed K_4C_{60} filled and empty state topography. Empty-state imaging of the K_4C_{60} ML thus allows us to

directly determine the spatial location where the largest structural distortion occurs for each individual C_{60} molecule.

7.4 Conclusions

Our combined DFT and STM results provide strong evidence that the JT distortion plays a central role in the metal-to-insulator transition from K_3C_{60} MLs to K_4C_{60} MLs. In particular, the JT effect and the intra-molecular Coulomb interaction act cooperatively. For an even number of electrons, the JT effect suppresses intermolecular electron hopping (via Pauli exclusion) and hence reduces metallicity. Less metallicity causes worsened screening which enhances intra-molecular Coulomb interaction [62, 130, 80] and thus enhances electron localization. Increased electronic localization, in turn, favors JT distortion (by reducing electron-number fluctuation on each molecule). Both Coulomb and JT interactions cooperatively contribute towards the insulating K_4C_{60} ML ground state.

A better understanding of the details in K_xC_{60} spectroscopic features will likely have to include interaction of the molecules with the K ions and with the Au substrate, as well as quasiparticle effects that go beyond DFT in the standard local-density approximation.

8

K_xC_{60} Monolayer Orientational Ordering

The previous chapter focused on the electronic properties of K_xC_{60} monolayers, but did not discuss the mechanisms that drive the ordering of the molecules. This chapter will discuss the possible underlying mechanisms causing C_{60} molecules to order in K_xC_{60} monolayers ($3 \leq x \leq 5$). It will address one of the main themes in this dissertation: how do molecule-molecule interactions influence the properties (in this case orientational ordering) of the constituent molecules. It is based mainly on our published paper, ref. [197].

8.1 Orientational Ordering

Unlike atoms, molecules have various distinct orientations, which leads to an additional type of ordering not possible in atoms: orientational ordering. In a lattice consisting of one type of molecule, orientational ordering is when the orientations of the molecules repeat in a pattern. Like the Jahn-Teller effect, orientational ordering also originates from symmetry breaking, but this time it is the broken symmetry of the environment of the molecule. When the molecular environment is not perfectly symmetric, the interaction between the molecule and the environment will cause certain molecular orientations to have a lower energy than others, creating preferred molecular orientations.

The high (icosahedral) symmetry of a C_{60} molecule makes monolayers of potassium doped C_{60} ideal systems for studying new orientational phases [77]. Orientational order also plays a vital role in shaping the rich electronic phase diagram of the fullerides that involves superconducting, metallic, insulating, and magnetic phases [62]. For example, the effect of molecular orientation on electronic structure was seen in angle-resolved photoemission experiments that reveal significant differences between metallic K_3C_{60} MLs on Ag(111) and Ag(001) [22].

8.2 K_xC_{60} Pinwheels

By performing STM experiments on K_xC_{60} MLs on Au(111), we find that $K_{4+\delta}C_{60}$ MLs with $0.1 < \delta < 0.5$ exhibit C_{60} molecules that retain the JT-split K_4C_{60} states (chapter 7), but display a new, complex 7-sublattice pinwheel-like orientational ordering. At $x = 5$ the system reenters a metallic phase (chapter 9) that exhibits a novel orientational structure markedly similar to the $x = 3$ metallic phase. In the JT-insulating K_xC_{60} MLs ($x \sim 4$), an intermolecular electron virtual hopping mechanism is proposed to be a crucial driving force for the cross and pinwheel phases. In the metallic phases $x = 3, 5$ the dominant mechanism for orientational ordering is the maximization of the overlap of partially occupied electron wave functions, resulting in direct intermolecular electron hopping.

Our experiments were conducted in UHV at $T = 7\,\mathrm{K}$ with a PtIr tip. C_{60} thin films were made by evaporating C_{60} molecules onto a clean Au(111) surface from a Knudsen cell evaporator (§5.4.1). Appropriate amounts of K atoms were dosed onto the C_{60} films from a SAES Getter (§5.4.3). The evaporation rates of the K and C_{60} evaporators were calibrated by depositing them separately onto a clean metal substrate, followed by directly counting the number of K atoms and C_{60} molecules per area in the STM images. This calibration was used to calculate the value of x in a K_xC_{60} monolayer. The K_xC_{60} monolayers were annealed at 200°C for 20 minutes before being cooled to 7 K for the experiments. Progressive doping was obtained by adding more K atoms onto the existing film followed by re-annealing. We found that in the highly doped samples ($x > 4$), the K content may be decreased by 200°C annealing; therefore, a lower annealing temperature of 140°C was used in this regime to avoid K loss. dI/dV spectra were measured through lock-in detection (§2.4) of the a.c. tunneling current driven by a 450 Hz, 1–10 mV (rms) signal added to the sample bias with the feedback off.

Figure 8.1a shows a typical STM image of the new "pinwheel" phase that occurs in $K_{4+\delta}C_{60}$ ($0.1 < \delta < 0.5$) MLs. An average K content in the range $4 < x < 5$ induces a rearrangement of the C_{60} molecules that destroys the long-range "cross" phase previously observed in K_4C_{60} MLs (figure 7.5), leading to a new locally ordered pinwheel-like structure (each pinwheel is highlighted in purple). dI/dV spectroscopy of the pinwheel molecules (figure 8.1b) reveals a DOS very similar to that of the insulating K_4C_{60} cross phase, suggesting that the C_{60} molecules in $K_{4+\delta}C_{60}$ still retain the C_{60}^{4-} charge state seen in the stoichiometric K_4C_{60} cross phase [191]. The difference between the cross and pinwheel phases lies purely in the C_{60} lattice structure and intermolecular orientational order.

As shown in figure 8.2b, each pinwheel consists of six "wheel" C_{60} molecules arranged hexagonally around a central "pin" molecule (each wheel molecule is rotated by $\sim 60°$ relative to its neighboring wheel molecule). The seven molecules in a pinwheel sit on a close-packed triangular lattice, which is a denser packing (by $\sim 5\%$) than the more open cross phase. Figure 8.2a shows an ordered domain of the 7-sublattice pinwheels forming a $\sqrt{7} \times \sqrt{7}R40.9°$ hexagonal superstructure. This suggests that the pinwheels are the structural unit of a new phase rather than merely defects. Both the number and size of the domains grow continuously as the average K content increases from $x \sim 4.1$ to 4.5, with a

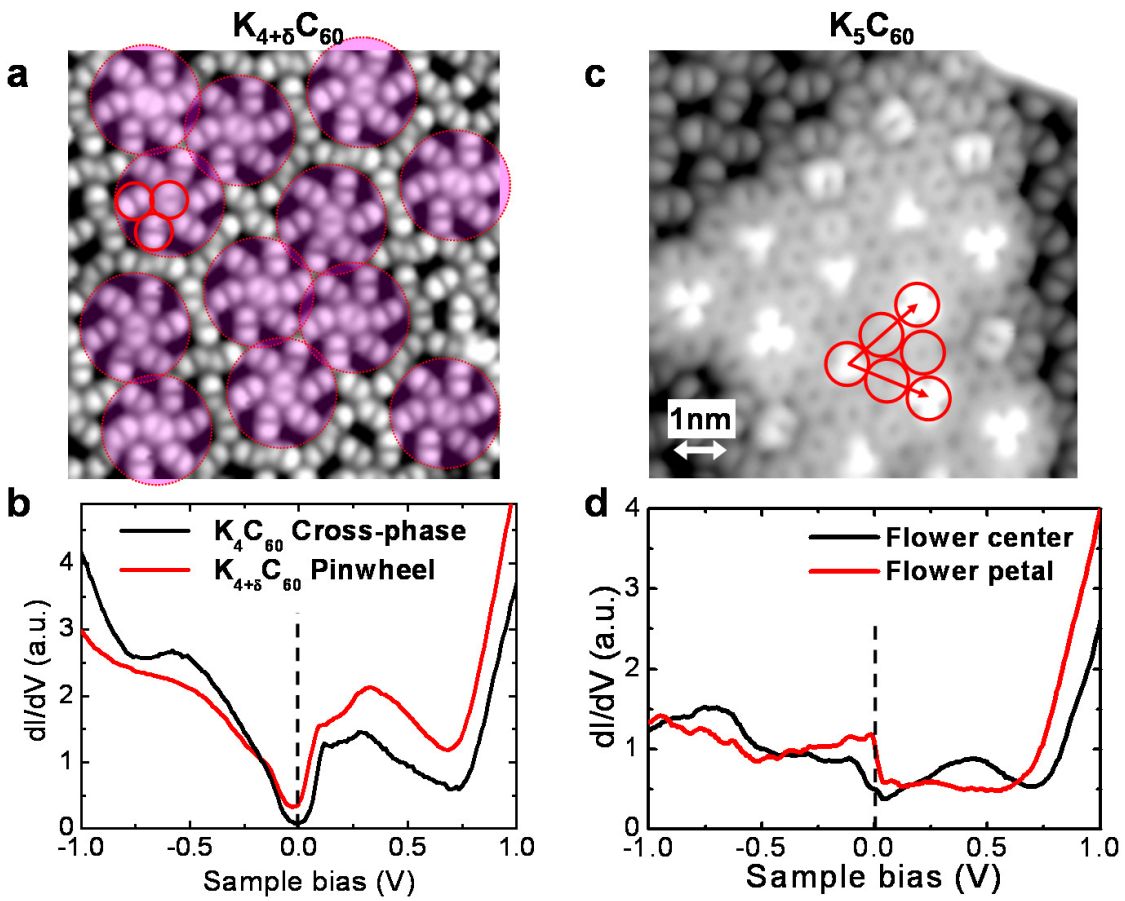

Figure 8.1: $K_{4+\delta}C_{60}$ pinwheels and K_5C_{60}. (a) Topography ($V = -0.2\,\mathrm{V}$, $I = 5\,\mathrm{pA}$) on a $K_{4+\delta}C_{60}$ ML showing pinwheels colored in purple. (b) dI/dV spectroscopy on $K_{4+\delta}C_{60}$ (red curve) compared with K_4C_{60} spectroscopy (black curve). (c) K_5C_{60} topography ($V = -0.2\,\mathrm{V}$, $I = 5\,\mathrm{pA}$) and (d) spectroscopy. Flower centers are the bright molecules and flower petals are the dim molecules. Single C_{60} molecules are circled in red in the topographs.

maximum of $\sim 10\%$ of the ML covered with pinwheels. This is accompanied by the growth of small C_{60}-free voids containing only K atoms on Au(111). Figure 8.3 shows an image with C_{60}-free voids and the inset shows a zoom-in on the edge of a void.

The orientation of the center pin molecule reveals another novel aspect of the pinwheel structure. Because of the threefold rotational symmetry of the underlying triangular lattice and the symmetry of the C_{60} molecule, the pin molecules are free to choose among three orientations. Experimentally, the three possible orientations are uniformly distributed among the pin molecules. This equivalency among different structures and orientation disorder it induces is a hallmark of geometric frustration for orientational ordering on a triangular lattice.

When the K content is increased further to $x \sim 5$, a new metallic phase emerges, as shown

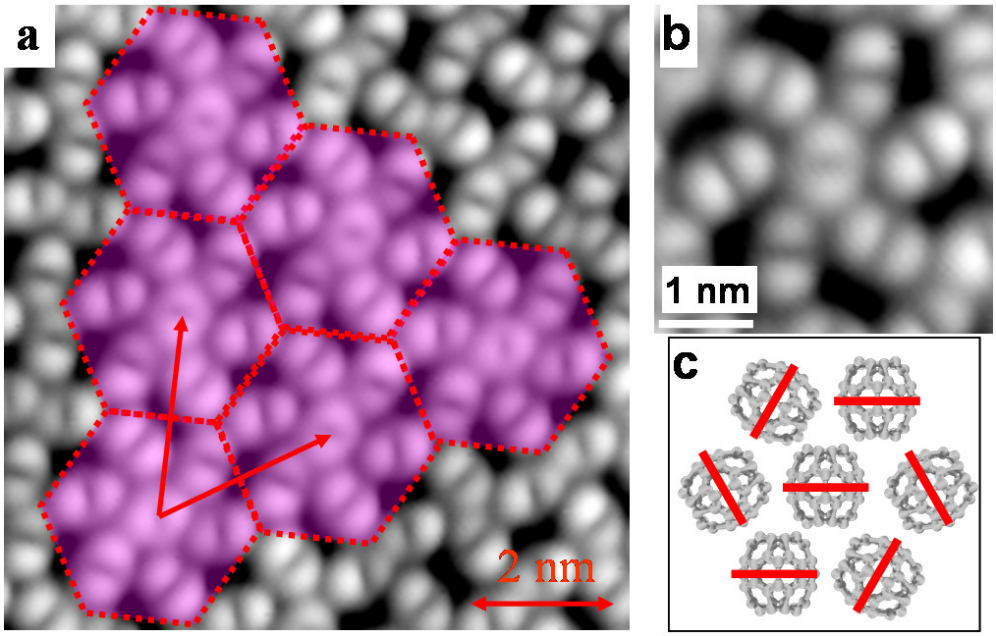

Figure 8.2: Structure of a $K_{4+\delta}C_{60}$ pinwheel. (a) Topography of an ordered domain of pinwheels ($V = -0.2\,\mathrm{V}$, $I = 10\,\mathrm{pA}$). (b) Zoom in on a single pinwheel ($V = -0.2\,\mathrm{V}$ $I = 5\,\mathrm{pA}$). (c) Structural model of the pinwheel. The red line represents the dark line node in the topographic image.

by the ordered domain of bright molecules in figure 8.1c. dI/dV spectra (figure 8.1d) reveals that the JT-insulating C_{60}^{4-} state disappears and a non-zero DOS exists at E_F, indicating a metallic ground state. This indicates that C_{60} molecules in this new phase are in a C_{60}^{5-} charge state where the fifth electron occupies an upper JT split band, as illustrated in figure 8.4b.

The K_5C_{60} molecules form a triangular lattice with a prominent 2×2 superstructure composed of bright molecules resembling a three pointed star, referred to here as a tri-star. Each tri-star molecule and its nearest neighbors form a "flowerlike" structural unit, where the tri-star (flower center) exhibits a C_{60} molecule with a hexagon facing up and the surrounding molecules (flower petals) exhibit C_{60} molecules with a 6-6 bond facing up (figure 8.4c) [129]. The orientational ordering of K_5C_{60} closely resembles that found in the metallic K_3C_{60} ML (figure 8.4a) in which C_{60} molecules form a $\sqrt{3} \times \sqrt{3}$ superstructure of bright molecules [191]. Figure 8.4c presents models of the orientational structure of K_3C_{60}, K_4C_{60}, and K_5C_{60}. In both metallic phases (K_3C_{60} and K_5C_{60}), the C_{60} molecules form a triangular lattice with all neighboring C_{60} molecules (except the central "bright" ones) contacting each other through their equatorial pentagons (blue regions).

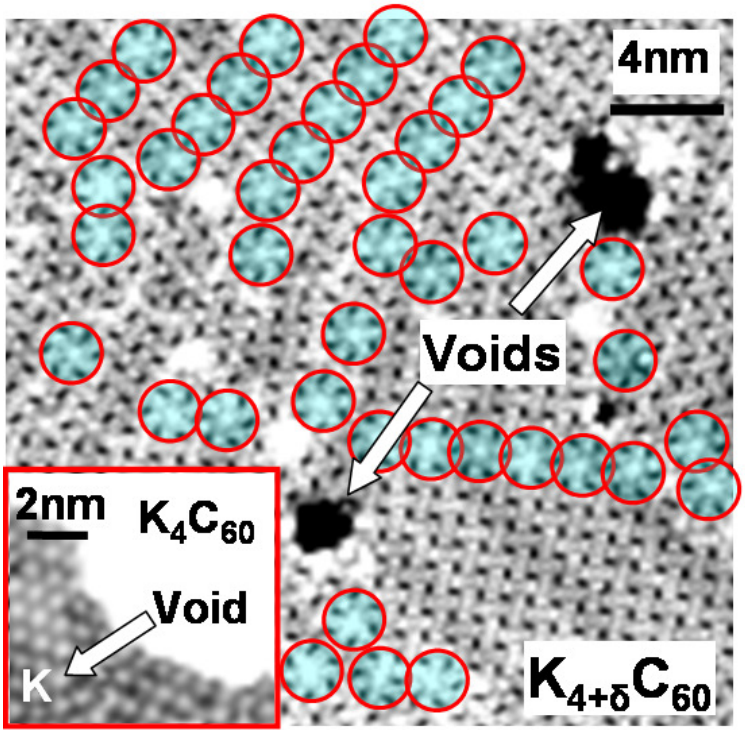

Figure 8.3: Constant current topograph ($V = 1\,\mathrm{V}$, $I = 5\,\mathrm{pA}$) of $K_{4+\delta}C_{60}$ on Au(111) showing C_{60} free voids and pinwheels colored in blue. The inset is a zoom-in of the edge of a void, showing the K atoms residing in the void.

8.3 Ordering mechanisms

C_{60} molecules will order in a way that minimizes their configurational energy. In general, there are two contributions to the electronic energy, potential and kinetic. Since molecules like C_{60} in a molecular solid tend to interact weakly, we may consider only the potential and kinetic energy of electrons in C_{60} due to interactions with the molecule's local surroundings. The local surroundings of a C_{60} molecule in K_xC_{60} MLs on Au(111) are the nearest K atoms, the nearest C_{60} molecule neighbors, and the Au(111) surface. The change in C_{60} energy due to interactions with K and Au(111) vary from $\sim 10\,\mathrm{meV}$ to $\sim 100\,\mathrm{meV}$ [194, 62]. The K-C_{60} interaction is difficult to take into account since the exact locations of the K atoms in K_xC_{60} are unknown. The effect of the Au(111) surface is also difficult to calculate.

However, the energy of the C_{60}-C_{60} interaction is straightforward to calculate and can be done quantitatively. This section will focus on the potential and kinetic contributions to the C_{60}-C_{60} energy. The potential energy is due to mainly electrostatic interactions while the kinetic interaction energy is mainly due to delocalization of electrons.

We will find that an important mechanism for all K_xC_{60} orientational phases is the minimization of electron kinetic energy by maximizing the overlap of relevant molecular orbitals. For the JT-insulating cross and pinwheel phases ($4 \leq x < 5$) the HOMO and

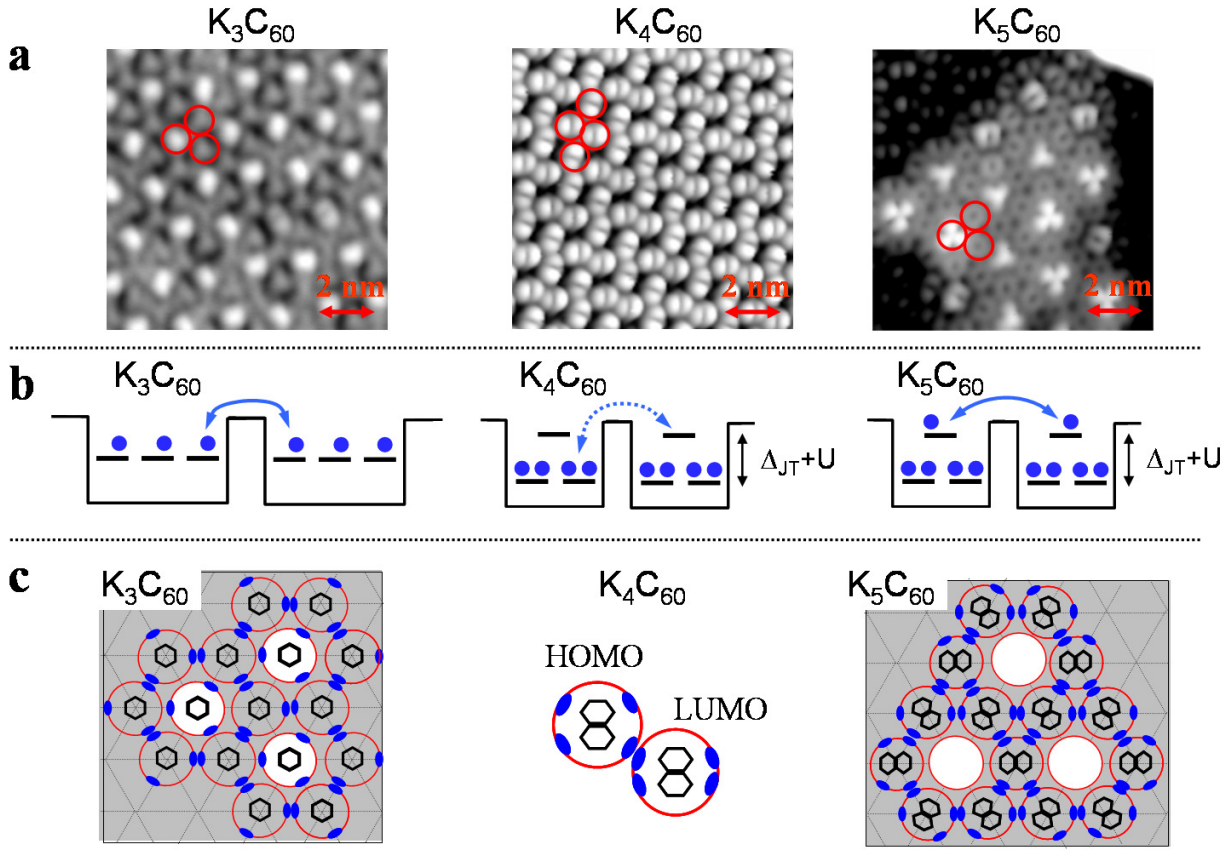

Figure 8.4: Orientation ordering found in K_xC_{60} for $x = 3$, 4, 5. (a) Topography of K_3C_{60} ($V = 0.4\,\mathrm{V}$, $I = 20\,\mathrm{pA}$), K_4C_{60} ($V = -0.1\,\mathrm{V}$, $I = 10\,\mathrm{pA}$), K_5C_{60} ($V = -0.2\,\mathrm{V}$, $I = 5\,\mathrm{pA}$). (b) Energy diagrams showing electron hopping between C_{60} LUMO orbitals on neighboring C_{60} molecules. The 3-fold degenerate LUMO in K_3C_{60} splits in K_4C_{60} and K_5C_{60}. (c) Structural models of K_xC_{60}. The blue regions mark equatorial pentagons.

LUMO orbitals maximize overlap to maximize virtual hopping of an electron between the HOMO of one C_{60}^{4-} to the LUMO of a neighboring C_{60}^{4-}. In the $x = 3$ and 5 phases, the LUMO orbitals maximize overlap to maximize direct electron hopping.

First, consider the $x = 3$ and 5 phases. These phases contain partially filled LUMO orbitals (figure 8.4b), between which electrons can directly hop. DFT calculations show these orbitals tend to be localized on the C_{60} pentagons [129, 63], so if we highlight the pentagons in blue (figure 8.4c), we see that the experimentally observed ordering tends to maximize overlap of the partially occupied C_{60} LUMO wavefunctions, thereby maximizing kinetic energy reduction by maximizing electron hopping.

Next, consider the potential and kinetic energies for the $x = 4$ phase. For the K_4C_{60} molecules in this phase, the potential energy is caused by electrostatic interactions. The leading order multipole moment of this molecule is the quadrupole moment, hence the electrostatic C_{60}-C_{60} interaction will be dominated by quadrupole-quadrupole interactions

between the C_{60} molecules in K_4C_{60}. DFT calculation indicates that JT distorted C_{60}^{4-} has a quadrupole moment of order $1e_c\,\text{Å}^2$, where e_c is the absolute value of the electron charge.

The orientation ordering of K_4C_{60} seen in figure 8.4a is reminiscent of orderings arising from electrostatic quadrupole interactions [17], which was proposed for other systems [211, 119, 70]. However, the energy difference between the observed structure and other metastable structures is small (on the order of 1 meV per molecule) and extensive computer simulations cannot reproduce the experimentally observed structures using only quadrupole interactions.

The other contribution to the C_{60}-C_{60} interaction energy is the kinetic energy arising from electron delocalization. This mechanism originates in the anisotropic electronic overlap integral between molecules [62, 63]. Because the HOMO orbitals peak near the C_{60} pentagons, one might expect pentagons on neighboring molecules to align so that intermolecular electron hopping can occur. However, for the K_4C_{60} and $K_{4+\delta}C_{60}$, the HOMO states are completely occupied, and direct hopping cannot occur. Virtual hopping (§4.2), on the other hand, can occur in these insulating systems. To get an idea of the effect of virtual hopping, tight binding calculations were performed.

8.4 Virtual hopping energies

From second order perturbation theory in tight binding (§4.2), the energy for an electron to hop from an occupied orbital to a neighboring unoccupied orbital is [63]

$$E = -2 \sum_{i \text{ occupied}} \sum_{j \text{ unoccupied}} \frac{\left|t_{ij}\right|^2}{E_j - E_i}$$

where the factor of 2 takes into account spin degeneracy and t_{ij} is the hopping integral (§4.2). Since the denominator is the smallest for the HOMO and LUMO states, the energy is approximately given by

$$E \approx -2 \sum \frac{\left|t_{\text{HOMO,LUMO}}\right|^2}{E_{\text{LUMO}} - E_{\text{HOMO}}} \tag{8.1}$$

where the sum is taken over degenerate HOMO and LUMO orbitals. $t_{\text{HOMO,LUMO}} \equiv t_{HL}$ is the hopping integral between HOMO and LUMO, which depends on the overlap between the HOMO and LUMO of adjacent molecules, and thus depends on their relative orientations.

Tight binding calculations were also used to calculate the HOMO and LUMO wavefunctions from which t_{HL} is found. The coordinates of the C atoms in C_{60}^{4-} were obtained from previous DFT calculations [191]. From previous C_{60} tight binding calculations [135, 188], only the p_z of the sp^2 bonded carbon atoms contribute to the HOMO and LUMO orbitals (page 8258 in [188]). Then the tight binding wavefunctions for the HOMO and

LUMO states can be written in terms of ϕ_i, the p_z orbital located on atom i,

$$\psi_{\text{HOMO}} = \sum_{i=1}^{60} a_i \phi_i, \quad \psi_{\text{LUMO}} = \sum_{j=1}^{60} b_j \phi_j.$$

The coefficients a_i and b_j are found by diagonalizing the tight binding Hamiltonian in the ϕ_i basis, taking the electron hopping between neighboring C atoms to be $t_c = -2.3(0.145\,\text{nm}/d)^2\,\text{eV}$, where d is the distance between nearest neighboring C atoms ([188], §4.2). The calculated wavefunctions from tight binding are shown in figure 8.5. They seem reasonable since they agree well with the DFT calculated wavefunctions shown below them.

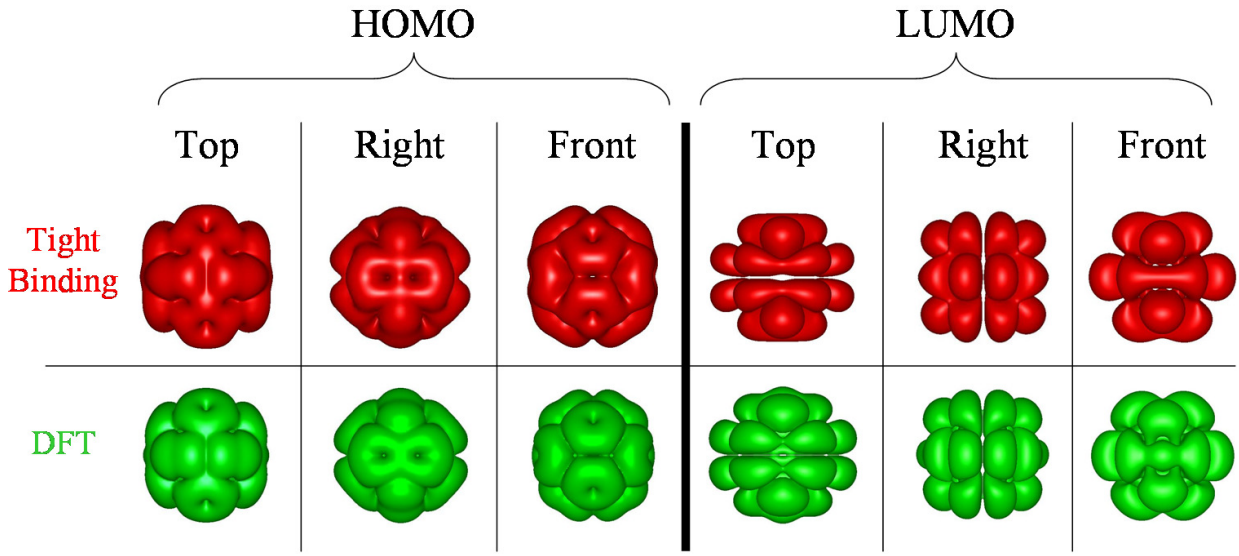

Figure 8.5: Comparison of the C_{60}^{4-} HOMO and LUMO wavefunctions calculated by tight binding and DFT. The HOMO wavefunctions is an isosurface plot of $\left|\psi_{\text{HOMO 1}}\right|^2 + \left|\psi_{\text{HOMO 2}}\right|^2$ while the LUMO wavefunctions are isosurface plots of $\left|\psi_{\text{LUMO}}\right|^2$.

The intermolecular hopping t_{HL} can be calculated from these expressions and from its

definition (equation (4.5))

$$\begin{aligned} t_{HL} &= \langle \psi_{\mathrm{HOMO}} | \Delta U | \psi_{\mathrm{LUMO}} \rangle \\ &= \Big\langle \sum_{i=1}^{60} a_i \phi_i \Big| \Delta U \Big| \sum_{j=1}^{60} b_j \phi_j \Big\rangle \\ &= \sum_{i,j=1}^{60} a_i^* b_j \langle \phi_i | \Delta U | \phi_j \rangle \\ &= \sum_{i,j=1}^{60} a_i^* b_j p_{ij} \; . \end{aligned}$$

The matrix element $p_{ij} = \langle \phi_i | \Delta U | \phi_j \rangle$ represents electron hopping between p_z orbitals on atoms i and j on neighboring C_{60} molecules. We take the following semi-empirical form for it [188]

$$p_{ij} = \begin{cases} V_0 \dfrac{r_{ij}}{d_0} e^{-(r_{ij}-d_0)/\lambda} & \text{for } 0 \le r_{ij} \le d_0, \\ 0, & \text{for } r_{ij} > d_0. \end{cases}$$

where $r_{ij} = |\vec{r}_i - \vec{r}_j|$, $\vec{r}_i$ is the position of atom i, $\lambda = 0.45\,\text{Å}$, $d_0 = 1.54\,\text{Å}$, $V_0 = 6.2\,\text{eV}$, and $d_c = 6.5\,\text{Å}$ [21].

The energy (8.1) was calculated between the two closest molecules in the unit cell of the $x = 4$ cross structure. We summed the contributions to the energy from the two HOMO wave functions. Energy from hopping between HOMO states of molecule 1 and the LUMO state of molecule 2 (figure 8.6) was summed with energy from hopping between HOMO states of molecule 2 and the LUMO state of molecule 1. $E_{\mathrm{LUMO}} - E_{\mathrm{HOMO}} = \Delta_{JT} + U = 200\,\text{meV}$ (the experimental HOMO-LUMO gap) was used. Molecule 1 was rotated in plane from the experimentally observed orientation by an amount $\Delta\theta_1$ and molecule 2 was rotated in plane from its experimentally observed orientation by $\Delta\theta_2$. The total virtual hopping energy of the two molecule system is plotted in figure 8.6 as a function of $\Delta\theta_1$ and $\Delta\theta_2$. $(\Delta\theta_1, \Delta\theta_2) = (0, 0)$ (the experimentally observed orientations) is found to be in the trough of a local minimum in energy, with a value of $-15\,\text{meV}$. This represents a significant energy gain for the cross-phase structure, and is much larger than the estimated quadrupole interaction ($\sim 1\,\text{meV}$). We take this level of agreement as an encouraging sign for the virtual hopping mechanism for orientational ordering.

In $K_{4+\delta}C_{60}$, the K-C_{60} interaction becomes important. The C_{60}^{4-} charge state seems more energetically favorable since the increase in K concentration causes the C_{60} packing density to increase over that of the more open K_4C_{60} cross phase, creating a C_{60}^{4-} charge state, even though more K atoms are present. The extra added K atoms reside in the C_{60}-voids created when the C_{60} molecules pack closer (figure 8.3). The new pinwheel ordering arises from this increase in C_{60} packing density. Adding K atoms to the K_4C_{60} ML thus has essentially the same effect as applying an external pressure, compressing the ML, which is a common

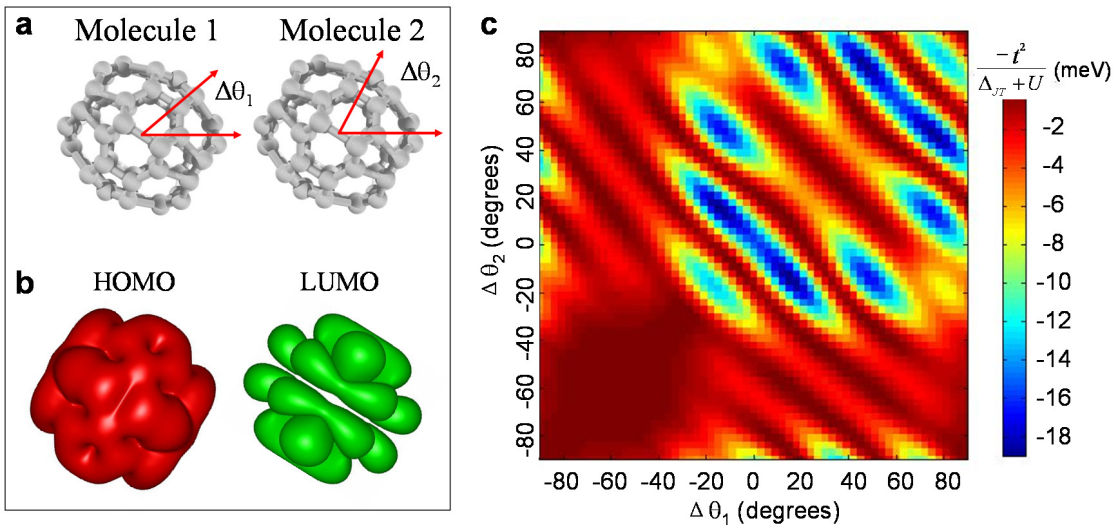

Figure 8.6: Tight binding calculations on C_{60}^{4-}. (a) Ball and stick model of the relative orientations of C_{60}^{4-} molecules observed experimentally. (b) HOMO and LUMO wavefunctions of C_{60}^{4-} from tight binding for the orientations of molecules shown in part (a). (c) Tight binding calculated $-t^2/(\Delta_{JT}+U)$ as a function of the angles $\Delta\theta_1$ and $\Delta\theta_2$ shown in part (a). $(\Delta\theta_1, \Delta\theta_2) = (0, 0)$ corresponds to the experimentally observed orientation.

driver for structural phase transitions.

8.5 Conclusions

We find that K_xC_{60} MLs undergo a metal-insulator-metal transition as x is varied from 3 to 5. Each electronic phase has a novel orientational ordering associated with it, including a highly complex, 7-sublattice pinwheel orientational structure in the insulating $K_{4+\delta}C_{60}$ phase and flower type of ordering in the $x = 3$ and 5 phases. Direct electron hopping or virtual electron hopping plays an important role in the orientational ordering of the phases and highlight the close interplay between orientational order and electronic structure in the fullerides.

9

Tuning Strong Correlations in K_xC_{60}

One type of many-body interaction, the electron-electron interaction, is relatively strong ($\sim 3\,\mathrm{eV}$) in C_{60} [3, 139]. Strong electron-electron interactions, also called *strong correlations*, can have a substantial affect on the properties of substances. For example, it is known that strong electron-electron interactions can cause a metal to become an insulator, known as a *Mott-Hubbard insulator* (§4.3).

The effects of electron-electron interactions are theoretically difficult to predict, and remain a subject of substantial research. Experiments where one can tune the strength of the interaction and analyze the resultant effects on the electronic properties of the system are of considerable importance to better understand both this interaction and many-body interactions in general. This chapter will discuss experimentally controlling the strength of the electron-electron interaction in K_xC_{60} multilayers on Au(111), and discuss how this leads to the transition of K_xC_{60} multilayers from metals to insulators. It addresses two of the principal topics in this dissertation: how do electron-electron and molecule-substrate interactions affect the properties of adsorbed molecules and molecular aggregates. Most of these results are presented in our published paper, ref. [198].

9.1 K_xC_{60} multilayers

The complexity of fulleride properties stems from the existence of many competing interactions, such as electron-electron repulsion, electron-vibration coupling and intermolecular electron hopping. The exact role of each interaction is controversial due to the difficulty of experimentally isolating the effects of a single interaction. Here, we isolate the effect of electron-electron interactions in K_xC_{60} ultrathin films experimentally through precise control of the layer thickness and accurate doping concentrations. We observe by STM a series of electronic and structural phase transitions as the fullerides evolve from two-dimensional monolayers to quasi three-dimensional multilayers. These results demonstrate the systematic evolution of fulleride electronic structure and molecular ordering by varying the K_xC_{60}

film layer thickness, and provide essential information about the electron-electron interactions in these systems.

Our experiments were conducted in UHV at $T = 7\,\mathrm{K}$ with a PtIr tip. C_{60} thin films with desired thickness were made by evaporating C_{60} molecules onto a clean Au(111) surface from a Knudsen cell evaporator (§5.4.1). Appropriate amounts of K atoms were dosed onto the C_{60} films from a SAES Getter (§5.4.3). The evaporation rates of the K and C_{60} evaporators were calibrated by depositing them separately onto a clean metal substrate, followed by directly counting the number of K atoms and C_{60} molecules per area in the STM images. This calibration was used to calculate the value of x in a K_xC_{60} multilayer. The K_xC_{60} thin films were annealed at 200°C for 20 minutes before being cooled to 7 K for the experiments. Progressive doping was obtained by adding more K atoms onto the existing film followed by re-annealing. We found that in the highly doped samples ($x > 4$), the K content may be decreased by 200°C annealing; therefore, a lower annealing temperature of 140°C was used in this regime to avoid K loss. dI/dV spectra were measured through lock-in detection (§2.4) of the a.c. tunneling current driven by a 450 Hz, 1–10 mV (rms) signal added to the sample bias with the feedback off.

The ability to tune interactions in the fullerides arises from our ability to grow well-controlled heterogeneous molecular films. Here, we describe measurements on K_xC_{60} ultra-thin films having variable thickness from one to three layers (layer index $i = 1$, 2, and 3) for four specific doping concentrations ($x = 0$, 3, 4, and 5). Figure 9.1a shows an STM topograph of a representative K_xC_{60} multilayer on Au(111) ($x = 4$ in this particular image), where the color scale highlights the different layer indices. Narrow slivers of C_{60}-free voids containing only K atoms (purple) exist between continuous patches of K_xC_{60}. Islands of second layer (blue) and third layer (red) K_xC_{60} can be seen residing on top of the first K_xC_{60} layer (green). The average layer thickness measured by STM is ~ 9.9 Å for K_xC_{60} ($x = 3$, 4, 5) while for C_{60} it is only 8 Å [59].

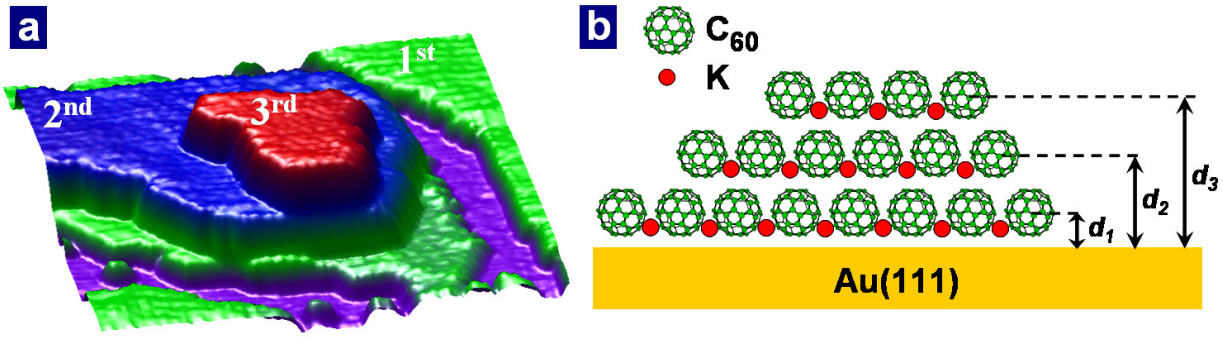

Figure 9.1: K_xC_{60} multilayer thin film on Au(111). (a) STM topograph of a K_xC_{60} multilayer thin film ($x = 4$ for this image) on Au(111) ($V = 1\,\mathrm{V}$, $I = 5\,\mathrm{pA}$). The C_{60}-free voids are purple, the first layer green, second layer blue, and third layer red. (b) Schematic side view of the multilayer (the actual position of the K atoms are unknown). The distances between the center of a C_{60} in each layer and the Au surface are d_1, d_2, and d_3.

We begin by describing our results for a C_{60} multilayer with no K (figure 9.2). dI/dV spectroscopy on the first layer shows the shoulder of the HOMO in the first layer around $-1.7\,\mathrm{V}$. This shoulder turns into a split peak centered at $-2.5\,\mathrm{V}$ for the second layer and $-2.7\,\mathrm{V}$ for the third layer. The LUMO of the first layer is centered around $0.8\,\mathrm{V}$. This peak increases to $1.5\,\mathrm{V}$ and $1.7\,\mathrm{V}$ in the second and third layers. Similarly the LUMO+1 peak increases in voltage, from $2.0\,\mathrm{V}$ to $3.0\,\mathrm{V}$ to $3.4\,\mathrm{V}$ for the first, second and third layers. The second and layers also show negative differential resistance (NDR) around $2.2\,\mathrm{V}$, but this is due to the voltage dependence of the tunneling barrier [59]. Topography on the first and second layer shows C_{60} molecules with various orientations.

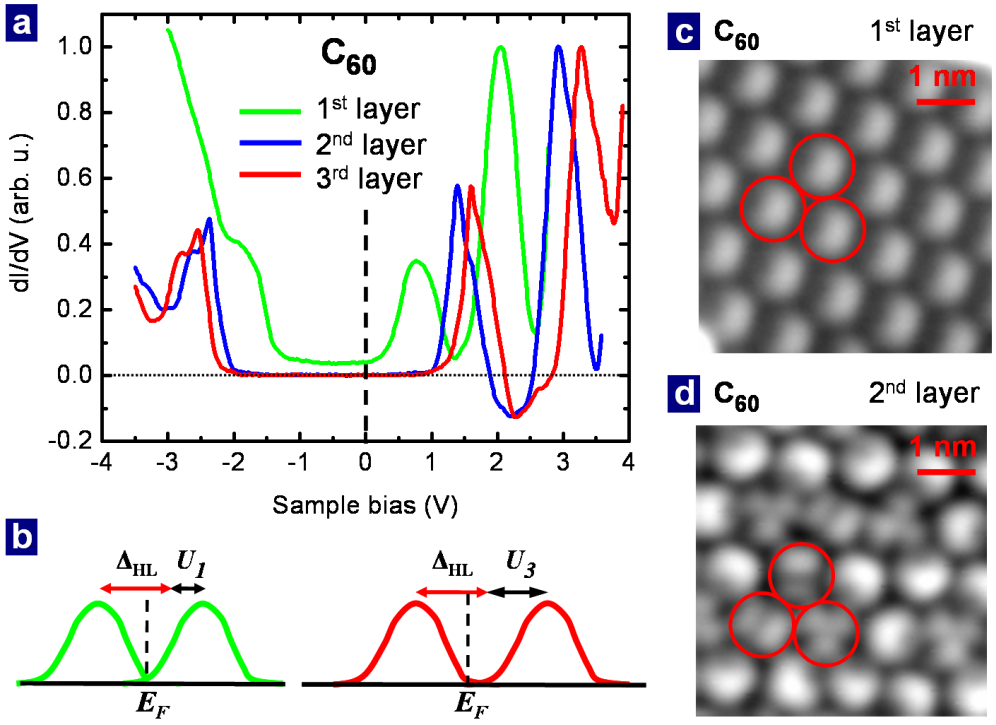

Figure 9.2: C_{60} multilayers on Au(111). (a) dI/dV spectroscopy on three different layers of C_{60} on Au(111). Each spectrum has been normalized so that the maximum dI/dV of the LUMO+1 is one. (b) Schematic diagram showing the STM measured HOMO-LUMO gap due to a combination of the real HOMO-LUMO gap Δ_{HL} and U. (c) Topography of the first layer showing a locally ordered area ($V = 2.8\,\mathrm{V}$, $I = 10\,\mathrm{pA}$). (d) Topography of the second layer showing more orientational variation ($V = 3\,\mathrm{V}$, $I = 10\,\mathrm{pA}$).

Next is the metallic K_3C_{60} multilayer system. Layer-dependent electronic structure in K_3C_{60} can be seen in figure 9.3a, which shows spatially averaged dI/dV spectra measured for three different layer indices. Within each layer, the spectrum is highly uniform with no sign of spatial inhomogeneity such as that found in the surface of bulk fullerides [177]. The first layer dI/dV exhibits a wide peak at the E_F, arising from the half filled LUMO-derived C_{60} band. In contrast, the second-layer spectrum shows a sharp dip at E_F, indicating the

emergence of an energy gap that tends to split the band in two. The gap-like feature persists in the third layer. The width of the gap-like feature (measured between adjacent local maxima) is $\sim 0.2\,\mathrm{eV}$, a much larger value than the superconducting gap $2\Delta_{SC} \sim 6\,\mathrm{meV}$ found in bulk K_3C_{60} (ref. [61]). The spectra at energies far above E_F, on the other hand, are nearly identical in all three layers. As these higher-energy features, such as the position of the LUMO+1 resonance, are sensitive to the doping level of K_xC_{60} (ref. [205]), this shows that there is no significant difference in K content for the different layers.

The orientational ordering of C_{60} molecules also changes markedly with layer index. The first layer of K_3C_{60} (figure 9.3c) exhibits a complex $\sqrt{3} \times \sqrt{3}$ superstructure of bright molecules having different orientations from their dimmer nearest neighbors [191]. However, in the second layer (figure 9.3d), C_{60} molecules form a very simple hexagonal lattice (lattice constant $a \sim 10.5\,\text{Å}$) with all molecules in the same orientation. The third-layer topograph (not shown) is the same as that of the second layer.

The insulating K_xC_{60} with $x = 4$ multilayer system exhibits a trend similar to K_3C_{60}. Figure 9.4a shows dI/dV spectra measured on a K_4C_{60} for layer indices $i = 1$ to 3. First layer spectra ($i = 1$) exhibit an insulating energy gap $\Delta \sim 0.2\,\mathrm{eV}$ that is induced by the molecular Jahn-Teller (JT) distortion [191]. As the layer index increases from i =1 to 3, the energy gap increases continuously (by layer 3, the gap has well-defined edges and a flat bottom). The gap widths observed here are estimated to be $\Delta \sim 0.6\,\mathrm{eV}$ and $0.8\,\mathrm{eV}$ for layers 2 and 3 respectively. As seen in the metallic $x = 3$ system, the geometric structure of the insulating $x = 4$ system simplifies as the layer index is increased. Complex 'cross-phase' orientational ordering observed in the K_4C_{60} first layer [191] (figure 9.4c) evolves to a much simpler hexagonal lattice (figure 9.4d) for higher layers. Layers 2 and 3 for the $x = 4$ film exhibit featureless C_{60} molecules with little discernible orientational ordering.

As doping is increased to $x = 5$, K_xC_{60} multilayers show metallicity for layer 1 (ref. [197]) and an evolution to insulating behavior by layer 3. At this doping level, the upper JT-split LUMO is only partially filled and the first-layer spectrum (figure 9.5a) exhibits a finite (although suppressed) electronic DOS at E_F. The DOS at E_F is suppressed further in the second layer, and develops into a pronounced energy gap $\Delta \sim 0.4\,\mathrm{eV}$ by the third layer. As with the $x = 3$ and $x = 4$ doping levels, complex structural ordering in the first layer of K_5C_{60} (the 2×2 superstructure in figure 9.5c) evolves into a much simpler hexagonal lattice in the second layer (figure 9.5d) and third layer (not shown).

9.2 Electron screening

Taken collectively, the experimental results clearly show that, for a fixed doping level, increasing film thickness suppresses metallicity and enhances the insulating tendency of K_xC_{60} thin films on Au(111). We propose that this trend arises from electron-electron Coulomb repulsion, characterized by the Hubbard U (§4.3). In fullerides, U is of the same order as the narrow bandwidth W (ref. [62]). The fullerides thus exist at the verge of a Mott insulator phase transition (§4.3) and small perturbations to the strength of U may significantly

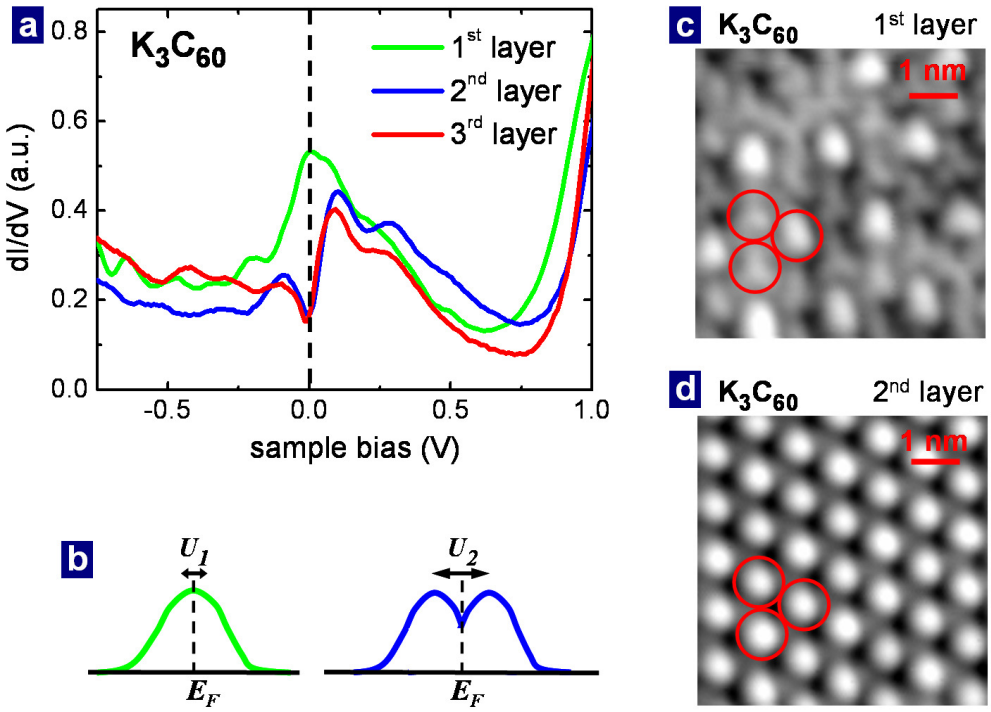

Figure 9.3: Electronic and structural properties of K_3C_{60} multilayers on Au(111). (a) Spatially averaged dI/dV spectra measured on three different layer indices of K_3C_{60}. The first-layer spectrum has a peak at E_F, whereas the second- and third-layer spectra show a sharp dip having a width of $\sim 0.2\,\text{eV}$. (b) Schematic diagram showing the effect of the Hubbard U on the electronic structure of K_3C_{60}. A small U_{eff} in the first layer (left) has negligible effect on the DOS, but a larger U_{eff} in higher layers (right) causes a dip around E_F. (c) K_3C_{60} first-layer topograph ($V = -0.1\,\text{V}$ and $I = 20\,\text{pA}$) shows a $\sqrt{3} \times \sqrt{3}$ superstructure. Each red circle represents one C_{60} molecule. (d) Topograph of the second layer ($V = -0.1\,\text{V}$ and $I = 10\,\text{pA}$) shows a simple hexagonal lattice with no superstructure.

alter their electronic ground state [28, 127, 64, 46, 68]. The metal to insulator transition observed here can be shown to result from changes in U caused by changes in the local screening environment.

Electron screening or *screening* refers to the attraction of positive charges around electrons in a material. Since positive charges attract other electrons, their presence around electrons reduces the electrostatic repulsion between electrons in the material. We now examine the effect of screening on electron-electron interactions in K_xC_{60} molecular films. For an isolated single C_{60} molecule, the bare Hubbard U (denoted by U_0) has been estimated to be approximately 3.0 eV (refs. [35, 3, 139, 125]). When C_{60} molecules form a solid, the value of U can be greatly reduced by screening from neighboring molecules. In our K_xC_{60} multilayers, screening originates from three distinct sources: the metal substrate, surrounding polarizable molecules, and itinerant charge carriers.

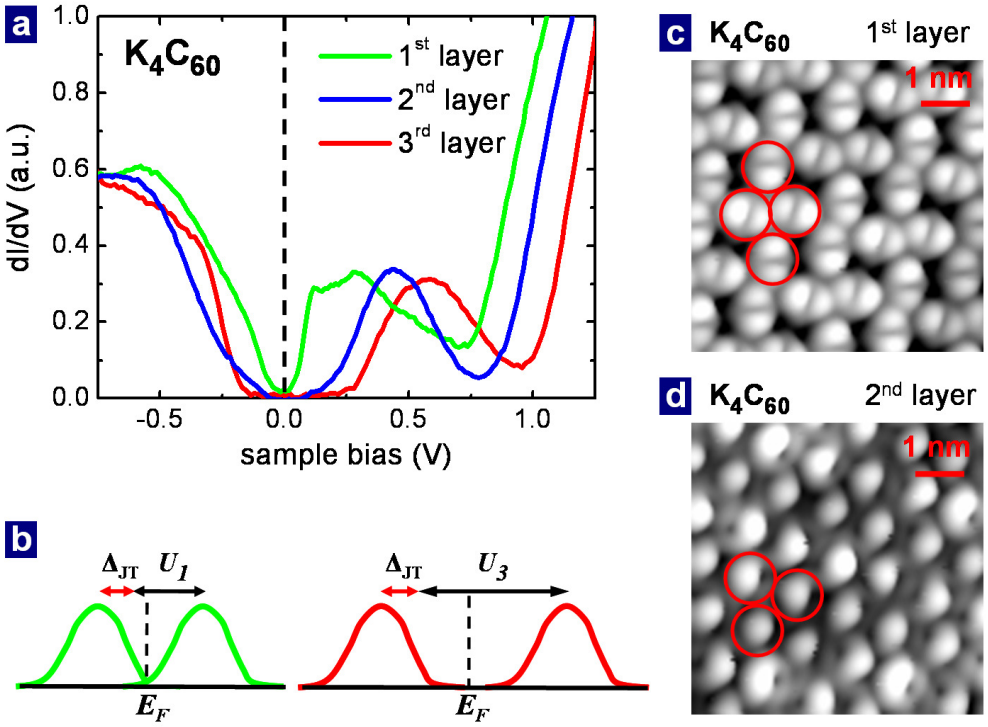

Figure 9.4: Electronic and structural properties of K_4C_{60} multilayers on Au(111). (a) dI/dV spectra of the JT-insulating K_4C_{60} measured on three different layers. The observed gap Δ increases from 0.2 eV in layer 1 to 0.6 eV and 0.8 eV in layers 2 and 3. (b) Schematic DOS of K_4C_{60}. Larger U_{eff} in layer 3 (right) leads to a much wider gap than that in layer 1 (left). (c) Topograph of K_4C_{60} layer 1 ($V = -0.2$ V and $I = 10$ pA) shows a 'cross'-like orientational ordering. (d) Topograph of K_4C_{60} layer 2 ($V = -0.4$ V and $I = 10$ pA) shows a simple hexagonal lattice with orientational ordering different from that of layer 1.

The first two screening mechanisms can be treated using simple electrostatics. As discussed by Hesper et al. [80], the change in U due to a nearby metal can be modeled using an image charge potential as

$$\delta U_S = \frac{1}{4\pi\epsilon_0}\frac{e_c^2}{2d} \tag{9.1}$$

where d is the distance from the center of a C_{60} molecule to the metal substrate (figure 9.1b) and e_c is the magnitude of the electron charge. The screening from nearby polarized molecules, which arises from induced molecular dipole moments, can be expressed as the electrostatic energy of two dipoles

$$\delta U_P = \frac{1}{4\pi\epsilon_0}\frac{z\alpha e_c^2}{R^4} \tag{9.2}$$

where z is the number of nearest neighbors, α is the molecular polarizability, and R is the

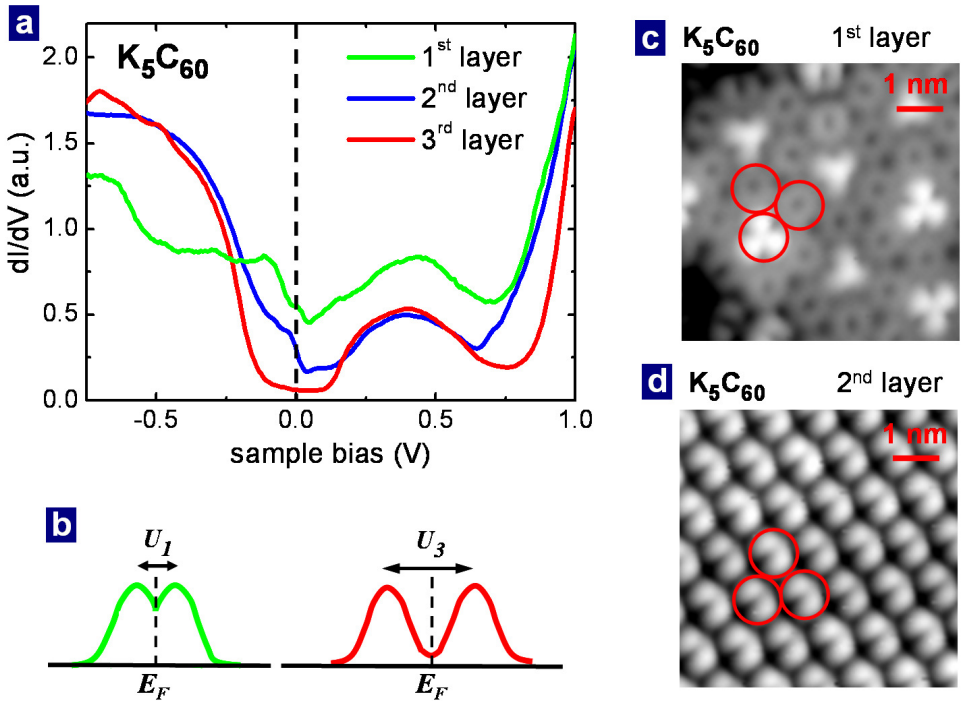

Figure 9.5: Electronic and structural properties of K_5C_{60} multilayers on Au(111). (a) dI/dV spectra of K_5C_{60} measured at three different layer indices. (b) Schematic electronic structure of K_5C_{60}. In layer 1 (left), U_{eff} causes a small suppression of DOS near E_{F}, but in layer 3 (right), the larger U_{eff} induces an energy gap around E_{F}. (c) Topography of layer 1 ($V = -0.2\,\text{V}$ and $I = 5\,\text{pA}$) shows complex orientational ordering with a 2×2 superstructure. (d) K_5C_{60} layer 2 shows a simpler hexagonal lattice ($V = +0.2\,\text{V}$ and $I = 5\,\text{pA}$).

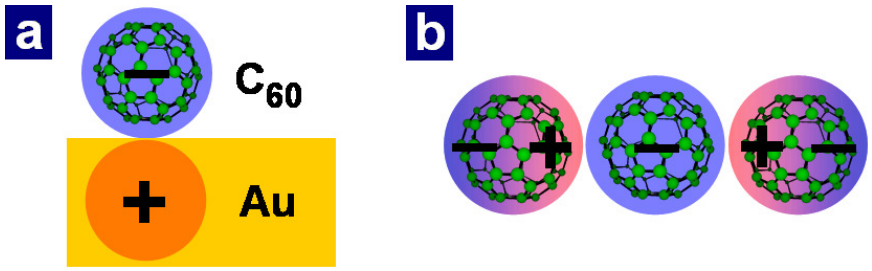

Figure 9.6: Screening of U. (a) Screening from the metallic substrate arising from the formation of an image charge. (b) Screening from neighboring molecules arising from the molecular polarization.

intermolecular distance [125]. The third mechanism, the change in U by itinerant electrons (δU_e), depends sensitively on the doping concentrations of the fullerides and is a more complex term [3, 139, 164, 118, 143]. The total change in the isolated molecule U_0 due to the molecular environment is the sum of the three terms:

$$\delta U = \delta U_S + \delta U_P + \delta U_e \tag{9.3}$$

and $U_{\text{eff}} = U_0 - \delta U$ is the final effective Hubbard U in the K_xC_{60} multilayer system. These relations show how varying the number of layers in our K_xC_{60} ultrathin films can provide a systematic technique to control electron-electron interactions (U_{eff}) by changing both the distance to the metal substrate (d) and the number of nearest neighbors (z).

This is seen most clearly in the insulating K_4C_{60} multilayers. The K_4C_{60} monolayer was found to be an insulator [191] since the strong Jahn-Teller effect at filling level $x = 4$ splits the degenerate C_{60} LUMO states and opens an energy gap in the DOS at E_F (figure 3b; ref. [69]). This implies $U_e = 0$ since there are no itinerant charge carriers. Assuming that the Jahn-Teller splitting remains unchanged with varied layer index, the layer dependence of U_{eff} in K_4C_{60}, and hence the layer dependence of the gap in the DOS around E_F (§3.4.2), is accounted for completely by equations (9.1) and (9.2). As the layer index increases from $i = 1$ to 3, δU_S (substrate screening) decreases from 1.5 eV to 0.3 eV according to equation (9.1). In contrast, z increases from 6 in the first layer to 9 for both the second and third layer (for molecules not at the edge of a layer), causing δU_P to increase from 0.6 eV to 0.9 eV via equation (9.2) (here we use $\alpha = 90\,\text{Å}^3$, the value for undoped C_{60}) [74]. The total reduction in U_{eff} due to screening (equation (9.3)) is thus $\delta U = 2.1$, 1.4 and 1.2 eV for $i = 1$, 2 and 3, respectively, leading to an increase in U_{eff} from 0.9 eV to 1.8 eV as i increases from 1 to 3. The calculated relative increase of U_{eff} by 0.7 eV (from $i = 1$ to 2) and 0.2 eV (from $i = 2$ to 3) is in reasonable agreement with the relative increase of the experimentally observed gap by 0.4 eV (from $i = 1$ to 2) and 0.2 eV (from i = 2 to 3). This agreement becomes much better if we use a larger α value for K_4C_{60} (a reasonable assumption). We note that some factors, such as screening from the STM tip, the effect of intermolecular electron hopping on the bandwidth, and correlations between different screening mechanisms are not

included in our simple phenomenological model. Nevertheless, the agreement between the observed experimental trend and the semi-quantitative analysis demonstrates that stronger electron-electron interactions in higher layers is responsible for the observed layer-dependent increase of gap in K_4C_{60}.

The electronic behavior of the K_3C_{60} multilayers is quite different from the insulating K_4C_{60} multilayers above due to itinerant charge carriers. The Jahn-Teller effect is much weaker at an uneven filling level $x = 3$, leading to a metallic ground state in bulk K_3C_{60} (refs [68, 69]) and itinerant charge carriers. In K_3C_{60} multilayers, the itinerant electron screening term (δU_e) becomes important, although the layer dependent DOS is still caused by layer dependence in U. How to determine the itinerant electron screening contribution to the renormalized U_{eff} in K_3C_{60} is quite controversial [62, 3, 164, 143]. Various theoretical calculations in bulk K_3C_{60} ($z = 12$) produce a combined screening strength ($\delta U_e + \delta U_P$) that ranges widely from 2.2 to 3.2 eV (refs [62, 118]). Using a mean value of $(\delta U_e + \delta U_P) = 2.7$ eV, and including Au(111) substrate screening (δU_S) through equation (9.1), we find that the effective U becomes $U_{\text{eff}} = U_0 - \delta U = 0.2$, 0.5, and 0.7 eV for $i = 1$, 2 and 3. However, note that since K_3C_{60} is metallic, the lower layers act as a metal substrate for the higher layers, so the distance of a C_{60} molecule to the metal substrate is no longer the distance to the Au(111) surface. This means that the substrate screening should be the same in the second and third layers since the distance to the metallic K_3C_{60} layer directly below them is the same. For $i = 1$, U_{eff} is too small compared with the bandwidth W to open a gap, whereas in layers 2 and 3, we expect a small gap of the same magnitude to begin opening as U_{eff} becomes comparable to W (figure 9.3b). This explains the appearance of the gap-like structure in the K_3C_{60} LDOS in figure 9.3a.

K_5C_{60} is an intermediate case between K_4C_{60} and K_3C_{60}. It is not insulating like K_4C_{60}, but it is not as good of a metal like K_3C_{60}. Here, the odd doping level makes the Jahn-Teller effect is weaker than in K_4C_{60}, and hence it is not insulating [69], but the high doping level also makes the effective bandwidth narrower than in K_3C_{60}, making it less metallic [111]. We thus expect the layer-dependent U_{eff} for K_5C_{60} to lie between the two extremes. This is indeed the case, as we see a relatively small suppression of electronic DOS in layer 1 (figure 9.5a), but by layer 3, a well-defined gap of width $\Delta \sim 0.4$ eV has emerged. This gap is about 0.4 eV smaller than that of the $i = 3$ layer in K_4C_{60}, (due to the reduced Jahn-Teller effect and enhanced metallic screening), while it is about 0.2 eV larger than the gap observed in the $i = 3$ layer of K_3C_{60} (due to the narrower bandwidth in K_5C_{60}).

9.3 Orientational ordering

The layer-index-dependent change in ordering seen for the three doping levels ($x = 3$, 4, and 5) as the index increases above $i = 1$ is less a direct result of electronic screening and more likely due to substrate-molecule interactions and intermolecular electron hopping via the overlap of molecular orbitals [22, 197, 63]. The complex structures found in layer 1 of K_xC_{60}, $x = 3$–5 (figures 9.3c, 9.4c and 9.5c) are characteristic of geometric frustration of

molecular orientational ordering in a two-dimensional (2D) lattice [171]. As the layer index is increased, the lack of interaction between the molecules and the Au(111) substrate, as well as further interaction with adjacent C_{60} molecules in the lower layers leads to quasi-3D-like intermolecular interactions. This creates a more isotropic local molecular environment and creates less geometric frustration, limiting the possibility of exotic molecular ordering. Therefore, the much simpler and more homogeneous spatial structures found in the higher layers of K_xC_{60} (figures 9.3d, 9.4d, and 9.5d) can be seen as a natural consequence of reduced frustration due to dimensional crossover from the 2D limit to the quasi-3D bulk regime.

9.4 Conclusions

Using accurately fabricated K_xC_{60} ultrathin films, we have demonstrated how electron correlation strength, a key factor in determining the properties of fullerides, can be experimentally controlled by varying the thickness of the layers and doping level. These results support the notion of tuning molecular electronics by controlling the layer structure and distance to metal contacts, and opens new routes towards engineering novel molecular devices and controlling electronic phases in strongly correlated molecular materials.

10

Mapping Electron-Vibration Coupling in Gd@C_{82}

Modification of fullerenes can be achieved by exohedral doping, such as in the K_xC_{60} experiments presented in the previous chapters, but can also be done endohedrally. The fullerene C_{82} with D_{2h} symmetry with a Gd atom inside, called Gd@C_{82}, is such an endohedral fullerene.

Gd@C_{82} should have a net spin due to charge transfer from the Gd atom to the C_{82} [52, 128, 106]. However, in our STM experiments on this molecule, we were not able to see any magnetic effect. Instead, we imaged the molecular orbitals and saw a C_{82} vibrational mode in IETS, as well as mapped out the spatial distribution of the IETS signal, which is also an important result. Comparison of DFT calculated electron-vibration coupling to the STM measured IETS shows that one vibrational mode of C_{82} dominates the IETS spectrum. The spatial distribution of the IETS signal is very inhomogeneous, and shows that the strongest IETS signal occurs where the LUMO wavefunction is modified the most due to the vibration, and not where the vibration has its largest amplitude of vibration (§2.6). This study verifies that the d^2I/dV^2 map is a map of electron-vibration coupling when the IETS signal arises from a molecular vibration. These results help us answer one of the fundamental questions in this dissertation: how do electron-vibration interactions affect molecular properties. Most of this work is based on our published paper, ref. [58].

The substrate used for the experiments was Ag(001) and the STM tip was W or PtIr. The surface was cleaned by sputtering and annealing (§5.3). The Ag substrate was then cooled to $\sim 80\,\mathrm{K}$ prior to depositing Gd@C_{82} onto the surface. The Gd@C_{82} molecules were synthesized by H. Kato and H. Shinohara. A small amount of C_{60} was simultaneously deposited with Gd@C_{82}. The Gd@C_{82} and C_{60} molecules were deposited from a Knudsen cell evaporator (§5.4.1) onto the Ag surface and the Ag substrate was placed into the 7 K STM. All sample preparation was done in UHV and experiments performed at 7 K. Over 50 Gd@C_{82} molecules were studied.

Figure 10.1 shows a typical STM image of two Gd@C_{82} molecules next to a C_{60} molecule. The C_{60} molecule was used as a reference to check the condition of the STM tip. Reproducible topographs and spectra on Gd@C_{82} molecules were achieved only when the same

tip gave C_{60} topographs and spectra similar to those in [129]. The spectroscopy and dI/dV maps taken on Gd@C_{82} can be found in [58].

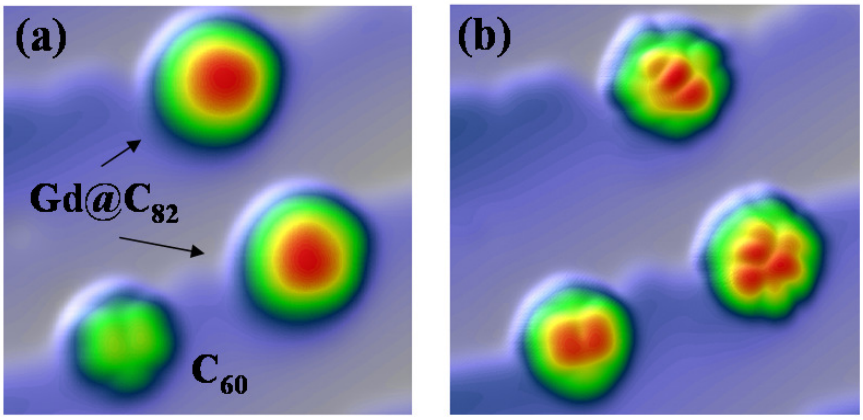

Figure 10.1: Constant current topographs (65 Å × 65 Å) of two Gd@C_{82} and a C_{60} molecule at step edges on Ag(001). (a) $V = 2.0\,\mathrm{V}$, $I = 1\,\mathrm{nA}$ and (b) $V = 0.1\,\mathrm{V}$, $I = 1\,\mathrm{nA}$.

d^2I/dV^2 spectra (figure 10.2 were obtained in the $\pm 100\,\mathrm{mV}$ range by numerically differentiating dI/dV spectra taken in the same voltage range. The d^2I/dV^2 spectrum on Gd@C_{82} reveals three main inelastic peaks at 43, 60, and 70 mV ($\pm 1\,\mathrm{mV}$) not present on the Ag(001) surface.

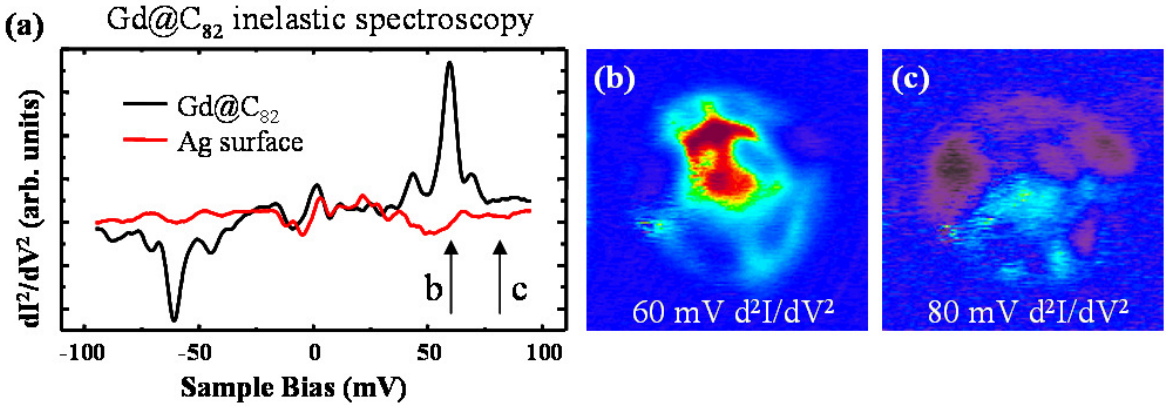

Figure 10.2: Inelastic spectroscopy on Gd@C_{82}. (a) d^2I/dV^2 measured on Gd@C_{82} as well as on the Ag surface. (b) d^2I/dV^2 map of Gd@C_{82} at $V = 60\,\mathrm{mV}$. (c) d^2I/dV^2 map taken at $V = 80\,\mathrm{mV}$.

d^2I/dV^2 maps taken at the voltage of the largest peak (60 mV) reveals the spatial localization of the inelastic signal (figure 10.2b). This image shows that the strongest d^2I/dV^2 signal (red region) occurs only on one small area of the molecule. A second d^2I/dV^2 map taken at 80 mV does not show the same features, indicating that the features seen in the

Gd@C_{82} d^2I/dV^2 map are due solely to the IETS signal and not other factors, such as tip trajectory.

It is unexpected that the main Gd@C_{82} vibrational mode produces such a spatially localized IETS signal, since molecular vibrations tend to be more delocalized. IETS images of simpler molecules, such as acetylene [182] and oxygen [67], typically reflect the spatial extent of the measured vibrational modes. In order to understand the localized behavior seen here, the inelastic theory presented in §2.6 combined with density functional theory was used. The calculations were done by K. H. Khoo in Steven G. Louie's group.

The details of the calculation are described in [130]. To simplify the computation, calculations on a free C_{82} with no interior Gd atom were done. Only the charge transfer from Gd to C_{82} was considered. Neglecting the inner Gd atom is justified by noting that (1) electronic cage states near E_F are only weakly perturbed by the inner atom [128, 178] and (2) our observed vibrational energies are in the range of bare C_{82} vibrational energies, indicating that C_{82} phonons are responsible for the inelastic signal [114]. Hence, the presence of the Gd atom should be only a small perturbation of C_{82} vibrations in our energy range. Charge transfer to the C_{82} cage from the Gd atom and substrate was treated as a single fitting parameter. The best theoretical fits were obtained for a molecular charge state of $-4.01 \approx -4$. This, as well as the molecular orientation on the surface, was determined by comparison of STS spectra, dI/dV maps, and electronic wavefunction symmetries. The charge state determines which molecular state is at E_F. The -4 charge state is reasonable since Gd is known to donate three electrons to the C_{82} cage [153] and Ag substrates are expected to donate charge to fullerenes [130].

The theoretical vibrational spectrum for an isolated C_{82}^{4-} is shown in figure 10.3(a), with each vibrational mode shown as a black vertical line. The theoretical d^2I/dV^2 as a function of energy (red lines) was obtained by calculating the electron-vibration coupling of each molecular vibrational mode to the C_{82} electronic states at E_F using equation 2.10. Only a few of the vibrational modes in this energy window show appreciable coupling to the C_{82} state at E_F, and in particular, there is one dominant mode, similar to the experimental d^2I/dV^2 where one vibrational mode dominates the spectrum. The relative strength of the electron-vibration coupling of these modes is in reasonable agreement with the experimental d^2I/dV^2 spectrum and indicates that the C_{82} mode with the theoretical energy of 52 meV is responsible for the dominant experimental inelastic tunneling channel.

To understand the origin of the spatial localization of the d^2I/dV^2 signal, the spatial dependence of the electron-vibration coupling for the 52 meV mode was calculated using equation (2.11). A simulated STM constant current surface was used, as in [129]. The resulting theoretical d^2I/dV^2 map shown in figure 10.3(b) shows that the strongest d^2I/dV^2 signal (red region) is localized to the upper half of the molecule, in good agreement with the experimental d^2I/dV^2 map [figure 10.2(b)]. The small deviation between calculated and experimental vibrational energies is likely due to effects of the substrate [108] and inner atom [106], which were not directly included in the calculation; they were only used to determine the charge state of C_{82}. However, the general agreement between theory and experiment suggests that these effects do not strongly influence the qualitative behavior of

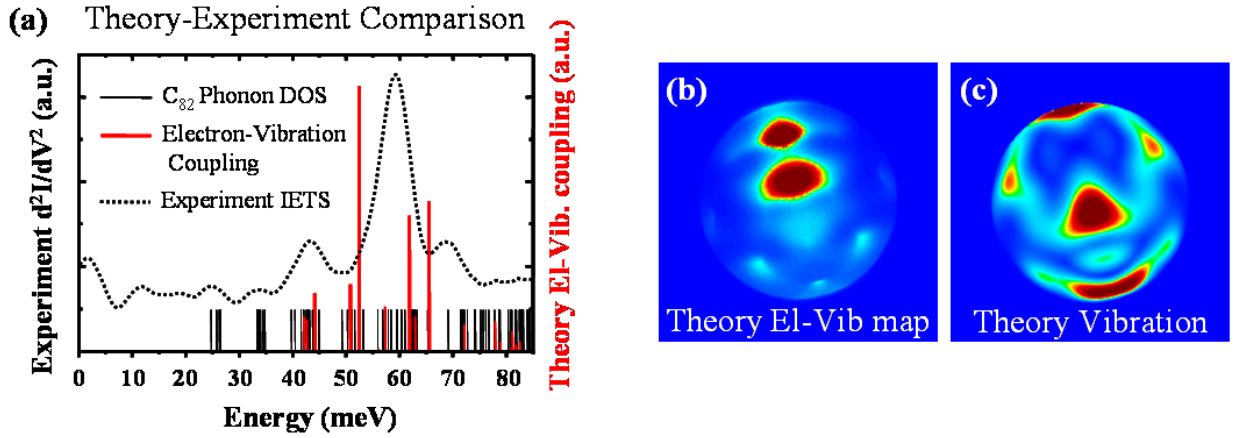

Figure 10.3: Gd@C_{82} theory. (a) DFT calculated vibrational mode energies (black lines) and strength of the electron-vibration coupling (red lines). The experimental d^2I/dV^2 curve (dashed) is shown for comparison. (b) DFT calculated spatial distribution of the electron-vibration coupling of the 52 meV vibrational mode to simulate an experimental d^2I/dV^2 map. Red = large electron-vibration coupling, blue = small. (c) Magnitude of the atomic displacements for the DFT calculated vibrational mode at 52 meV which has the largest electron-vibration coupling. Red = large atomic displacement, blue = small.

electron-vibration coupling in Gd@C_{82}.

When we compare the spatial dependence of the molecular electron-vibration coupling at 52 meV with the spatial distribution of atomic displacement magnitudes for the C_{82} vibrational mode at 52 meV [figure 10.3(b) vs figure 10.3(c)], we see that regions of large atomic displacement (red regions) are nearly anti-correlated with the regions of large d^2I/dV^2 (red regions). This occurs since the spatial distribution of inelastic tunneling is determined by the amount electronic wave functions change due to molecular vibrations (§2.6). Regions where the wavefunction changes the most will have the largest inelastic tunneling signal and these regions need not be where the atoms have the largest displacement. This can produce a surprising localization in the inelastic tunneling, as seen in Gd@C_{82}. Localization may explain the larger number of vibrational modes detected in molecular film transport measurements compared to IETS measurements. Molecular films contain a large number of molecular configurations and transport measurements on such films are thus more likely to average over many configurations with the resulting inelastic signal containing vibrational signals due to many different parts of the molecule.

In this chapter, we have demonstrated how IETS can be used to spatially map the strength of the electron-vibration interaction of a single molecule. By using DFT, we found that the strong localization of the electron-vibration interaction can be explained by changes in the LUMO wavefunction due to the oscillation of a vibration. The parts of the LUMO wavefunction which change the most due to a particular vibrational mode will show the strongest IETS signal. For this particular molecule, Gd@C_{82}, it was also found that the

inner Gd atom did not significantly affect the electron-vibration coupling.

11

Electronic Properties of Molecular Diamond

sp^2 bonded carbon molecular materials have unique and useful properties due to the influence of delocalized π-bond networks, as demonstrated in the previous chapters. Here we describe our studies of sp^3-bonded carbon molecular structures, where novel behavior arises from a very different source: tetrahedrally arranged carbon σ-bonds. These molecules are nanometer-sized pieces of diamond with dangling bonds terminated with hydrogen, and are called diamondoids. There are many types of diamondoids; the one we studied is called [121]tetramantane. Figure 11.1a has a ball and stick model of this molecule. The [121]tetramantane diamondoid studied here consists of four diamond cages face-fused into a straight rod with a chemical formula $C_{22}H_{28}$ (ref. [36]). The 28 surface dangling carbon bonds are all saturated by hydrogen atoms.

In this chapter, the atomic-scale properties of tetramantane will be investigated. In the sp^3 bonded tetramantane, we find a number of differences from the sp^2 bonded fullerenes. The topographs of tetramantane were almost featureless at negative biases while they showed much structure at positive biases, unlike fullerenes which show topographic features at both polarities. This difference was directly due to the sp^3 bonding: the HOMO orbital is localized between atoms and is difficult to image since the STM tip is a few Ångstroms above the molecule, while the LUMO orbital extends very far away from the molecule and contains much structure due to the CH_2 bonds that do not exist in fullerenes. The spectroscopy on tetramantane showed no resonances (unlike fullerenes which show many resonances), which is due to the large gap in sp^3 bonded materials, as well as the localization of the HOMO between atoms in sp^3 bonded materials. However, like $Gd@C_{82}$, there was strong electron-vibration coupling in tetramantane which was spatially localized. These results will help us understand two main topics of this dissertation: how do electron-vibration and molecule-substrate interactions affect molecular properties? Most of the results presented in this chapter are based on our published paper, ref. [196].

The molecules were provided by Jeremy E. Dahl and Robert M. K. Carlson at Chevron Technology Ventures. The [121]tetramantane molecules were extracted from petroleum and isolated and purified to a white crystalline powder with purity greater than 99% by

weight. Purification procedures included distillation, thermal processing and both size- and shape selective high-performance liquid chromatography, as described in [37]. Tetramantane molecules were thermally evaporated from a Knudsen cell evaporator (§5.4.1) onto a clean Au(111) substrate held at room temperature in ultrahigh vacuum. The sample was then placed into the STM at $T = 7\,\mathrm{K}$ and all data was taken at that temperature. Topography was performed in constant-current mode, and dI/dV spectra and images were measured through lock-in detection of the a.c. tunneling current driven by a 450 Hz, 1-10mV (rms) signal added to the sample bias (§2.4). The molecular manipulation method used here is the 'sliding' technique [42], with typical manipulation parameters $V = 5\,\mathrm{mV}$ and $I = 1\,\mathrm{nA}$.

11.1 Tetramantane Electronic Structure

Tetramantane self assembles into an ordered overlayer on Au(111). Figure 11.1b shows an STM topograph taken of a sub-monolayer of tetramantane on Au(111) where the oval-shaped tetramantane molecules form a close-packed structure with lattice constants $11.4\,\mathrm{Å} \times 8.3\,\mathrm{Å}$ (see red arrows) and an apparent height of $3.3\,\mathrm{Å}$. The Au(111) surface herringbone reconstruction has negligible effect on the molecular ordering. Long-range ordering at room temperature implies high molecular mobility and weak bonding between the diamondoids and the Au(111) surface.

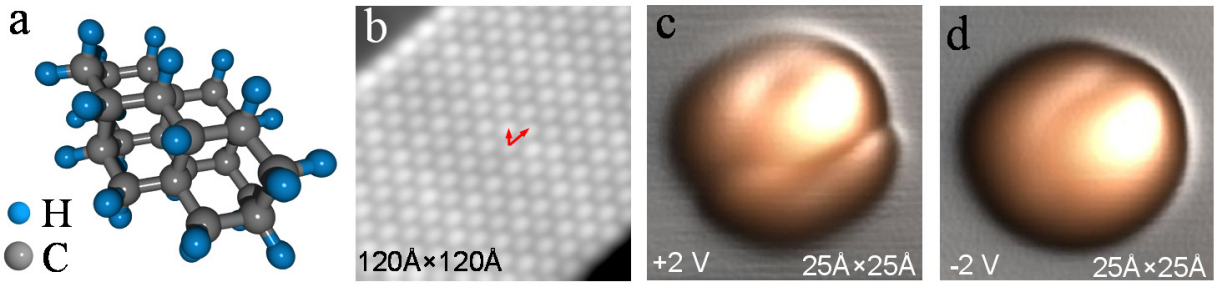

Figure 11.1: (a) Ball and stick model of [121]tetramantane. (b) Ordered layer of tetramantane on Au(111). (c) individual tetramantane at $-2\,\mathrm{V}$ and (d) same molecule at $V = +2\,\mathrm{V}$.

To study single isolated molecules, individual tetramantane diamondoids were manipulated from the edge of an island onto an empty Au(111) terrace at $T = 7\,\mathrm{K}$ using the STM tip (ref. [42]). Figures 11.1c,d show STM topographs of the same individual diamondoid taken with different sample biases. The image taken at sample bias $V = +2\,\mathrm{V}$ (figure 11.1c), shows pronounced line nodes across the molecular surface, while the image taken at $V = -2\,\mathrm{V}$ (figure 11.1d) is smoother, showing a much weaker spatial dependence of the occupied electronic states.

Individual tetramantane molecules were found to have a number of different orientations on Au(111). Figure 11.2a shows STM topographs of three individual tetramantane molecules on Au(111) with different orientations, as seen by the different line node patterns.

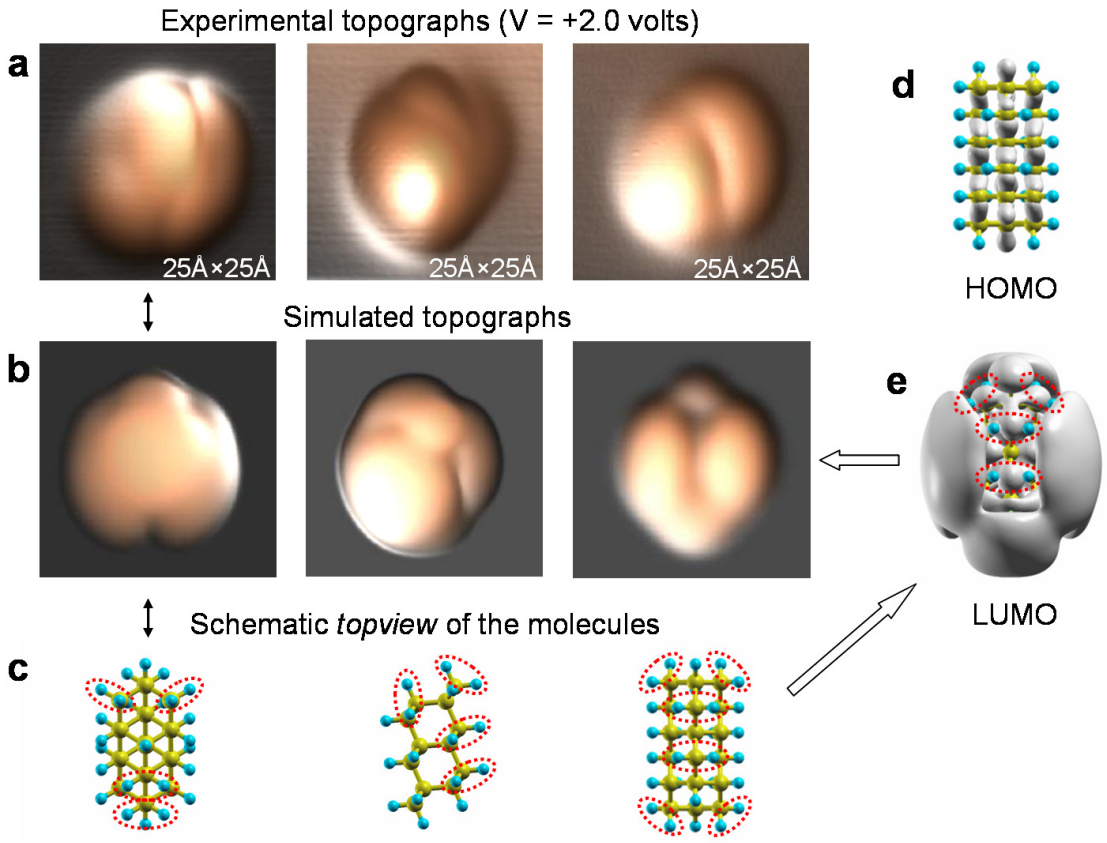

Figure 11.2: (a) Experimental topographs of three different orientations of individual tetramantane molecules on Au(111). (b) DFT simulated topographs of the same three orientations shown in (a). (c) Ball and stick models corresponding to the topographs shown in (b). (d) DFT calculated HOMO and (e) DFT calculated LUMO. The values of the isosurfaces are the same for both states.

Figure 11.3 shows that individual tetramantane molecules can be switched between different orientations by dragging and rotating the molecules with the STM tip.

STS was used to examine the local electronic properties of tetramantane. Figure 11.4a shows the dI/dV spectrum of the bare Au(111) substrate (black curve), the spatially averaged dI/dV spectrum of an individual tetramantane molecule on Au(111) (green curve), and the difference between these two spectra (red curve). The red curve shows that the diamondoid makes a small contribution to the total surface electronic LDOS. The molecular electronic LDOS (red curve) is quite low in the energy range from -2.5 eV to $+2.5$ eV, consistent with an insulating ground state having an energy gap > 5 eV around E_F (refs [40, 203, 202]). Although no sharp resonances related to the HOMO or the LUMO were observed, the gentle increase of subtracted dI/dV (red curve) above E_F may represent the end of a broad resonance arising from hybridization between the LUMO and the Au states.

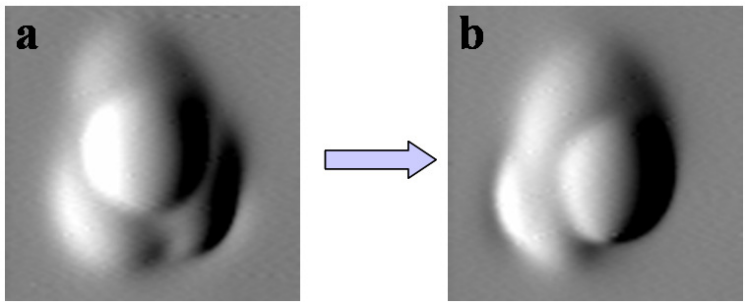

Figure 11.3: Constant current topographs showing the same individual tetramantane molecule (a) before and (b) after rotation with the STM tip. The images have been differentiated in the horizontal direction.

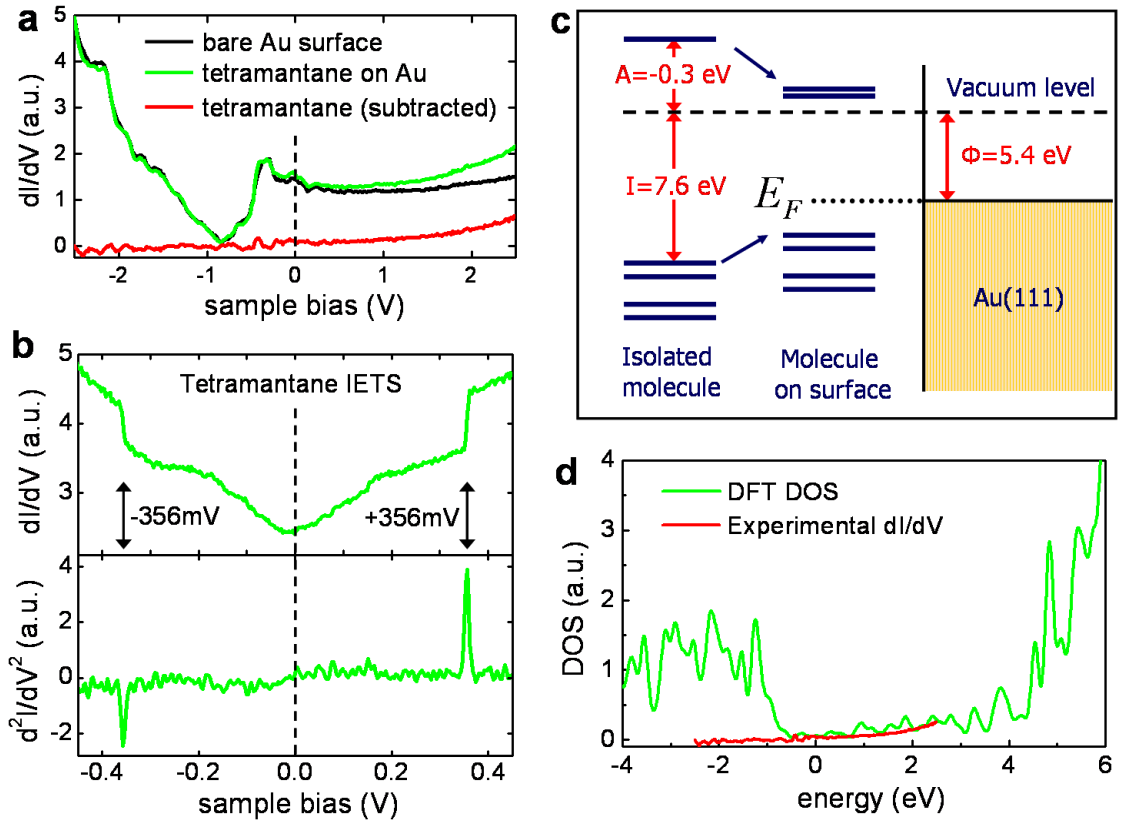

Figure 11.4: (a) dI/dV Spectroscopy of tetramantane in a $\pm 2.5\,\mathrm{V}$ range shows no features different from spectroscopy on Au(111). (b) dI/dV spectroscopy in a $\pm 450\,\mathrm{mV}$ range shows inelastic features at $\pm 356\,\mathrm{mV}$ which can be seen as a dip at $-356\,\mathrm{mV}$ and a peak at $356\,\mathrm{mV}$ in d^2I/dV^2. (c) DFT calculations of the energy levels of tetramantane. (c) Tetramantane DFT DOS compared with the experimental LDOS.

11.2 Tetramantane Electron-Vibration Coupling

dI/dV spectroscopy in the low bias range (±450 mV) reveals a V-like feature centered at E_F and two sudden jumps in dI/dV at ±356 mV (upper panel in figure 11.4b). The numerical derivative of this curve (d^2I/dV^2) correspondingly shows a narrow dip at −356 mV and a narrow peak at +356 mV (lower panel in figure 11.4b). This is the signature of inelastic electron tunneling spectroscopy (IETS), in which electronic excitations opens a new tunneling channel, which causes a sudden increase in dI/dV (ref. [181]). In this case, the excitation is a vibration since the energy 356 meV corresponds with the known vibrational energy of a C-H bond stretch mode, as has been observed in numerous other hydrocarbons [84]. The V-like feature in dI/dV between ±200 mV might also be related to inelastic tunneling of electrons, where the electrons excite the quasi-continuous, low-frequency vibrations of tetramantane [107].

To understand the spatial dependence of the electron-vibration coupling across the surface of an individual tetramantane, we performed d^2I/dV^2 maps on the molecules [182, 67, 58]. We find that the pronounced inelastic signals at ±356 mV only exist on certain parts of the molecules, and become negligibly small elsewhere. Figure 11.5a shows d^2I/dV^2 maps of the inelastic signal at 356 mV for three individual diamondoids having different orientations, demonstrating unambiguously that the vibronic coupling strength is strongly localized to narrow slices on the molecular surfaces. Comparing the d^2I/dV^2 maps of the tetramantane molecules with their respective topographs directly below (figure 11.5b) reveals an anti-correlation between the topography and d^2I/dV^2 maps: the IETS signal is the strongest at the depressions in topography.

Such localization of the inelastic signal is unexpected because the 28 C-H bonds surrounding the tetramantane form a dense and nearly uniform surface which one might expect to give rise to a spatially uniform inelastic signal. Moreover, it might naively be expected that regions with a higher topography also have larger inelastic tunneling (as there is then more electron density in those regions and thus a higher probability for electrons to excite vibrations) [126], opposite to the anti-correlation observed here.

11.3 DFT Calculations of Tetramantane

To understand the anti-correlation between topography and d^2I/dV^2 maps, *ab initio* pseudopotential density functional theory (DFT) calculations within the local density approximation (LDA) were performed on a [121]tetramantane molecule on Au(111) by Emmanouil Kioupakis in Steven Louie's group. Calculations were first done by using a plane-wave pseudopotential (PW-PP) code (60 Ry cutoff, 40 × 40 × 50 grid in units of Bohr radii) to obtain the properties of isolated tetramantane without the Au(111) surface [88]. The Au(111) surface was then added to the molecule as three layers of 56 gold atoms each (in a supercell geometry) and the properties of the combined diamondoid/Au(111) system were calculated using the SIESTA code [180], which uses a localized double-ζ+polarization ba-

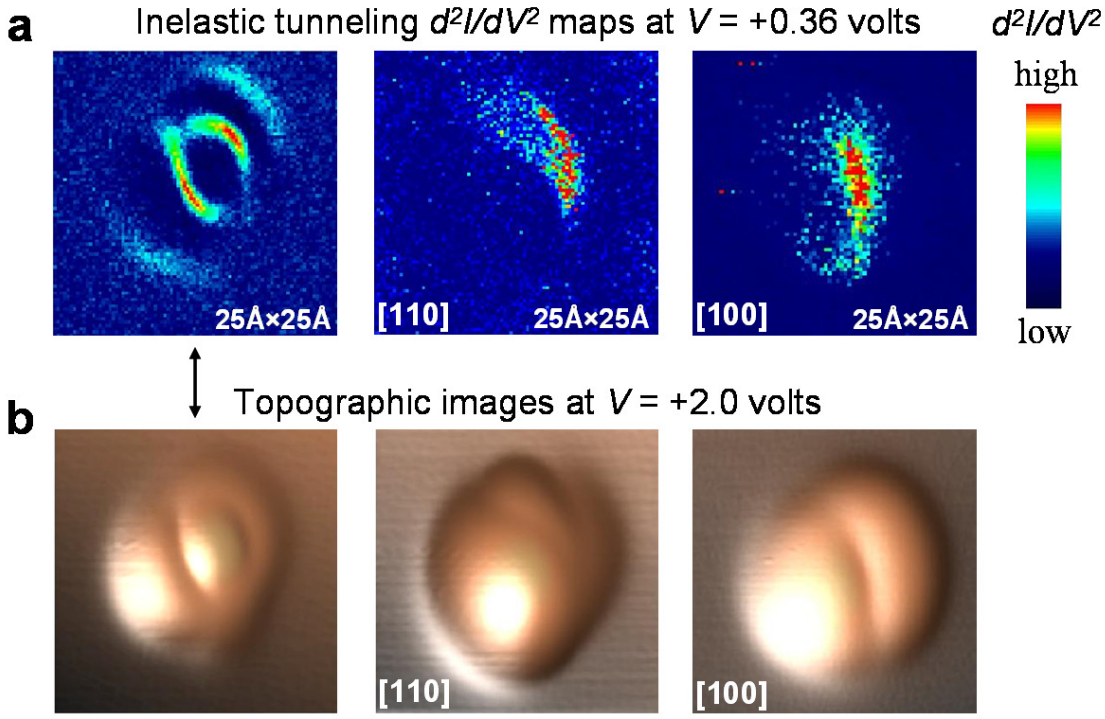

Figure 11.5: IETS on Tetramantane. (a) Experimental d^2I/dV^2 maps taken at $V = +36\,\mathrm{mV}$ on three individual tetramantane molecules in different orientations. (b) Topographs of the same molecules shown in (a).

sis set, because the use of plane waves for the combined calculation would be much more expensive (§4.5). We expect that the PW-PP code will reproduce states which extend far away ($> 4\,\text{Å}$) from the molecule better than the SIESTA code due to the localized basis used in SIESTA (see §4.5). To ensure that the SIESTA results reproduce states which extend far away from the molecule accurately, the SIESTA results for an isolated molecule were checked to be consistent with the plane-wave code when a grid of ghost atoms (§4.5) were introduced that were spaced 4 Bohr radii apart, with 2 *s*-like orbitals per ghost atom.

Figure 11.4c shows the schematic energy diagram of the tetramantane-Au(111) system. The theoretical Kohn-Sham HOMO-LUMO gap of the isolated molecule (no Au surface) is found to be 5.2 eV, which is an underestimation of the true quasiparticle HOMO-LUMO gap (§3.4.2, §4.5 and [87]). The electron affinity (EA) and ionization energy (IE) for isolated molecules (no Au surface) were obtained by computing the total energy of singly negatively and positively charged molecules, and were calculated to be -0.3 eV and 7.6 eV respectively. This implies a quasiparticle HOMO-LUMO gap of 7.9 eV (§3.4.2). The values of the Kohn-Sham HOMO-LUMO gap and the quasiparticle gap calculated from IE and EA agree well with quantum Monte Carlo calculations reported previously for the larger diamondoid $C_{29}H_{35}$ (ref. [40]). We find that diamondoids have an intrinsic negative electron affinity, as first pointed out in [40], which means that an electron in the LUMO is not

stable there and will readily leave the molecule, releasing an energy 0.3 eV. This makes diamondoids promising candidates for electron-emission devices. Recent photoemission data have indeed demonstrated strong monochromatic low-kinetic-energy electron emission from functionalized diamondoid monolayers on Au(111) (ref. [208]).

Figure 11.4d shows the DFT-calculated electronic DOS of a tetramantane molecule on Au(111). The calculated HOMO and LUMO levels are approximately at -1.0 eV and $+3.9$ eV relative to E_{F}, leading to a reduced Kohn-Sham HOMO-LUMO gap of 4.9 eV due to screening from the metal substrate. The LDOS of the LUMO is energy-broadened due to interaction with the surface (§4.4.1), and extends into the HOMO-LUMO gap as a shallow tail, consistent with the experimental LDOS (the dI/dV curve). However, the theoretical HOMO LDOS resonance at -1.0 eV is not observed in the experimental LDOS, even down to -2.5 eV.

This discrepancy can be understood by calculating the spatial distribution of the HOMO and LUMO wavefunctions ψ_{HOMO} and ψ_{LUMO}. Figures 11.2d and e show the calculated isosurfaces of $|\psi_{\mathrm{HOMO}}|^2$ and $|\psi_{\mathrm{LUMO}}|^2$ at an isosurface where 50% of $|\psi|^2$ for each state is contained within the isosurface. The calculations were done for an isolated tetramantane molecule with the molecular orientation shown in figure 11.2d. The HOMO orbital is concentrated on the centers of the C-C bonds, reflecting the spatial localization of the sp^3 bonding orbitals. Such confined states are difficult for STM to detect (with the tip at several angstroms above the molecule), which explains the featureless negative-bias topographies and the absence of the HOMO resonance in the dI/dV spectrum of tetramantane. The calculated LUMO orbital, on the other hand, is much more delocalized in space and exhibits pronounced line nodes similar to those seen experimentally. The LUMO state has previously been shown to be responsible for the negative electron affinity and anomalous quantum size effect of the diamondoids [40].

Closer comparison of the tetramantane LUMO isosurface and its corresponding molecular structure uncovers an intriguing trend: the strong line nodes in the LUMO orbitals is closely related to the surface hydrogen terminations. The large, delocalized LUMO wavefunction exists only at the 12 singly hydrogenated CH sites, and the LUMO wavefunction forms a continuous region in these CH-rich areas. The 8 doubly hydrogenated CH_2 sites (circled by red dashed lines in figure 11.2c), in contrast, exhibit little wavefunction density and form line nodes in the LUMO isosurface plot. This is can be explained by a simple tight binding model. The LUMO orbital on the CH_2 sites is constructed by a linear combination of the anti-bonding wavefunctions formed between the two canted carbon sp^3 orbitals and between the two hydrogen s orbitals [99]. The derived CH_2 wavefunction, called the $\sigma^*_{\mathrm{CH_2}}$ orbital, has a pronounced node on the mirror plane that bisects the H-C-H complex.

This behavior can be seen better in figure 11.2b, which shows calculated LUMO STM topographs of isolated tetramantane molecules in three different orientations (Au surface not included in calculation). The schematic top views in figure 11.2c reveal that the three molecules lie on the Au substrate so that the substrate [111] direction is parallel to the diamond crystallographic [111], [110] and [100] directions, respectively (from left to right). These simulated topographs agree well with the essential features (the line nodes) of the

corresponding STM topographs taken at +2.0 V (figure 11.2a). The agreement between theory and experiment demonstrates that the pronounced nodal features found in the tetramantane STM images result from the suppressed LUMO wavefunction density at the CH_2 sites.

Next, we turn to IETS. The strength of electronic coupling to the C-H stretch mode has been evaluated using DFT by calculating the change of the molecular electronic energy eigenvalues with respect to displacements along the canonical phonon coordinates [58, 126]. Out of the 28 C-H stretch modes, we have identified three that interact strongly with electrons within 15 meV of the experimental signal at 356 meV. Simulations of the spatial distribution of the IETS signal, however, did not reproduce the experimental d^2I/dV^2 maps, so the question remains as to why the experimental IETS signal is enhanced in the CH_2-terminated regions of tetramantane and suppressed in the CH regions. One possibility this occurs is because the CH_2 region has a denser concentration of C-H bonds, and hence a higher probability of electronic interactions with the C-H stretch mode compared with the singly hydrogenated CH region.

11.4 Conclusions

The sp^3 bonded tetramantane shows distinct differences from the sp^2 bonded fullerenes. Both the electronic as well as the vibrational properties of the diamondoid depend substantially on the type of hydrogen termination. The LUMO contains nodes at the CH_2 sites, and the strongest electron-vibration coupling happens at exactly these same sites. This information is potentially useful for molecular electronics since substitution of other atoms for hydrogen may significantly alter the electronic and vibrational properties of the diamondoids, allowing one to control the functionality of a specific device incorporating diamondoids.

Part III

Magnetic Molecules

12

Molecular Dissociation of Titanocene

The titanocene chloride dimer, $[Cp_2TiCl]_2$ with $Cp = C_5H_5$ (figure 12.1a), is known for its utility as an inexpensive reducing agent in organic synthesis, as well as for its magnetic properties. Its various uses in synthesis include catalysis of radical ring opening in epoxides [170], reduction and pinacol coupling of carbonyls [54], and an agent in single electron transfer [12, 6]. Its magnetic properties stem from the anti-ferromagnetic coupling between the spins of the two titanium atoms and makes the molecule a promising candidate for studying magnetism at nanometer length scales [101].

One goal of this study was to measure intra-molecular exchange coupling through spin excitations caused by inelastic tunneling. Unfortunately, we did not see spin excitations in our experiments, but we did discover new molecular orderings on the gold surface, and strong ordering-dependent electronic structure. This result is important since potential nanotechnological applications of this molecule (e.g., single molecule transistors) would involve attaching it to conducting surfaces, which requires precise control and detailed knowledge of molecule-surface chemistry [159, 122, 187]. Since the influence of metal substrates on the adsorption and catalytic properties of titanocene chloride dimers is currently not well-known, and previous studies on other molecules have shown that the metal substrate may have a substantial influence on the molecular properties [82, 141, 13], the results here are potentially useful for future applications of this molecule, and will address one of the important themes of this dissertation, the impact of a metal substrate on molecular properties.

To investigate the impact of a metal substrate on the behavior of titanocene chloride dimers, we used a combination of STM and DFT methods to study titanocene chloride dimer molecules on Au(111). Our STM topographs reveal isolated molecules at gold step edges for low molecular coverages, as well as two different coexisting phases at higher coverages closer to a monolayer. The LDOS of both the isolated molecules and the higher coverage monolayer phases were experimentally studied via dI/dV spectroscopy. Large and reproducible differences in dI/dV spectra were observed between the different molecular morphologies. To explain this behavior, the DOS of an isolated (gas phase) titanocene chloride dimer was calculated using DFT. The calculated properties of a dimer, however, do not

account for all of the experimental spectra. One possible explanation for the unaccounted for spectra (which include a spin-induced Kondo resonance) is the coexistence of Cp_2Ti and Cp_2TiCl_2 monomers in one of the monolayer phases, suggesting that a fraction of titanocene chloride dimers split into monomers on Au(111). This chapter will describe the influence of the Au(111) substrate on the properties of titanocene chloride dimers, most of which is published in our paper, reference [206].

12.1 Various titanocene phases

All experimental data presented here were taken in UHV at 7 K with a PtIr tip. Titanocene chloride molecules were synthesized by using the second method provided by Green and Lucas [56], and further purified by sublimation. The single-crystal Au(111) substrate was cleaned in UHV prior to deposition of titanocene chloride dimers from a Knudsen cell at 85°C onto a room temperature substrate. The dI/dV spectra were measured with a lock-in (§2.4) using a 451 Hz, 1–10 mV (rms) signal added to the sample bias with feedback off.

We first used an Omicron VT-STM to scan titanocene on Au(111). These experiments showed substantial molecular ordering on Au(111). However, when we did these experiments on the home built LT STM, we saw very disordered structures on the surface. Spectroscopy on these disordered structures showed inelastic effects and the Kondo effect, but these effects were not reproducible. We eventually found that the lack of ordering in the home built LT STM experiments was due to the FE coarse approach which is why we now use mainly the capacitance approach (§5.1.6). The high voltages used during the FE approach was destroying either the molecules or the molecular ordering. The Omicron VT-STM does not use the FE coarse approach.

Isolated titanocene chloride dimer molecules preferentially stick at Au(111) step edges (figure 12.1b). Individual molecules appear as slightly asymmetrical protrusions with an apparent height of 2.2 Å, measured at $V = 1.0$ V and $I = 20$ pA. The molecular shape remains mostly featureless when imaged at different biases in a (1.5 V window). The exact orientation of the molecule on the surface cannot be determined from STM topographs, but little variation was observed between different isolated molecules. The dI/dV spectrum of single molecules (figure 12.1c) clearly shows a LUMO resonance around 0.8 V.

When greater than $\sim 10\%$ of a monolayer of titanocene is deposited onto Au(111), two new phases were discovered to coexist, here referred to as phase 1 and phase 2 (figure 12.2a). Topographs of phase 1 (figure 12.2b) reveal a periodic network of protrusions having varying shapes and heights. When imaged with $V = -1.0$ V, dim protrusions in this phase appear elongated while brighter protrusions are circular (seven dim protrusions surround each bright one). The morphology of phase 2 is quite different, as the shapes of all protrusions here appear more circular, and the molecular arrangement has a honeycomb-like structure (every phase 2 bright protrusion is surrounded by three bright and three dim protrusions, when imaged at $V = -0.5$ V). Attempts to match the experimentally observed two-dimensional structures to surface terminations of known bulk geometries of $[Cp_2TiCl]_2$ were unsuccess-

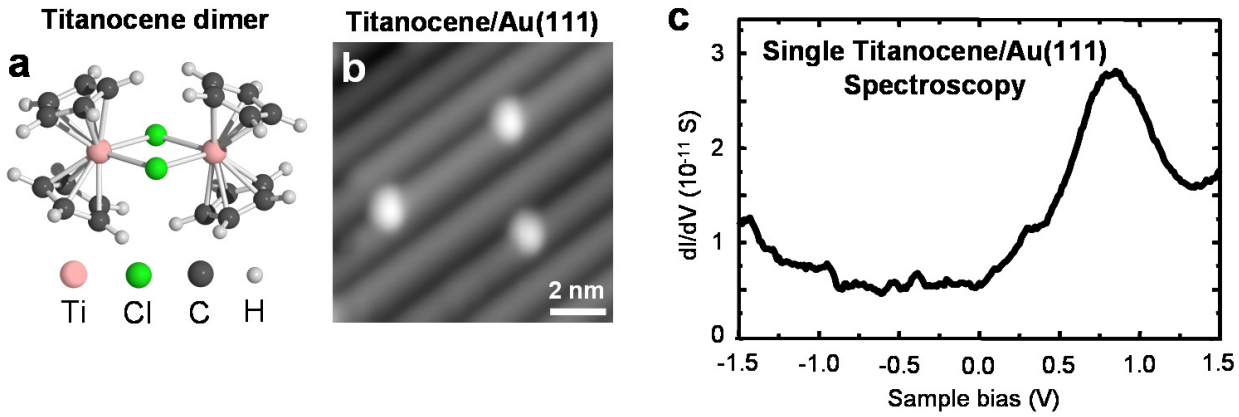

Figure 12.1: (a) Titanocene chloride dimer ball and stick model, as calculated by DFT (b) Topograph of single titanocene at narrow terraces on Au(111) ($V = 1.0\,\mathrm{V}$, $I = 20\,\mathrm{pA}$, $T = 7\,\mathrm{K}$). (c) dI/dV spectroscopy of isolated titanocene averaged over many molecules. The LUMO resonance appears around 0.8 V.

ful [101, 16, 115] implying that the Au(111) surface induces a new two-dimensional molecular ordering.

The LDOS of phase 1 and phase 2 monolayers was measured by dI/dV spectroscopy. dI/dV spectra of phase 1 (figure 12.3a) reveal peaks at different energies and peak amplitudes that depend on the spatial location of the spectrum. Spectra taken over the brighter phase 1 protrusions (circled in red in figure 12.3b) show two distinct peaks, a LUMO at about 0.5 V and a HOMO at about $-1.0\,\mathrm{V}$ as well as a shoulder around 1.3 V. However, spectroscopy on the dimmer regions (circled in green) show only one distinct resonance at around 1.3 V. The slight dip in both curves is due to the Au(111) surface state. Spectroscopy at higher voltages was not possible since it caused irreversible damage to the monolayer phases.

dI/dV spectroscopy on monolayer phase 2 (figure 12.4a) again shows resonant peaks, but at different energies than those seen in phase 1. The brighter protrusions (circled in red in figure 12.4b) display one significant peak at $-0.3\,\mathrm{V}$ while the dimmer regions (circled in green) display two peaks at $-1.1\,\mathrm{V}$ and 0.3 V. The spectrum in the dimmer region stops at 0.3 V since the dI/dV signal becomes unstable at larger biases. If we zoom in on $V = 0\,\mathrm{V}$ in the dim region spectrum, a Kondo peak can be seen (figure 12.4a, inset). Such a peak is only seen in phase 2 and never seen in phase 1. Fitting the Kondo resonance to a Fano line shape (including thermal deconvolution [150], §3.1) yields a line width of $\Gamma = 8.6\,\mathrm{meV}$, from which a Kondo temperature of $T = 50\,\mathrm{K}$ is derived ([81], §4.4.3).

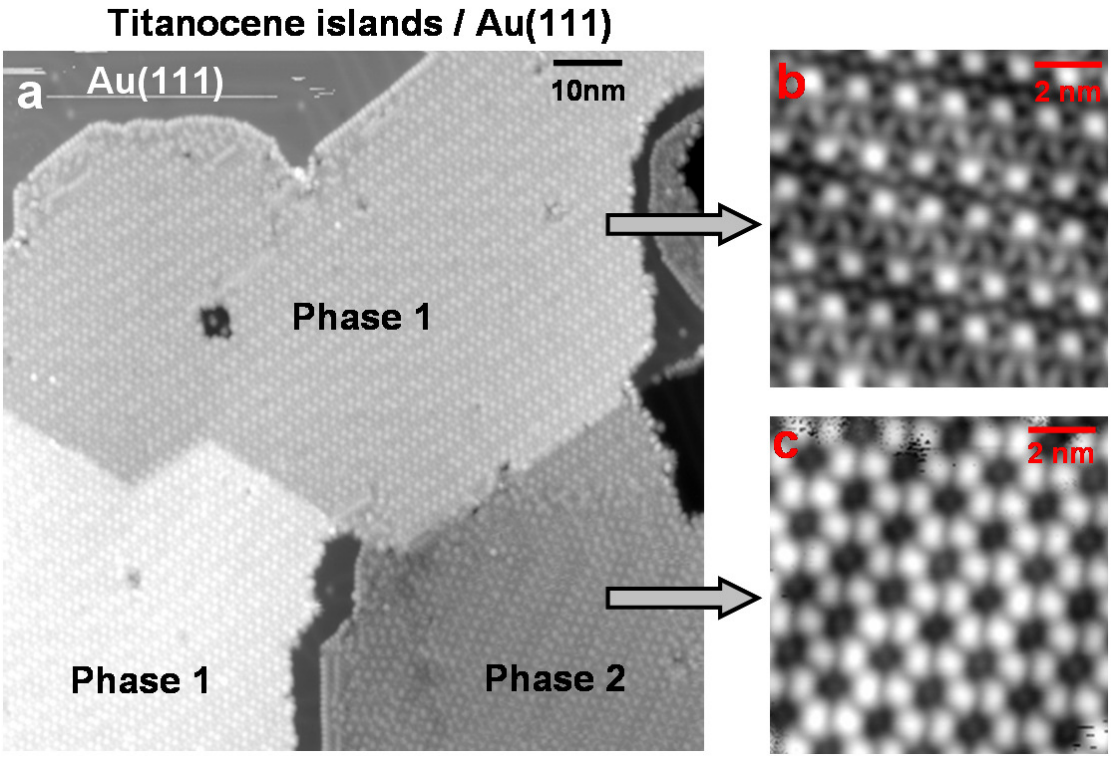

Figure 12.2: Titanocene monolayer phases. (a) Topograph of the two coexisting titanocene monolayer phases with patches of clean Au(111) ($V = 1.0\,\mathrm{V}$, $I = 5\,\mathrm{pA}$, $T = 7\,\mathrm{K}$). (b) Topography of phase 1 ($V = -1.4\,\mathrm{V}$, $I = 10\,\mathrm{pA}$) and (c) topography of phase 2 ($V = -0.2\,\mathrm{V}$, $I = 4\,\mathrm{pA}$).

12.2 DFT on titanocene

To understand the wide range of experimental spectra, Mark Pederson performed first-principles DFT calculations on free titanocene chloride dimers using the NRLMOL code [161, 169]. Effects of the surface can be important, but were not included since we do not know the exact molecular arrangement from experiment and performing a calculation for every one of the many possible arrangements is prohibitively expensive. However, free molecule calculations can still give a qualitative understanding of the experimental data. All atoms in the calculation were treated within an all-electron approach (no pseudopotentials) [161], §4.5. The basis sets used in these calculations are roughly equivalent to triple-ζ or better [168]. The generalized gradient approximation (PBE-GGA) was used to approximate the exchange-correlation functional [165]. The free molecules were relaxed until all forces were below $0.01\,\mathrm{eV/Å}$.

Roughly, the two Cp rings attached to a Ti atom each suck up one electron, while each Cl atom sucks up around $\frac{1}{2}$ of an electron from Ti. This means each Ti is in a Ti(III) state; i.e., each Ti has a net charge of +3. As each neutral Ti atom has four valence

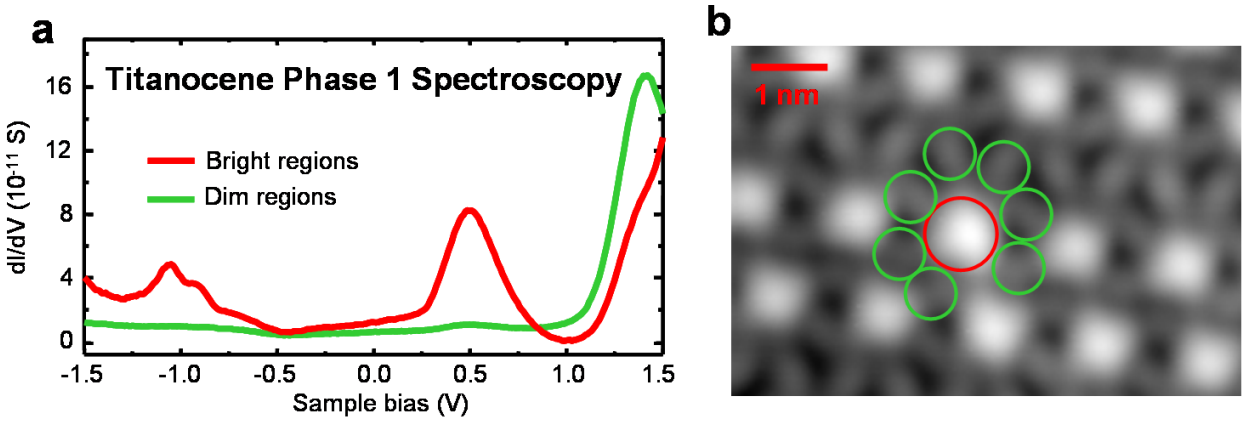

Figure 12.3: Spectroscopy on titanocene monolayer phase 1. (a) The green curve is the spatial average of dI/dV spectra taken over different dim regions, while the red curve is the spatial average of spectra taken at different bright regions. (b) Topograph ($V = 0.5\,\mathrm{V}$, $I = 10\,\mathrm{pA}$) of phase 1 showing the dim regions (green circles) and red regions (red circles).

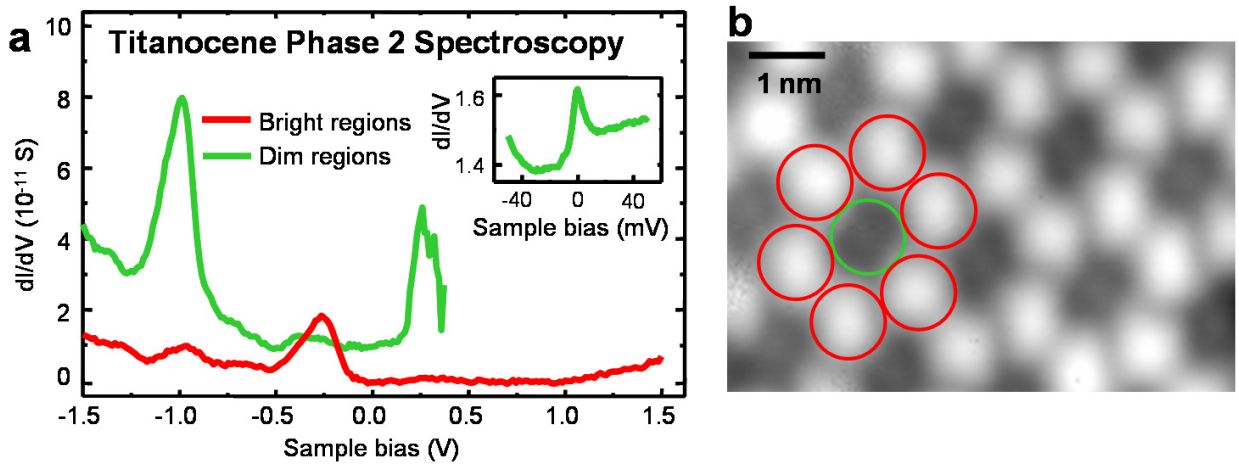

Figure 12.4: Spectroscopy on titanocene monolayer phase 2. (a) Both curves are the spatial average of dI/dV spectroscopy taken over different regions in the phase 2 monolayer. Green curve = average over dim regions, red curve = average over brighter regions. A Kondo resonance (inset) appears only in the dim regions of phase 2. (b) Topograph of phase 2 ($V = -0.5\,\mathrm{V}$, $I = 5\,\mathrm{pA}$) showing both dim regions (green circles) and brighter regions (red circles).

electrons, the Ti(III) atom then has only one valence electron. The DFT calculated ground state of $[Cp_2TiCl]_2$ is found to have anti-ferromagnetic coupling between the two Ti(III) atoms' spins with a singlet-to-triplet transition energy of 13.3 meV, consistent with previous bulk measurements [101]. Figure 12.5a (lower panel) shows the DOS calculated for a free titanocene chloride dimer. The calculated DOS has been rigidly energetically shifted to

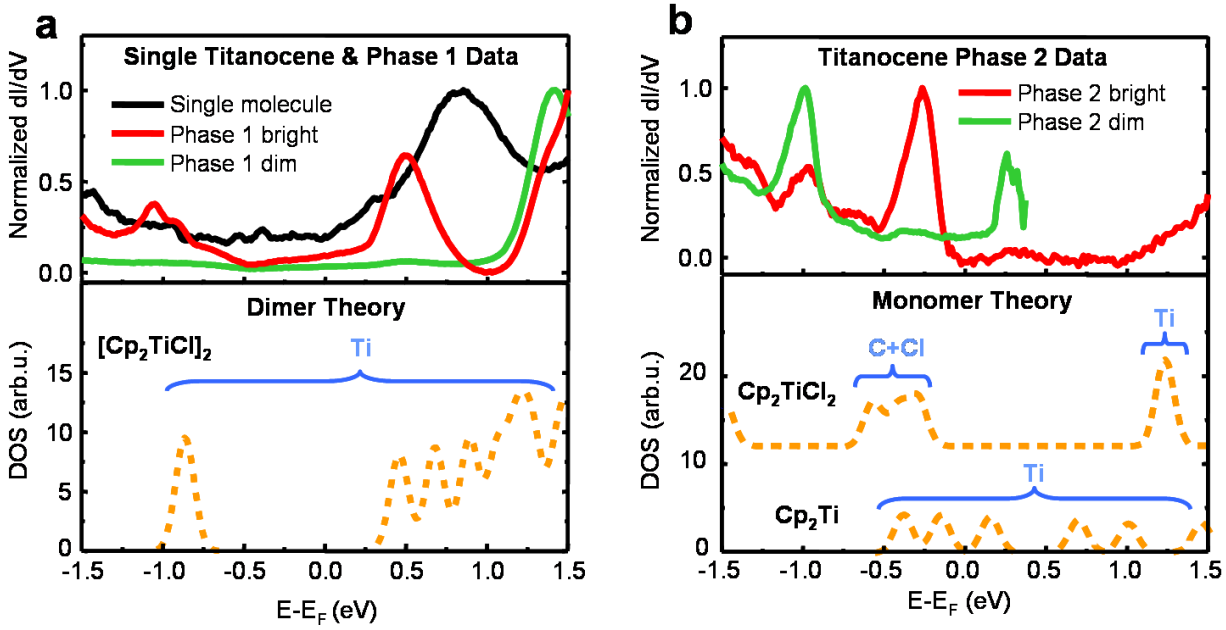

Figure 12.5: DFT on free titanocene. (a) The upper panel shows again the experimental dI/dV spectra for the isolated molecules and phase 1 monolayer on Au(111), but each spectrum has been multiplied by a factor so that the highest point has the value 1. The lower panel i the broadened DFT calculated DOS for a free titanocene chloride dimer. The elements with the most significant contribution to the DOS in an energy range is written the curve. (b) The upper panel shows again the experimental dI/dV spectrum for the phase 2 monolayer, but the spectrum has been normalized as in part (a). The lower panel shows the broadened DFT calculated DOS for the two free monomers Cp_2TiCl_2 and Cp_2Ti. The curves are vertically offset for clarity.

align the energetic positions of the theoretical HOMO/LUMO peaks with our experimental HOMO/LUMO peaks since the precise location of the Fermi energy is not well defined for a free molecule with a wide HOMO-LUMO gap. As seen in figure 12.5a (top panel) the calculated peaks line up reasonably well with the experimental peaks for both the isolated dimer molecules as well as the phase 1 monolayer. This suggests that the experimentally observed isolated molecules and phase 1 monolayer molecules are both titanocene chloride dimers. However, the peak positions and magnitudes of the isolated molecule and phase 1 monolayer spectra differ. These variations are likely due to differing molecular orientations on the surface. The specific orientations are difficult to determine from STM topographs and a wide number of possible structures could potentially fit our data.

The peaks seen in the experimental spectra for phase 2 molecules show a dramatic departure from the isolated molecule and phase 1 behavior, which the DFT dimer calculations do not account for. We also note that the phase 2 topographic molecular features are more circular in comparison to the elongated features of phase 1 molecules. As a result of

these spectroscopic and topographic differences between phase 1 and phase 2, we propose that phase 2 does not consist of titanocene chloride dimers; it is composed of dissociated titanocene dimers (titanocene monomers). Molecular dissociation may happen during the thermal evaporation process, or may occur on the surface, which is known to occur for other metallocenes [20]. A well-known stable fragment of the titanocene chloride dimer is titanocene dichloride (Cp_2TiCl_2). Since Cp_2TiCl_2 + Cp_2Ti = $[Cp_2TiCl]_2$, the presence of titanocene dichloride on the Au(111) surface suggests the simultaneous existence of the non-chlorinated titanocene monomer (Cp_2Ti).

This interpretation is supported by comparisons of our measured dI/dV spectra with DFT calculations of the DOS of Cp_2TiCl_2 and Cp_2Ti. The lower panel of figure 12.5b shows the calculated DOS for both free Cp_2TiCl_2 and Cp_2Ti monomers (these results are also consistent with previous total DOS calculations [195, 51]). The element which contributes the most to the DOS in a specific energy window is written above the DOS. The Fermi energy of a free molecule is not well defined; it can be anywhere in the HOMO-LUMO gap. So, to compare the free molecule calculations with the experimental LDOS (with a well defined E_F), we may energetically shift the theoretical spectrum of Cp_2TiCl_2 rigidly within the HOMO-LUMO gap to align the calculated and experimental peaks. The calculated free molecule Cp_2Ti DOS, on the other hand, has a more well-defined E_F since the HOMO-LUMO gap here is small, and so its energy alignment is pinned. Both types of monomers are seen to have new states near E_F in the calculated DOS that do not exist in the dimer calculations, consistent with experimental phase 2 spectra, and thus supporting the proposal that phase 2 consists of titanocene monomers instead of dimers. The calculated Cp_2TiCl_2 spectrum, for example, has filled states similar to filled state features seen in the experimental spectra for phase 2 bright regions (figure 12.5b, top panel) while the calculated spectrum for Cp_2Ti has unoccupied states near E_F, similar to the unoccupied states in dim regions of phase 2. This suggests that the bright regions in phase 2 are Cp_2TiCl_2 monomers while the dim regions are Cp_2Ti monomers. The experimentally observed Kondo peak in the phase 2 dim regions is consistent with magnetism predicted in the calculations for Cp_2Ti ($S = 1$), while the lack of a Kondo peak in phase 2 bright regions is consistent with the non-magnetic $S = 0$ ground state of Cp_2TiCl_2 from the calculations [51]. The exact molecular orientations and adsorption sites of the two monomers in this phase could not be uniquely determined from STM topographs, so the Au(111) surface was not included in the calculation for the same reasons stated above regarding phase 1. We also note that the experimental ratio of Cp_2Ti to Cp_2TiCl_2 is 1:2, which deviates from the expected 1:1 ratio. This is possibly due to a smaller sticking probability for Cp_2Ti on Au(111) at room temperature, which causes a fraction of them to desorb from the Au(111) surface.

12.3 Conclusions

We have studied the behavior of titanocene chloride dimers on Au(111) using STM and DFT. Isolated molecules and two new monolayer phases were experimentally observed on

the Au(111) surface. DFT calculations of free molecules suggest that titanocene chloride dimers, as well as dissociated dimers, the non-magnetic Cp_2TiCl_2 and magnetic Cp_2Ti, coexist on Au(111). The molecular adsorption geometries could not be uniquely determined by STM, so effects of the surface were not included in the calculations. The agreement between experimental spectroscopy and theoretical DOS can be improved if effects of the surface (such as surface hybridization, relaxation, and charge transfer) and overlap between tip and molecule wave functions were included in future calculations.

13

Spin Coupling Mediated by TCNE

Magnetic molecule-based spintronics raises new possibilities for electronic and magnetic devices [19, 90]. In this field, molecules based on transition metal atoms and cyano-organic molecules show much promise due to their high Curie temperatures. An important cyano-organic molecule is tetracyanoethylene (TCNE) since V_x(TCNE) with $x \sim 2$ has an unusually high Curie temperature of around 400 K [136, 167, 185, 113]. The structure of TCNE is shown in figure 13.1. However, the mechanisms which cause the high Curie temperature are not well understood, mainly due to the disordered growth of bulk TCNE compounds. Experimental probes to determine the spin interactions, such as XMCD and XPS, have not been conclusive [167, 72, 185].

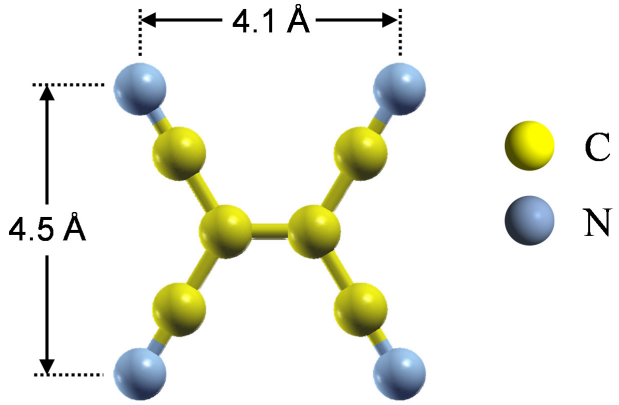

Figure 13.1: Structure of the TCNE molecule from DFT calculations.

To address this problem, a local probe such as an STM is ideal. Using the molecular manipulation capabilities of an STM, we can manipulate TCNE to vanadium atoms and can control both the stoichiometry and structure of $V_x TCNE_y$ complexes. We can then study the electronic and magnetic properties of these structures while knowing precisely what the

structure of the complexes are. This work sheds light on a number of important themes in this dissertation—how can we control properties of single molecules at atomic scales, and how do molecule-substrate and molecule-atom interactions affect molecular properties.

We will see that the TCNE-substrate interaction is largely determined by the lattice structure of the noble metal substrate. We will also see evidence for controllable spin coupling through TCNE in $V_x(TCNE)_y$ structures created by STM manipulation, suggesting that spin coupling can be controlled at atomic length scales. These results are based on our published papers, refs. [199, 200].

13.1 TCNE-Substrate Interactions

The first step in this work was to find a suitable substrate to do the experiments on, since there is not much previous work exploring TCNE on different substrates [43, 44, 157]. TCNE molecules were deposited onto various substrates at room temperature using a room temperature leak valve evaporator (§5.4.4). Three noble metal single crystal substrates were used, Au(111), Ag(001), Cu(001). All substrates were cleaned according to §5.3. The TCNE molecules had a purity of 99% and were prepared before evaporation according to §5.4.4. All substrates were at room temperature during the deposition of TCNE.

On Au(111), the TCNE molecules saturated the step edges and formed small islands in the fcc corners of the Au(111) Herringbone reconstruction [204]. Most of the surface displayed disordered arrangements of TCNE except for small ordered islands. Each molecule appears as a 6 Å × 9 Å kidney-bean shaped protrusion with an apparent height of ∼1.2 Å (figure 13.2). The molecules do not seem to stick to the Au(111) surface very strongly since

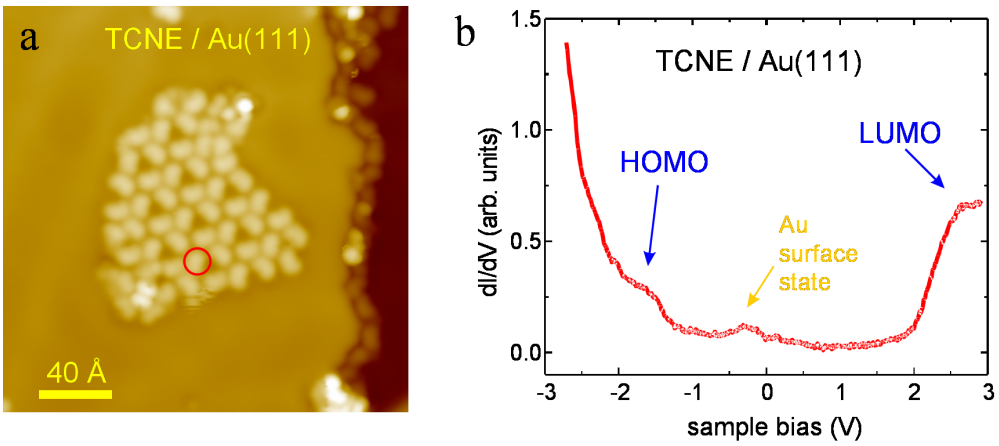

Figure 13.2: TCNE deposited onto Au(111) at RT and imaged at $T = 7\,\mathrm{K}$. (a) Topography of a small island of TCNE ($V = 0.1\,\mathrm{V}$, $I = 5\,\mathrm{pA}$). A single TCNE molecule is circled in red. (b) dI/dV spectroscopy of TCNE on Au(111), showing the HOMO and LUMO. The feature around $-0.5\,\mathrm{V}$ is due to the Au(111) surface state.

we need low currents to image them (∼ 1 pA). Manipulation performed with settings around

50 mV, 3 nA would usually pick the molecules off the surface.

dI/dV spectroscopy was also performed on the molecules in the islands (figure 13.2). The spectrum shows two peaks which are the HOMO at around −1.5 V and LUMO around 2.5 V. There is little difference between dI/dV maps taken at different energies.

For TCNE on Ag(001) (figure 13.3), the molecules also saturate the step edges, but exist as isolated molecules on terraces at low coverages. At higher coverages, the molecules can exist either as isolated molecules or as ordered islands. The isolated molecules appear as an oval with dark stripes around it. dI/dV spectroscopy on the isolated molecules shows only

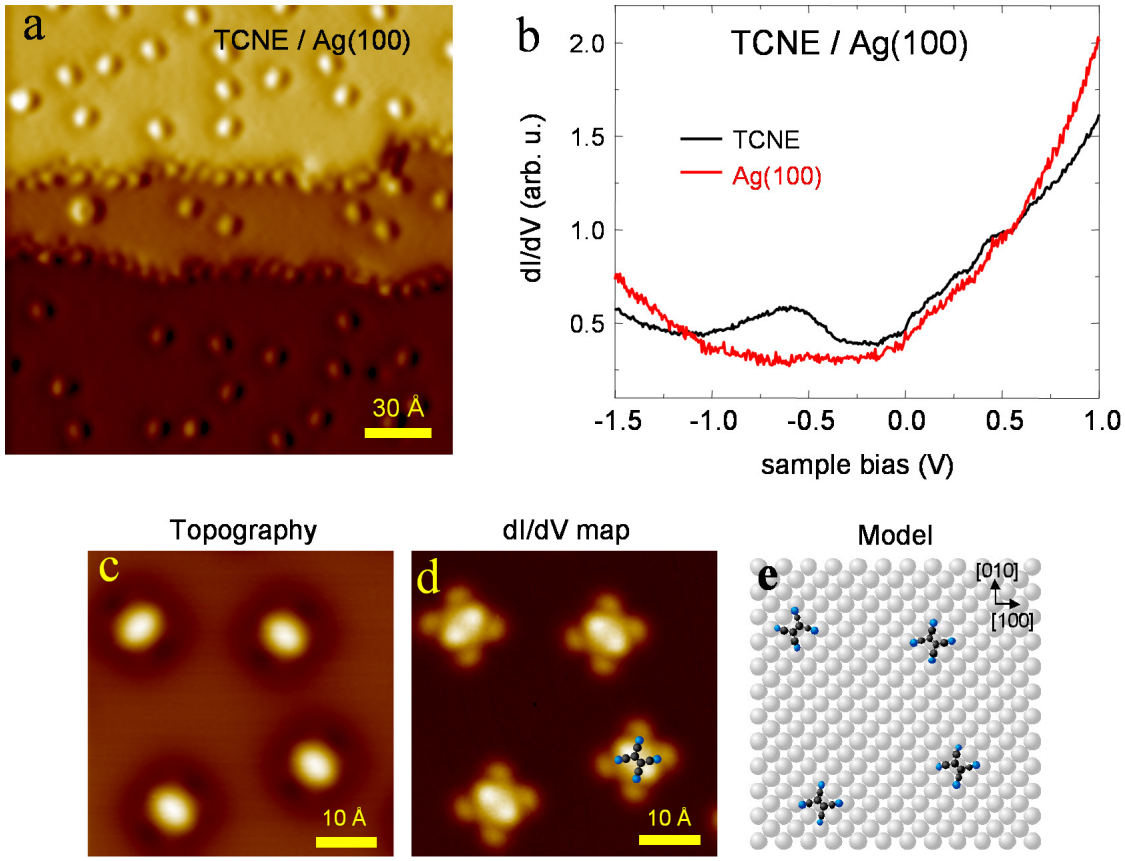

Figure 13.3: TCNE on Ag(001). (a) Topography at $V = -0.6\,\mathrm{V}$, $I = 10\,\mathrm{pA}$. (b) dI/dV spectroscopy of TCNE on Ag(001), showing the HOMO resonance at $V = -0.6\,\mathrm{V}$. (c) Topography of four TCNE molecules ($V = -0.6\,\mathrm{V}$, $I = 30\,\mathrm{pA}$). (d) dI/dV map at $V = -0.6\,\mathrm{V}$ (the HOMO energy). (e) Structural model of the images in (c) and (d).

one molecular state, a HOMO at around −0.6 V. dI/dV maps of the isolated molecules taken at the energy of the HOMO shows the spatial distribution of the HOMO (§2.5).

TCNE on Cu(001) forms long ordered chains (figure 13.4), unlike TCNE on Ag(001) or Au(111). Topographs of these long chains have a different structure from TCNE on Ag(001). At low biases, we can see a central oval shaped protrusion, but a few of these protrusions

have additional circular protrusions around them. dI/dV spectroscopy on TCNE on Cu(001)

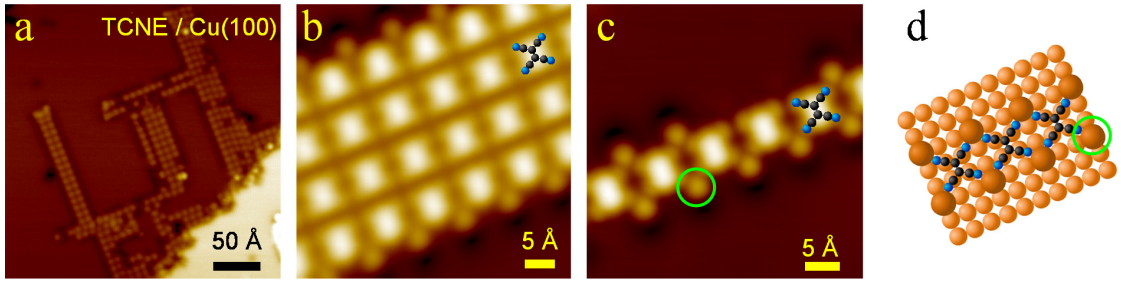

Figure 13.4: TCNE on Cu(001). (a) Topography ($V = 1\,\mathrm{V}$, $I = 5\,\mathrm{pA}$. (b) Topograph of a small island ($V = 10\,\mathrm{mV}$, $I = 5\,\mathrm{nA}$. (c) Topograph of a chain ($V = 1\,\mathrm{mV}$, $I = 5\,\mathrm{nA}$. (d) Structural model of part of the image in (c). The green circle around the buckled Cu atom in the model corresponds to the green circle in (c).

shows no distinct peaks within $\pm 2\,\mathrm{eV}$ of E_F.

The behavior of TCNE on the different noble metals can be explained in terms of the different metals' work functions, as well as the TCNE electron affinity. Since TCNE has a high electron affinity, 3.1 eV [33], it likes to suck up electrons. The work function gives us an idea of how much the metal is willing to give up its electrons. So lower work function metals are more likely to donate electrons to TCNE and create an ionic bond. The work functions for Au(111), Ag(100), and Cu(100) are 5.3 eV, 4.6 eV, and 5.1 eV [123]. We would then expect the ionic bonding between TCNE and Au to be the weakest while the ionic bonding between TCNE and Cu to be weak while the bonding between TCNE and Ag to be the strongest.

We would then naively expect the behavior of TCNE on Ag(001) and Cu(001) to be opposite of what is experimentally observed: TCNE should cause larger interactions with Ag than with Cu, but that is not the case. To explain the discrepancy, we must also take into account the differing lattice constants of Ag and Cu, as well as the differing binding energies between Ag atoms and Cu atoms.

Since the lattice constant of Cu is 2.55 Å, the nitrogen atoms of TCNE are all close to a Cu atom; the distance between Cu and N is 2.37 Å from the structural model. This is similar to the distance between transition metals and TCNE in metal-TCNE complexes [72, 79, 103, 147]. However, Ag has a larger lattice constant and so the distance between Ag and N would be 3.13 Å, which is substantially larger than for Cu. Hence, due to a better structural fit with the lattice, we expect the interaction between Cu and TCNE to be stronger than the interaction between Ag and TCNE.

We must also consider the Ag-Ag and Cu-Cu binding energies, since the metal with a smaller binding energy is more likely to buckle. These energies may be found from the heat of vaporization. We find that the Cu-Cu binding energy is actually larger than the Ag-Ag binding energy. So it seems that the lattice matching between TCNE and Cu plays the dominant role in determining the lattice buckling.

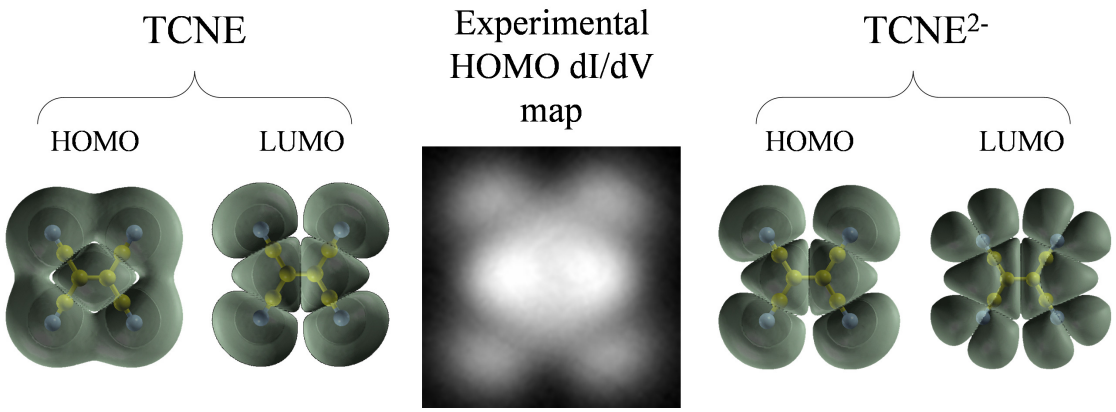

Figure 13.5: DFT calculated isosurfaces for the HOMO and LUMO of TCNE and $TCNE^{2-}$, with the experimental dI/dV map of the HOMO in the middle for comparison.

Another possibility for Cu atoms attached to the TCNE molecules on Cu(001) is from adatom diffusion. Since we deposit TCNE onto a Cu(001) substrate at room temperature and Cu atoms are diffusing on the surface at room temperature, it is possible that the diffusing TCNE and Cu hit each other and grow into ordered structures. There is experimental and theoretical evidence, however, that this is not the case. Experimentally, the height of the observed circular protrusions are small, $\lesssim 0.3\,\text{Å}$ (imaged at $V = 0.01\,\text{V}$, $I = 10\,\text{pA}$), much smaller than the $0.7\,\text{Å}$ to $1.2\,\text{Å}$ heights of Cu adatoms or small Cu clusters on other Cu substrates [154, 116, 117], suggesting that the observed protrusions are not Cu adatoms. Also, we experimentally observe holes near the circular protrusions, suggesting that they are Cu atoms that have been pulled out of the surface. Theoretically, DFT calculations that support the buckling model and not the adatom diffusion model have been done [15].

13.2 DFT Calculations on TCNE

To model the observed molecular orbital, DFT calculations were performed using SIESTA. A double-ζ + polarization basis was used and the local density approximation was used for the exchange-correlation functional (§4.5). The free TCNE molecule was relaxed until all forces were less than $0.001\,\text{eV/Å}$.

The energy eigenvalues of the free TCNE molecule were calculated and the HOMO and LUMO wavefunctions were also calculated. The agreement between the dI/dV HOMO images and the calculated free molecule HOMO do not agree well (figure 13.5). However, if one or two negative charges are added and the calculation repeated, we find that the HOMO wavefunction does indeed look like the experimental dI/dV images (figure 13.5). This implies that the TCNE absorbs electrons from the Ag(001) surface, which is likely since TCNE is known to have a high electron affinity ($\sim 3\,\text{eV}$).

13.3 $V_x(TCNE)_y$ Complexes

Once we found that Ag(001) works the best for manipulation, we created various V_xTCNE_y structures on Ag(001). The main structures that were built were V(TCNE), V_2(TCNE), and V(TCNE)$_2$. Although direct (atom-atom) and substrate-mediated (atom-substrate-atom) magnetic coupling between atomic spin centers has been measured previously using STM-based techniques [30, 94, 83, 192, 142], precisely controlling the spin coupling through a single molecular linker (atom-molecule-atom) in an artificial molecular structure has not yet been performed.

After depositing TCNE from a leak valve evaporator (§5.4.4) onto a Ag(001) single crystal held at room temperature, the Ag(001) was moved to the STM until it cooled down to 7 K. Vanadium atoms were then deposited from an *e*-beam evaporator (§5.4.2). Figure 13.6 shows the surface after the deposition of TCNE and V.

The V atoms cannot be manipulated on the Ag(001) surface, but the TCNE molecules can be moved towards the V atoms using the sliding technique [42]. After TCNE is moved towards a V atom, it spontaneously combines with it to form V(TCNE) (figure 13.6b,e). This V(TCNE) complex can then be manipulated as a single unit towards another V to create V_2(TCNE) (figure 13.6f). A TCNE molecule can also be moved towards V(TCNE) to create V(TCNE)$_2$ (figure 13.6c).

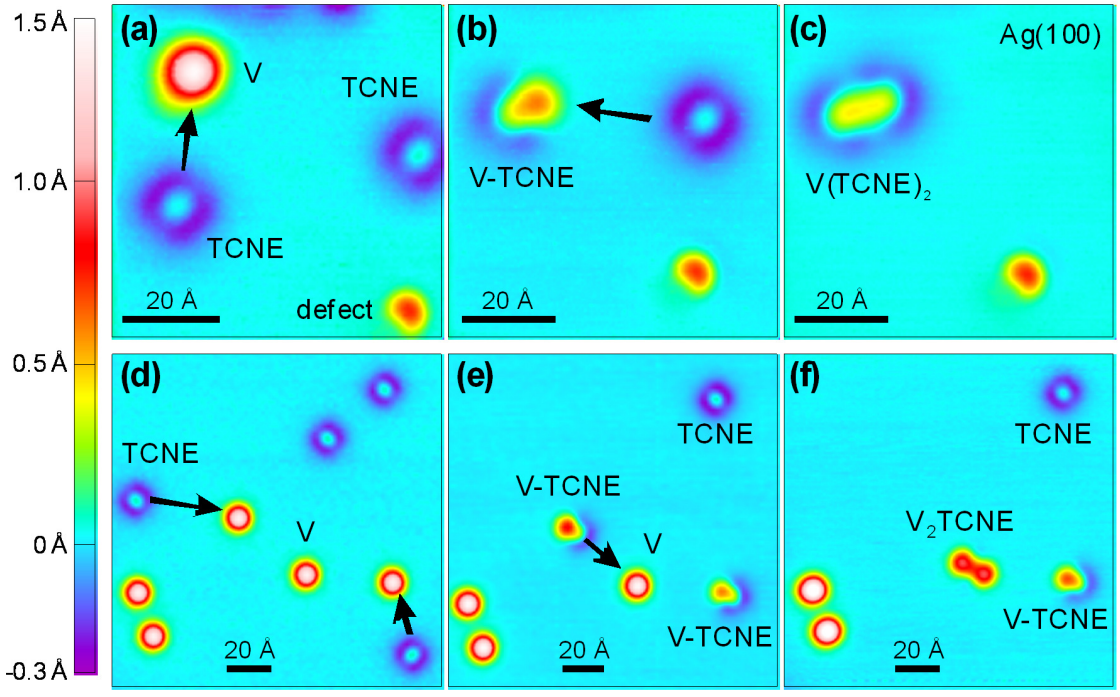

Figure 13.6: Construction of $V_x(TCNE)_y$ on Ag(001) using molecular manipulation. (a)–(c): formation of V(TCNE)$_2$ ($V = 1$ V, $I = 5$ pA). (d)–(f): formation of trans-V_2(TCNE) ($V = 1$ V, $I = 10$ pA).

There are many different structures which can be built by manipulation (13.7). However, there are also various different stable isomers for each $V_x(TCNE)_y$. A particular isomer can sometimes be obtained by carefully controlling the manipulation process, but often one constructs an undesired isomer instead. This lack of complete control makes it difficult to

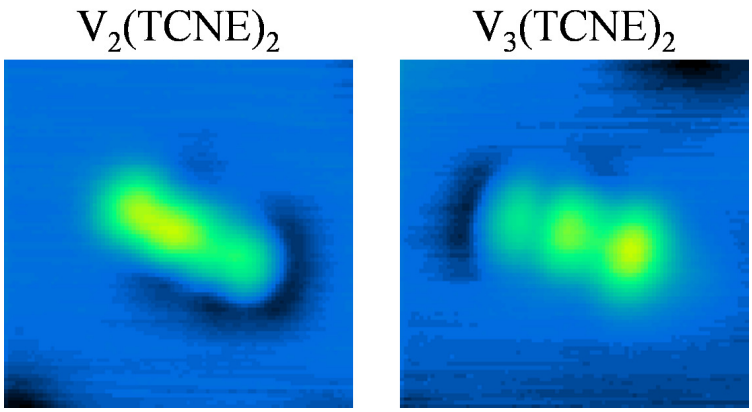

Figure 13.7: 4 nm×4 nm topographs of $V_2(TCNE)_2$ ($V = 0.1$ V, $I = 30$ pA) and $V_3(TCNE)_3$ ($V = 0.1$ V, $I = 30$ pA).

reproducibly create large $V_x(TCNE)_y$ structures, and makes it harder to get good statistics on each structure. However, for the smaller $V_x(TCNE)_y$ structures, there are less possible ways a V atom can attach to the V(TCNE), making it easier to get reproducibility.

The structures that we were able to get good statistics on were V(TCNE), linear $V(TCNE)_2$, cis-V_2(TCNE), trans-V_2(TCNE)@27° and trans-V_2(TCNE)@11°. The angle in the names of the two trans-V_2(TCNE)s denotes the different orientations with respect to the [100] direction of the Ag(001) surface. The first orientation has the line joining the two V atoms rotated 27° counterclockwise from the [100] direction while the second orientation has the line joining the V atoms rotated by 11° from the [100] direction. By analyzing the molecular resonances and Kondo effect in these various structures, and by comparison with DFT calculations, we can draw some conclusions about the magnetic interactions in these structures.

Figure 13.8 shows STM topographs, as well as structural models derived from atomic resolution images of these structures. Atomic resolution was achieved by getting adsorbates on the tip (§3.2).

Spectroscopy done at higher biases (±1 V) on V-TCNE, $V(TCNE)_2$, trans-V_2(TCNE), and cis-V_2(TCNE) is shown in figure 13.9. The main feature in the spectroscopy in this energy range is the peak at around −0.2 V. This peak exists on both the V and TCNE in V-TCNE, but only on V in $V(TCNE)_2$.

Figure 13.10 shows spectroscopy in the low bias ±80 mV range for TCNE, V-TCNE, and $V(TCNE)_2$. Data for V_2(TCNE) will be presented later. TCNE shows a sharp decrease in dI/dV near −30 mV and a sharp rise in dI/dV near +30 mV (figure 13.10a). These features are easier to see in d^2I/dV^2, where they appear as a dip and a peak. In V-TCNE, a sharp resonance around 0 V and additional faint features appear at ±45 mV on V and ±30 mV

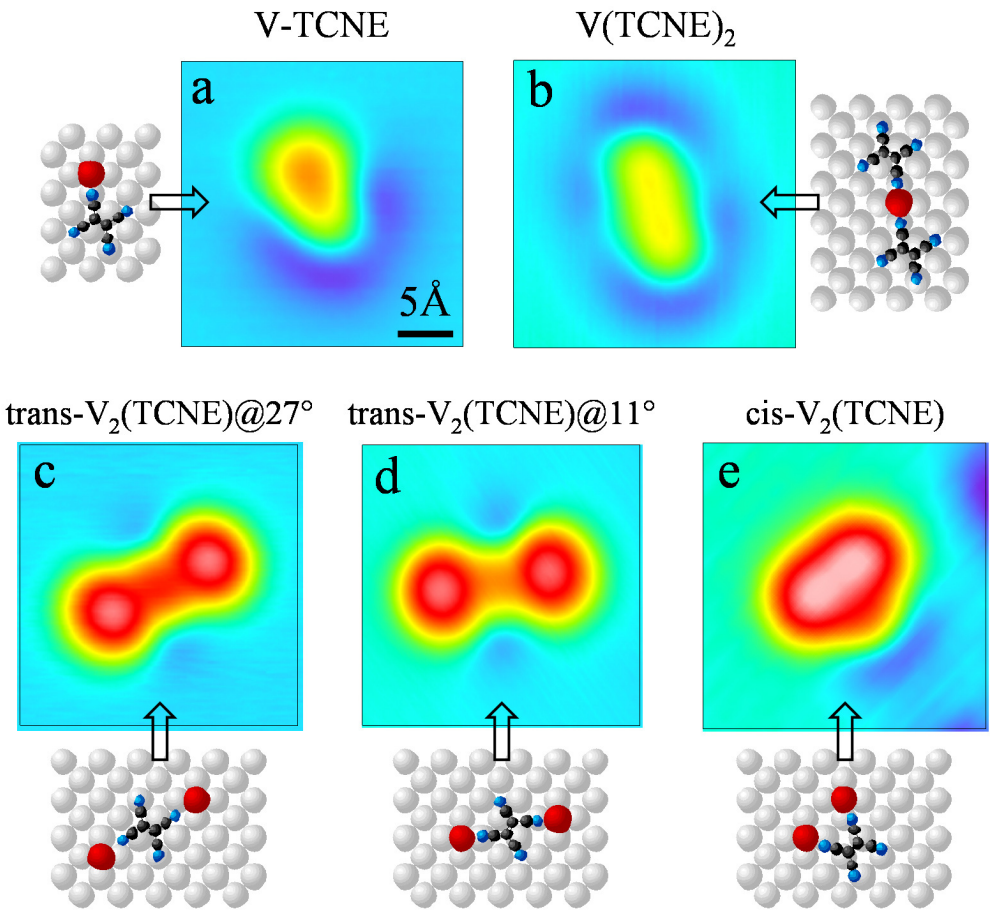

Figure 13.8: Topographs and structural models of (a) V-TCNE (1 V, 10 pA), (b) $V(TCNE)_2$ (1 V, 5 pA), (c) trans-V_2(TCNE)@27° (1 V, 50 pA), (d) trans-V_2(TCNE)@11° (1 V, 5 pA), and (e) cis-V_2(TCNE) 1 V, 5 pA.

on TCNE. These faint features in dI/dV are more apparent in d^2I/dV^2, where they appear as dips at −45 mV (on V) and −30 mV (on TCNE) and peaks at 45 mV (on V) and 30 mV (on TCNE). On $V(TCNE)_2$, there is a sharp peak near 0 V, and again faint features in d^2I/dV^2 at ±30 mV on TCNE. The peak near 0 V in V-TCNE and $V(TCNE)_2$ is likely due to a Kondo effect (§4.4.3). The dips and peaks in d^I/dV^2 in all spectra are are inelastic features (§2.6) which are likely due to molecular vibrations. The IETS feature at 30 mV is likely the known wagging or rocking mode of TCNE from DFT and optical spectroscopy measurements [145, 23]. The inelastic feature at 45 mV is likely due to V-N vibrations since the V-N stretch mode of other structures lies at this energy [10]. The existence of this mode only when V is attached to TCNE shows that a true covalent bond is being formed between V and TCNE.

The final types of structures we analyzed in detail are the trans-V_2(TCNE)@27° and trans-V_2(TCNE)@11° complexes shown in figure 13.8. In V_2(TCNE)@27°, spectroscopy in

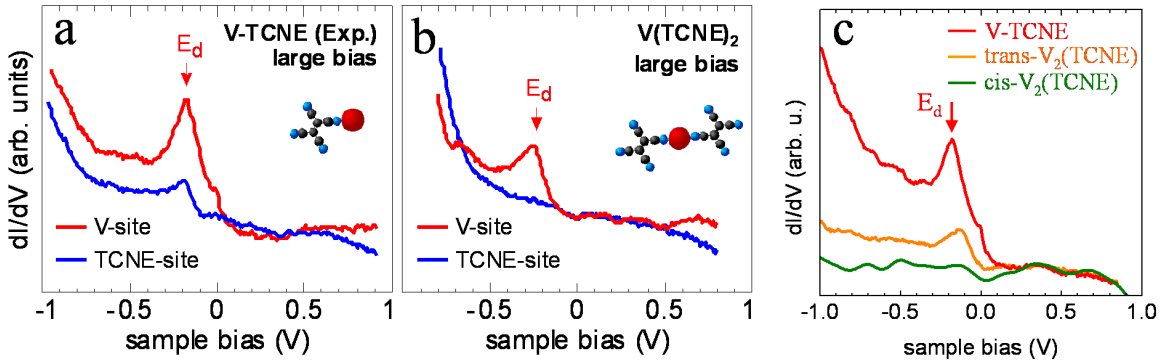

Figure 13.9: Spectroscopy on (a) V-TCNE, (b) $V(TCNE)_2$, and (c) a comparison of spectroscopy between V-TCNE, trans-V_2(TCNE), and cis-V_2(TCNE). The state believed to arise from the V d-orbital is labeled with E_d.

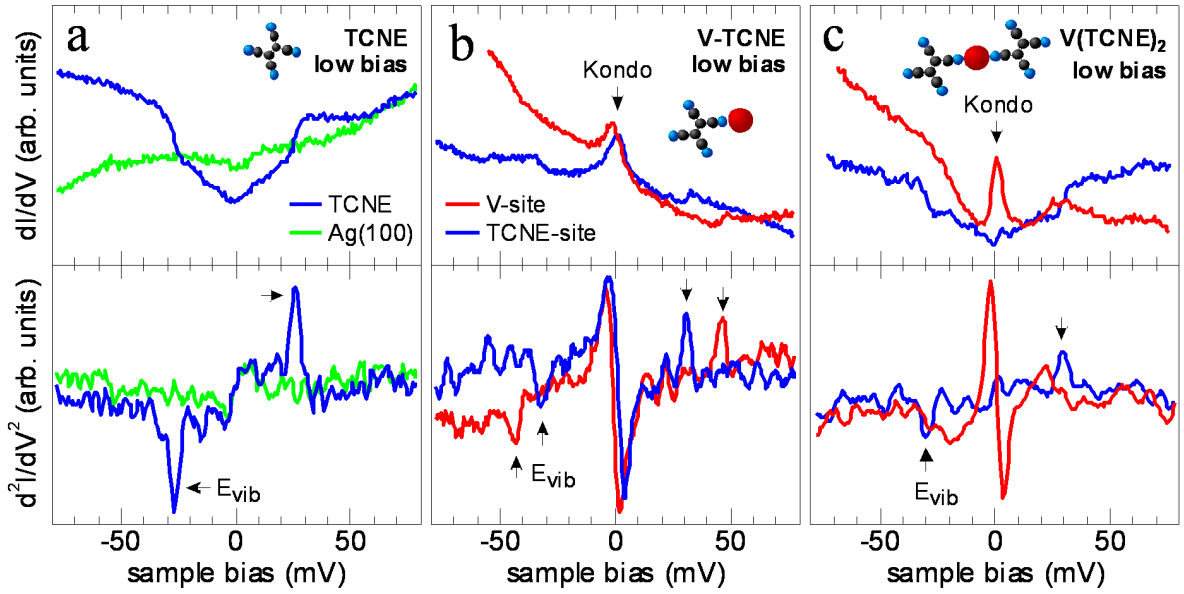

Figure 13.10: dI/dV and d^2I/dV^2 spectra for (a) TCNE, (b) V-TCNE, (c) $V(TCNE)_2$. The arrows mark the position of either IETS signals caused by molecular vibrations (labeled E_{vib}) or the Kondo resonance. The Ag(001) spectroscopy curve (green curve in (a)), was subtracted from all other dI/dV spectra to help deconvolute the non-constant tip DOS from the spectra (appendix B).

the $\pm 1\,\text{V}$ range shows a resonance around $-0.15\,\text{V}$ on both V and TCNE, although the resonance on TCNE is broader (figure 13.11a). In the $\pm 80\,\text{mV}$ range, a narrow resonance appears near E_F (figure 13.11c).

In V_2(TCNE)@11°, spectroscopy in the $\pm 1\,\text{V}$ range looks very similar to the spectroscopy

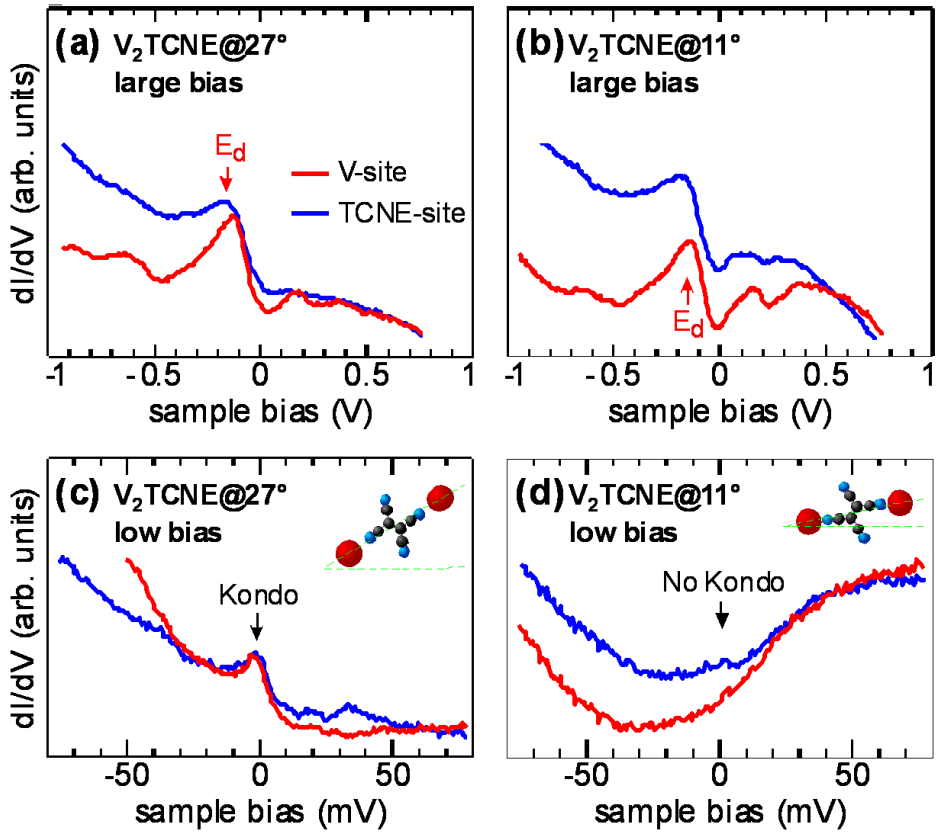

Figure 13.11: High bias dI/dV spectroscopy on (a) V_2(TCNE)@27°, (b) V_2(TCNE)@11°, and low bias spectroscopy on (c) V_2(TCNE)@27°, and (d) V_2(TCNE)@11°. The Ag background was subtracted from the spectra in (c) and (d) to deconvolute the non-constant tip DOS (appendix B). The state believed to arise from the V d-orbital is labeled E_d.

on trans-V_2(TCNE)@27° in the same voltage range—there is a resonance around -0.15 V on both V and TCNE, and the resonance on TCNE is broader. However, at lower biases, unlike spectroscopy on trans-V_2(TCNE)@27°, spectroscopy on trans-V_2(TCNE)@11° reveals no narrow resonance near E_F.

To help explain the data, SP-DFT calculations by Tunna Baruah and Mark Pederson were done using NRLMOL [162, 91, 163, 161]. The basis functions were similar to triple-ζ and PBE-GGA was used for the exchange-correlation functional [165].

Calculations were performed on free V(TCNE) and V_2(TCNE). The substrate was not included in the calculations, but we suspect that an electron is donated from the surface to V_x(TCNE), so the structures were singly negatively charged. V atoms on Ag(001) are found to be neutral. It is assumed that they acquire no additional charge from the substrate in V_x(TCNE) complexes. The DFT LDOS of these structures reveal a resonance at ~ -0.2 V, which is due to a singly occupied V atom d-state (figure 13.12). This is in good agreement with the experimentally observed peak at ~ -0.2 V in both V(TCNE) and V_2(TCNE). The

agreement between experiment and theory only occurs when the V_x(TCNE) structures are singly negatively charged; neutral and twice negatively charged structures do not have the strong resonance near −0.2 V.

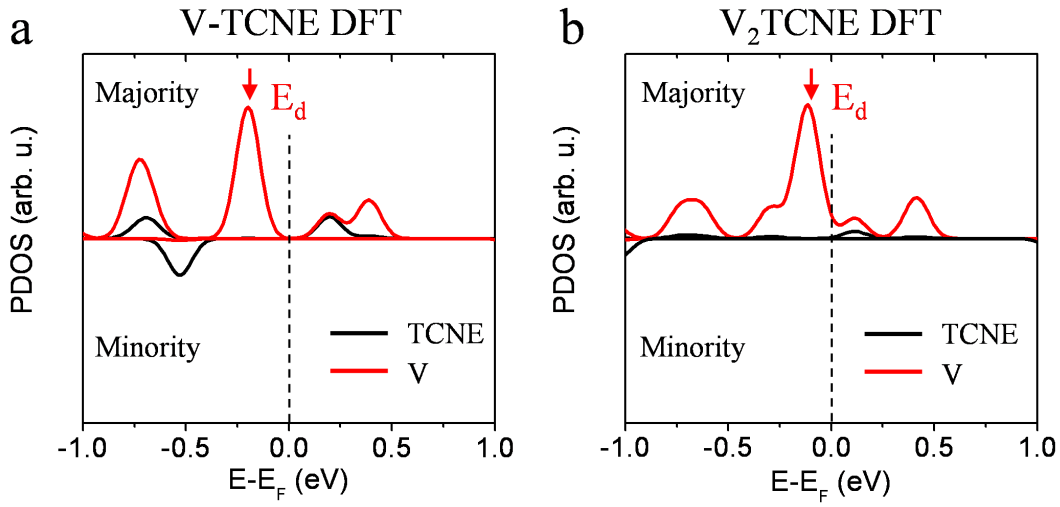

Figure 13.12: V-TCNE and V_2(TCNE) SP-DFT calculations. The state believed to arise from the V d-orbital is marked with E_d.

Since the resonance near 0 V is has a narrow width ∼20 mV, it is much narrower than expected for molecular orbitals hybridized with a surface. This suggests that the resonance near 0 V is a Kondo resonance (§4.4.3, [120, 131]). We expect that the spatial distribution of the Kondo state is the same as the molecular orbital which leads to it. Since the narrow resonance near 0 V has the same spatial distribution as the resonance near −0.2 V for all $V_x(TCNE)_y$ structures, it is likely that the Kondo resonance is caused by the single electron in the V d-orbital.

Since the Kondo effect is a many body effect due to the interaction between the $V_x(TCNE)_y$ complex and the surface, DFT cannot reproduce this effect correctly. However, we may still explain qualitatively why V_2(TCNE)@27° has a Kondo while V_2(TCNE)@11° does not. We first note that the distance between V atoms is around 1 nm, which is much larger than expected for coupling through the surface [30, 192]. Hence, we expect coupling through the TCNE molecule. We then note that the distance between V atoms in V_2(TCNE)@11° is ≈ 1 Å smaller than in V_2(TCNE)@27°. This means that the V atoms will interact more strongly with TCNE in V_2(TCNE)@11°. SP-DFT predicts that the singly charged V_2(TCNE) will have a single spin on each V atom that interacts ferromagnetically, and hence the ferromagnetic interaction will be stronger in V_2(TCNE)@11°. It is known that ferromagnetic interactions between spins can lower the Kondo temperature [96], and hence, V_2(TCNE)@11° has no Kondo resonance due to its lower Kondo temperature.

The Kondo temperature may also change due to changes in the energy of the d-state, changes in the hybridization, or changes in the Coulomb energy U. However, changes in

these variables are not likely since the *d*-state energy and width are the same for both V_2(TCNE) structures, according to the data. The lowering of the Kondo temperature due to ferromagnetic interaction is then supported by the data.

13.4 V(TCNE) on NaCl

Magnetic structures on a metallic surfaces can interact with the electrons of the surface, altering its intrinsic magnetic properties. To overcome this problem, a thin insulating layer can be grown on a metallic surface. NaCl is an easily grown insulator which was used to accomplish this. Figure 13.13 shows topography of TCNE on second and third layers of NaCl. Spectroscopy shows a LUMO around 1.5 V for TCNE on a second layer NaCl and 1.8 V for TCNE on a third layer of NaCl. Unfortunately, after depositing V and manipulating TCNE molecules and V atoms together (only TCNE could be manipulated controllably on NaCl), we did not see any evidence of spin in V(TCNE) and we were not able to manipulate V(TCNE) or V to create larger structures.

13.5 Conclusions

This chapter discussed both the interactions between TCNE and noble metal substrates, as well as controlling the TCNE-mediated spin coupling between electrons on different V atoms via STM molecular manipulation. We found that the ionic binding between TCNE and noble metals, as well as any TCNE-induced surface reconstruction, is more strongly influenced by the lattice structure of the metal surface than by the surface work functions of the different metals. We also found that $V_x(TCNE)_y$ complexes on Ag(001) can be created with STM molecular manipulation, and in trans-V_2(TCNE), there is evidence suggesting that the TCNE-mediated coupling of spins between the two V atoms can be controlled by changing the distance between V and TCNE.

This concludes part III of this dissertation. Following this chapter are extensive technical appendices describing the experimental techniques in greater detail.

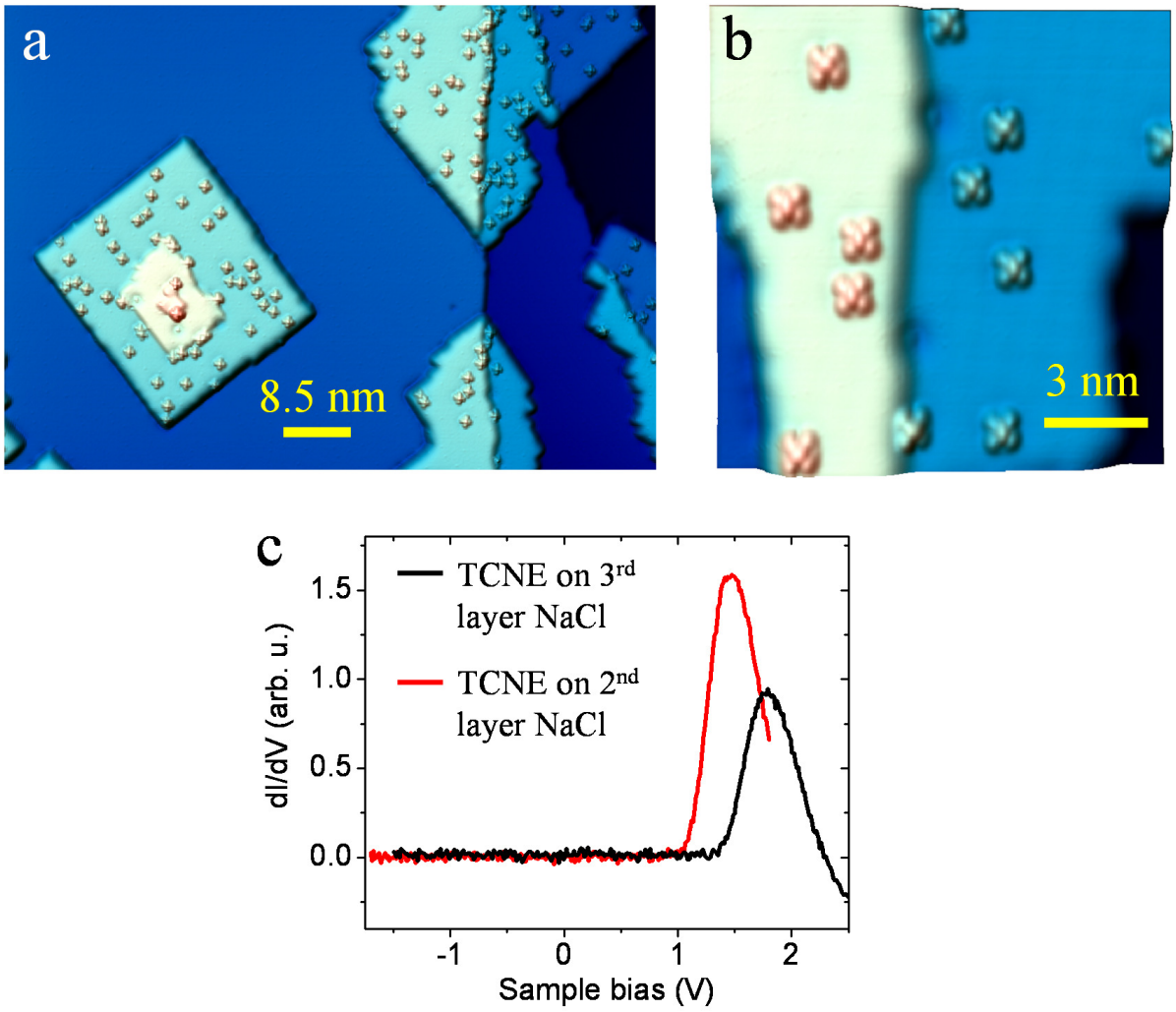

Figure 13.13: Topograph of TCNE on NaCl (a) Large area showing mainly second layer NaCl islands with isolated TCNE colored brown on it ($V = 1.4\,\mathrm{V}$, $I = 1\,\mathrm{pA}$). (b) Zoom in on a second layer NaCl island with isolated TCNE molecules colored brown. (c) Spectroscopy on TCNE on the second and third layer NaCl islands. The NDR around 2.4 V is likely due to the voltage dependence of the tunneling barrier (§3.3.1).

A The Lock-in Amplifier

When we calculate dI/dV, we may simply numerically differentiate $I(V)$ with respect to V. However, to take a numerical derivative, we need $I(V)$ to be very noise-free, since any noise in $I(V)$ will become much larger in its derivative. Since $I(V)$ contains noise at many different frequencies, its derivative dI/dV will also contain much noise. To calculate dI/dV with little noise, we need a way of removing the noise at various frequencies. The lock-in amplifier allows us to do that, and it does it with a much better quality factor than a typical band-pass filter.

We will see that if we apply a small oscillating voltage with angular frequency ω_0 to the STM tip and measure the tunneling current with a lock-in amplifier, the output of the lock-in amplifier will be proportional to dI/dV (§A.3). However, the noise in dI/dV will be due to only the noise at frequency ω_0 and no other frequency, so the lock-in amplifier allows us to eliminate most of the noise from dI/dV.

A.1 The Ideal Lock-in

Here we describe the theoretical basis of the ideal lock-in amplifier. If we have a voltage signal $f(t)$ that oscillates with periodicity T, we may write it as a Fourier series

$$f(t) = \frac{B_0}{2} + \sum_{n=1}^{\infty} A_n \sin(n\omega_0 t) + B_n \cos(n\omega_0 t) \,. \tag{A.1}$$

where $\omega_0 = 2\pi/T$. A_n and B_n are called the Fourier coefficients.

Often, we want to find A_n and B_n. To calculate the Fourier coefficients A_n or B_n by hand, we would multiply $f(t)$ by $\sin n\omega_0 t$ or $\cos n\omega_0 t$ and integrate over a complete period

$T = 2\pi/\omega_0$, then multiply the result by ω_0/π. Mathematically, this is

$$A_n = \frac{\omega_0}{\pi} \int_{t_0}^{t_0+2\pi/\omega_0} f(t) \sin n\omega_0 t \, dt \tag{A.2}$$

$$B_n = \frac{\omega_0}{\pi} \int_{t_0}^{t_0+2\pi/\omega_0} f(t) \cos n\omega_0 t \, dt \tag{A.3}$$

where t_0 is any real number.

A *lock-in amplifier* (or simply, a *lock-in*) is a device that allows us to extract the Fourier coefficients from the periodic signal $f(t)$ by doing something very similar (via analog or digital electronics) to the process described above: it takes the input signal $f(t)$, multiplies it by another signal $\sin(n\omega_{\text{ref}}t + \phi_n)$, integrates over a complete period, then multiplies the result by $\omega_0/(\pi\sqrt{2})$. Mathematically, the process that the ideal lock-in performs can be written as

$$V_{\text{ideal}} = \frac{\omega_0}{\pi\sqrt{2}} \int_{t_0}^{t_0+2\pi/\omega_0} f(t) \sin(n\omega_{\text{ref}}t + \phi_n) \, dt \, . \tag{A.4}$$

This expression leads to a voltage which is proportional to the voltage on one of the outputs of the lock-in.

When we compare the mathematical procedure for calculating Fourier coefficients [equation (A.2)] with the procedure the lock-in performs [equation (A.4)], we see that they are very similar; they only differ in three places: ω_{ref} instead of ω_0, an additional phase ϕ_n in the sine, and an overall extra factor of $\sqrt{2}$. Since ω_{ref} and ϕ_n are user-adjustable parameters, if we set $\omega_{\text{ref}} = \omega_0$ and $\phi_n = 0$, then the lock-in will calculate the voltage $A_n/\sqrt{2}$. Hence, the lock-in allows us to measure the Fourier coefficients of a periodic signal.

This was a brief introduction to what an ideal lock-in is supposed to do and how it does it. The next sections will describe in greater detail the inputs, outputs, and adjustable parameters of an ideal lock-in.

A.1.1 Inputs

A lock-in amplifier generally takes two input signals. One input signal is the experimental signal, which is a periodic signal $f(t)$ [equation (A.1)] from which we want to extract Fourier coefficients from, and the other is called the reference signal $V_{\text{ref}}(t) = \sin(\omega_{\text{ref}}t + \phi)$ (in units of volts), which normally comes from a function generator. Sometimes the lock-in has a built-in function generator, so the reference signal is an internal signal in the lock-in, and the reference signal input is not used. As discussed above, normally we choose $\omega_{\text{ref}} = \omega_0$.

A.1.2 Outputs

A lock-in has two output signals (this assumes we have a dual-phase lock-in); the value of these signals depends on what output mode the user selects. The most common output signals are called X, Y, R, and θ, and the user can select any two of these four to output.

Different lock-in's will have different ways of selecting these outputs; for example, on a PAR 5210, one must select XY-mode to get outputs X and Y, or $R\theta$-mode to get R and θ.

X and Y

This is how the lock-in calculates the values of the X and Y outputs. If we input the two signals, $f(t)$ [equation (A.1)] and $V_{\text{ref}}(t) = \sin(\omega_{\text{ref}}t + \phi)$ into the lock-in, the lock-in first internally multiplies the reference signal frequency by an integer factor n and changes the phase of it to ϕ_n (both n and ϕ_n are chosen by the user as described in the next section). The phase ϕ_n is not necessarily the same as the reference voltage phase ϕ. The modified reference signal is then $\tilde{V}_{\text{ref}}(t) = \sin(n\omega_{\text{ref}}t + \phi_n)$.

The procedure to calculate the X output then follows that given in deriving (A.4): we multiply $f(t)$ by $\tilde{V}_{\text{ref}}(t)$, integrate the result over a complete period $T = 2\pi/\omega_0$, and multiply that result by $\omega_0/\pi\sqrt{2}$. The Y output has the exact same procedure, except we shift the phase of $\tilde{V}_{\text{ref}}(t)$ by 90° before multiplying with $f(t)$.

This procedure yields voltages, which are normally displayed on the front panel of the lock-in. With $\omega_{\text{ref}} = \omega_0$, they are

$$V_{\text{x}} = \frac{\omega_0}{\pi\sqrt{2}} \int_{t_0}^{t_0+2\pi/\omega_0} f(t) \sin(n\omega_0 t + \phi_n)\, dt \tag{A.5}$$

$$V_{\text{y}} = \frac{\omega_0}{\pi\sqrt{2}} \int_{t_0}^{t_0+2\pi/\omega_0} f(t) \cos(n\omega_0 t + \phi_n)\, dt\,. \tag{A.6}$$

By plugging in $f(t)$ [equation (A.1)] and performing the integral, these expressions simplify to

$$V_{\text{x}} = \frac{1}{\sqrt{2}}(B_n \sin\phi_n + A_n \cos\phi_n) \tag{A.7}$$

$$V_{\text{y}} = \frac{1}{\sqrt{2}}(B_n \cos\phi_n - A_n \sin\phi_n) \tag{A.8}$$

The number n [which denotes the n^{th} term in the Fourier series of $f(t)$] is also referred to as the n^{th} *harmonic*, so, for example, $n = 2$ would be the second harmonic.

The actual voltages on the output of the lock-in are different than the numbers displayed on the front panel. The actual output voltages are proportional to V_{x} and V_{y}

$$V_{\text{out 1}} = C\, V_{\text{x}}$$
$$V_{\text{out 2}} = C\, V_{\text{y}}$$

where the constant of of proportionality C is determined by the settings of the lock-in and may be different for different lock-in's. One must read the manual for the lock-in to determine its value. Alternatively, to determine C, one may apply a signal $f(t) = V_0 \sin(\omega t)$ with a known amplitude V_0 to the input of the lock-in and compare the two output voltages

of the lock-in to the values V_x and V_y.

R and θ

If we consider the two voltages V_x and V_y of the lock-in as the x and y components of a 2-D vector in Cartesian coordinates $\vec{r} = (V_x, V_y)$, then this vector would have polar coordinates

$$R = \sqrt{V_x^2 + V_y^2}$$
$$\theta = \tan^{-1} \frac{V_y}{V_x}$$

These values of R and θ are the values displayed on the lock-in front panel. The actual output voltages are proportional to the R and θ values, with the same proportionality factor C as for the X and Y outputs.

A.1.3 Adjustable parameters

The ideal lock-in also has two adjustable parameters, the harmonic number n, and the phase ϕ_n, which are chosen based on what we want to measure (§A.3.4, §A.4.2 discuss how to choose the phase to measure dI/dV and d^2I/dV^2). Normally we set $n = 1$ or 2, and $\phi_n = 0$.

For example, if we want to measure the Fourier coefficients of the signal $f(t)$ at the frequency ω_0 (the first harmonic), we set $n = 1$ and adjust the phase $\phi_1 = 0$, so that the lock-in will display the voltages

$$V_x = A_1/\sqrt{2}$$
$$V_y = B_1/\sqrt{2}\,.$$

If we set $n = 1$ and adjust the phase so that $\phi_1 = 90°$, the lock-in will display $B_1/\sqrt{2}$ and $-A_1/\sqrt{2}$.

This is all that is really needed to know to use a lock-in. However, to truly understand any measurement using a lock-in, it is important to understand how the real lock-in computes the Fourier coefficients A_n and B_n.

A.2 The Real Lock-in

The real lock-in has the same inputs and outputs as the ideal lock-in. The difference comes in how it calculates the Fourier coefficients. The non-ideal behavior of the lock-in will also force us to have additional adjustable parameters described in §A.2.3, which help us optimize the lock-in performance.

A.2.1 Calculating the Fourier coefficients

The main point of this section is to show that the way the ideal lock-in calculates Fourier coefficients is a good approximation to the way a real lock-in does it.

The real lock-in uses a slightly different method to measure Fourier coefficients than the ideal lock-in. It first multiplies the signal $f(t)$ given by (A.1) by $\tilde{V}_{\text{ref}}(t) = \sin(n\omega_0 t + \phi_n)$, like the ideal lock-in, but then it passes this signal through a low-pass filter instead of actually integrating the signal. By working through all the mathematical details, we will see next that the low pass filter is a good approximation to integrating over a complete period. Consider how the real lock-in calculates the X output for the n^{th} harmonic.

1. As stated earlier, the lock-in multiplies the frequency of the reference signal by n to get the modified reference signal $\tilde{V}_{\text{ref}}(t) = \sin(n\omega_0 t + \phi_n)$, where ϕ_n is a phase which depends on n and is not necessarily the same as the original reference signal phase ϕ.

2. The lock-in then multiples $f(t)$ by $\tilde{V}_{\text{ref}}(t)$ to get $f(t)\sin(n\omega_0 t + \phi_n)$. The resulting function may be expanded in a series as

$$f(t)\sin(n\omega_0 t + \phi_n) = \frac{1}{2}\sum_{m=-\infty}^{\infty} B_{n-m}\sin(m\omega_0 t + \phi_n) + A_{n-m}\cos(m\omega_0 t + \phi_n) \quad \text{(A.9)}$$

   where we define $A_{-m} = -A_m$ (which implies $A_0 = 0$) and $B_{-m} = B_m$. This can be rewritten in terms of a constant part (the $m = 0$ term) and oscillating parts

$$\begin{aligned} f(t)\sin(n\omega_0 t + \phi_n) = {} & \frac{1}{2}(B_n \sin\phi_n + A_n \cos\phi_n) \\ & + \frac{1}{2}\sum_{\substack{m=-\infty \\ m\neq 0}}^{\infty} B_{n-m}\sin(m\omega_0 t + \phi_n) + A_{n-m}\cos(m\omega_0 t + \phi_n) \end{aligned}$$

   So the Fourier coefficients that we want, A_n and B_n, are proportional to the constant part of $f(t)\sin(n\omega_0 t + \phi_n)$, or equivalently, it is proportional to the DC part of the oscillating signal $f(t)(\sin n\omega_0 t + \phi_n)$.

3. So after the lock-in multiplies $f(t)$ by $\sin(n\omega_0 t + \phi_n)$, it passes the result through a low pass filter to recover $\frac{1}{2}(B_n \sin\phi_n + A_n \cos\phi_n)$, the DC part of $f(t)\sin(n\omega_0 t + \phi_n)$.

   In reality, the low pass filter is not ideal. If the gain of the low pass filter at frequency ω is $G(\omega, \omega_c)$ where ω_c is an adjustable parameter (§A.2.3) called the cutoff frequency

of the filter, then the actual output of the low pass filter will be

$$\frac{1}{2}(B_n \sin\phi_n + A_n \cos\phi_n) + \frac{1}{2}\sum_{\substack{m=-\infty \\ m\neq 0}}^{\infty} G(|m\omega_0|,\omega_c)\big[B_{n-m}\sin(m\omega_0 t+\phi_n) + A_{n-m}\cos(m\omega_0 t+\phi_n)\big]$$

4. The lock-in then multiplies the result of part 3 by $2/\sqrt{2}$ to give us a voltage $V_{\rm x}$. The value of this voltage is normally displayed on the front panel of the lock-in.

Voltage $V_{\rm x}$ for a real lock-in can then be written as

$$V_{\rm x} = \frac{1}{\sqrt{2}}(B_n \sin\phi_n + A_n \cos\phi_n) + \frac{1}{\sqrt{2}}\sum_{\substack{m=-\infty \\ m\neq 0}}^{\infty} G(|m\omega_0|,\omega_c)\big[B_{n-m}\sin(m\omega_0 t+\phi_n) + A_{n-m}\cos(m\omega_0 t+\phi_n)\big] \quad \text{(A.10)}$$

Ideally, the low pass filter will only allow the DC part of the signal to get through, so that $V_{\rm x} \approx \frac{1}{\sqrt{2}}(B_n \sin\phi_n + A_n \cos\phi_n)$. To get an idea of how good an approximation this is, consider a typical filter, a second order Butterworth filter. A second order Butterworth low pass filter has a slope of 12 dB/octave and gain $G(\omega,\omega_c) = (1+(\omega/\omega_c)^4)^{-1/2}$, and typically we adjust ω_c so that $\omega_c = \omega_0/10$ (§A.2.3). With this filter, the amplitude of every AC term in the Fourier series (A.10), will be reduced by at least 10^2. Hence, to a good approximation, we may filter out the AC components of the signal (A.10), and we will recover its DC component, $\frac{1}{\sqrt{2}}(B_n \sin\phi_n + A_n \cos\phi_n)$.

So finally, when a signal $f(t)$ given by (A.1) with period $T = 2\pi/\omega_0$ is put into a lock-in, we see that to a good approximation, the voltage $V_{\rm x}$ displayed on the lock-in front panel will simply be $\frac{1}{\sqrt{2}}(B_n \sin\phi_n + A_n \cos\phi_n)$, which is exactly the same as the ideal lock-in expression for $V_{\rm x}$, equation (A.7). We may then use the ideal lock-in equations (A.5) and (A.7) to calculate $V_{\rm x}$

$$V_{\rm x} \approx \frac{1}{\sqrt{2}}(B_n \sin\phi_n + A_n \cos\phi_n) = \frac{1}{\sqrt{2}}\frac{\omega_0}{\pi}\int_{t_0}^{t_0+2\pi/\omega_0} f(t)\sin(n\omega_0 t+\phi_n)\,dt \quad \text{(A.11)}$$

$$= \frac{1}{\sqrt{2}}\frac{\omega_0}{\pi}\int_{t_0}^{t_0+2\pi/\omega_0} f(t)\tilde{V}_{\rm ref}(t)\,dt\,. \quad \text{(A.12)}$$

This is a useful approximation that will be used often in the next sections.

To calculate the actual voltage on output 1 from the displayed voltage $V_{\rm x}$, one must

multiply by the constant C, as discussed in §A.1.2

$$\begin{aligned} V_{\text{out 1}} &= C\, V_{\text{x}} \\ &\approx \frac{C}{\sqrt{2}} \frac{\omega_0}{\pi} \int_{t_0}^{t_0+2\pi/\omega_0} f(t) \sin(n\omega_0 t + \phi_n)\, dt\ . \end{aligned}$$

A.2.2 Effects of noise

In the preceding section, the signal was assumed to be periodic with period T. However, if there is noise in the signal, the noise need not be periodic, and this is where the real lock-in output will deviate from the approximate lock-in output given by (A.11). From the preceding section, we can get an idea of how noise on the input to the lock-in will affect the output.

Suppose that the noise has angular frequency γ and amplitude $A(\gamma)$, so that the noise can be written as $N(t) = A(\gamma) \sin \gamma t$. Following the steps in the preceding section, output 1 of the lock-in due to this noise will be

$$V_{\text{out 1}} = C \frac{A(\gamma)}{\sqrt{2}} \big[G(n\omega_0 - \gamma, \omega_c) \cos(n\omega_0 - \gamma)t - G(n\omega_0 + \gamma, \omega_c) \cos(n\omega_0 + \gamma)t \big]$$

Since $G(\omega, \omega_c) \approx 1$ for $\omega \leq \omega_c$ and is approximately zero otherwise, from this expression for $V_{\text{out 1}}$, we see that by choosing $\omega_c < \omega_0$, we can always make the second term vanish. However, no matter how small ω_c is, for frequencies γ which satisfy $|n\omega_0 - \gamma| \leq \omega_c$ (or equivalently $n\omega_0 - \omega_c \leq \gamma \leq n\omega_0 + \omega_c$), the first term will still contribute to the output of the lock-in. So the lock-in does not filter out noise at frequencies within ω_c of $n\omega_0$. The smaller we adjust ω_c in the low pass filter (§A.2.3), the more noise we will filter out.

A.2.3 Additional adjustable parameters

The real lock-in has many parameters in addition to the parameters of the ideal lock-in. The two most important are the output range (usually called the sensitivity) and the time constant mentioned in §A.2.1. If the output voltage of the lock-in will only be between $-100\,\text{mV}$ to $100\,\text{mV}$, we should set the output voltage range to $100\,\text{mV}$. This will optimize the signal-to-noise ratio of the lock-in output voltages.

The cutoff frequency ω_c of the low pass filter described in the previous sections can be adjusted. The parameter that controls it is called the *lock-in time constant*. The lock-in time constant τ is related to ω_c by $\tau = 2\pi/\omega_c$. As mentioned in §A.2.1, if we want to measure the Fourier coefficient at frequency $n\omega_0$, we must adjust the time constant properly so we effectively filter out the effect of all frequencies not at $n\omega_0$. However, in addition, there is usually noise at various frequencies, and a larger time constant means we filter out more of that noise (§A.2.2). So choosing a larger time constant is always better to achieve lower noise on the lock-in output. The only drawback to a longer time constant is that the lock-in takes a few time constants ($\sim 3\tau$) to adjust its output voltage to its final value. This

means that a larger time constant means we have to wait longer before the voltage displayed on the front panel on the lock-in is at the value given by (A.11).

Typically we have $\tau = 30\,\text{ms}$ and $\omega_0 = 2\pi(451\,\text{Hz}) \approx 2834\,\text{Hz}$, so that $\omega_c = 2\pi/\tau \approx 209\,\text{Hz} \approx \omega_0/14$.

A.3 dI/dV Measurements

To measure dI/dV with a lock-in, we first add a small oscillating voltage $\Delta V = \delta V \sin\omega_0 t$ to the DC voltage V on the STM tip, so that the tunneling current becomes $I(V+\Delta V)$. We then pass the tunneling current through a current to voltage converter to get $I(V+\Delta V)/G$ where G is the gain of the current to voltage converter; typically $G = 10^{-9}\,\text{A/V}$. Next, the output of the current to voltage converter is put into a lock-in to measure the rms amplitude of its first harmonic (the rms Fourier component of $I(V+\Delta V)/G$ at the frequency ω_0 and phase $\phi_1 = 0$). We will see below [equation (A.16)] that the X output voltage of the lock-in is proportional to $dI(V)/dV$ in the limit of small δV, and hence the lock-in can be used the measure dI/dV. Furthermore, equation (A.14) will show exactly how the lock-in broadens dI/dV when δV is non-zero.

To see why the first harmonic of $I(V+\Delta V)$ is $\propto dI/dV$ qualitatively, expand $I(V+\Delta V)$ in a Taylor series to first order $I(V+\Delta V) \approx I(V) + \frac{dI(V)}{dV}\Delta V = I(V) + \frac{dI(V)}{dV}\delta V \sin\omega_0 t$. To first order, the tunneling current is then sinusoidal with frequency ω_0, and if we use the lock-in to find the Fourier component at frequency ω_0, then the X output of the lock-in will be proportional to $dI(V)/dV$.

A.3.1 dI/dV measured by a lock-in

For the situation mentioned above, the X output voltage V_x displayed on the front panel of the lock-in can be calculated with (A.11). With $\phi_n = 0$, $f(t) = I(V+\Delta V)/G = I(V+\delta V\sin\omega_0 t)/G$, $t_0 = -\frac{\pi}{2\omega_0}$, and $x = -\delta V \sin\omega_0 t$, (A.11) can be partially written in terms of x as

$$V_\text{x}(V) = \frac{1}{G}\frac{\omega_0}{\pi\sqrt{2}}\int_{t=-\pi/2\omega_0}^{t=3\pi/2\omega_0} I(V-x)\frac{x}{\delta V}\frac{dx}{\delta V\omega_0\cos\omega_0 t}\,dx$$

To completely write the integral as a function of x, substitute

$$\cos\omega_0 t = \begin{cases} \sqrt{1-\frac{x^2}{\delta V^2}} & \text{for } -\frac{\pi}{2\omega_0} \le t < \frac{\pi}{2\omega_0} \\ -\sqrt{1-\frac{x^2}{\delta V^2}} & \text{for } \frac{\pi}{2\omega_0} \le t < \frac{3\pi}{2\omega_0} \end{cases} \tag{A.13}$$

and split the integral into two parts, $\int_{t=-\pi/2\omega_0}^{\pi/2\omega_0} + \int_{t=\pi/2\omega_0}^{3\pi/2\omega_0}$, using the appropriate substitution of $\cos\omega_0 t$ for each part. These two parts are equal to each other so their sum gives

$$V_{\mathrm{x}}(V) = -\frac{1}{G}\frac{1}{\sqrt{2}}\frac{2}{\pi\delta V^2}\int_{-\delta V}^{\delta V} I(V-x)x\left(1-\frac{x^2}{\delta V^2}\right)^{-1/2} dx$$

Applying integration by parts to this expression gives

$$V_{\mathrm{x}}(V) = \frac{1}{G}\frac{\delta V}{\sqrt{2}}\int_{-\delta V}^{\delta V}\frac{dI(V-x)}{dV}\frac{2}{\pi\delta V^2}\sqrt{\delta V^2 - x^2}\, dx$$

which can be written as the convolution

$$V_{\mathrm{x}}(V) = \frac{1}{G}\frac{\delta V}{\sqrt{2}}\left(\frac{dI}{dV} * B_{L1}\right) = \frac{1}{G}\frac{\delta V}{\sqrt{2}}\int_{-\infty}^{\infty}\frac{dI(V-x)}{dV}B_{L1}(x)\, dx \tag{A.14}$$

$$\text{with}\quad B_{L1}(x) = \begin{cases} \frac{2}{\pi\delta V^2}\sqrt{\delta V^2 - x^2} & \text{for } |x| < \delta V \\ 0 & \text{for } |x| \geq \delta V\ . \end{cases} \tag{A.15}$$

Hence, we see that voltage V_{x} displayed on the front of the lock-in will be dI/dV convoluted with the broadening function B_{L1}. $B_{L1}(x)$ is sketched in figure A.1.

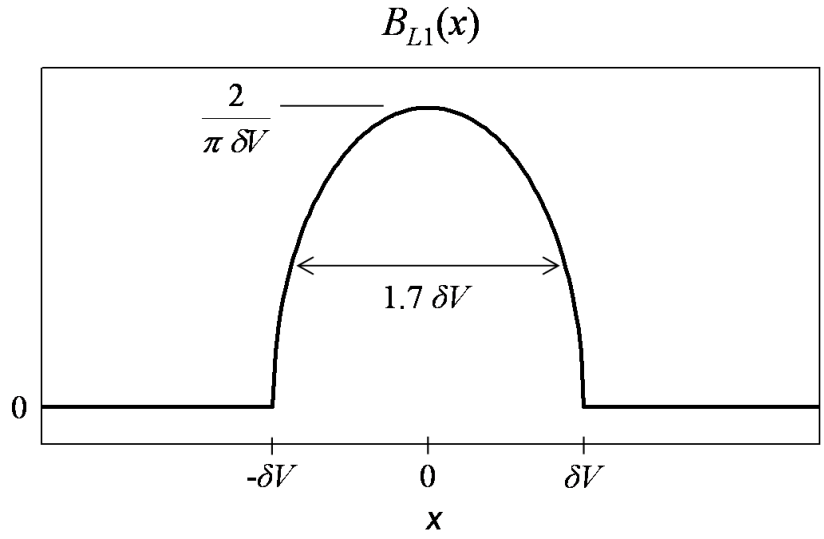

Figure A.1: Lock-in dI/dV broadening function $B_{L1}(x)$. It has a height $2/\pi\delta V$ and FWHM $1.7\delta V$.

In the limit $\delta V \to 0$, the broadening function $B_{L1}(x) \to \delta(x)$, and hence,

$$\lim_{\delta V \to 0} V_{\mathrm{x}} \frac{G}{\delta V/\sqrt{2}} = \frac{dI(V)}{dV} .$$

This means that for small δV, we may calculate dI/dV as

$$\frac{dI(V)}{dV} \approx G \frac{V_{\mathrm{x}}}{\delta V_{\mathrm{rms}}} \tag{A.16}$$

where $\delta V_{\mathrm{rms}} = \delta V/\sqrt{2}$, and G is again the current to voltage converter gain in A/V. This equation shows that the X output of the lock-in when we apply a voltage $V + \delta V \sin \omega_0 t$ to the tip is proportional to $dI(V)/dV$.

To relate this result to the actual voltage output of the lock-in $V_{\mathrm{out\ 1}}$, we must divide this result by the constant C, as discussed in §A.1.2

$$\frac{dI(V)}{dV} \approx G \frac{V_{\mathrm{x}}}{\delta V_{\mathrm{rms}}} = \frac{G}{C} \frac{V_{\mathrm{out\ 1}}}{\delta V_{\mathrm{rms}}} .$$

This equation gives us dI/dV with the correct units in terms of the output voltage of the lock-in.

A.3.2 dI/dV broadening from the lock-in

Equation (A.14) gives us a way to think about how the lock-in measured dI/dV, $[dI/dV]_{\text{lock-in}} = GV_{\mathrm{x}}/\delta V_{\mathrm{rms}}$, deviates from the true dI/dV, call it $[dI/dV]_{\text{true}}$. It shows that peaks in $[dI/dV]_{\text{lock-in}}$ are broadened relative to peaks in $[dI/dV]_{\text{true}}$. For example, if $G = 1\,\mathrm{A/V}$ and $[dI/dV]_{\text{true}}$ is an infinitely sharp delta-function peak, $[dI(V)/dV]_{\text{true}} = \delta(V)$ (in arbitrary units), then

$$\left[\frac{dI}{dV}\right]_{\text{lock-in}} = \frac{V_{\mathrm{x}}}{\delta V_{\mathrm{rms}}} = B_{L1}(V) .$$

So $[dI/dV]_{\text{lock-in}}$ in this case is not a infinitely sharp peak, it is the broadening function B_{L1} shown in figure A.1. Since the FWHM of $B_{L1}(V)$ is $\delta V\sqrt{3}$, we see that peaks in $[dI/dV]_{\text{true}}$ are broader in $[dI/dV]_{\text{lock-in}}$ by about $\delta V\sqrt{3} = 1.7\delta V = 2.4\delta V_{\mathrm{rms}}$.

However, the effect of broadening is not always so intuitive. For example, if $G = 1\,\frac{\mathrm{A}}{\mathrm{V}}$ and $I(V)$ is quadratic, $I(V) = V^2$, then $[dI/dV]_{\text{lock-in}}$ calculated from (A.14), will be the exact first derivative

$$\left[\frac{dI}{dV}\right]_{\text{lock-in}} = \frac{V_{\mathrm{x}}}{\delta V_{\mathrm{rms}}} = 2V = \left[\frac{dI}{dV}\right]_{\text{true}} .$$

However, if $I(V) = V^3$, then $[dI/dV]_{\text{lock-in}}$ will be

$$\left[\frac{dI}{dV}\right]_{\text{lock-in}} = \frac{V_{\mathrm{x}}}{\delta V_{\mathrm{rms}}} = 3V^2 + \frac{3}{4}\delta V^2 = \left[\frac{dI}{dV}\right]_{\text{true}} + \frac{3}{4}\delta V^2 .$$

So $[dI/dV]_{\text{lock-in}}$ in this case is not really a broadened $[dI/dV]_{\text{true}}$; it is shifted from $[dI/dV]_{\text{true}}$ by the constant $3\delta V^2/4$.

A.3.3 Deconvoluting the lock-in broadening

Since (A.14) represents the convolution of dI/dV with the function B_{L1}, in principle, we may recover dI/dV from the lock-in signal by deconvolution. We use the convolution theorem to express the true dI/dV in terms of the Fourier transforms of $[dI/dV]_{\text{lock-in}} = GV_{\text{x}}/\delta V_{\text{rms}}$ and B_{L1}

$$\left[\frac{dI(V)}{dV}\right]_{\text{true}} = \text{FT}^{-1}\left[\frac{\text{FT}\left[\frac{dI}{dV}\right]_{\text{lock-in}}}{\text{FT}[B_{L1}]}\right]. \tag{A.17}$$

Although in principle we may deconvolute B_{L1} from dI/dV, in reality, the function $\text{FT}[B_{L1}]$ is a Bessel function with many zeros, and whenever $\text{FT}[B_{L1}] = 0$, the right hand side of (A.17) goes to ∞, unless the numerator is also zero. The numerator is rarely zero because of noise or offsets in the data. One way to overcome this problem is to deconvolute only a certain range of values in $[dI/dV]_{\text{true}}$, where we limit the deconvolution to the range where $\text{FT}[B_{L1}]$ is not zero.

Figure A.2 shows the result of using (A.17) where the modified function

$$\tilde{\text{FT}}[B_{L1}] = \begin{cases} \text{FT}[B_{L1}] & \text{for } \text{FT}[B_{L1}] > \max\Big\{\text{FT}[B_{L1}]\Big\}/5 \\ \max\Big\{\text{FT}[B_{L1}]\Big\}/5 & \text{otherwise.} \end{cases}$$

was used instead of $\text{FT}[B_{L1}]$. This modified function effectively limits the range of data that is deconvoluted to the range where $\text{FT}[B_{L1}]$ is not too small. The black curve in figure A.2 is a spectrum taken on Au(111) with an rms modulation voltage of $\delta V_{\text{rms}} = 20\,\text{mV}$. The red curve is the deconvolution of the black curve. The green curve is a spectrum taken at the exact same location and using the exact same settings as the black curve, but the rms modulation voltage was $\delta V_{\text{rms}} = 2\,\text{mV}$. Ideally, the red and green curves would look the same, and there are features like the two peaks around $-0.4\,\text{V}$ in the red curve that look like the features in the green curve. These features are not visible in the black curve, so the deconvolution worked to remove the broadening in the black curve and make these peaks resolvable. However, there are artifacts around $\pm 1\,\text{V}$ in the red curve that make this method not always reliable.

Another more reliable method of deconvolution is the same as the one presented in §3.1, but one must know the exact functional form of $[dI/dV]_{\text{true}}$ for this method to work. In this scheme, one fits the convolution $[dI/dV]_{\text{true}} * B_{L1}$ to the data $[dI/dV]_{\text{lock-in}}$. The best fit then yields parameters that tells one what $[dI/dV]_{\text{true}}$ is.

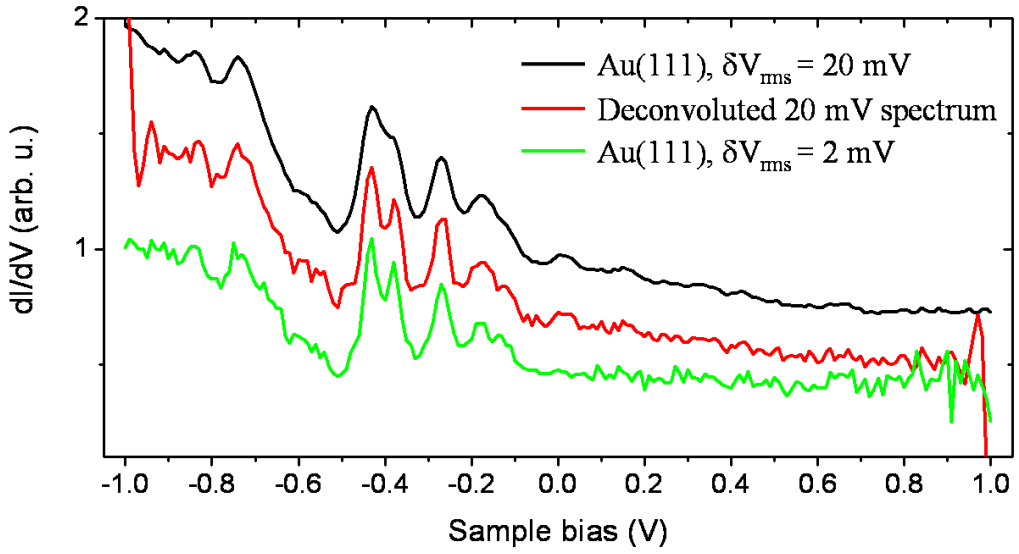

Figure A.2: Deconvoluting the broadening due to a non-zero modulation voltage from a dI/dV signal. The black curve is a spectrum taken with an rms modulation voltage of $\delta V_{\text{rms}} = 20\,\text{mV}$. The red curve is the black curve with the modulation induced broadening removed. The green curve was taken using the same settings as the black curve, except $\delta V_{\text{rms}} = 2\,\text{mV}$.

A.3.4 Adjusting the Phase

When we measure dI/dV with a lock-in, we need to adjust the phase difference ϕ_1 between the reference signal and the modified tunneling current so that $\phi_1 = 0$; the modified tunneling current is the tunneling current after it has passed through electronics, like the current to voltage converter, before entering the lock-in. The phase difference ϕ_1 is complicated since it depends on all the electronics that the tunneling current passes through before reaching the lock-in.

There is also another complication in a dI/dV measurement. To measure dI/dV, we need to apply a small oscillating voltage to the STM tip and measure the oscillating tunneling current. The tip and sample are two conducting materials that are placed close together, so they are also a capacitor. Any change in voltage on the tip will induce a current in the sample, purely due to the tip-sample capacitance. When we apply an oscillating voltage to the tip, we want to only measure the contribution to the current due to the oscillating tunneling current, not from the tip-sample capacitance current.

Both issues of determining the phase ϕ_1 and removing the tip-sample capacitance current can be dealt with using a procedure which will now be explained. The tunneling barrier acts as a resistor, so the tunneling current is the current through a resistor, which is in

phase with any oscillating voltage applied to the tip. The current due to the tip-sample capacitance is 90° behind any oscillating voltage applied to the tip, which means it is also 90° behind the oscillating tunneling current. If we can first find the phase of the capacitance current (after it has passed through all the electronics between the sample and lock-in) relative to the reference signal, we can then adjust that phase by 90° to get the phase of the modified tunneling current (the current after it has passed through the same electronics as the capacitance current) relative to the reference signal. Once we know the phase of the modified tunneling current relative to the reference signal, we can then adjust the lock-in phase so that the reference signal is in phase with the modified tunneling current ($\phi_1 = 0$), which is the phase we need. When the reference signal and modified tunneling current are in phase, the X output of the lock-in (the output used to measure dI/dV) will be determined solely by the tunneling current, since any signal 90° out of phase with the reference signal (like the capacitance current) will not contribute to the lock-in X output signal; this can be derived from equation (A.11).

To summarize, once we determine the phase of the capacitance current relative to the reference signal, we can adjust the phase so that the reference signal and the tunneling current are in phase ($\phi_1 = 0$), which eliminates the capacitance current from the X output of the lock-in, and since the X output is the one we use to measure dI/dV, the dI/dV signal contains no contribution from the capacitance. Hence, once we determine the phase of the capacitance current relative to the reference signal, we can eliminate the two problems of adjusting the lock-in to the correct phase and removing the capacitance current from the dI/dV measurements.

The procedure above relies on finding the phase of the tip-sample capacitance current relative to the reference signal. To find this phase,

1. we first position the tip so that we have a tunneling current.

2. Then we move the tip a few Ångstroms away from the surface, so that there is no tunneling current.

3. We apply an oscillating voltage to the tip. The current is converted to a voltage using the same current to voltage converter that we use to measure the tunneling current. The current we measure will be mainly due to the tip-sample capacitance.

4. The output voltage from the current to voltage converter goes into the lock-in. (The other input to the lock-in is the reference signal at the same frequency as the oscillating tip voltage). We then "autophase" the lock-in. It does not matter what output mode (§A.1.2) we are in when we do this. "Autophase" will adjust the lock-in reference signal phase to maximize the X output voltage (§A.1.2) of the lock-in (and the Y output will be 0). The lock-in can display what this phase is; call it θ_c. θ_c represents the phase that must be added to the reference signal so that the reference signal is in phase with the tip-sample capacitance current.

Once we know the phase θ_c, if we subtract 90° from it, we get the phase $\theta_I = \theta_c - 90°$, which is the phase that must be added to the reference signal so that it is in phase with the tunneling current. We can then set the lock-in phase equal to θ_I, which will add θ_I to the reference signal, making it in phase with the tunneling current, and eliminating the tip-sample capacitance current from dI/dV, as mentioned earlier.

A.4 d^2I/dV^2 Measurements

There are different ways of calculating d^2I/dV^2: one can numerically differentiate dI/dV, or one can use a lock-in amplifier. For the first method, one needs to average over many dI/dV curves to get a curve sufficiently low in noise to take a numerical derivative since noise from random fluctuations decreases like $1/\sqrt{N}$ [18].

Measuring d^2I/dV^2 with a lock-in is similar to measuring dI/dV, we first add a small oscillating voltage $\Delta V = \delta V \sin\omega_0 t$ to the DC voltage V on the STM tip, so that the tunneling current becomes $I(V + \Delta V)$. We then pass the tunneling current through a current to voltage converter to get $I(V + \Delta V)/G$ where G is the gain (in A/V) of the converter. Next, the output of the current to voltage converter is put into a lock-in, but instead of measuring the $n = 1$ first harmonic, we set the lock-in to measure the $n = 2$ second harmonic. The X output voltage then gives us the Fourier component of $I(V + \Delta V)/G$ at the frequency $2\omega_0$.

In addition, we must be sure that we choose the frequency ω_0 such that we do not filter out the signal at $2\omega_0$ with our other electronics, e.g. the current to voltage preamplifier. We must also adjust the phase between the reference signal and the input signal to the lock-in correctly, as described in §A.4.2.

We will see below [equation (A.20)] that the X output voltage of the lock-in in this situation is proportional to $d^2I(V)/dV^2$ in the limit of small δV, and hence the lock-in can be used the measure d^2I/dV^2. Furthermore, equation (A.18) will show exactly how the lock-in broadens d^2I/dV^2 when δV is non-zero.

A.4.1 d^2I/dV^2 measured by a lock-in

To show how the second harmonic is related to d^2I/dV^2, we may again use equation (A.11). However, by equation (A.26), we need to adjust the phase ϕ_2 so that $\phi_2 = -\pi/2$. The modified reference signal in this case is $\tilde{V}_{\text{ref}}(t) = \sin(2\omega_0 t + \phi_2) = -\cos 2\omega_0 t$. With this phase, we detect the coefficient $-B_2$ in the Fourier expansion (A.1). It will be shown below that $-B_2$ is proportional to d^2I/dV^2.

With $\phi_2 = -\pi/2$, the voltage V_{x} of the lock-in [equation (A.11)] is then, with $f(t) = \frac{1}{G}I(V + \delta V \sin\omega_0 t)$, $n = 2$, and $t_0 = -\frac{\pi}{2\omega_0}$,

$$V_{\text{x}} = -\frac{B_2}{\sqrt{2}} = -\frac{1}{G}\frac{\omega_0}{\pi\sqrt{2}}\int_{t=-\pi/2\omega_0}^{t=3\pi/2\omega_0} I(V + \delta V \sin\omega_0 t)\cos 2\omega_0 t\, dt$$

Like the calculation of dI/dV, partially rewrite the above integral in terms of the new variable x by using the substitutions $x = -\delta V \sin\omega_0 t$ and $\cos 2\omega_0 t = 1 - 2\sin^2\omega_0 t = 1 - 2x^2/\delta V^2$

$$V_{\mathrm{x}} = -\frac{1}{G}\frac{\omega_0}{\pi\sqrt{2}}\int_{t=-\pi/2\omega_0}^{t=3\pi/2\omega_0} I(V-x)\left(1-2\frac{x^2}{\delta V^2}\right)\frac{dx}{-\delta V\omega_0\cos\omega_0 t}\,.$$

Using the same procedure as for the calculation of dI/dV, the integral will be split into the sum of two parts $\int_{t=-\pi/2\omega_0}^{\pi/2\omega_0}$ and $\int_{t=\pi/2\omega_0}^{3\pi/2\omega_0}$. Using the appropriate substitution for $\cos\omega_0 t$ [equation (A.13)] for each part gives

$$V_{\mathrm{x}} = -\frac{1}{G}\frac{2}{\pi\sqrt{2}}\frac{1}{\delta V}\int_{-\delta V}^{\delta V} I(V-x)\left(1-2\frac{x^2}{\delta V^2}\right)\left(1-\frac{x^2}{\delta V^2}\right)^{-1/2}\,dx\,.$$

Applying integration by parts once gives

$$V_{\mathrm{x}} = -\frac{1}{G}\frac{\sqrt{2}}{\pi\delta V^2}\int_{-\delta V}^{\delta V}\frac{dI(V-x)}{dV}x\sqrt{\delta V^2-x^2}\,dx$$

and applying integration by parts again gives

$$V_{\mathrm{x}} = \frac{1}{G}\frac{\sqrt{2}}{3\pi\delta V^2}\int_{-\delta V}^{\delta V}\frac{d^2I(V-x)}{dV^2}(\delta V^2-x^2)^{3/2}\,dx$$

This last result can be written as the convolution [109]

$$V_{\mathrm{x}}(V) = \frac{1}{4G}\frac{\delta V^2}{\sqrt{2}}\left(\frac{d^2I}{dV^2} * B_{L2}\right) = \frac{1}{4G}\frac{\delta V^2}{\sqrt{2}}\int_{-\infty}^{\infty}\frac{d^2I(V-x)}{dV^2}B_{L2}(x)\,dx \tag{A.18}$$

$$\text{with}\quad B_{L2}(x) = \begin{cases}\frac{8}{3\pi\delta V^4}(\delta V^2-x^2)^{3/2} & \text{for } |x|<\delta V\\ 0 & \text{for } |x|\geq\delta V\end{cases} \tag{A.19}$$

A sketch of B_{L2} is given in figure A.3.

In the limit $\delta V \to 0$, $B_{L2}(x) \to \delta(x)$, so

$$\lim_{\delta V\to 0} V_{\mathrm{x}}\frac{4G\sqrt{2}}{\delta V^2} = \frac{d^2I(V)}{dV^2}$$

For small δV, we may then approximate d^2I/dV^2 as

$$\frac{d^2I(V)}{dV^2} \approx 2\sqrt{2}G\frac{V_{\mathrm{x}}}{(\delta V_{\mathrm{rms}})^2} \tag{A.20}$$

To express d^2I/dV^2 in terms of the actual output voltage $V_{\mathrm{out}\ 1}$ of the lock-in, we must again

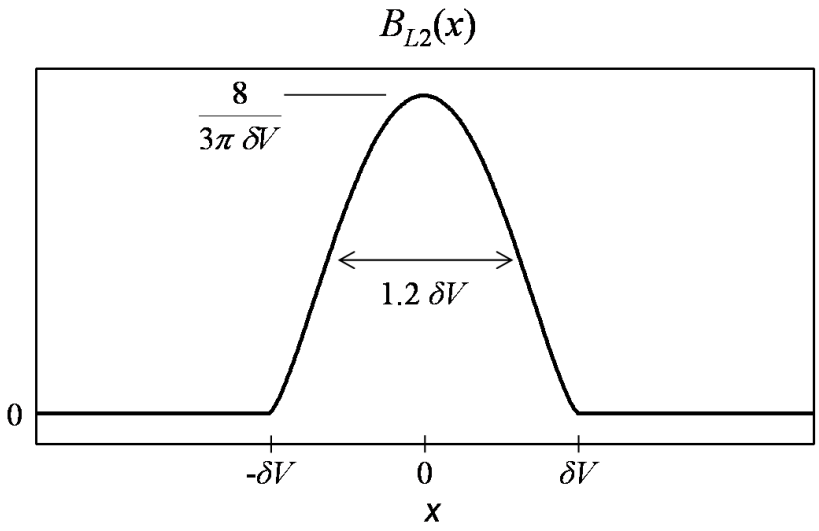

Figure A.3: Lock-in d^2I/dV^2 broadening function $B_{L2}(x)$. It has a height of $8/3\pi\delta V$ and FWHM $1.2\delta V$.

divide this result by the constant C, as described in §A.1.2.

Like dI/dV, equation (A.18) implies that the effect of the lock-in is to convolute the true d^2I/dV^2 with a broadening function. Like the discussion after equation (A.14), the convolution will broaden peaks in the true d^2I/dV^2, but with a different broadening function, B_{L2}. The FWHM of B_{L2} is $2\sqrt{1-2^{-2/3}}\delta V = 1.22\delta V = 1.72\delta V_{\rm rms}$, so peaks in d^2I/dV^2 will appear broadened in the lock-in output by $\sim 1.72\delta V_{\rm rms}$.

A.4.2 Adjusting the phase

For d^2I/dV^2 measurements, we do not have to worry about the tip-sample capacitance current since it does not contribute to d^2I/dV^2: $I = V/(i\omega C_0)$ for a capacitor with capacitance C_0, so that $d^2I/dV^2 = 0$ for a capacitor. This is unlike dI/dV measurements, where we must take into account the tip-sample capacitance current (§A.3.4). Since the capacitance makes no contribution to d^2I/dV^2, when we measure d^2I/dV^2 by measuring the second harmonic, we only get a contribution from the tunneling current.

The correct phase ϕ_2 for d^2I/dV^2 measurements is still complicated because of all the electronics which alters the phase of the tunneling current before it reaches the lock-in. However, finding the correct phase can be done by simply adjusting the lock-in phase to maximize or minimize the second harmonic lock-in X output signal $V_{\rm x}$. To determine whether the signal should be a maximum or minimum, we must look at dI/dV at some arbitrary voltage V_0 where $dI/dV \neq 0$ (the phase is independent of voltage, so any voltage V_0 can be used). If dI/dV is increasing at voltage V_0, then we should adjust the phase so that the second harmonic lock-in output is maximum at voltage V_0. If dI/dV is decreasing

at V_0, the phase is adjusted to minimize the second harmonic lock-in output at V_0.

The justification for the procedure to determine the phase ϕ_2 comes from equations (A.28) and (A.11). Equation (A.28) implies that when we apply the oscillating voltage $V_0 + \delta V \sin(\omega_0 t)$ to the tip, the second harmonic in the tunneling current only contains a term proportional to $\cos 2\omega_0 t$ (no $\sin 2\omega_0 t$ term). So if we expand the tunneling current $I(V_0 + \delta V \sin \omega_0 t)$ in a Fourier series [equation (A.1)], the Fourier coefficient of $\sin 2\omega_0 t$, which is A_2, must be zero. From equation (A.11) with $n = 2$ and $A_2 = 0$, $V_{\rm x} = \frac{1}{\sqrt{2}} B_2 \sin \phi_2$. Note that, if we vary the phase ϕ_2, the phase that we want, $\phi_2 = -\pi/2$ (from §A.4), will minimize $V_{\rm x}$ if $B_2 > 0$ and maximize $V_{\rm x}$ if $B_2 < 0$. By §A.4, since $B_2 \propto -d^2I/dV^2$, the phase that we want will maximize $V_{\rm x}$ when $d^2I/dV^2 > 0$ or minimize $V_{\rm x}$ when $d^2I/dV^2 < 0$.

Figure A.4 shows how $V_{\rm x}$ varies with phase for a EG&G Princeton Applied Research 5210 lock-in. From the graph, the phases which will maximize the second harmonic 2F

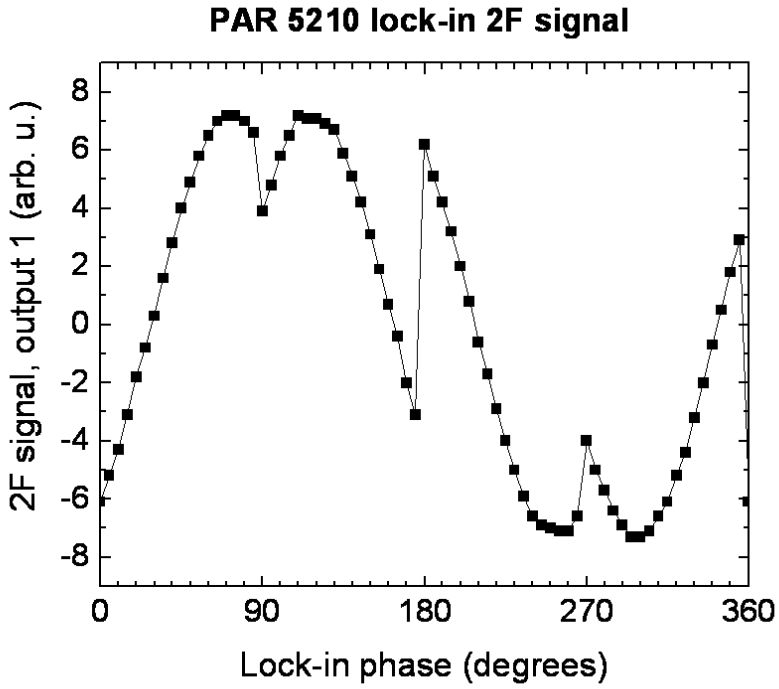

Figure A.4: Second harmonic measured from output 1 on a PAR 5210 lock-in in XY-mode.

signal occur at $\theta \approx 70°$ and $\theta \approx 115°$. We may set these phases manually, or alternatively, we can simply press "Autophase" on the lock-in and it will automatically adjust the phase to maximize the second harmonic signal.

A.5 d^nI/dV^n Measurements

When a small modulation voltage $\Delta V = \delta V \sin\omega_0 t$ is applied to the tunneling voltage V, the tunneling current $I(V+\Delta V)$ will also oscillate. In general, if we use a lock-in to measure the n^{th} harmonic of the oscillating current, the output will be proportional to d^nI/dV^n. To see this, first expand $I(V+\Delta V)$ in a Taylor series around V

$$I(V+\Delta V) = \sum_{m=0}^{\infty} \frac{1}{m!}\frac{d^mI(V)}{dV^m}(\Delta V)^m \tag{A.21}$$

$$= \sum_{m=0}^{\infty} \frac{1}{m!}\frac{d^mI(V)}{dV^m}(\delta V)^m \sin^m\omega_0 t \tag{A.22}$$

$$= I(V) + \frac{dI(V)}{dV}\delta V \sin\omega_0 t + \frac{1}{2}\frac{d^2I(V)}{dV^2}(\delta V \sin\omega_0 t)^2 + \ldots \tag{A.23}$$

We may substitute for $\sin^n\omega_0 t$ using the general expression for $\sin^m\theta$

$$\sin^m\theta = \begin{cases} \frac{(-1)^{m/2}}{2^{m-1}}\cos m\theta - \sum_{k=0}^{(m-2)/2} a_k \cos(2k\theta) & \text{for even } m \\ \frac{(-1)^{(m-1)/2}}{2^{m-1}}\sin m\theta - \sum_{k=0}^{(m-3)/2} b_k \sin(2k+1)\theta & \text{for odd } m \end{cases} \tag{A.24}$$

where a_k and b_k are some coefficients. (The expression (A.24) can be derived using deMoivre's Theorem $(\cos\theta + i\sin\theta)^m = \cos m\theta + i\sin m\theta$ and the binomial theorem.) From the Taylor expansion of $I(V+\Delta V)$, we see that the n^{th} term in the Taylor series expansion for $I(V+\Delta V)$, which contains the term $\sin^n\omega_0 t$, actually contains the term $\sin n\omega_0 t$ or $\cos n\omega_0 t$ by (A.24). Therefore, if we use a lock-in to measure the n^{th} harmonic, the main contribution will come from the n^{th} term in the Taylor series, which is proportional to $d^nI(V)/dV^n$.

However, by (A.24), the proportionality constant may be negative, and we want a positive proportionality constant. This can be accomplished by adjusting the phase ϕ_n of the lock-in so that the modified reference signal (§A.1.2) is

$$\tilde{V}_{\text{ref}}(t) = \sin(n\omega_0 t + \phi_n) = \begin{cases} (-1)^{n/2}\cos n\omega_0 t & \text{for even } n \\ (-1)^{(n-1)/2}\sin n\omega_0 t & \text{for odd } n, \end{cases} \tag{A.25}$$

which implies the phase is

$$\phi_n = \begin{cases} (-1)^{n/2}\dfrac{\pi}{2} & \text{for even } n \\ \dfrac{\pi}{2} - (-1)^{(n-1)/2}\dfrac{\pi}{2} & \text{for odd } n. \end{cases} \tag{A.26}$$

It is good to note that the n^{th} term in the Taylor series is not the only term which contributes to the n^{th} harmonic; i.e., it is not the only term which contains $\sin n\omega_0 t$ or $\cos n\omega_0 t$. If we write out the sum in equation A.24 explicitly, we will see that $\sin^{n+2}\theta$,

$\sin^{n+4}\theta$, etc., also contain the n^{th} harmonic. Hence, the $(n+2)^{\text{th}}, (n+4)^{\text{th}}, \ldots$ terms in the Taylor series (A.22) will also contain the n^{th} harmonic, but since these terms are higher in the Taylor series, they are typically orders of magnitude smaller than the n^{th} term, and can be neglected. Therefore, when we measure the n^{th} harmonic, the largest contribution comes from the n^{th} term in the Taylor series (A.22), which is proportional to d^nI/dV^n.

So if we want to measure $d^nI(V)/dV^n$, we add $\Delta V = \delta V \sin\omega_0 t$ to the tip voltage V, pass the tunneling current through a current to voltage converter with gain G (in units of A/V), measure the n^{th} harmonic of the output of the current to voltage converter $I(V+\Delta V)/G$ with a lock-in, and adjust the phase ϕ_n according to (A.26), then the X output of the lock-in will be proportional to the rms coefficient of the n^{th} term in the Taylor series of $I(V+\Delta V)$

$$V_{\text{out }1} = CV_{\text{x}} \approx \frac{C}{G\sqrt{2}}\frac{1}{2^{n-1}n!}(\delta V)^n\frac{d^nI}{dV^n} \tag{A.27}$$

which is proportional to d^nI/dV^n. The constant C is discussed in §A.1.2.

As an explicit example, take $n=2$. Since $\sin^2\omega_0 t = (1-\cos 2\omega_0 t)/2$, we get that

$$I(V+\Delta V) = I(V) + \frac{dI(V)}{dV}\delta V\sin\omega_0 t + \frac{1}{4}\frac{d^2I(V)}{dV^2}(\delta V)^2 - \frac{1}{4}\frac{d^2I(V)}{dV^2}(\delta V)^2\cos(2\omega_0 t) + \ldots \tag{A.28}$$

So when we use a lock-in amplifier to measure the second harmonic (the coefficient of $\cos 2\omega_0 t$), the main contribution to the signal is proportional to d^2I/dV^2.

Although d^2I/dV^2 is proportional to $\cos 2\omega_0 t$, it is not the only term in (A.22) proportional to $\cos 2\omega_0 t$. Since $\sin^m\omega_0 t = \cos 2\omega_0 t + \cdots + (-1)^{m/2}2^{1-m}\cos m\omega_0 t$ whenever m is even (from (A.24)), every term in (A.22) with even $m \geq 2$ also contains a term proportional to $\cos 2\omega_0 t$. So we can only say that d^2I/dV^2 is the leading contribution to the second harmonic.

B

Tip DOS Deconvolution by Subtracting Spectra

Whenever we take a dI/dV spectrum of a sample, what we measure is the convolution of the tip DOS with the sample DOS [equation (2.2)]. We usually assume that the STM tip DOS is constant, so that a dI/dV spectrum tells us the sample DOS. However, in practice, a constant tip DOS rarely occurs, and much tip preparation work is needed to get a constant tip DOS. In fact, for spectra taken at low biases, it is very difficult to get constant tip DOS. We then need a method of deconvoluting the tip DOS from a dI/dV spectrum to recover the sample DOS. General methods to deconvolute the tip DOS from dI/dV spectra using Volterra equations are given in §14.5 in [29]. However, having a simple method which allows one to extract the sample DOS from a spectrum when the tip DOS is non-constant will be helpful as it allows one to roughly extract the deconvoluted spectrum by eye, and it gives us an easy way to check the results of general deconvolution methods. The simple deconvolution method will be presented here.

The main result will be that, at low biases, if we take a dI/dV spectrum over an adsorbate and take another spectrum over the metallic surface, deconvoluting the tip DOS from the adsorbate dI/dV spectrum is approximately the same as subtracting the adsorbate and surface dI/dV spectra. This has been shown in [193] and will be re-derived here.

First, we will approximate the general expression for an STM tunneling current (2.2) for low biases and low temperatures. We may assume for low biases that the matrix element is a constant and at low temperatures

$$f(E - e_c V) - f(E) = \begin{cases} 1 & \text{for } 0 < E < e_c V \\ 0 & \text{otherwise,} \end{cases}$$

so that (2.2) may be written as

$$I(V) = M \int_0^{e_c V} \rho_t(E - e_c V)\rho_s(E)\, dE\,. \tag{B.1}$$

where M is independent of energy, but depends on the settings used to take the dI/dV spectrum and the object the spectrum is taken over. ρ_t and ρ_s are again the tip DOS and sample DOS.

We will use (B.1) to express dI/dV spectra taken on an adsorbate and on a metallic surface. If we do spectroscopy on a metallic surface at low voltages, we can assume that the surface DOS, ρ_{surf}, is constant. Doing a change of variables $E' = E - e_cV$, combined with the fundamental theorem of calculus $\frac{d}{dx}\int_a^x f(u)\,du = f(x)$, we can calculate dI/dV for the surface from (B.1) using $\rho_s(E) = \rho_{\text{surf}}$

$$\frac{dI_{\text{surf}}(V)}{dV} = M_{\text{surf}}\rho_{\text{surf}}\frac{d}{dV}\int_{-e_cV}^{0}\rho_t(E')\,dE' = M_{\text{surf}}\rho_{\text{surf}}e_c\rho_t(-e_cV)\,. \tag{B.2}$$

We now calculate the dI/dV spectrum taken on the adsorbate from (B.1) by using $\rho_s(E) = \rho_{\text{ads}}(E)$. Using the chain rule

$$\frac{d}{dV}G(x,y) = \frac{\partial G}{\partial x}\frac{dx}{dV} + \frac{\partial G}{\partial y}\frac{dy}{dV}$$

and the fundamental theorem of calculus, one can compute dI/dV using

$$G(x,y) = \int_0^x \rho_t(E-y)\rho_{\text{ads}}(E)\,dE$$

with $x = y = e_cV$ to get

$$\frac{dI_{\text{ads}}(V)}{dV} = e_cM_{\text{ads}}\rho_t(E-e_cV)\rho_{\text{ads}}(E)\bigg|_{E=e_cV} + e_cM_{\text{ads}}\int_0^{e_cV}\frac{\partial}{\partial y}\rho_t(E-y)\rho_{\text{ads}}(E)\,dE\,.$$

Since $\frac{\partial}{\partial y}\rho_t(E-y) = -\frac{\partial}{\partial E}\rho_t(E-y)$, we get

$$\frac{dI_{\text{ads}}(V)}{dV} = M_{\text{ads}}e_c\rho_t(0)\rho_{\text{ads}}(e_cV) - e_cM_{\text{ads}}\int_0^{e_cV}\frac{d}{dE}\rho_t(E-e_cV)\rho_{\text{ads}}(E)\,dE\,.$$

What we want is ρ_{ads}. We may solve for ρ_{ads} if we expand the ρ_{ads} inside the integral (but not the ρ_{ads} outside the integral) in a Taylor series around $E = 0$, $\rho_{\text{ads}} = \rho_{\text{ads}}(0) + \rho'_{\text{ads}}(0)E + \cdots$ and keep the zeroth order (constant) term. Then we may evaluate the integral and solve for $\rho_{\text{ads}}(e_cV)$, using (B.2) to express ρ_t in terms of dI_{surf}/dV

$$\rho_{\text{ads}}(e_cV) = C_1\left(\frac{dI_{\text{ads}}(V)}{dV} - C_2\frac{dI_{\text{surf}}(V)}{dV} + \frac{dI_{\text{ads}}(0)}{dV}\right)$$

$$\text{where}\quad C_1 = \frac{\rho_{\text{surf}}M_{\text{surf}}}{M_{\text{ads}}\frac{dI_{\text{surf}}(0)}{dV}}\quad\text{and}\quad C_2 = \frac{\frac{dI_{\text{ads}}(0)}{dV}}{\frac{dI_{\text{surf}}(0)}{dV}}$$

This equation implies that if we simply multiply dI/dV taken on the surface by the normalization constant C_2, then subtract it from dI/dV taken on the adsorbate, we will get an expression which is approximately proportional to the adsorbate density of states ($\rho_{\mathrm{ads}}(e_cV)$) offset by a constant. The major assumption was that the surface DOS is constant, which is usually a valid assumption at energies within 100 mV of E_{F}.

To get an idea of the accuracy of this subtraction procedure, comparisons between this simple subtraction of spectra method to a true deconvolution of the tip DOS from dI/dV spectra have been done in [193]. From these results, one sees that the simple subtraction method works quite well, and gives some justification for its use in our data. This method also allows one to simply look at the data and quickly get a rough idea of what features in the data may be due to the tip DOS.

C

Building the STM Walker Plate and Scanner

This appendix will describe building some of the important parts of the STM that are used for the coarse approach and scanning: the walker plate, the body piezo, and the bug. Figure 5.2 shows a drawing of these various components on the STM stage.

C.1 The walker plate

The walker plate consists of a thick glass slide (a microscope slide cut in half) with electrodes deposited onto it and another 3 mil thin glass slide over the electrodes. A side view of part of a generic walker plate is shown in figure C.1.

The walker plates that are currently being used with the STM, and have been used for at least the last 7 years, were made in UC Berkeley. Although these plates work, sometimes the coarse movement is not always great, as described in §5.1.6. To attempt to improve the coarse movement, we considered making a new walker plate, and contacted Gabriel Zeltzer in Hari Manoharan's group at Stanford University, who was also building an STM similar to ours. We found from Gabriel that the Stanford Nanofabrication Facility had better equipment for making the walker plate, so walker plates built there may be better than the ones built at Berkeley. We have two walker plates that were made using the Stanford facilities, both of which have never been used in our system. Figure C.2 has a photo of walker plates made at Berkeley and at Stanford.

This section will describe how to build walker plates at Berkeley and at Stanford. The general procedure to build the walker plate are the same at Berkeley and Stanford; it is only the facilities and equipment used that differ. The general procedure is

1. Cut a microscope slide in half. Only half the slide is necessary for one walker plate. The other half may be used to build another walker plate.

2. Clean the $\frac{1}{2}$-microscope slide and a thin glass slide (1 in $\times$ 1 in $\times$ 3 mil, from Ace Glass Inc.) with nitric acid or piranha ($3H_2SO_4$: H_2O_2) to remove any metals from the

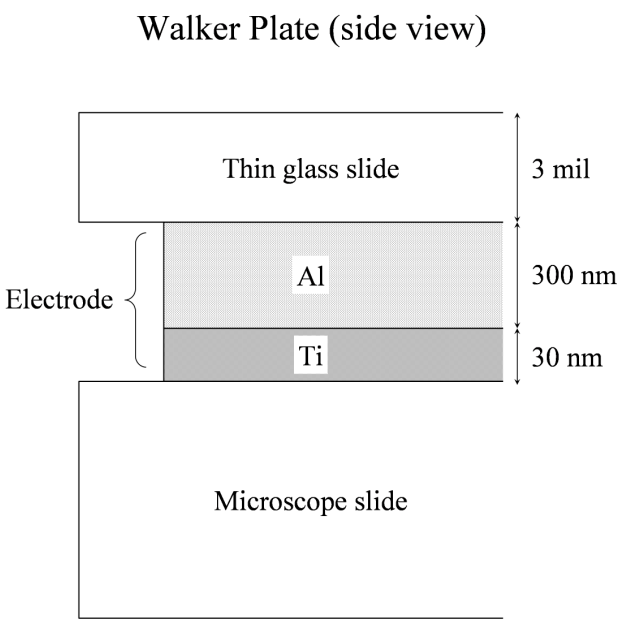

Figure C.1: Side view of the STM walker plate (not to scale).

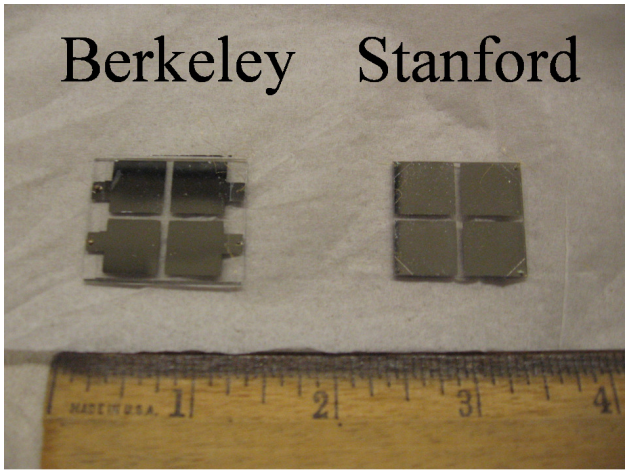

Figure C.2: Photo of walker plates built at Berkeley (left) and Stanford (right). The ruler is in inches.

surface.

3. Then clean the $\frac{1}{2}$-microscope slide and thin glass slide with tricholoroethane (or tikapur), acetone, and methanol, so that it is clean for UHV.

4. In vacuum, deposit a thin layer (30 nm thick) of titanium on the $\frac{1}{2}$-microscope slide through a shadow mask, then deposit a thick layer (300 nm thick) of aluminum through the shadow mask on the titanium. This step makes the electrodes of the walker plate.

It is necessary to deposit Ti first onto the glass since it sticks better to the glass. However, since Ti is hard to evaporate, it would be difficult to grow a thick electrode with only Ti, so only a thin layer of Ti is evaporated and then a thick layer of Al (which is easier to evaporate) is deposited on the Ti.

5. Anodically bond the thin glass slide onto the electrodes. Anodic bonding is a process where we apply a high voltage between glass and another substance at high temperature, which causes the glass and substance to bond. A general review of anodic bonding and the mechanisms behind it are in [110].

The specific details of the equipment and procedures used to build the Berkeley and Stanford walker plates for each of the steps listed above will be given below.

C.1.1 Berkeley walker plates

All steps to build the walker plate listed above up to step 3 can be done in our lab using our chemicals in the fume hood. The walker plate currently in the STM chamber may not have been cleaned with nitric acid (step 2 above), but if walker plates are made at Berkeley in the future, they should be.

For step 4, the electrodes were deposited using an evaporation chamber from the Séamus Davis group, which probably no longer exists. The shadow mask used is shown in figure C.3. The 30 nm of Ti was evaporated onto the microscope slide by placing Ti in a tungsten boat

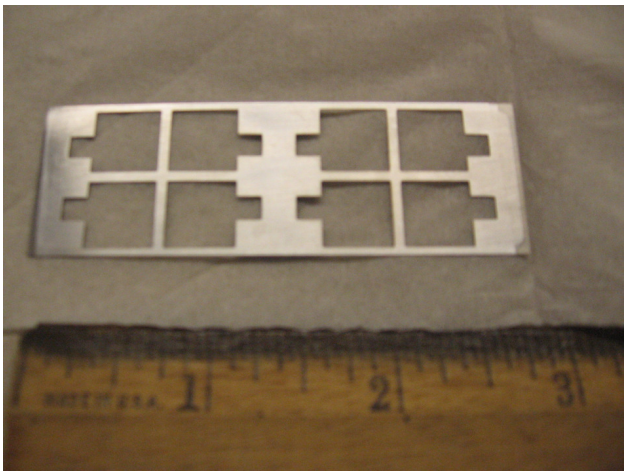

Figure C.3: Shadow mask used when depositing the electrodes onto the walker plate glass. The ruler is in inches.

and running ≈ 70 A through the boat. The 300 nm of Al was deposited by placing Al in a W boat and running ≈ 20 A running through the W boat.

For step 5, the anodic bonding was done manually. Following figure C.4, we place metal on a flat glass microscope slide on the thin glass slide. Then we apply 350 V for 1 hour at

300°C. The metal piece on the glass slide should also have enough weight so that it pushes down on the thin glass slide, causing the thin glass slide to make good contact with the electrodes.

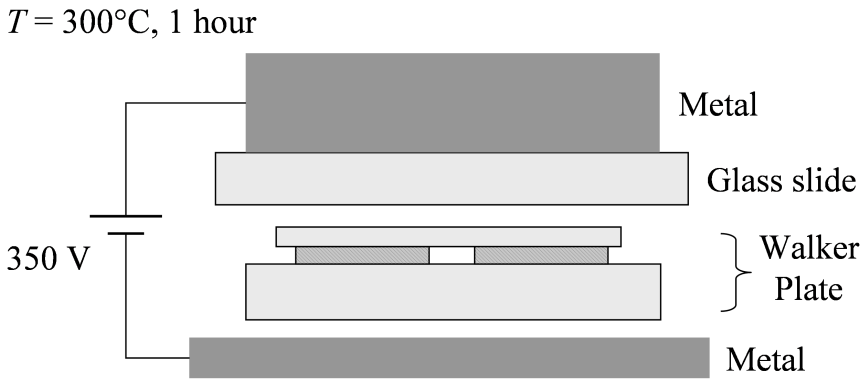

Figure C.4: Setup to anodically bond the thin glass slide to the metal electrodes

C.1.2 Stanford walker plates

The Stanford Nanofabrication Facility at Stanford University has commercial equipment to build the walker plates. The Stanford facilities has the chemicals to clean the glass slides (steps 2 and 3), metal deposition systems to deposit the electrodes (step 4), and an Electronic Visions 501 Bonder to anodically bond the metal to glass (step 5). The anodic bonder bonds the thin glass slide to the electrodes very uniformly, making a flatter glass surface than the Berkeley plates, and should help the bug to move across the thin glass slide without getting stuck.

C.2 The bug

The STM bug consists of insulating macor parts that were machined in the physics department machine shop, as well as piezoelectrics that were purchased from Staveley Sensors (now EBL Products, Inc.). The parts are glued together using Torr-Seal from Varian. A picture of the bug is given in figure C.5.

AutoCAD drawings and photos of all the bug parts, except for the body piezo, are given in figures C.6 and C.7. The AutoCAD drawings of these parts will be used later to pictorially describe how to build the bug.

There are also special tools to help build the bug. They are shown in figure C.8. There are also AutoCAD files for all the tools in figure C.8.

The general steps to build the bug are

1. Attach the Z-piezo to the cylinder.

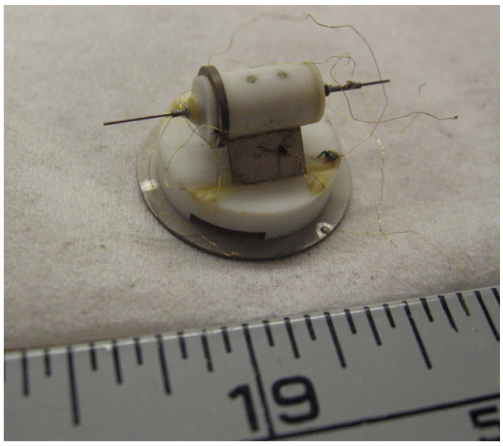

Figure C.5: Picture of the STM bug. The ruler is in inches; each small division is 1/16".

2. Attach the front plug to the Z-piezo.
3. Attach the back plug to the cylinder.
4. Attach the tip holder/tip shield to the front and back plugs.
5. Attach the X and Y piezos to the cylinder and foot.
6. Attach the body piezo to the foot.

The next figures will describe each step in the building process above, except for the last step, which will be described in another section due to its complexity. There are many spare or broken bug parts that can be used to practice building the bug.

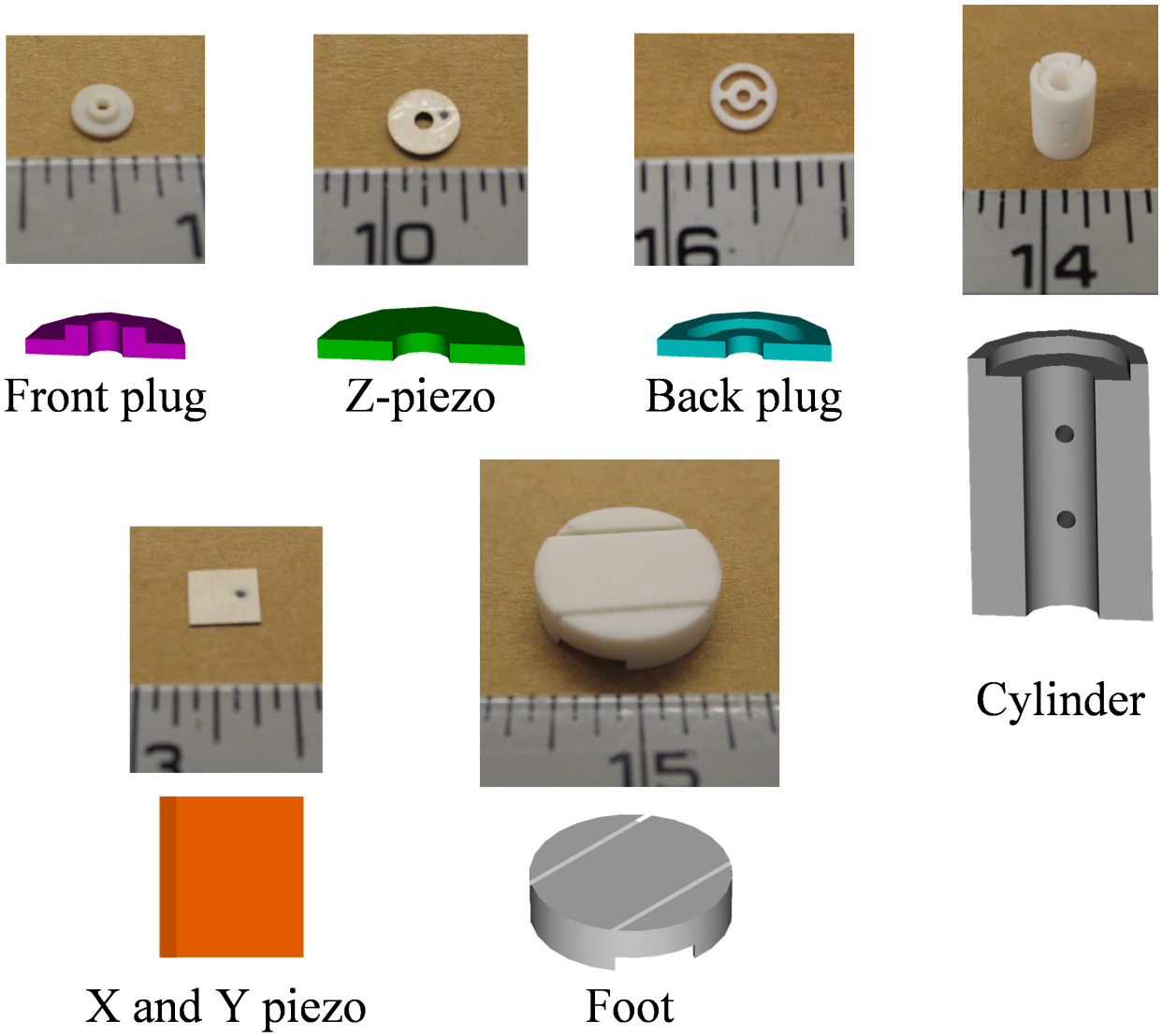

Figure C.6: AutoCAD drawings and photos of the various bug parts. The top row of bug parts have cross-sectional views for the AutoCAD drawings, while the the AutoCAD drawings for the bottom two bug parts are not cross-sectional views. The dots on the piezos in the photos marks their + side. The ruler in all photos is in inches with 1/16" divisions.

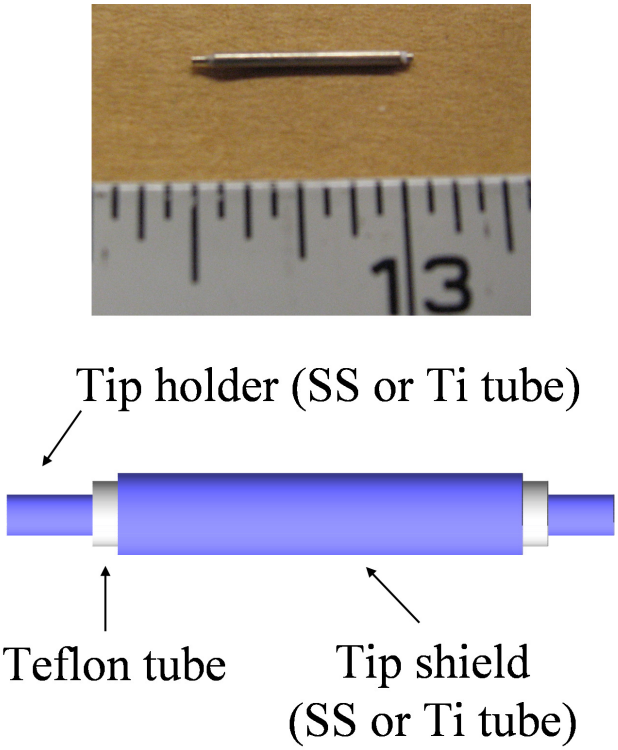

Figure C.7: Drawing of the STM tip holder and tip shield with a photo of it above. The ruler in the photo is in inches with 1/16" divisions.

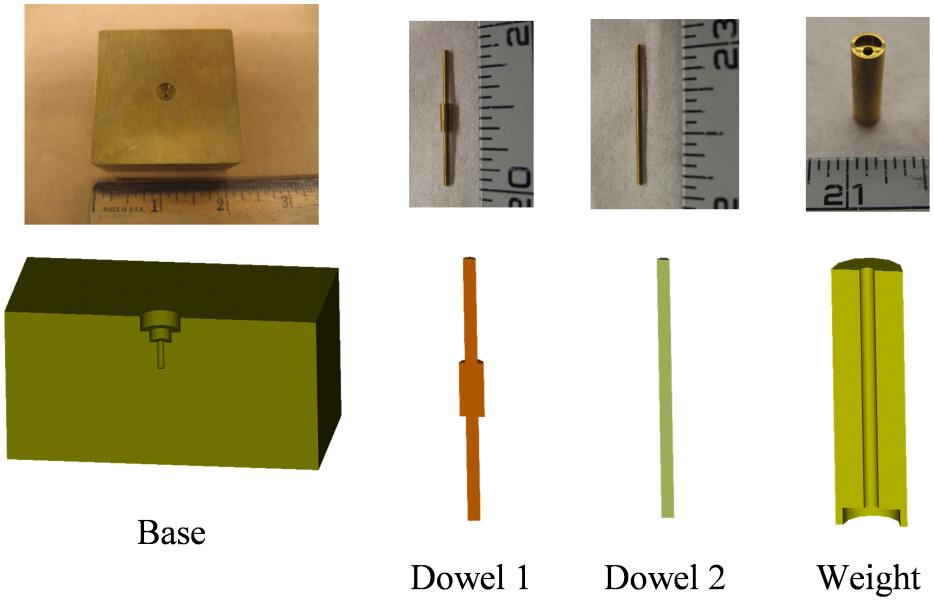

Figure C.8: AutoCAD cross-sectional views, with photos above them, of the various special parts used to help build the bug. The ruler in all the photos is in inches with 1/16" divisions.

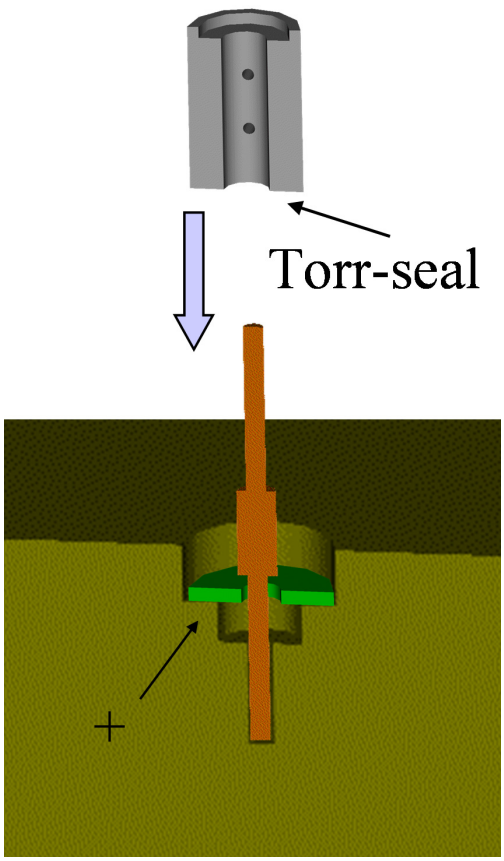

(a) Put Z-piezo in the base with the + side down. The plus side is usually marked with a + or a dot. Put dowel 1 into the base through the hole in the Z-piezo. Apply some Torr-seal to the end of the cylinder. Note that the two ends of the cylinder are not the same, so apply Torr-seal to the correct end.

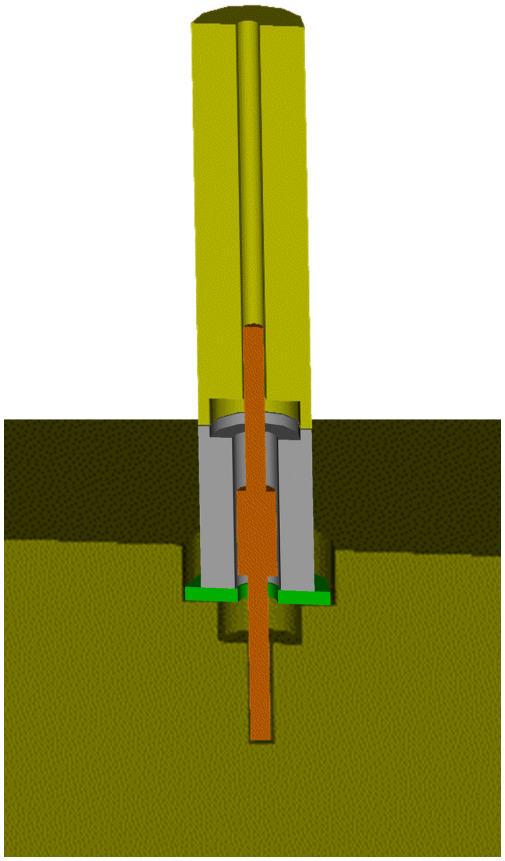

(b) Put the cylinder on the Z-piezo and put the weight on the cylinder. Remove most of the excess Torr-seal from the Z-piezo (we have to glue wires to the Z-piezo later, so it can't be covered with Torr-seal). Also make sure there is not too much Torr-seal inside the cylinder, or else the dowel may become glued to the cylinder. Methanol removes excess Torr-seal well. Let the Torr-seal harden.

Figure C.9: Step 1: Attaching the Z-piezo.

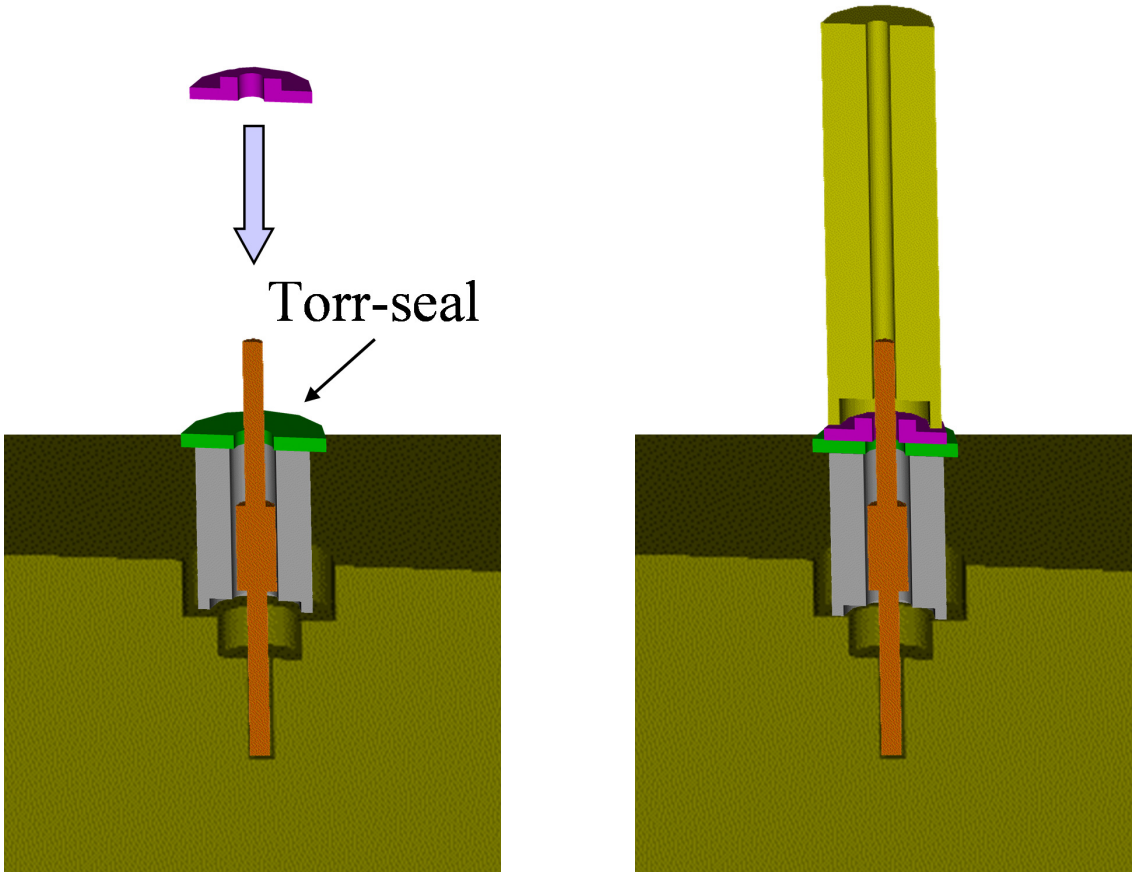

(a) Remove the weight and dowel, then flip the cylinder upside down. Put dowel 1 in the base and place the cylinder through dowel 1 on the base, as shown. Apply Torr-seal to the z-piezo in the area where the front plug will touch it.

(b) Put the front plug on the Z-piezo and put the weight on the front plug. Remove any excess Torr-seal, especially on the inside of the cylinder, or else the dowel may become glued to the Z-piezo. Allow the Torr-seal to harden.

Figure C.10: Step 2: Attaching the front plug.

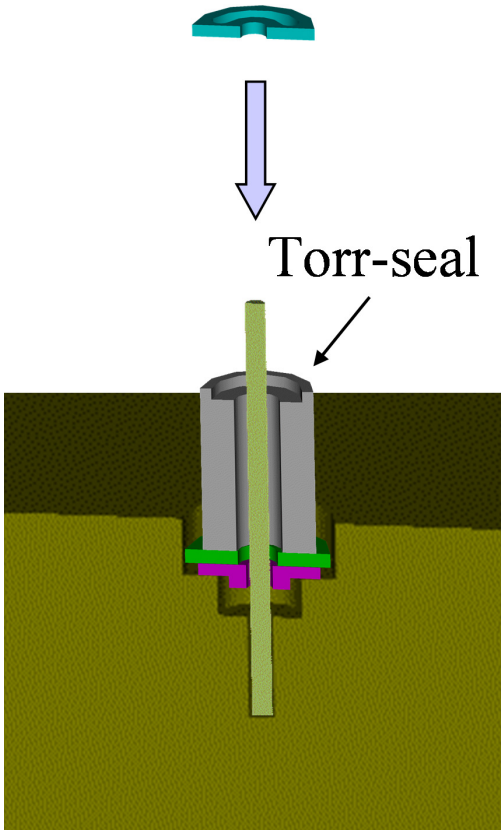

(a) Remove the weight and dowel, then flip the cylinder upside down again. Now put dowel 2 (not dowel 1) in the base and put the cylinder on the base. Apply Torr-seal to the rim of the cylinder; i.e., apply Torr-seal to the area that will touch the back plug shown in the next step.

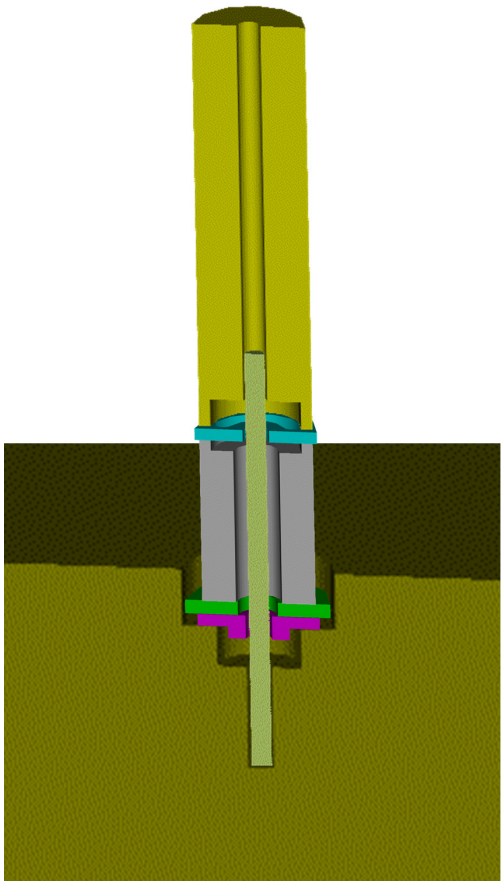

(b) Put the back plug on the cylinder and put the weight on the back plug. Remove excess Torr-seal from the inside and outside of the cylinder and allow the Torr-seal to harden.

Figure C.11: Step 3: Attaching the back plug.

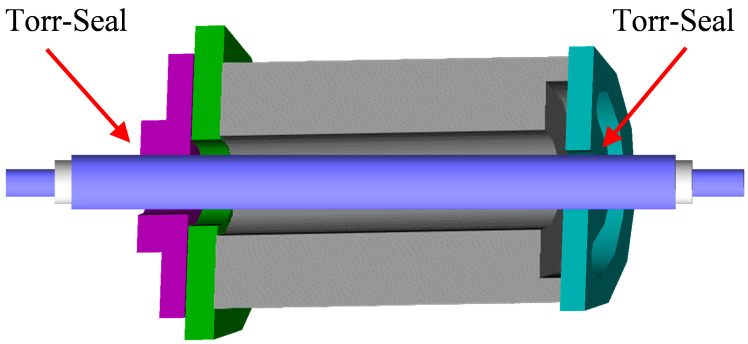

Figure C.12: Step 4. After the Torr-seal hardens, remove the dowel and remove the partially built bug from the base. Put the tip shield and tip holder through the front and back plugs. Then apply Torr-seal between the tip shield and front plug and between the tip shield and back plug. Move the tip holder/tip shield back and forth a little so that some of the Torr-seal goes into the holes in the front and back plugs. Let the Torr-seal harden.

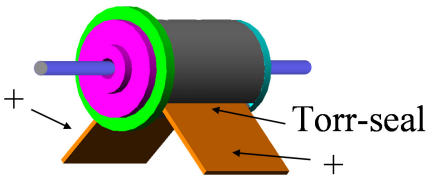

(a) Glue the longer edge of the X and Y piezos into the slots in the cylinder with Torr-seal with the positive sides of the piezos facing outward. The positive side is usually marked with a + or a dot. Do not let the Torr-seal harden.

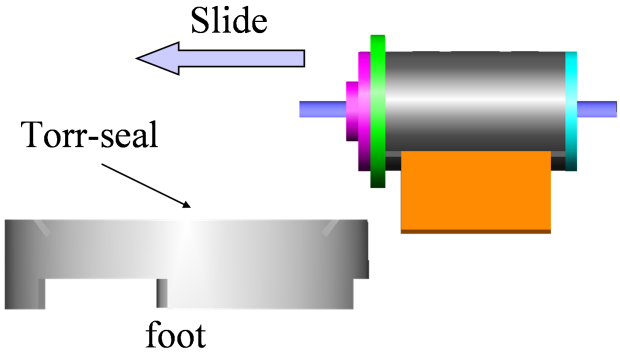

(b) Then put a little Torr-seal into the slots in the bug foot. Note the orientation of the foot in the figure. Slide the cylinder and X/Y piezos into the slots on the foot. Then add more Torr-seal around the foot slots to glue the X and Y piezos to the foot. Try to position the cylinder so that the X and Y piezos look perpendicular. Allow the Torr-seal to harden.

Figure C.13: Step 5: Attaching the X and Y piezos.

C.2.1 The body piezo

The final step in building the bug is to attach the body piezo. It is more involved since it first requires modification of the body piezo.

Modifying the body piezo

The body piezos were made by EBL Products, Inc. (formerly Staveley Sensors). They are discs 0.75 in in diameter and 16.5 mil thick, made from EBL #2 with Ni electrodes. Usually the positive side of the piezo is marked with a + or a dot. Figure C.14 is a photo of the body piezo with a dot marking the + side.

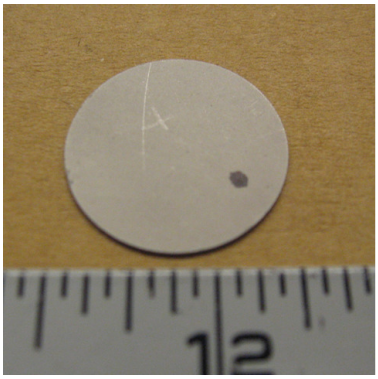

Figure C.14: Photo of the body piezo. The dot marks the + side of the piezo. The ruler is in inches with 1/16" divisions.

These are the steps to modify the body piezo.

1. As shown in the next figure, with the edge of a diamond file, make a small notch on the negative polarity side of the body piezo (the side without the + or dot). Once a notch is made with the diamond file, one can shape it more precisely with a scalpel or a dentist pick.

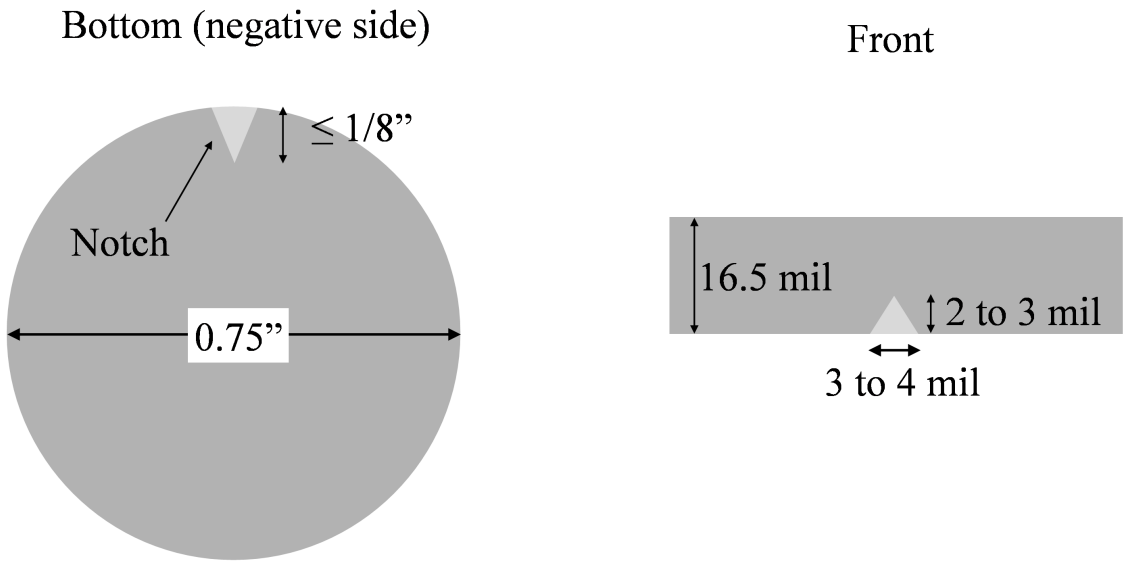

2. Glue a 2 mil annealed Au wire in the grove using Epotek H20E silver epoxy, as shown in the next figure. The Au wire was annealed in atmosphere by running a few amps of current through it until it turned red (which took a few seconds).

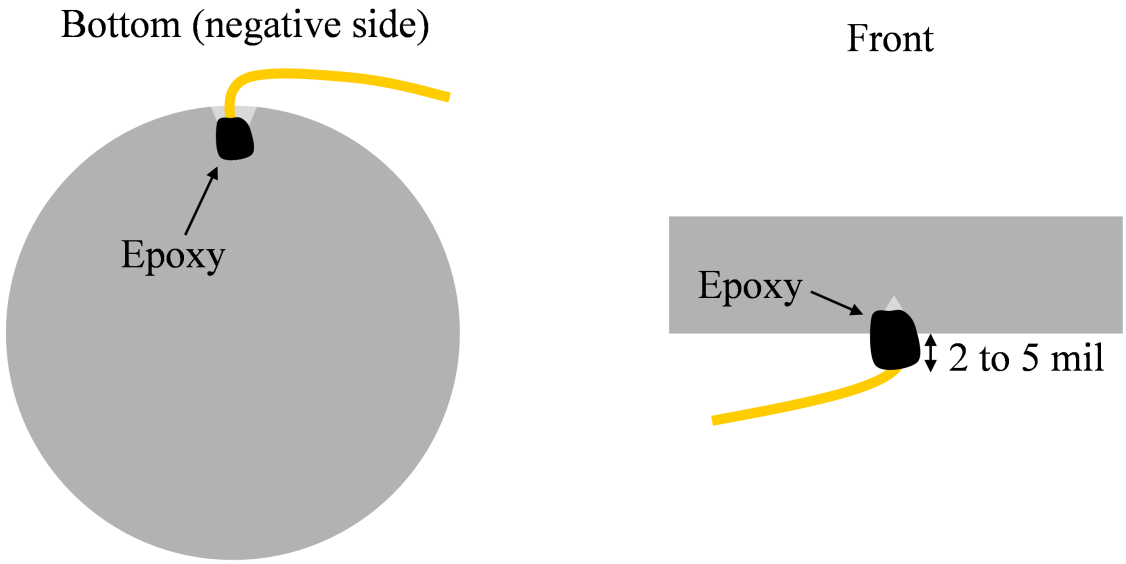

Figure C.15: The 2 mil annealed Au wire is glued into the grove with H20E silver epoxy.

3. Using the outline below as a guide,

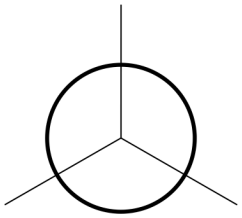

place small amounts of H20E epoxy on the negative side of the body piezo at two additional points so that the additional epoxy, together with the epoxy in the groove, lie at the corners of an equilateral triangle, as shown in the next figure. The epoxy at

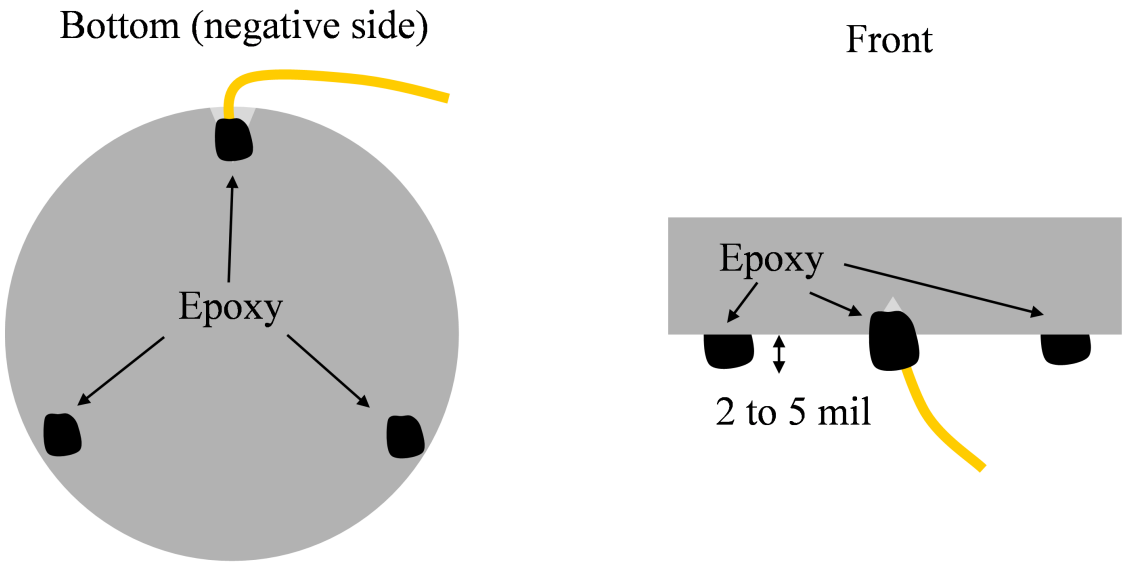

Figure C.16: Epoxy tripod on the negative polarity side of the body piezo. The sizes of the clumps of epoxy in the bottom view are exaggerated; they should be around half the length and half the width.

the three points of the triangle form the legs of a tripod, and when the bug is completed, it will touch the walker plate only at these three points, making it mechanically stable.

4. Next, place the body piezo in the vacuum oven. Then pump out the vacuum oven and vent it with nitrogen. Then heat the oven to 100°C for 1 hour. Do not heat the piezo when the oven is under vacuum, since the epoxy will expand under vacuum and baking it under that condition makes it flaky when hardened.

5. While looking at the body piezo through an optical microscope, file down the hardened H20E epoxy with a diamond file until the epoxy is only around 1–2 mil high, as in the

front view in figure C.17. Use a micrometer to measure the height, and make sure all epoxy tripod legs are the same height.

6. Next, flip the piezo over and attach, using H20E epoxy, another annealed 2 mil Au wire to the + side of the piezo, at a point directly above the epoxy on the negative piezo side, as shown in the next figure. The wire should be glued at a position directly over the epoxy that is adjacent clockwise from the wire for the negative piezo electrode.

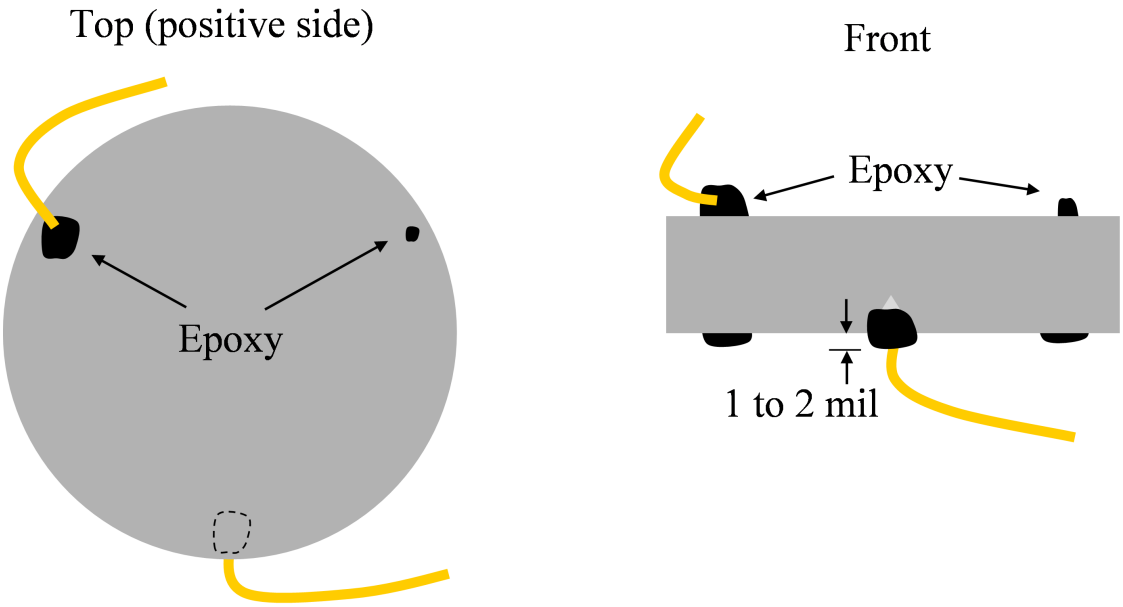

Figure C.17: Top of body piezo after filing down the tripod and attaching another Au wire to the positive electrode.

7. In addition to the epoxy for the Au wire, place another small amount of epoxy on the + piezo side, directly above the epoxy on the negative piezo side, as shown in figure C.17. This epoxy will be used later as a marker to help align the body piezo with the rest of the bug. One may alternatively scratch the surface a little where the epoxy would go instead of actually placing epoxy since the only purpose of the epoxy is to mark the surface of the piezo.

8. Bake the piezo in the oven at 100°C for 1 hour under nitrogen to harden the epoxy.

9. After the epoxy has hardened, pole the piezo by applying 350 V across of it while heating it at 120°C for 1 hour. The current through the piezo during poling is typically less than 0.1 mA. To stop the poling process, first cool down the piezo to room temperature, then reduce the voltage to zero.

Attaching the body piezo

After the body piezo has been modified following the steps in the previous section, it may be attached to the rest of the bug. It is not necessary to build the rest of bug before attaching the body piezo, but it is easier to align the body piezo with the macor bug foot when the rest of the bug is already built, so its better to attach the body piezo as the last step.

In the past, we would take a completely built bug that was not walking well and replace only the body piezo, hoping that would improve the walking. This is probably not necessary anymore since the problems with coarse approach are usually fixed by warming up the STM stage while keeping the walker plate electrodes grounded.

However, if there is any reason why only the body piezo needs to be replaced on a bug that is already completely built, there a few steps to remove the old body piezo.

1. First break off the body piezo with tweezers, cutters, etc.

2. Then sand the bottom of the bug foot so that both the macor tripod and center stump are even. The next figure identifies which parts of the foot are the tripod and stump.

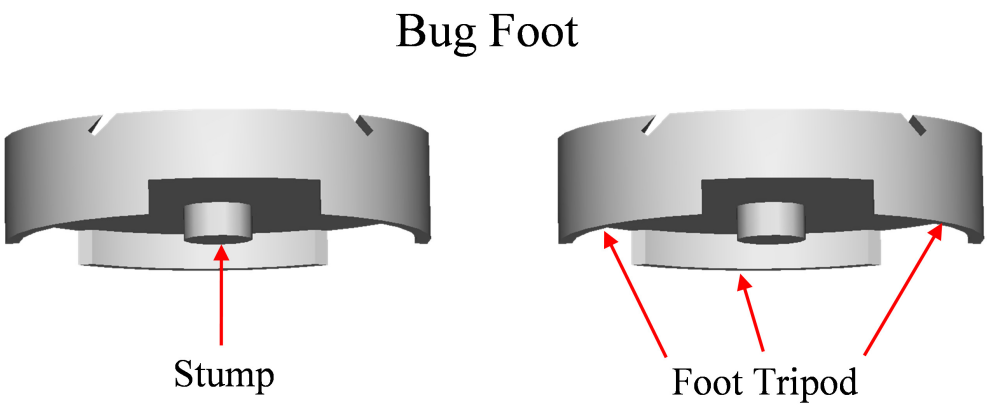

Figure C.18: Stump and tripod of the bug foot.

3. Once the foot tripod and center stump are even, using a diamond file, make the stump around 1–2 mil shorter than the tripod, as shown in figure C.19. One can measure the height of the stump with a micrometer or by trying to slide a 2 mil Au wire under the stump.

After the steps given above, the new body piezo can be attached.

The next steps below deal with attaching the body piezo to the macor bug foot. These steps are the same whether one is only replacing the body piezo, or building a completely new bug.

To attach the body piezo to the bug foot, one first needs Epotek H20E silver epoxy to glue the piezo to the bug foot and a special tool to hold the piezo against the bug foot while the epoxy hardens. A picture of the tool, called the piezo bower, is shown in figure C.20.

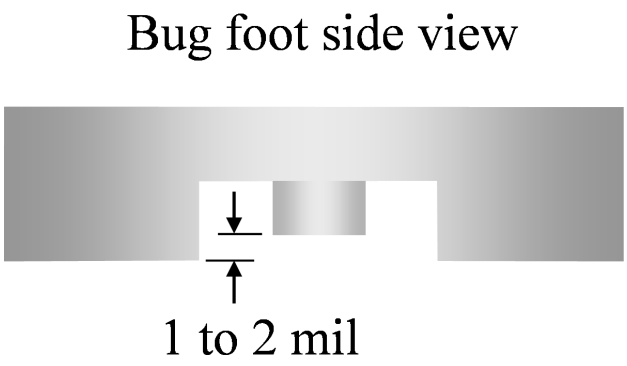

Figure C.19: Correct height of the stump relative to the foot tripod. Drawing not to scale.

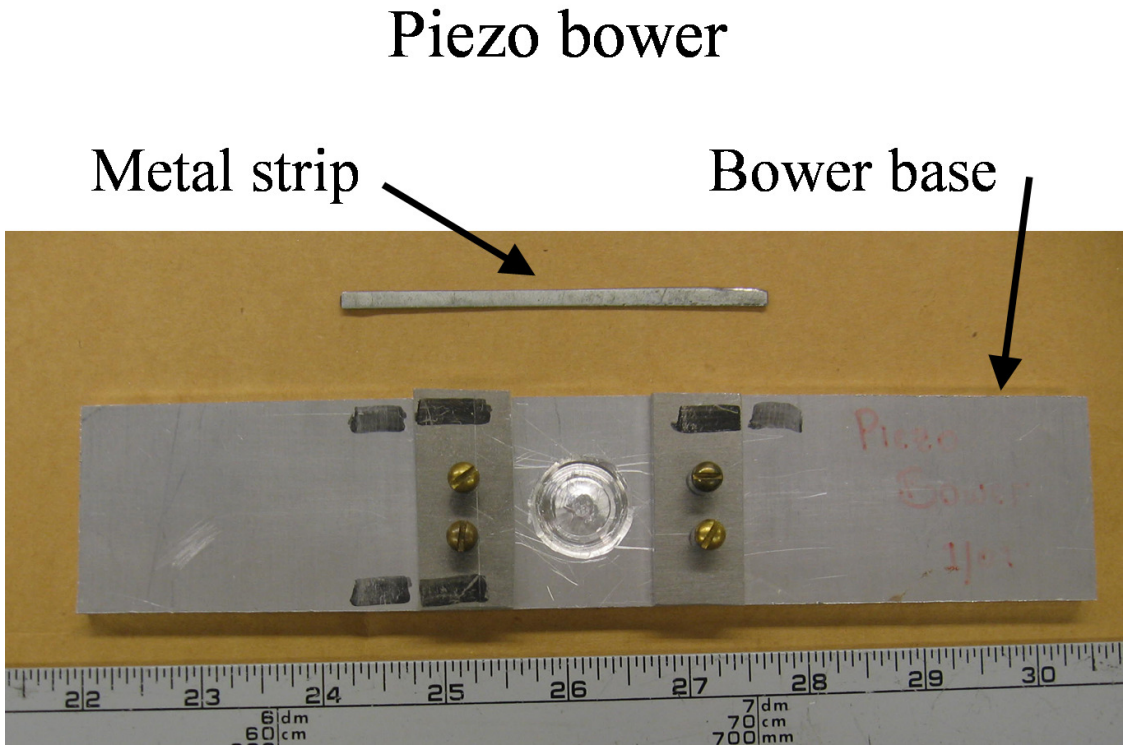

Figure C.20: Tool, called the piezo bower, to help attach the body piezo to the macor bug foot. The ruler is in inches.

Using this tool, the steps to attach the body piezo to the foot are

1. Place the new body piezo on the center of the piezo bower, centered on the domed region, with the + side of the piezo facing up, being careful not to break any Au wires on the piezo.

2. Put a little H20E epoxy on the foot stump. This epoxy will be used to attach the

body piezo to the bug foot. The body piezo will be attached to the bug foot only at the stump so that the body piezo can expand and contract in all directions.

3. Place the foot on the body piezo and align the foot and body piezo so that the foot is centered on the piezo and the STM tip is directly over the small amount of epoxy on the + side of the body piezo, as shown in the next figure.

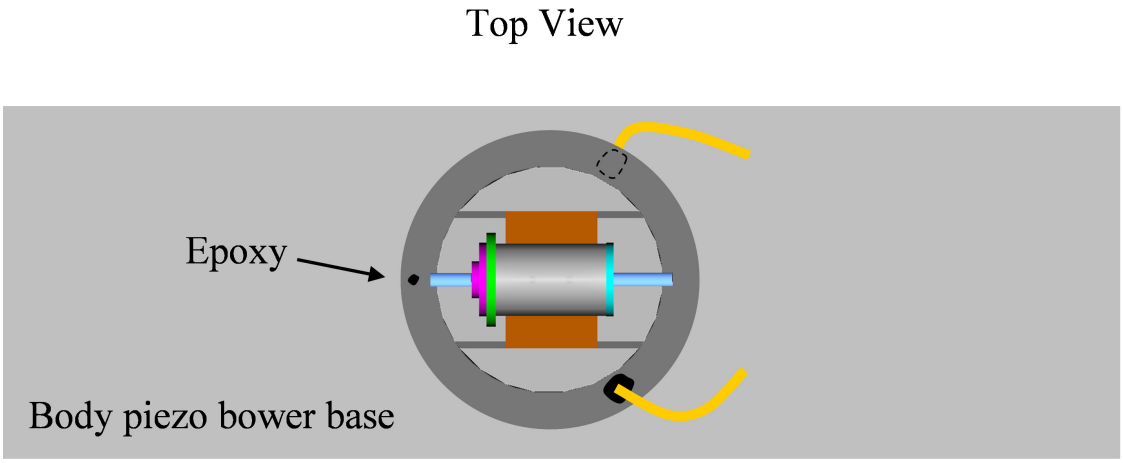

Figure C.21: Alignment of the piezo bower, bug, and body piezo.

4. Place the metal strip between the X and Y piezos as shown in the next figure, and recheck the alignment between foot and body piezo.

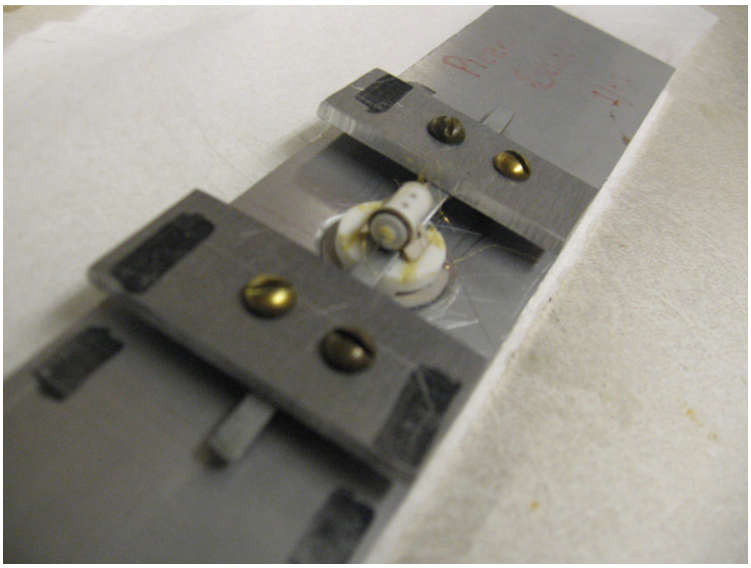

Figure C.22: The metal strip is placed between the X and Y piezos.

5. Tighten the screws clamping the metal strip so that the strip bends a little, as shown in the next figure. The ends of the strip should be around 2 to 3 mm above the piezo bower base. Pushing the metal strip against the bug foot forces the bug foot against

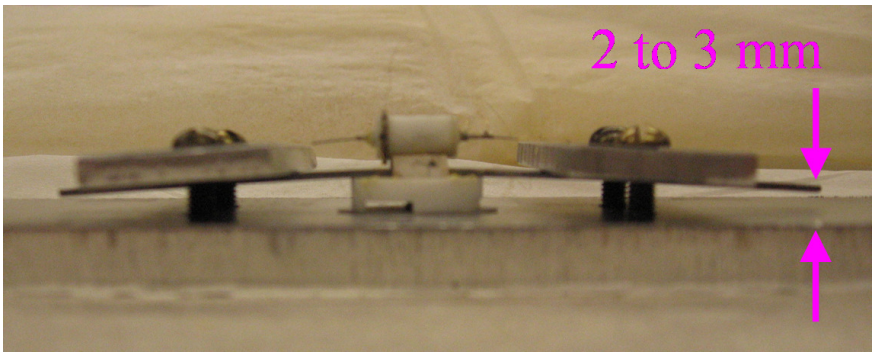

the body piezo. Since the stump of the bug foot is slightly shorter than the bug foot tripod (figure C.19), the body piezo will bend slightly under this force. This slight bowing of the body piezo makes it rigidly attached to the bug foot, making the entire bug more mechanically stable.

6. Put everything in the oven for 90 minutes at 80°C.

7. After everything has cooled down, remove the bug from the piezo bower and test the coarse movement with a spare walker plate and test the body piezo capacitance.

Frequency characterization of the body piezo

When we bend the piezo, we do not want to bend it so much that it may crack or break. To indirectly test the amount of stress on the body piezo, we measured the piezo impedance as a function of frequency while differing amounts of bowing was applied by the piezo bower. Figure C.23 shows a graph of the frequency dependence of the impedance of the body piezo, showing the resonant dip at ~ 107 kHz and the anti-resonant peak at ~ 126 kHz (reference [4]). The black curve is when there is no bowing. The green curve is obtained when the amount of bowing is similar to the amount used to attach the body piezo to the bug foot. The red curve is obtained when the piezo is bowed more than the amount used to obtain the green curve.

From the graph, we see that the amount of stress applied to the piezo when we attach it to the bug foot alters the piezo impedance some, but not as much as the amount of stress used to obtain the red curve. So the amount of stress applied to the piezo during attachment to the bug foot is less likely to damage the piezo than the amount of stress used to obtain the red curve. This is how we chose the amount of bowing to use when attaching the body piezo to the bug foot.

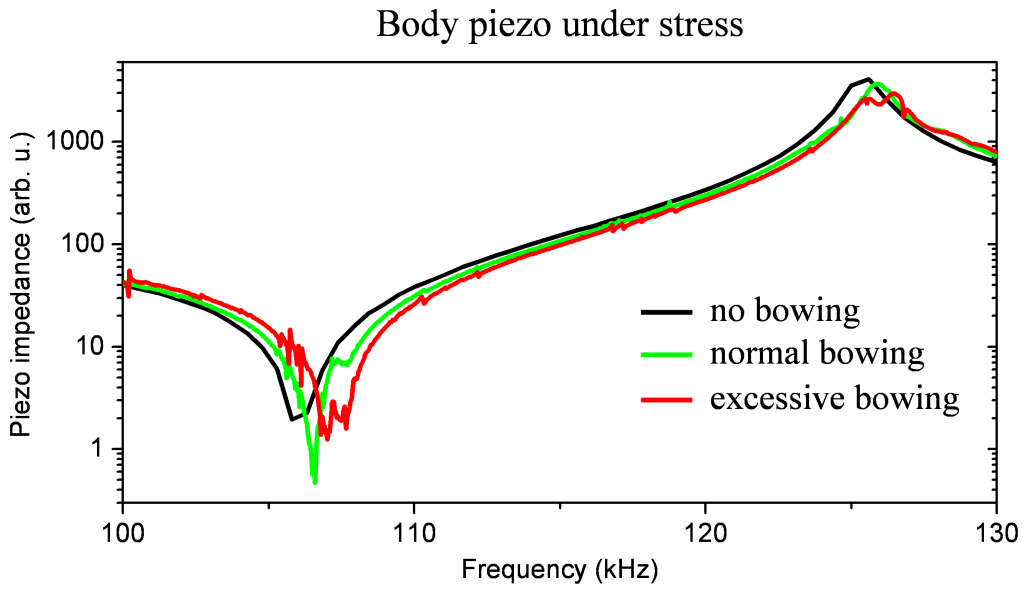

Figure C.23: Impedance of the body piezo as a function of frequency for different amounts of stress.

Bibliography

[1] Pierre-Marc Allemand, Kishan C. Khemani, Andrew Koch, Fred Wudl, Karoly Holczer, Steven Donovan, George Grner, and Joe D. Thompson. Organic molecular soft ferromagnetism in a fullerene C_{60}. *Science*, 253(5017):301–303, 1991.

[2] P. W. Anderson. Localized magnetic states in metals. *Physical Review*, 124(1):41–53, 1961.

[3] V. P. Antropov, O. Gunnarsson, and O. Jepsen. Coulomb integrals and model Hamiltonians for C_{60}. *Physical Review B*, 46(20):13647–13650, Nov 1992.

[4] APC International, Ltd. *Piezoelectric Ceramics: Principles and Applications*. APC International, Ltd., Jan 2002.

[5] Joel A. Appelbaum and W. F. Brinkman. Theory of many-body effects in tunneling. *Physical Review*, 186(2):464–470, Oct 1969.

[6] Alexandru D. Asandei and Yanhui Chen. Cp_2TiCl-catalyzed SET reduction of aldehydes: A new initiating protocol for living radical polymerization. *Macromolecules*, 39(22):7549–7554, Oct 31 2006.

[7] Neil W. Ashcroft and N. David Mermin. *Solid State Physics*. Thomson Learning, Inc., 1976.

[8] Dionys Baeriswyl, David K. Campbell, Jose M. P. Carmelo, Francisco Guinea, and Enrique Louis, editors. *The Hubbard Model: Its Physics and Mathematical Physics*, volume 343 of *B*. Springer, 1 edition, 1995.

[9] Vincenzo Balzani, Margherita Venturi, and Alberto Credi. *Molecular Devices and Machines: A Journey into the Nanoworld*. Wiley-VCH Verlag GmbH & Co., 2003.

[10] E. J. Baran and K. H. Lii. Vibrational spectra of the layered compound $[(VO_2)_2(4,4\text{-bipy})_{0.5}(4,4'\text{-Hbipy})(PO_4)]\cdot H_2O$. *Zeitschrift für Naturforschung Section B—A Journal of Chemical Sciences*, 58(5):485–488, May 2003.

[11] J. Bardeen. Tunneling from a many-particle point of view. *Physics Review Letters*, 6(2):57–59, January 1961.

[12] M. C. Barden and J. Schwartz. Stereoselective pinacol coupling in aqueous media. *Journal of the American Chemical Society*, 118(23):5484–5485, Jun 12 1996.

[13] D. E. Barlow, L. Scudiero, and K. W. Hipps. Scanning tunneling microscopy study of the structure and orbital-mediated tunneling spectra of cobalt(II) phthalocyanine and cobalt(II) tetraphenylporphyrin on Au(111): Mixed composition films. *Langmuir*, 20(11):4413–4421, May 25 2004.

[14] Salvador Barraza-Lopez, Michael C. Avery, and Kyungwha Park. First-principles study of a single-molecule magnet Mn_{12} monolayer on the Au(111) surface. *Physical Review B (Condensed Matter and Materials Physics)*, 76(22):224413, 2007.

[15] Stéphane Bedwani, Daniel Wegner, Michael F. Crommie, and Alain Rochefort. Strongly reshaped organic-metal interfaces: Tetracyanoethylene on Cu(100). *Physical Review Letters*, 101(21):216105, November 2008.

[16] V. K. Belskii, I. V. Sokolova, B. M. Bulychev, and A. I. Sizov. New crystalline modification of dimeric bicyclopentadienyltitanium(iii) chloride—$C_{20}H_{20}Ti_2Cl_2$. *Journal of Structural Chemistry*, 28(2):328–329, Mar–Apr 1987.

[17] A. J. Berlinsky and A. B. Harris. Orientational phases of hydrogen molecules on a triangular lattice. *Physical Review Letters*, 40(24):1579–1582, Jun 1978.

[18] Philip R. Bevington and D. Keith Robinson. *Data Reduction and Error Analysis for the Physical Sciences*. WCB/McGraw-Hill, second edition, 1992.

[19] Lapo Bogani and Wolfgang Wernsdorfer. Molecular spintronics using single-molecule magnets. *Nature Materials*, 7(3):179–186, Mar 2008.

[20] K.-F. Braun, V. Iancu, N. Pertaya, K.-H. Rieder, and S.-W. Hla. Decompositional incommensurate growth of ferrocene molecules on a Au(111) surface. *Physical Review Letters*, 96(24):246102, 2006.

[21] V. Brouet, H. Alloul, S. Garaj, and L. Forro. NMR studies of insulating, metallic, and superconducting fullerides: Importance of correlations and Jahn-Teller distortions. In *Fullerene-Based Materials: Structures and Properties*, volume 109 of *Structure and Bonding*, pages 165–199. Springer-Verlag Berlin, Heidelberger Platz 3, D-14197 Berlin, Germany, 2004.

[22] V. Brouet, W. L. Yang, X. J. Zhou, H. J. Choi, S. G. Louie, M. L. Cohen, A. Goldoni, F. Parmigiani, Z. Hussain, and Z. X. Shen. Orientation-dependent C_{60} electronic structures revealed by photoemission spectroscopy. *Physical Review Letters*, 93(19):197601, Nov 2004.

[23] S. T. Brown, J. C. Rienstra-Kiracofe, and H. F. Schaefer. A systematic application of density functional theory to some carbon-containing molecules and their anions. *Journal of Physical Chemistry A*, 103(20):4065–4077, May 20 1999.

[24] Richard L. Burden and J. Douglas Faires. *Numerical Analysis*. Thomson Brooks/Cole, 2005.

[25] Massimo Capone, Michele Fabrizio, Paolo Giannozzi, and Erio Tosatti. Theory of the metal-nonmagnetic Mott-Jahn-Teller insulator transition in A_4C_{60}. *Physical Review B*, 62(11):7619–7624, Sep 2000.

[26] C. Cepek, M. Sancrotti, T. Greber, and J. Osterwalder. Electronic structure of K doped C_{60} monolayers on Ag(001). *Surface Science*, 454:467–471, May 20 2000.

[27] A. Ceulemans. The structure of Jahn-Teller surfaces. *Journal of Chemical Physics*, 87(9):5374–5385, Nov 1 1987.

[28] Sudip Chakravarty, Martin P. Gelfand, and Steven Kivelson. Electronic correlation effects and superconductivity in doped fullerenes. *Science*, 254(5034):970–974, 1991.

[29] C. Julian Chen. *Introduction to Scanning Tunneling Microscopy*. Oxford University Press, second edition, 2008.

[30] W. Chen, T. Jamneala, V. Madhavan, and M. F. Crommie. Disappearance of the Kondo resonance for atomically fabricated cobalt dimers. *Physical Review B*, 60(12):R8529–R8532, Sep 1999.

[31] Wei Chen. *STM Investigations of Pristine Au(111) at Low Temperature and Surface-Supported Magnetic Clusters*. PhD thesis, Boston University, 1999.

[32] L. F. Chibotaru, A. Ceulemans, and S. P. Cojocaru. Electronic structure of A_4C_{60}: Joint effect of electron correlation and vibronic interactions. *Physical Review B*, 59(20):R12728–R12731, May 1999.

[33] Swapan Chowdhury and Paul Kebarle. Electron affinities of di- and tetracyanoethylene and cyanobenzenes based on measurements of gas-phase electron-transfer equilibria. *Journal of the American Chemical Society*, 108(18):5453–5459, September 1986.

[34] T. A. Costi and A. C. Hewson. A new approach to the calculation of spectra for strongly correlated systems. *Physica B: Condensed Matter*, 163(1–3):179–181, 1990.

[35] D. M. Cox, D. J. Trevor, K. C. Reichmann, and A. Kaldor. $C_{60}La$—A deflated soccer ball. *Journal of the American Chemical Society*, 108(9):2457–2458, Apr 30 1986.

[36] J. E. Dahl, S. G. Liu, and R. M. K. Carlson. Isolation and structure of higher diamondoids, nanometer-sized diamond molecules. *Science*, 299(5603):96–99, Jan 3 2003.

[37] J. E. P. Dahl, J. M. Moldowan, T M. Peakman, J. C. Clardy, E. Lobkovsky, M. M. Olmstead, P. W. May, T. J. Davis, J. W. Steeds, K. E. Peters, A. Pepper, A. Ekuan, and R. M. K. Carlson. Isolation and structural proof of the large diamond molecule, cyclohexamantane ($C_{26}H_{30}$). *Angewandte Chemie—International Edition*, 42(18):2040–2044, 2003.

[38] P. Dahlke and M. J. Rosseinsky. Molecular structure, orientational order, and Jahn-Teller distortion of the C_{60}^{4-} anion in Cs_4C_{60}. *Chemistry of Materials*, 14(3):1285–1291, Mar 2002.

[39] Lorenzo De Leo and Michele Fabrizio. Surprises in the phase diagram of an Anderson impurity model for a single C_{60}^{n-} molecule. *Physical Review Letters*, 94(23):236401, Jun 2005.

[40] N. D. Drummond, A. J. Williamson, R. J. Needs, and G. Galli. Electron emission from diamondoids: A diffusion quantum Monte Carlo study. *Physical Review Letters*, 95(9), Aug 26 2005.

[41] P. Durand, G. R. Darling, Y. Dubitsky, A. Zaopo, and M. J. Rosseinsky. The Mott-Hubbard insulating state and orbital degeneracy in the superconducting C_{60}^{3-} fulleride family. *Nature Materials*, 2(9):605–610, Sep 2003.

[42] D. M. Eigler and E. K. Schweizer. Positioning single atoms with a scanning tunneling microscope. *Nature*, 344(6266):524–526, Apr 5 1990.

[43] W. Erley. Reflection absorption infrared-spectroscopy of tetracyanoethylene adsorbed on Cu(111)—observation of vibronic interaction. *Journal of Physical Chemistry*, 91(24):6092–6094, Nov 19 1987.

[44] W. Erley and H. Ibach. Spectroscopic evidence for surface anion radical formation of tetracyanoethylene adsorbed on Cu(111) at 100 K—a high-resolution electron-energy loss study. *Journal of Physical Chemistry*, 91(11):2947–2950, May 21 1987.

[45] Steven C. Erwin and Mark R. Pederson. Electronic structure of crystalline K_6C_{60}. *Physical Review Letters*, 67(12):1610–1613, Sep 1991.

[46] Michele Fabrizio and Erio Tosatti. Nonmagnetic molecular Jahn-Teller Mott insulators. *Physical Review B*, 55(20):13465–13472, May 1997.

[47] U. Fano. Effects of configuration interaction on intensities and phase shifts. *Physical Review*, 124(6):1866–1878, December 1961.

[48] Duan Feng and Guojun Jin. *Introduction to Condensed Matter Physics*, volume 1. World Scientific Publishing Company, 2005.

[49] A. M. Fennimore, T. D. Yuzvinsky, W. Q. Han, M. S. Fuhrer, J. Cumings, and A. Zettl. Rotational actuators based on carbon nanotubes. *Nature*, 424(6947):408–410, Jul 24 2003.

[50] R. Foster. *Organic charge-transfer complexes*. Academic Press: New York, 1969.

[51] M. A. Freitag and M. S. Gordon. On the electronic structure of bis(η^5-cyclopentadienyl) titanium. *Journal of Physical Chemistry A*, 106(34):7921–7926, Aug 29 2002.

[52] Hideyuki Funasaka, Koji Sakurai, Yoshihiro Oda, Kazunori Yamamoto, and Takeshi Takahashi. Magnetic properties of Gd@C_{82} metallofullerene. *Chemical Physics Letters*, 232(3):273–277, 1995.

[53] J. W. Gadzuk. Resonance-tunneling spectroscopy of atoms adsorbed on metal surfaces: Theory. *Physical Review B*, 1(5):2110–2129, Mar 1970.

[54] A. Gansauer. Pinacol coupling of aromatic aldehydes catalysed by a titanocene complex: A transition metal catalysed radical reaction. *Chemical Communications*, (5):457–458, Mar 7 1997.

[55] A. Goldoni, L. Sangaletti, S. L. Friedmann, Z.-X. Shen, M. Peloi, F. Parmigiani, G. Comelli, and G. Paolucci. Temperature dependence of the electronic properties of K_3C_{60} and K_4C_{60} single-phase films investigated by means of electron spectroscopies. *Journal of Chemical Physics*, 113(18):8266–8275, Nov 8 2000.

[56] M. L. H. Green and C. R. Lucas. Some *d* bis-π-cyclopentadienyl titanium complexes with nitrogen or phosphorus ligands. *Journal of the Chemical Society—Dalton Transactions*, (8–9):1000–1003, 1972.

[57] D. J. Griffiths. *Introduction to Quantum Mechanics*. Wiley, third edition, 1998.

[58] M. Grobis, K. H. Khoo, R. Yamachika, Xinghua Lu, K. Nagaoka, Steven G. Louie, M. F. Crommie, H. Kato, and H. Shinohara. Spatially dependent inelastic tunneling in a single metallofullerene. *Physical Review Letters*, 94(13):136802, April 2005.

[59] M. Grobis, A. Wachowiak, R. Yamachika, and M. F. Crommie. Tuning negative differential resistance in a molecular film. *Applied Physics Letters*, 86:204102, May 2005.

[60] Michael Grobis. *Scanning Tunneling Spectroscopy of Fullerene Nanostructures*. PhD thesis, University of California, Berkeley, 2005.

[61] O. Gunnarsson. Superconductivity in fullerides. *Reviews of Modern Physics*, 69(2):575–606, Apr 1997.

[62] O. Gunnarsson. *Alkali-Doped Fullerides: Narrow-Band Solids with Unusual Properties*. World Scientific, River Edge, NJ, 2004.

[63] O. Gunnarsson, S. Satpathy, O. Jepsen, and O. K. Andersen. Orientation of C_{60} clusters in solids. *Physical Review Letters*, 67(21):3002–3005, Nov 1991.

[64] Olle Gunnarsson, Erik Koch, and Richard M. Martin. Mott transition in degenerate Hubbard models: Application to doped fullerenes. *Physical Review B*, 54(16):R11026–R11029, Oct 1996.

[65] J. A. Gupta, C. P. Lutz, A. J. Heinrich, and D. M. Eigler. Strongly coverage-dependent excitations of adsorbed molecular hydrogen. *Physical Review B*, 71:115416, March 2005.

[66] Michele Gusso. Study on the maximum accuracy of the pseudopotential density functional method with localized atomic orbitals versus plane-wave basis sets. *The Journal of Chemical Physics*, 128:044102, 2008.

[67] J. R. Hahn, H. J. Lee, and W. Ho. Electronic resonance and symmetry in single-molecule inelastic electron tunneling. *Physical Review Letters*, 85(9):1914–1917, Aug 2000.

[68] J. E. Han, O. Gunnarsson, and V. H. Crespi. Strong superconductivity with local Jahn-Teller phonons in C_{60} solids. *Physical Review Letters*, 90(16):167006, Apr 2003.

[69] J. E. Han, E. Koch, and O. Gunnarsson. Metal-insulator transitions: Influence of lattice structure, Jahn-Teller effect, and Hund's rule coupling. *Physical Review Letters*, 84(6):1276–1279, Feb 2000.

[70] P. Han, E. C. H. Sykes, T. P. Pearl, and P. S. Weiss. A comparative scanning tunneling microscopy study of physisorbed linear quadrupolar molecules: C_2N_2 and CS_2 on Au{111} at 4 K. *Journal of Physical Chemistry A*, 107(40):8124–8129, Oct 9 2003.

[71] Walter A. Harrison. *Electronic Structure and the Properties of Solids*. Dover Publications, Inc., New York, corrected edition, 1989.

[72] D. Haskel, Z. Islam, J. Lang, C. Kmety, G. Srajer, K. I. Pokhodnya, A. J. Epstein, and Joel S. Miller. Local structural order in the disordered vanadium tetracyanoethylene room-temperature molecule-based magnet. *Physical Review B*, 70(5):054422, Aug 2004.

[73] James R. Heath and Mark A. Ratner. Molecular electronics. *Physics Today*, 56(5):43–49, 2003.

[74] A. F. Hebard, R. C. Haddon, R. M. Fleming, and A. R. Kortan. Deposition and characterization of fullerene films. *Applied Physics Letters*, 59(17):2109–2111, 1991.

[75] A. F. Hebard, M. J. Rosseinsky, R. C. Haddon, D. W. Murphy, S. H. Glarum, T. T. M. Palstra, A. P. Ramirez, and A. R. Kortan. Superconductivity at 18 K in potassium-doped C_{60}. *Nature*, 350(6319):600–601, Apr 18 1991.

[76] Lars Hedin. New method for calculating the one-particle Green's function with application to the electron-gas problem. *Physical Review*, 139(3A):A796–A823, Aug 1965.

[77] Paul A. Heiney, John E. Fischer, Andrew R. McGhie, William J. Romanow, Arnold M. Denenstein, John P. McCauley Jr., Amos B. Smith, and David E. Cox. Orientational ordering transition in solid C_{60}. *Physical Review Letters*, 66(22):2911–2914, Jun 1991.

[78] A. J. Heinrich, C. P. Lutz, J. A. Gupta, and D. M. Eigler. Molecule cascades. *Science*, 298(5597):1381–1387, Nov 15 2002.

[79] Jae-Hyuk Her, Peter W. Stephens, Konstantin I. Pokhodnya, Michael Bonner, and Joel S. Miller. Cross-linked layered structure of magnetically ordered $[Fe(TCNE)_2] \cdot zCH_2Cl_2$ determined by rietveld refinement of synchrotron powder diffraction data. *Angewandte Chemie—International Edition*, 46(9):1521–1524, 2007.

[80] R. Hesper, L. H. Tjeng, and G. A. Sawatzky. Strongly reduced band gap in a correlated insulator in close proximity to a metal. *EPL (Europhysics Letters)*, 40(2):177–182, 1997.

[81] A. C. Hewson. *The Kondo Problem to Heavy Fermions*. Cambridge University Press: Cambridge, UK, 1993.

[82] K. W. Hipps, D. E. Barlow, and U. Mazur. Orbital mediated tunneling in vanadyl phthalocyanine observed in both tunnel diode and STM environments. *Journal of Physical Chemistry B*, 104(11):2444–2447, Mar 23 2000.

[83] Cyrus F. Hirjibehedin, Christopher P. Lutz, and Andreas J. Heinrich. Spin coupling in engineered atomic structures. *Science*, 312(5776):1021–1024, 2006.

[84] W. Ho. Single-molecule chemistry. *Journal of Chemical Physics*, 117(24):11033–11061, Dec 22 2002.

[85] B. W. Hoogenboom, R. Hesper, L. H. Tjeng, and G. A. Sawatzky. Charge transfer and doping-dependent hybridization of C_{60} on noble metals. *Physical Review B*, 57(19):11939, May 1998.

[86] J. G. Hou, J. L. Yang, H. Q. Wang, Q. X. Li, C. G. Zeng, L. F. Yuan, B. Wang, D. M. Chen, and Q. S. Zhu. Surface science—Topology of two-dimensional C_{60} domains. *Nature*, 409(6818):304–305, Jan 18 2001.

[87] Mark S. Hybertsen and Steven G. Louie. Electron correlation in semiconductors and insulators: Band gaps and quasiparticle energies. *Physical Review B*, 34(8):5390–5413, Oct 1986.

[88] J. Ihm, A. Zunger, and M. L. Cohen. Momentum-space formalism for the total energy of solids. *Journal of Physics C—Solid State Physics*, 12(21):4409–4422, 1979.

[89] Y. Iwasa and T. Takenobu. Superconductivity, Mott-Hubbard states, and molecular orbital order in intercalated fullerides. *Journal of Physics—Condensed Matter*, 15(13):R495–R519, Apr 9 2003.

[90] P. Yang (editor) J. R. Long. *Chemistry of Nanostructured Materials*, page 291. World Scientific, Hong Kong, 2003.

[91] Koblar Jackson and Mark R. Pederson. Accurate forces in a local-orbital approach to the local-density approximation. *Physical Review B*, 42(6):3276–3281, Aug 1990.

[92] H. A. Jahn and E. Teller. Stability of polyatomic molecules in degenerate electronic states. I. orbital degeneracy. *Proceedings of the Royal Society of London Series A—Mathematical and Physical Sciences*, 161(A905):220–235, Jul 1937.

[93] Rajsapan Jain, Khayrul Kabir, Joe B. Gilroy, Keith A. R. Mitchell, Kin-Chung Wong, and Robin G. Hicks. High-temperature metal-organic magnets. *Nature*, 445(7125):291–294, Jan 18 2007.

[94] T. Jamneala, V. Madhavan, and M. F. Crommie. Kondo response of a single antiferromagnetic chromium trimer. *Physical Review Letters*, 87(25):256804, Nov 2001.

[95] Tiberiu Jamneala. *Tunneling Measurements of the Electronic Structure of Magnetic Nanostructures on Surfaces*. PhD thesis, University of California, Berkeley, 2001.

[96] C. Jayaprakash, H. R. Krishna-murthy, and J. W. Wilkins. Two-impurity Kondo problem. *Physical Review Letters*, 47(10):737–740, Sep 1981.

[97] K. Jensen, J. Weldon, H. Garcia, and A. Zettl. Nanotube radio. *Nano Letters*, 7(11):3508–3511, Nov 2007.

[98] Jr. João Florêncio and K. A. Chao. Antiferromagnetic ground state in the *s*-band Hubbard model. *Physical Review Letters*, 35(11):741–744, 1975.

[99] W. L. Jorgensen and L. Salem. *The Organic Chemist's Book of Orbitals*. Academic, New York, 1973.

[100] T. A. Jung, R. R. Schlittler, J. K. Gimzewski, H. Tang, and C. Joachim. Controlled room-temperature positioning of individual molecules: Molecular flexure and motion. *Science*, 271(5246):181–184, 1996.

[101] R. Jungst, D. Sekutowski, J. Davis, M. Luly, and G. Stucky. Structural and magnetic properties of Di-μ-chloro-bis[bis(η_5-cyclopentadienyl)titanium(III)] and Di-μ-chloro and Di-*mu*-bromo-bis[bis(η_5-methylcyclopentadienyl)titanium(III)]. *Inorganic Chemistry*, 16(7):1645–1655, 1977.

[102] Javier Junquera, Óscar Paz, Daniel Sánchez-Portal, and Emilio Artacho. Numerical atomic orbitals for linear-scaling calculations. *Physical Review B*, 64(23):235111, Nov 2001.

[103] W. Kaim and M. Moscherosch. The coordination chemistry of TCNE, TCNQ and related polynitrile π acceptors. *Coordination Chemistry Reviews*, 129(1-2):157–193, Jan 1994.

[104] K. Kamarás, G. Klupp, D. B. Tanner, A. F. Hebard, N. M. Nemes, and J. E. Fischer. Ordered low-temperature structure in K_4C_{60} detected by infrared spectroscopy. *Physical Review B*, 65(5):052103, Jan 2002.

[105] R. Kerkoud, P. Auban-Senzier, D. Jérome, S. Brazovskii, I. Luk'Yanchuk, N. Kirova, F. Rachdi, and C. Goze. Insulator-metal transition in Rb_4C_{60} under pressure from ^{13}C-NMR. *Journal of Physics and Chemistry of Solids*, 57(2):143–152, 1996.

[106] B. Kessler, A. Bringer, S. Cramm, C. Schlebusch, W. Eberhardt, S. Suzuki, Y. Achiba, F. Esch, M. Barnaba, and D. Cocco. Evidence for incomplete charge transfer and La-derived states in the valence bands of endohedrally doped La@C_{82}. *Physical Review Letters*, 79(12):2289–2292, Sep 1997.

[107] J. R. Kirtley, S. Washburn, and D. J. Scalapino. Origin of the linear tunneling conductance background. *Physical Review B*, 45(1):336–346, Jan 1992.

[108] John Kirtley and Paul K. Hansma. Vibrational-mode shifts in inelastic electron tunneling spectroscopy: Effects due to superconductivity and surface interactions. *Physical Review B*, 13(7):2910–2917, Apr 1976.

[109] J. Klein, A. Léger, M. Belin, D. Défourneau, and M. J. L. Sangster. Inelastic-electron-tunneling spectroscopy of metal-insulator-metal junctions. *Physical Review B*, 7(6):2336–2348, Mar 1973.

[110] K. M. Knowles and A. T. J. van Helvoort. Anodic bonding. *International Materials Reviews*, 51(5):273–311, Oct 2006.

[111] Erik Koch, Olle Gunnarsson, and Richard M. Martin. Filling dependence of the Mott transition in the degenerate Hubbard model. *Physical Review B*, 60(23):15714–15720, Dec 1999.

[112] N. Koga and K. Morokuma. Ab initio MO study of the C_{60} anion radical—The Jahn-Teller distortion and electronic structure. *Chemical Physics Letters*, 196(1-2):191–196, Aug 7 1992.

[113] J. B. Kortright, D. M. Lincoln, R. Shima Edelstein, and A. J. Epstein. Bonding, backbonding, and spin-polarized molecular orbitals: Basis for magnetism and semiconducting transport in $V[TCNE]_{x\sim2}$. *Physical Review Letters*, 100(25):257204, 2008.

[114] M. Krause, P. Kuran, U. Kirbach, and L. Dunsch. Raman and infrared spectra of $Tm@C_{82}$ and $Gd@C_{82}$. *Carbon*, 37(1):113–115, 1999.

[115] F. Lacroix, C. E. Plecnik, S. M. Liu, F. C. Liu, E. A. Meyers, and S. G. Shore. Cyclic organohydroborate complexes of metallocenes VIII. triphenylsiloxy derivatives of group IV organometallic systems, $Cp_2M(OSiPh_3)X$ (M = Ti, Zr, Hf; X = Cl, $\{(\mu\text{-}H)_2BC_8H_{14}\}$). *Journal of Organometallic Chemistry*, 687(1):69–77, Dec 1 2003.

[116] Jérôme Lagoute, Xi Liu, and Stefan Fölsch. Link between adatom resonances and the Cu(111) Shockley surface state. *Physical Review Letters*, 95(13):136801, Sep 2005.

[117] Jérôme Lagoute, Xi Liu, and Stefan Fölsch. Electronic properties of straight, kinked, and branched Cu/Cu(111) quantum wires: A low-temperature scanning tunneling microscopy and spectroscopy study. *Physical Review B*, 74(12):125410, 2006.

[118] P. E. Lammert, D. S. Rokhsar, S. Chakravarty, S. Kivelson, and M. I. Salkola. Metallic screening and correlation effects in superconducting fullerenes. *Physical Review Letters*, 74(6):996–999, Feb 1995.

[119] B. Leinböck, B. Krömker, H. Wiechert, and M. Hofmann. Orientational ordering of N_2O molecules adsorbed on graphite(0001): A novel commensurate pinwheel structure. *Physical Review Letters*, 84(9):1954–1957, Feb 2000.

[120] Jiutao Li, Wolf-Dieter Schneider, Richard Berndt, and Bernard Delley. Kondo scattering observed at a single magnetic impurity. *Physical Review Letters*, 80(13):2893–2896, Mar 1998.

[121] Zhenqin Li and Harold A. Scheraga. Monte carlo-minimization approach to the multiple-minima problem in protein folding. *Proceedings of the National Academy of Sciences of the United States of America*, 84:6611–6615, October 1987.

[122] W. J. Liang, M. P. Shores, M. Bockrath, J. R. Long, and H. Park. Kondo resonance in a single-molecule transistor. *Nature*, 417(6890):725–729, Jun 13 2002.

[123] David R. Lide, editor. *CRC Handbook of Chemistry and Physics*. CRC Press/Taylor and Francis, Boca Raton, FL, 89$^{\text{th}}$ edition, Internet Version 2009.

[124] Elliott H. Lieb and F. Y. Wu. Absence of Mott transition in an exact solution of the short-range, one-band model in one dimension. *Physical Review Letters*, 20(25):1445–1448, June 1968.

[125] R. W. Lof, M. A. van Veenendaal, B. Koopmans, H. T. Jonkman, and G. A. Sawatzky. Band gap, excitons, and Coulomb interaction in solid C_{60}. *Physical Review Letters*, 68(26):3924–3927, Jun 1992.

[126] N. Lorente and M. Persson. Theory of single molecule vibrational spectroscopy and microscopy. *Physical Review Letters*, 85(14):2997–3000, Oct 2000.

[127] Jian Ping Lu. Metal-insulator transitions in degenerate Hubbard models and A_xC_{60}. *Physical Review B*, 49(8):5687–5690, Feb 1994.

[128] Jing Lu, Xinwei Zhang, Xiangeng Zhao, Shigeru Nagase, and Kaoru Kobayashi. Strong metal-cage hybridization in endohedral La@C_{82}, Y@C_{82} and Sc@C_{82}. *Chemical Physics Letters*, 332(3–4):219–224, 2000.

[129] Xinghua Lu, M. Grobis, K. H. Khoo, Steven G. Louie, and M. F. Crommie. Spatially mapping the spectral density of a single C_{60} molecule. *Physical Review Letters*, 90(9):096802, March 2003.

[130] Xinghua Lu, M. Grobis, K. H. Khoo, Steven G. Louie, and M. F. Crommie. Charge transfer and screening in individual C_{60} molecules on metal substrates: A scanning tunneling spectroscopy and theoretical study. *Physical Review B*, 70:115418, September 2004.

[131] V. Madhavan, W. Chen, T. Jamneala, M. F. Crommie, and N. S. Wingreen. Tunneling into a single magnetic atom: Spectroscopic evidence of the Kondo resonance. *Science*, 280(5363):567–569, 1998.

[132] Vidya Madhavan. *Electronic Properties of Magnetic Nanoclusters: A Scanning Tunneling Microscope Study of Transition Metal Atoms on Au(111)*. PhD thesis, Boston University, 2000.

[133] Gerald D. Mahan. *Many Particle Physics*. Kluwer Academic/Plenum Publishers, 2000.

[134] Nicola Manini, Erio Tosatti, and Assa Auerbach. Electron-vibron interactions in charged fullerenes. II. pair energies and spectra. *Physical Review B*, 49(18):13008–13016, May 1994.

[135] Efstratios Manousakis. Electronic structure of C_{60} within the tight-binding approximation. *Physical Review B*, 44(19):10991–10994, Nov 1991.

[136] Juan M. Manriquez, Gordon T. Yee, R. Scott Mclean, Arthur J. Epstein, and Joel S. Miller. A room-temperature molecular/organic-based magnet. *Science*, 252(5011):1415–1417, 1991.

[137] Alan P. Marchand. CHEMISTRY: Diamondoid hydrocarbons-delving into nature's bounty. *Science*, 299(5603):52–53, 2003.

[138] Michael P. Marder. *Condensed Matter Physics*. John Wiley and Sons, Inc., 2000.

[139] Richard L. Martin and James P. Ritchie. Coulomb and exchange interactions in C_{60}^{n-}. *Physical Review B*, 48(7):4845–4849, Aug 1993.

[140] J. M. Masnovi and J. K. Kochi. Cycloreversion induced by charge-transfer excitation of electron-donor acceptor complexes—wavelength-dependent photochemistry of dianthracene. *Journal of the American Chemical Society*, 107(24):6781–6788, 1985.

[141] U. Mazur, M. Leonetti, W. A. English, and K. W. Hipps. Spontaneous solution-phase redox deposition of a dense cobalt(II) phthalocyanine monolayer on gold. *Journal of Physical Chemistry B*, 108(44):17003–17006, Nov 4 2004.

[142] Focko Meier, Lihui Zhou, Jens Wiebe, and Roland Wiesendanger. Revealing magnetic interactions from single-atom magnetization curves. *Science*, 320(5872):82–86, 2008.

[143] M. B. J. Meinders, L. H. Tjeng, and G. A. Sawatzky. Comment on "C 1s autoionization study of electron hopping rates in solid C_{60}". *Physical Review Letters*, 73(21):2937, Nov 1994.

[144] Allan J. Melmed. The art and science and other aspects of making sharp tips. *Journal of Vacuum Science and Technology B*, 9(2):601–608, 1991.

[145] K. H. Michaelian, K. E. Rieckhoff, and E. M. Voigt. Valence force-field analysis of tetracyanoethylene. *Journal of Molecular Spectroscopy*, 95(1):1–8, 1982.

[146] J. S. Miller. Organometallic- and organic-based magnets: New chemistry and new materials for the new millennium. *Inorganic Chemistry*, 39(20):4392–4408, Oct 2 2000.

[147] J. S. Miller. Tetracyanoethylene (TCNE): The characteristic geometries and vibrational absorptions of its numerous structures. *Angewandte Chemie—International Edition*, 45(16):2508–2525, 2006.

[148] G. E. Moore. Cramming more components onto integrated circuits (Reprinted from Electronics, pg 114-117, April 19, 1965). *Proceedings of the IEEE*, 86(1):82–85, Jan 1998.

[149] R. G. Musket, W. McLean, C. A. Colmenares, D. M. Makowiecki, and W. J. Siekhaus. Preparation of atomically clean surfaces of selected elements: A review. *Applications of Surface Science*, 10:143–207, 1982.

[150] K. Nagaoka, T. Jamneala, M. Grobis, and M. F. Crommie. Temperature dependence of a single Kondo impurity. *Physical Review Letters*, 88(7):077205, Feb 2002.

[151] J. B. Neaton, Mark S. Hybertsen, and Steven G. Louie. Renormalization of molecular electronic levels at metal-molecule interfaces. *Physical Review Letters*, 97(21), Nov 24 2006.

[152] D. M. Newns. Self-consistent model of hydrogen chemisorption. *Physical Review*, 178(3):1123–1135, February 1969.

[153] Eiji Nishibori, Kenichi Iwata, Makoto Sakata, Masaki Takata, Hiroshi Tanaka, Haruhito Kato, and Hisanori Shinohara. Anomalous endohedral structure of Gd@C_{82} metallofullerenes. *Physical Review B*, 69(11):113412, Mar 2004.

[154] F. E. Olsson, M. Persson, A. G. Borisov, J.-P. Gauyacq, J. Lagoute, and S. Fölsch. Localization of the Cu(111) surface state by single Cu adatoms. *Physical Review Letters*, 93(20):206803, Nov 2004.

[155] Paul A. Packan. DEVICE PHYSICS: Pushing the limits. *Science*, 285(5436):2079–2081, 1999.

[156] W. W. Pai, C. L. Hsu, K. C. Lin, L. Y. Sin, and T. B. Tang. Characterization and control of molecular ordering on adsorbate-induced reconstructed surfaces. *Applied Surface Science*, 241(1–2):194–198, Feb 28 2005.

[157] F. M. Pan, J. C. Hemminger, and S. Ushioda. Adsorption of tetracyanoethylene on a nickel(111) surface studied by Auger-electron spectroscopy, thermal-desorption spectroscopy, and Raman-spectroscopy. *Journal of Physical Chemistry*, 89(5):862–867, 1985.

[158] H. Park, J. Park, A. K. L. Lim, E. H. Anderson, A. P. Alivisatos, and P. L. McEuen. Nanomechanical oscillations in a single-C_{60} transistor. *Nature*, 407(6800):57–60, Sep 7 2000.

[159] J. Park, A. N. Pasupathy, J. I. Goldsmith, C. Chang, Y. Yaish, J. R. Petta, M. Rinkoski, J. P. Sethna, H. D. Abruna, P. L. McEuen, and D. C. Ralph. Coulomb blockade and the Kondo effect in single-atom transistors. *Nature*, 417(6890):722–725, Jun 13 2002.

[160] P. Paul, Z. W. Xie, R. Bau, P. D. W. Boyd, and C. A. Reed. Ordered structure of a distorted C_{60}^{2-} fulleride ion. *Journal of the American Chemical Society*, 116(9):4145–4146, May 4 1994.

[161] M. R. Pederson, D. V. Porezag, J. Kortus, and D. C. Patton. Strategies for massively parallel local-orbital-based electronic structure methods. *Physica Status Solidi B—Basic Research*, 217(1):197–218, Jan 2000.

[162] Mark R. Pederson and Koblar A. Jackson. Variational mesh for quantum-mechanical simulations. *Physical Review B*, 41(11):7453–7461, Apr 1990.

[163] Mark R. Pederson and Koblar A. Jackson. Pseudoenergies for simulations on metallic systems. *Physical Review B*, 43(9):7312–7315, Mar 1991.

[164] Mark R. Pederson and Andrew A. Quong. Polarizabilities, charge states, and vibrational modes of isolated fullerene molecules. *Physical Review B*, 46(20):13584–13591, Nov 1992.

[165] John P. Perdew, Kieron Burke, and Matthias Ernzerhof. Generalized gradient approximation made simple. *Physical Review Letters*, 77(18):3865–3868, Oct 1996.

[166] Philip Phillips. *Advanced Solid State Physics*. Westview Press, 2003.

[167] K. I. Pokhodnya, A. J. Epstein, and J. S. Miller. Thin-film V[TCNE]$_x$ magnets. *Advanced Materials*, 12(6):410–413, Mar 16 2000.

[168] Dirk Porezag and Mark R. Pederson. Optimization of gaussian basis sets for density-functional calculations. *Physical Review A*, 60(4):2840–2847, Oct 1999.

[169] Dirk Porezag, Mark R. Pederson, and Amy Y. Liu. Importance of nonlinear core corrections for density-functional based pseudopotential calculations. *Physical Review B*, 60(20):14132–14139, Nov 1999.

[170] T. V. Rajanbabu and W. A. Nugent. Selective generation of free-radicals from epoxides using a transition-metal radical—A powerful new tool for organic-synthesis. *Journal of the American Chemical Society*, 116(3):986–997, Feb 9 1994.

[171] A. P. Ramirez. Geometrically frustrated matter—Magnets to molecules. *MRS Bulletin*, 30(6):447–451, Jun 2005.

[172] J. Y. Raty and G. Galli. Ultradispersity of diamond at the nanoscale. *Nature Materials*, 2(12):792–795, Dec 2003.

[173] B. L. Rogers, J. G. Shapter, W. M. Skinner, and K. Gascoigne. A method for production of cheap, reliable Pt-Ir tips. *Review of Scientific Instruments*, 71(4):1702–1705, 2000.

[174] J. J. Sakurai. *Modern Quantum Mechanics*. Addison-Wesley Publishing Company, Inc., revised edition, 1994.

[175] Otto F. Sankey and David J. Niklewski. Ab initio multicenter tight-binding model for molecular-dynamics simulations and other applications in covalent systems. *Physical Review B*, 40(6):3979–3995, Aug 1989.

[176] Jay D. Sau, J. B. Neaton, Hyoung Joon Choi, Steven G. Louie, and Marvin L. Cohen. Electronic energy levels of weakly coupled nanostructures: C_{60}-metal interfaces. *Physical Review Letters*, 101(2):026804, July 2008.

[177] J. Schiessling, L. Kjeldgaard, T. Käämbre, I. Marenne, J. N. O'Shea, J. Schnadt, C. J. Glover, M. Nagasono, D. Nordlund, M. G. Garnier, L. Qian, J.-E. Rubensson, P. Rudolf, N. Mårtensson, J. Nordgren, and P. A. Brühwiler. Bulk and surface charge states of K_3C_{60}. *Physical Review B*, 71(16):165420, Apr 2005.

[178] L. Senapati, J. Schrier, and K. B. Whaley. Electronic transport, structure, and energetics of endohedral $Gd@C_{82}$ metallofullerenes. *Nano Letters*, 4(11):2073–2078, Nov 2004.

[179] D. M. Seo, V. Meenakshi, W. Teizer, H. Zhao, and K. R. Dunbar. Enhanced magnetic anisotropy of Mn_{12}-acetate. *Journal of Magnetism and Magnetic Materials*, 301(1):31–36, Jun 2006.

[180] J. M. Soler, E. Artacho, J. D. Gale, A. Garcia, J. Junquera, P. Ordejon, and D. Sanchez-Portal. The SIESTA method for ab initio order-N materials simulation. *Journal of Physics—Condensed Matter*, 14(11):2745–2779, Mar 25 2002.

[181] B. C. Stipe, M. A. Rezaei, and W. Ho. Single-molecule vibrational spectroscopy and microscopy. *Science*, 280(5370):1732–1735, Jun 12 1998.

[182] B. C. Stipe, M. A. Rezaei, and W. Ho. Localization of inelastic tunneling and the determination of atomic-scale structure with chemical specificity. *Physical Review Letters*, 82(8):1724–1727, Feb 1999.

[183] S. M. Sze. *Semiconductor Devices: Physics and Technology*. Wiley, New York, second edition, 2001.

[184] Philip L. Taylor and Olle Heinonen. *A Quantum Approach to Condensed Matter Physics*. Cambridge University Press, 2002.

[185] C. Tengstedt, M. P. de Jong, A. Kanciurzewska, E. Carlegrim, and M. Fahlman. X-ray magnetic circular dichroism and resonant photomission of $V(TCNE)_x$ hybrid magnets. *Physical Review Letters*, 96(5):057209, 2006.

[186] J. Tersoff and D. R. Hamann. Theory of the scanning tunneling microscope. *Physical Review B*, 31(2):805–813, 1985.

[187] J. M. Thomas and R. Raja. Catalytic significance of organometallic compounds immobilized on mesoporous silica: economically and environmentally important examples. *Journal of Organometallic Chemistry*, 689(24, Sp. Iss. SI):4110–4124, Nov 29 2004.

[188] N. Tit and V. Kumar. Empirical tight-binding parameters for solid C_{60}. *Journal of Physics: Condensed Matter*, 5(44):8255–8264, 1993.

[189] L. H. Tjeng, R. Hesper, A. C. L. Heessels, A. Heeres, H. T. Jonkman, and G. A. Sawatzky. Development of the electronic structure in a K-doped C_{60} monolayer on a Ag(111) surface. *Solid State Communications*, 103(1):31–35, Jul 1997.

[190] N. Troullier and José Luriaas Martins. Efficient pseudopotentials for plane-wave calculations. *Physical Review B*, 43(3):1993–2006, Jan 1991.

[191] A. Wachowiak, R. Yamachika, K. H. Khoo, Y. Wang, M. Grobis, D.-H. Lee, Steven G. Louie, and M. F. Crommie. Visualization of the molecular Jahn-Teller effect in an insulating K_4C_{60} monolayer. *Science*, 310(5747):468–470, 2005.

[192] P. Wahl, P. Simon, L. Diekhöner, V. S. Stepanyuk, P. Bruno, M. A. Schneider, and K. Kern. Exchange interaction between single magnetic adatoms. *Physical Review Letters*, 98(5):056601, 2007.

[193] Peter Wahl. *Local Spectroscopy of Correlated Electron Systems at Metal Surfaces*. PhD thesis, Universität Konstanz, 2005.

[194] Lin-Lin Wang and Hai-Ping Cheng. Density functional study of the adsorption of a C_{60} monolayer on Ag(111) and Au(111) surfaces. *Physical Review B*, 69(16):165417, Apr 2004.

[195] X. J. Wang, L. Chen, A. Endou, M. Kubo, and A. Miyamoto. A study on the excitations of ligand-to-metal charge transfer in complexes Cp_2MCl_2 (Cp = π-C_5H_5, M = Ti, Zr, Hf) by density functional theory. *Journal of Organometallic Chemistry*, 678(1–2):156–165, Jul 15 2003.

[196] Yayu Wang, Emmanouil Kioupakis, Xinghua Lu, Daniel Wegner, Ryan Yamachika, Jeremy E. Dahl, Robert M. K. Carlson, Steven G. Louie, and Michael F. Crommie. Spatially resolved electronic and vibronic properties of single diamondoid molecules. *Nature Materials*, 7(1):38–42, Jan 2008.

[197] Yayu Wang, R. Yamachika, A. Wachowiak, M. Grobis, K. H. Khoo, D.-H. Lee, Steven G. Louie, and M. F. Crommie. Novel orientational ordering and reentrant metallicity in K_xC_{60} monolayers for $3 \leq x \leq 5$. *Physical Review Letters*, 99(8):086402, 2007.

[198] Yayu Wang, Ryan Yamachika, Andre Wachowiak, Michael Grobis, and Michael F. Crommie. Tuning fulleride electronic structure and molecular ordering via variable layer index. *Nature Materials*, 7(3):194–197, Mar 2008.

[199] Daniel Wegner, Ryan Yamachika, Yayu Wang, Victor W. Brar, Bart M. Bartlett, Jeffrey R. Long, and Michael F. Crommie. Single-molecule charge transfer and bonding at an organic/inorganic interface: Tetracyanoethylene on noble metals. *Nano Letters*, 8(1):131–135, Jan 2008.

[200] Daniel Wegner, Ryan Yamachika, Xiaowei Zhang, Yayu Wang, Tunna Baruah, Mark R. Pederson, Bart M. Bartlett, Jeffrey R. Long, and Michael F. Crommie. Tuning molecule-mediated spin coupling in bottom-up-fabricated vanadium-tetracyanoethylene nanostructures. *Physical Review Letters*, 103(8):087205, 2009.

[201] G. K. Wertheim, J. E. Rowe, D. N. E. Buchanan, E. E. Chaban, A. F. Hebard, A. R. Kortan, A. V. Makhija, and R. C. Haddon. Photoemission spectra and electronic properties of K_xC_{60}. *Science*, 252(5011):1419–1421, 1991.

[202] T. M. Willey, C. Bostedt, T. van Buuren, J. E. Dahl, S. G. Liu, R. M. K. Carlson, R. W. Meulenberg, E. J. Nelson, and L. J. Terminello. Observation of quantum confinement in the occupied states of diamond clusters. *Physical Review B*, 74(20), Nov 2006.

[203] T. M. Willey, C. Bostedt, T. van Buuren, J. E. Dahl, S. G. Liu, R. M. K. Carlson, L. J. Terminello, and T. Moller. Molecular limits to the quantum confinement model in diamond clusters. *Physical Review Letters*, 95(11), Sep 9 2005.

[204] Ch. Wöll, S. Chiang, R. J. Wilson, and P. H. Lippel. Determination of atom positions at stacking-fault dislocations on Au(111) by scanning tunneling microscopy. *Physical Review B*, 39(11):7988–7991, Apr 1989.

[205] R. Yamachika, M. Grobis, A. Wachowiak, and M. F. Crommie. Controlled atomic doping of a single C_{60} molecule. *Science*, 304:281–284, 2004.

[206] Ryan Yamachika, Xinghua Lu, Daniel Wegner, Yayu Wang, Andre Wachowiak, Michael Grobis, Lianne M. C. Beltran, Jeffrey R. Long, Mark Pederson, and Michael F. Crommie. Local electronic properties of titanocene chloride dimer molecules on a metal surface. *Journal of Physical Chemistry C*, 113(2):677–680, Jan 15 2009.

[207] W. L. Yang, V. Brouet, X. J. Zhou, Hyoung J. Choi, Steven G. Louie, Marvin L. Cohen, S. A. Kellar, P. V. Bogdanov, A. Lanzara, A. Goldoni, F. Parmigiani, Z. Hussain, and Z.-X. Shen. Band structure and fermi surface of electron-doped C_{60} monolayers. *Science*, 300(5617):303–307, 2003.

[208] W. L. Yang, J. D. Fabbri, T. M. Willey, J. R. I. Lee, J. E. Dahl, R. M. K. Carlson, P. R. Schreiner, A. A. Fokin, B. A. Tkachenko, N. A. Fokina, W. Meevasana, N. Mannella, K. Tanaka, X. J. Zhou, T. van Buuren, M. A. Kelly, Z. Hussain, N. A. Melosh, and Z.-X. Shen. Monochromatic electron photoemission from diamondoid monolayers. *Science*, 316(5830):1460–1462, Jun 8 2007.

[209] T. Yildirim, L. Barbedette, J. E. Fischer, C. L. Lin, J. Robert, P. Petit, and T. T. M. Palstra. T_c vs carrier concentration in cubic fulleride superconductors. *Physical Review Letters*, 77(1):167–170, Jul 1996.

[210] M. T. Yin and Marvin L. Cohen. Theory of ab initio pseudopotential calculations. *Physical Review B*, 25(12):7403–7412, Jun 1982.

[211] P. Zeppenfeld, J. Goerge, V. Diercks, R. Halmer, R. David, G. Comsa, A. Marmier, C. Ramseyer, and C. Girardet. Orientational ordering on a corrugated substrate: Novel pinwheel structure for N_2 adsorbed on Cu(110). *Physical Review Letters*, 78(8):1504–1507, Feb 1997.

[212] J. Zhang, J. Ensling, V. Ksenofontov, P. Gutlich, A. J. Epstein, and J. S. Miller. $[M^{II}(tcne)_2] \cdot xCH_2Cl_2$ (M=Mn, Fe, Co, Ni) molecule-based magnets with T_c values above 100 K and coercive fields up to 6500 Oe. *Angewandte Chemie—International Edition*, 37(5):657–660, Mar 16 1998.

[213] J. M. Ziman. *Principles of the Theory of Solids*. Cambridge University Press, second edition, 1972.

Index